Study of triple and quartic gauge boson couplings in e^+e^- collisions between 180 and 800 GeV

Dissertation

zur

Erlangung des Doktorgrades (Dr. rer. nat.)

der

Mathematisch-Naturwissenschaftlichen Fakultät

der

Rheinischen Friedrich-Wilhelms-Universität Bonn

vorgelegt von

Stefano Rosati

aus

Rom

Bonn 2002

Angefertigt mit Genehmigung der Mathematisch-Naturwissenschaftlichen Fakultät der Rheinischen Friedrich-Wilhelms-Universität Bonn

1. Referent:	Prof. Dr. M. Kobel
2. Referent:	Prof. Dr. I. Brock
Tag der Promotion:	15. Oktober 2002

Contents

1. Introduction

The purpose of elementary particle physics is the study of the fundamental interactions of matter, and their description in a theoretical model supported by experimental proofs. According to our actual knowledge, the elementary constituents of matter are fermions (i.e. spin 1/2 particles) which can be further grouped into leptons (ν_e, e),(ν_μ, μ), (ν_τ, τ) and quarks (u,d),(c,s),(t,b). The interactions which are relevant on a microscopic scale are the *electromagnetic*, the *weak* and the *strong* force; Each of these three interactions occurs through the exchange of a boson (i.e. a spin 1 particle): the photon for the electromagnetic interaction, the $W^\pm$ and Z bosons for the weak interaction, and the gluons for the strong interaction.

The theoretical description of the interactions among elementary particles is based on the concept that the invariance of the model under any continuous transformation leads to the conservation of physical quantities. This result, known as Noether's theorem, had its first application in the formulation of the electromagnetic interaction as a field theory whose Lagrangian is invariant under local phase transformations, which are transformations of the 1-dimensional unitary group $U(1)$. The request for the model to be invariant under $U(1)$ local phase transformations leads directly to the conservation of charge in electromagnetic interactions. The Maxwell equations, which had been classically formulated, can be re-proposed in the framework of quantum field theory as well. Following the success of this Quantum Electro Dynamic (QED) model, S. Glashow, S. Weinberg and A. Salam formulated in 1967 the standard theory of unified electroweak interactions [1], the so-called *Standard Model*. The Standard Model is based on the invariance under transformations of the gauge group $SU(2) \otimes U(1)$. The theory foresees the existence of four gauge bosons, i.e. the photon and the three weak gauge bosons. Two of the weak bosons, the $W^\pm$ bosons, are charged, and one is neutral, the Z boson. Couplings among three or four gauge bosons are allowed in the Standard Model. The measure of these couplings represents a fundamental test of the Standard Model gauge structure.

Couplings among three gauge bosons are foreseen in the Standard Model at tree level, only if two of the bosons involved are charged, i.e. only if at least a W^+ and a W^- are involved. Vertices of three neutral bosons, γZZ or ZZZ are forbidden at tree level. New physics beyond the Standard Model can nevertheless lead to non-vanishing couplings. The study of the production of Z boson pairs in e^+e^- collisions offers the possibility of measuring eventual anomalous couplings between three neutral gauge bosons. If case no deviations from the Standard Model are observed, limits on the values of the anomalous couplings can be set.

The LEP e^+e^- collider at CERN has been operating, since the year 1997, at center of mass energies above the kinematic threshold for the process $e^+e^- \rightarrow$ZZ (i.e. at center of mass energies greater than 183 GeV). The measure of the Z boson pair production cross section, and of possible anomalous triple gauge couplings, has been since then one of the central topics of its research program. In the first part of this work, an analysis of the data taken with the OPAL detector at LEP in the years 1999 and 2000 will be presented. The data have been taken at the highest center of mass energies ever reached by an e^+e^- collider, ranging from 192 up to 208 GeV.

The second part of this work will be dedicated to quartic gauge boson couplings, and to their relation with the spontaneous breaking of the $SU(2) \otimes U(1)$ symmetry. The realization of the spontaneous symmetry breaking is needed to introduce boson and fermion masses in the electroweak Lagrangian. The W and Z bosons acquire masses and longitudinal degrees of freedom through the introduction of a complex scalar field. A new massive scalar particle H, the Higgs boson, whose mass is a free parameter of the theory, appears in the Lagrangian. The Higgs boson has been not observed until now; the data taken by the four experiments at the LEP e^+e^- collider have allowed anyway to exclude the existence of a Standard Model Higgs boson with a mass smaller than 114.4 GeV [2].

The existence of the Higgs field is also needed to solve the problem of unitarity violation in the scattering of massive vector bosons $VV \to VV$, where V denotes a $W^\pm$ or a Z boson. These processes violate unitarity at an energy scale of ~1 TeV, but the additional amplitudes due to the Higgs boson exchange cancel the asymptotic rise of the scattering amplitudes and restore the unitarity of the model. However, if no Higgs boson with a mass smaller than ~800 GeV exists, a second solution is possible: the W and Z bosons become strongly interacting particles at TeV energies. The upper bound of ~1 TeV can be re-intepreted as the cut-off scale up to which the Standard Model can be extended before new physical interactions become apparent. A larger symmetry should exist, breaking down to $SU(2) \otimes U(1)$ and giving longitudinal components and masses to the W and Z bosons (the so-called *Strong Electroweak Symmetry Breaking*). One of the classical test grounds for these new interactions is the $VV \to VV$ scattering of massive vector bosons. The study of $VV \to VV$ scattering in e^+e^- collisions requires center of mass energies higher than those reached by LEP, which will be provided by a future e^+e^- linear collider. An experimental study of the processes $e^+e^- \to ZZ\nu\bar{\nu} \to q\bar{q}q\bar{q}\nu\bar{\nu}$ and $e^+e^- \to W^+W^-\nu\bar{\nu} \to q\bar{q}q\bar{q}\nu\bar{\nu}$, involving respectively the two scattering sub-processes WW→ZZ and WW→WW, will be presented in the second part of this work. The study has been realised according to the setup of the proposed TESLA Linear Collider, assuming an e^+e^- center of mass energy of 800 GeV, and exploiting the possibility of operating with polarised beams.

This work is organised as follows: in the second chapter an introduction on triple and quartic gauge boson couplings in the Standard Model, and in its possible extensions, will be given. The third chapter introduces the OPAL experiment at LEP, and gives a description of the physics processes relevant for an analysis of Z boson pair production at LEP2. In the fourth chapter, the Monte Carlo simulation of the events, and their reconstruction in the OPAL detector will be described. The algorithm for the identification of b-quarks, which is particularly relevant for the optimisation of the ZZ event selection, will be outlined. The fifth chapter will describe the selection of ZZ events, and in particular the selection of fully hadronic events. The last part of the chapter will treat the combination of the various ZZ decay channels in a fit of the total $e^+e^- \to ZZ$ cross section. The fit of the anomalous triple gauge couplings has been performed using the method of optimal observables. The method used and the results will be described in the sixth chapter.

The second part of this work is dedicated to the study of quartic gauge boson couplings at the proposed TESLA Linear Collider. The seventh chapter will give a description of the TESLA project, and of the design of the detector. The physics processes which are relevant for the study of WW→ZZ and WW→WW scattering will be introduced, together with a discussion of the Monte Carlo generators and of the detector simulation used to perform the study. The eighth chapter will describe the experimental analyses of the processes $e^+e^- \to ZZ\nu\bar{\nu} \to q\bar{q}q\bar{q}\nu\bar{\nu}$ and $e^+e^- \to W^+W^-\nu\bar{\nu} \to q\bar{q}q\bar{q}\nu\bar{\nu}$ at TESLA. The event selections, taking into account all relevant background processes, will be outlined. The sensitivity to signals of Strong Electroweak Symmetry Breaking will be derived in the framework of the electroweak chiral Lagrangian, which describes effectively the scattering of W and Z bosons at low energies. A binned maximum likelihood fit to the differential distributions of the selected events will be performed to estimate the sensitivity.

2. Gauge boson couplings in the Standard Model and beyond

In this chapter a general introduction on the Standard Model Lagrangian will be given, and on the symmetry principles which the Lagrangian is based on. Then a more detailed treatment of three- and four-boson couplings will follow, at first in the framework of the Standard Model, then describing possible extensions related to new physics. The Effective Lagrangians will be introduced as basis for the description of new physics beyond the Standard Model. Two cases will be treated in more detail, the neutral triple couplings and the quartic couplings; the experimental measurements which can be performed at LEP and at future e^+e^- colliders, studying respectively the production of pairs of real Z bosons and the scattering of W,Z bosons will be also described.

2.1 Introduction

The Lagrangian of the Standard Model describes the electroweak interactions among the elementary constituents of matter, which are leptons and quarks, both fermions with spin 1/2, through the exchange of bosons with spin 1. The form of the Lagrangian is dictated by symmetry principles and by the constraints coming from experimental results. The idea that all particle interactions must satisfy the so-called local gauge symmetries is intimately connected with the local conservation of physical quantities (e.g. the electromagnetic charge).

The experimental results on weak interactions have established the $V - A$ (i.e. *Vector-Axial*) structure of the charged currents; this means that the Lagrangian must be constructed by left-handed fermions. The minimal gauge group which includes charged vector currents is the $SU(2)$ group, so any theory of weak interactions has to include $SU(2)_L$ symmetry as a subgroup (where the subscript L denotes the grouping of fermions in left-handed doublets).

On the other hand, photons interact with both left- and right-handed fermions, and to build a unified electroweak Lagrangian the $U(1)$ local phase transformations, which lead to the QED (Quantum-electrodynamics) Lagrangian, must be included in the group of gauge symmetry. So the minimal choice of the symmetry group for the electroweak Lagrangian is $SU(2)_L \otimes U(1)$

2.2 SU(2)⊗U(1) Theory of Electroweak Interactions

The electroweak Lagrangian can be built in analogy to the QED Lagrangian, which describes electromagnetic interactions of charged particles through the exchange of a massless boson. More in detail, the Lagrangian of a free fermion of mass m is given by:

$$\mathcal{L} = \bar{\psi}(i\gamma^\mu \partial_\mu - m)\psi \tag{2.1}$$

This Lagrangian is not invariant under local gauge transformations:

$$\psi \to \psi' = e^{iQ\alpha(x)}\psi \tag{2.2}$$

To have the local gauge invariance satisfied, the derivative ∂_μ must be substituted by a "covariant derivative" D_μ which transforms itself under local phase transformations:

$$D_\mu \psi \to e^{iQ\alpha(x)} D_\mu \psi \tag{2.3}$$

To form the covariant derivative a vector field A_μ must be added to the normal derivative ∂_μ, with proper phase transformation properties:

$$D_\mu \equiv \partial_\mu + iQA_\mu \tag{2.4}$$

where A_μ transforms as:

$$A_\mu \rightarrow A_\mu + \partial_\mu \alpha(x) \tag{2.5}$$

The invariance of the Lagrangian 2.1 is then achieved by replacing ∂_μ by D_μ:

$$\mathcal{L} = \bar{\psi}(i\gamma^\mu \partial_\mu - m)\psi - Q\bar{\psi}\gamma^\mu \psi A_\mu. \tag{2.6}$$

Hence, by demanding local phase invariance, one is forced to the introduction of a vector gauge field A_μ which couples to the fermions. After adding a gauge invariant term corresponding to the kinetic energy of the boson field, the Lagrangian of QED takes the form:

$$\mathcal{L} = \bar{\psi}(i\gamma^\mu \partial_\mu - m)\psi - Q\bar{\psi}\gamma^\mu \psi A_\mu - \frac{1}{4}F_{\mu\nu}F^{\mu\nu} \tag{2.7}$$

The first term contains the kinetic energy and the mass of the fermion, the second term the interaction with the photon field, the last one the kinetic energy of the photon, where $F_{\mu\nu} = \partial_\mu A_\nu - \partial_\nu A_\mu$.

To build the Lagrangian of electroweak interactions the invariance under $SU(2)_L$ transformations is required in addition to local gauge $U(1)$ invariance. The general form of a transformation of the group $SU(2)_L \otimes U(1)$ depends now on 4 parameters:

$$\psi(x) \rightarrow \psi' = e^{i\vec{\tau}\cdot\vec{\alpha}(x)/2} e^{i\frac{Y}{2}\beta(x)} \tag{2.8}$$

Where $\vec{\tau}$ are the generators of the $SU(2)$ transformations, represented for example by the Pauli matrices, and Y is the weak hyper-charge which generates the $U(1)_Y$ local phase transformations. This leads to the introduction of the covariant derivative D_μ, now containing 4 different gauge bosons:

$$\partial_\mu \rightarrow D_\mu = \partial_\mu + ig\frac{\vec{\tau}}{2}\vec{W}_\mu + ig'\frac{Y_W}{2}B_\mu \tag{2.9}$$

Indicating now with χ_L left-handed fermion doublets and with ψ_R right-handed fermion singlet, it is possible to write the Lagrangian:

$$\mathcal{L} = \bar{\chi}_L\gamma^\mu[i\partial_\mu - g\frac{\vec{\tau}}{2}\vec{W}_\mu - g'\frac{Y_W}{2}B_\mu]\chi_L + \bar{\psi}_R[i\partial_\mu - g'\frac{Y_W}{2}B_\mu]\psi_R \tag{2.10}$$

which is invariant under local $SU(2)_L \otimes U(1)$ transformations. In order to build the gauge-invariant kinetic term for the gauge fields, the corresponding field strengths must be introduced:

$$B_{\mu\nu} \equiv \partial_\mu B_\nu - \partial_\nu B_\mu, \qquad \vec{\mathrm{W}}_{\mu\nu} \equiv \partial_\mu \vec{\mathrm{W}}_\nu - \partial_\nu \vec{\mathrm{W}}_\mu + g\vec{\mathrm{W}}_\mu \times \vec{\mathrm{W}}_\nu. \tag{2.11}$$

and the kinetic Lagrangian is given by:

$$\mathcal{L}_{Kin} = -\frac{1}{4}B_{\mu\nu}B^{\mu\nu} - \frac{1}{2}\mathrm{Tr}(\vec{\mathrm{W}}_{\mu\nu}\vec{\mathrm{W}}^{\mu\nu}) \tag{2.12}$$

The non-abelian gauge structure of the $SU(2)$ group generates here an important difference with QED. Since the field strengths $\mathrm{W}_{\mu\nu}$ contain a quadratic term, the Lagrangian $\mathcal{L}_{Kin}$ gives rise to cubic and quartic self-interactions among the gauge fields.

The Lagrangian 2.10 contains the interactions of the fermion fields with the gauge bosons. The charged current interactions occur through the physical fields $\mathrm{W}^\pm_\mu = (\mathrm{W}^1_\mu \mp i\mathrm{W}^2_\mu)/\sqrt{2}$, while physical fields corresponding to the Z and the γ are linear combinations of the gauge fields W_μ^3 and B_μ:

$$Z_\mu = W_\mu^3 \cos\theta_W - B_\mu \sin\theta_W \qquad A_\mu = W_\mu^3 \sin\theta_W + B_\mu \cos\theta_W \tag{2.13}$$

where θ_W is the weak mixing angle (Weinberg angle). The following conditions must be valid, to have the correct couplings of the fermions to the photon:

$$Q = \frac{Y}{2} + I_W^3 \tag{2.14}$$
$$e = g\sin\theta_W = g'\cos\theta_W \tag{2.15}$$

The quarks and leptons which figure in the Standard Model Lagrangian are summarised in table 2.2. Their quantum numbers relevant for the coupling to the bosons are also shown in the table. They are the electric charge Q, the weak hypercharge Y and the third component of the weak isospin I_W^3.

	Leptons						Quarks					
	Q	Y	I_W^3	3 Generations			Q	Y	I_W^3	3 Generations		
Doublets	0 -1	-1 -1	$1/2$ $-1/2$	$\binom{\nu_e}{e}_L$	$\binom{\nu_\mu}{\mu}_L$	$\binom{\nu_\tau}{\tau}_L$	$2/3$ $-1/3$	$1/3$ $1/3$	$1/2$ $-1/2$	$\binom{\mathrm{u}}{\mathrm{d}}_L$	$\binom{\mathrm{c}}{\mathrm{s}}_L$	$\binom{\mathrm{t}}{\mathrm{b}}_L$
Singlets	0	0	0	ν_R	ν_R	ν_R	$2/3$	$4/3$	0	u_R	c_R	t_R
	-1	-2	0	e_R	μ_R	τ_R	$-1/3$	$-2/3$	0	d_R	s_R	b_R

Table 2.1: *A summary of Leptons and Quarks and of their quantum numbers relevant for the electroweak interaction: the electric charge Q, the weak hypercharge Y and the third component of the weak isospin I_W^3. The subscripts L and R indicate the left-handed weak isospin doublets and the right-handed singlets, respectively.*

2.2.1 Gauge bosons self-couplings

In addition to the usual kinetic terms, the Lagrangian 2.12 generates cubic and quartic self-interactions among the gauge bosons:

$$\begin{aligned}\mathcal{L}_3 = & -ie\cot\theta_W[(\partial^\mu \mathrm{W}^\nu - \partial^\nu \mathrm{W}^\mu)\mathrm{W}_\mu^\dagger \mathrm{Z}_\nu - (\partial^\mu \mathrm{W}^{\nu\dagger} - \partial^\nu \mathrm{W}^{\mu\dagger})\mathrm{W}_\mu \mathrm{Z}_\nu + \mathrm{W}_\mu \mathrm{W}_\nu^\dagger(\partial^\mu \mathrm{Z}^\nu - \partial^\nu \mathrm{Z}^\mu)] \\ & -ie[(\partial^\mu \mathrm{W}^\nu - \partial^\nu \mathrm{W}^\mu)\mathrm{W}_\mu^\dagger A_\nu - (\partial^\mu \mathrm{W}^{\nu\dagger} - \partial^\nu \mathrm{W}^{\mu\dagger})\mathrm{W}_\mu A_\nu + \mathrm{W}_\mu \mathrm{W}_\nu^\dagger(\partial^\mu A^\nu - \partial^\nu A^\mu)]\end{aligned}$$

$$\begin{aligned}\mathcal{L}_4 = & -\frac{e^2}{2\sin^2\theta_W}[(\mathrm{W}_\mu^\dagger \mathrm{W}^\mu)^2 - \mathrm{W}_\mu^\dagger \mathrm{W}^{\mu\dagger} \mathrm{W}_\nu \mathrm{W}^\nu] - e^2\cot^2\theta_W[\mathrm{W}_\mu^\dagger \mathrm{W}^\mu \mathrm{Z}_\nu \mathrm{Z}^\nu - \mathrm{W}_\mu^\dagger \mathrm{Z}^\mu \mathrm{W}_\nu \mathrm{Z}^\nu] \\ & -e\cot\theta_W[2\mathrm{W}_\mu^\dagger \mathrm{W}^\mu \mathrm{Z}_\nu A^\nu - \mathrm{W}_\mu^\dagger \mathrm{Z}^\mu \mathrm{W}_\nu A^\nu - \mathrm{W}_\mu^\dagger A^\mu \mathrm{W}_\nu \mathrm{Z}^\nu \\ & -e^2[\mathrm{W}_\mu^\dagger \mathrm{W}^\mu A_\nu A^\nu - \mathrm{W}_\mu^\dagger A^\mu \mathrm{W}_\nu A^\nu]\end{aligned} \tag{2.16}$$

The term $\mathcal{L}_3$, generating triple couplings, contains only interactions of two charged W's and one neutral (Z or γ) boson (Figure 2.2.1.a). So, vertices of three neutral gauge bosons are forbidden in the Standard Model at tree level. The term $\mathcal{L}_4$, which generates quartic couplings, contains only vertices in which 2 or 4 charged W's are present (Figure 2.2.1.b and 2.2.1.c).

2.2.2 Spontaneous symmetry breaking

The $SU(2)_L$ gauge symmetry forbids to write mass terms for the gauge bosons and for the fermions. In order to generate the masses, the gauge symmetry must be broken in some way.

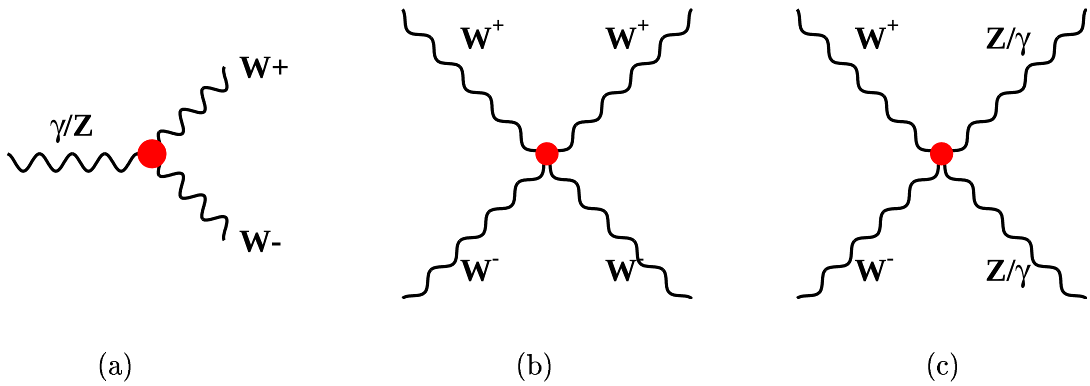

Figure 2.1: *Triple and quartic gauge boson vertices in the Standard Model.*

A possible solution to this problem consists in the Higgs mechanism, or spontaneous symmetry breaking [5], based on the fact that it is possible to get non-symmetric solutions from a symmetric Lagrangian. To realise the spontaneous symmetry breaking a $SU(2)_L$ doublet of a complex scalar fields is introduced, whose Lagrangian is invariant under $SU(2)_L \otimes U(1)_Y$ ([5], [6], [4]). The potential figuring in the Lagrangian (Goldstone Lagrangian) has an infinite set of degenerate states with minimum energy. Once a particular ground state is chosen, the $SU(2)_L \otimes U(1)_Y$ gets spontaneously broken to the electromagnetic subgroup of QED $U(1)_{QED}$. According to Goldstone theorem [6], a number of massless states equal to the number of broken generators (in this case 3) must appear.

In detail, the $SU(2) \otimes U(1)$ invariant scalar Lagrangian of the Goldstone model, and the covariant derivative, are:

$$\begin{aligned} \mathcal{L}_S &= (D_\mu\phi)^\dagger D^\mu\phi - \mu^2\phi^\dagger\phi - h(\phi^\dagger\phi)^2 \qquad && (h > 0, \mu^2 < 0) \\ D^\mu\phi &= \left[\partial_\mu - ig\tfrac{\vec{\tau}}{2}\cdot\vec{\mathrm{W}}_\mu - ig'y_\phi B_\mu\right]\phi \qquad && (y_\phi = 1/2) \end{aligned}$$

$\phi(x)$ is a complex scalar doublet which can be parametrised in the form:

$$\phi(x) = exp\left(i\frac{\vec{\tau}}{2}\cdot\vec{\theta}(x)\right)\frac{1}{\sqrt{2}}\begin{pmatrix} 0 \\ v + H(x) \end{pmatrix} \tag{2.17}$$

with 4 real fields $\vec{\theta}(x)$ and $H(x)$, and where $v/\sqrt{2}$ is the expectation value of the infinite set of degenerate states with minimum energy. Using a non-scalar field would violate the Lorentz invariance of the Lagrangian [8]. Besides, the scalar field must be neutral because $U(1)_{QED}$ must remain an unbroken symmetry.

The local $SU(2)_L$ invariance of the Lagrangian allows to rotate away any dependence on $\vec{\theta}(x)$. If one takes the so-called unitary gauge $\vec{\theta}(x) = \vec{0}$, the kinetic term of the Higgs Lagrangian takes the form:

$$(D_\mu\phi)^\dagger(D^\mu\phi) = \frac{1}{2}\partial_\mu H\partial^\mu H + (v+H)^2\left(\frac{g^2}{4}\mathrm{W}_\mu^\dagger\mathrm{W}^\mu + \frac{g^2}{8\cos^2\theta_W}\mathrm{Z}_\mu\mathrm{Z}^\mu\right) \tag{2.18}$$

The vacuum expectation value of the neutral scalar has generated a quadratic term for the $\mathrm{W}^\pm$ and the Z, i.e. the gauge bosons have acquired masses which satisfy the relation:

$$M_Z\cos\theta_W = M_W = vg/2. \tag{2.19}$$

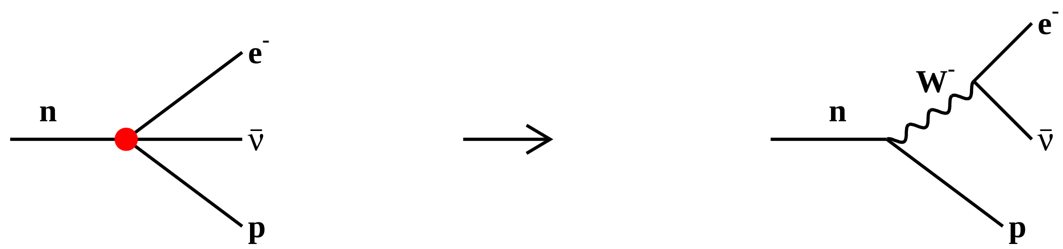

Figure 2.2: *From the neutron decay as described by the Fermi effective Lagrangian as a contact interaction, to the Intermediate Vector Boson model.*

Therefore, to give masses to the gauge bosons is sufficient to add the Goldstone Lagrangian $\mathcal{L}_S$ to the Standard Model Lagrangian. The total Lagrangian is invariant under gauge transformations, which guarantees [7] the renormalizability of the associated theory. The 3 broken generators give rise to 3 massless Goldstone bosons; besides, the $W^{\pm}$ and the Z acquire masses, but not the γ because $U(1)_{em}$ remains an unbroken symmetry. A new massive scalar particle H, the Higgs boson, appears in the Lagrangian. Before the spontaneous symmetry breaking, the Langrangian contains massless $W^{\pm}$ and Z bosons, which, as massless spin-1 fields, may have only 2 possible polarisations. After spontaneous symmetry breaking, the 3 massless Goldstone bosons are absorbed by the weak gauge bosons, which become massive and therefore acquire one additional longitudinal polarisation.

The realisation of spontaneous symmetry breaking is thus necessary to introduce the masses of the bosons and the fermions in the Standard Model. In its minimal realization, the symmetry breaking has as a consequence the existence of a massive neutral scalar particle, the Higgs boson, whose mass is a free parameter of the model. The Higgs boson has not yet been experimentally observed. The experimental searches carried on up to now, the most recent at LEP2, have made possible to exclude the existence of a Standard Model Higgs boson up to a value of the mass M_H=114.4 GeV [2]

2.3 Effective Lagrangians

Gauge boson couplings, and in particular possible anomalous contributions not foreseen in the Standard Model, can be considered in the framework of Effective Lagrangians [9]. Here the basic assumption is that there exist new physics dynamics whose degrees of freedom are so heavy (of mass scale Λ) that they cannot be produced at present or planned colliders. The only observable effects should then be anomalous interactions of the gauge bosons. Under this assumptions, the observable effects can be described by an Effective Lagrangian constructed in terms of operators involving only Standard Model fields.

An analogy can be seen with the Fermi theory of β decay [13]. The first theoretical description of the neutron decay ($\mathrm{n} \to \mathrm{p} + e^- + \bar{\nu}_e$) was treating the decay as a contact interaction between the four fermions involved (Figure 2.2); the Fermi Lagrangian was initially written as the most general Lorentz-invariant Lagrangian involving the four fermion fields. Only after the GWS-theory was developed [1], the β decay could be instead described through the exchange of a virtual massive particle, the W boson. Thus, the effects of the charged current weak interaction could be observed well before the W boson could be actually discovered in 1983 [14].

2.3.1 Triple gauge couplings

The general form of 3-boson couplings can be written, in a model independent way, in terms of a set of seven Lorentz and $U(1)_{em}$ invariant operators. This general description has been applied to both charged (γWW, ZWW) and neutral ($\gamma\gamma$Z, γZZ, ZZZ) sectors ([10], [11]). Each operator should be hermitian, multiplied by a constant coupling. As long as Λ is much larger than the actual energy range, the operators with lowest possible dimensions are dominating; contributions from higher dimensional operators are suppressed by powers of s/Λ^2, where s indicates the center of mass energy of the the bosons squared and Λ is the new physics mass scale.

Seven operators are sufficient due to the fact that only seven out of the nine helicity states of the boson pair can be reached by s-channel vector boson exchange ($J = 1$ channel). The other two helicity combinations have both boson spins pointing in the same direction and thus have $J = 2$ [11].

The measurement of 7 independent parameters would be however very difficult to perform. The set of independent operators (couplings) can be further restricted using symmetry requirements. In the charged sector (γWW, ZWW vertices) the invariance under gauge transformations and the conservation of C, P and CP are required (where C and P indicate the charge conjugation and parity operator, respectively). Other assumptions come from measurements at lower energies [11], like for example the measurement of the electron or muon dipole-moment.

In a following a more detailed description of the neutral sector will be given, in particular of the effective Lagrangian describing γZZ and ZZZ vertices.

2.3.2 Neutral triple gauge couplings

In the case of Z$\gamma\gamma$, ZZγ and ZZZ vertices one must add to the Lorentz and $SU(2) \otimes U(1)$ invariance requirements the constraint due to Bose statistics, as always two identical particles are involved. This forbids vertices of three neutral bosons when all particles are on-shell [10]. The most general form involves 2 independent couplings for each of the VZZ vertices and 4 independent couplings for each of the VZγ vertices (where V=γ or Z). As shown in section 2.2.1, vertices of three neutral gauge bosons of the kind shown in Figure 2.3.2 are forbidden in the Standard Model at tree level[1]. Thus, in contrast to the effective Lagrangian of the charged sector, which receives contributions at tree level from the Standard Model vertices, the one of the neutral sector can be seen as purely related to New Physics. The corresponding couplings are thus usually denoted as "anomalous" couplings.

Restricting the discussion to the case of VZZ vertices, the most general effective Lagrangian describing possible New Physics effects is given by [11]:

$$\mathcal{L}_{NP} = \frac{e^2}{m_Z^2}\left[-[f_4^\gamma(\partial_\mu F^{\mu\beta}) + f_4^Z(\partial_\mu Z^{\mu\beta})]Z_\alpha(\partial^\alpha Z_\beta) + [f_5^\gamma(\partial^\sigma F_{\sigma\mu}) + f_5^Z(\partial^\sigma Z_{\sigma\mu})]\tilde{Z}^{\mu\beta}Z_\beta\right] \quad (2.20)$$

where $\tilde{Z}_{\mu\nu} = 1/2\epsilon_{\mu\nu\rho\sigma}Z^{\rho\sigma}$, $Z_{\mu\nu} = \partial_\mu Z_\nu - \partial_\nu Z_\mu$ and $A_{\mu\nu} = \partial_\mu A_\nu - \partial_\nu A_\mu$.

The Lagrangian depends on four independent complex couplings, f_4^V and f_5^V, with V=γ or Z. The couplings f_4^V violate CP invariance, while the couplings f_5^V conserve it. A description of the observable effects of non-zero anomalous couplings in the study of the process $e^+e^- \to$ZZ will be given in the following.

[1] Higher order contributions from Standard Model diagrams are non-vanishing. They will be discussed in the following sections together with possible contributions from new physics beyond the Standard Model

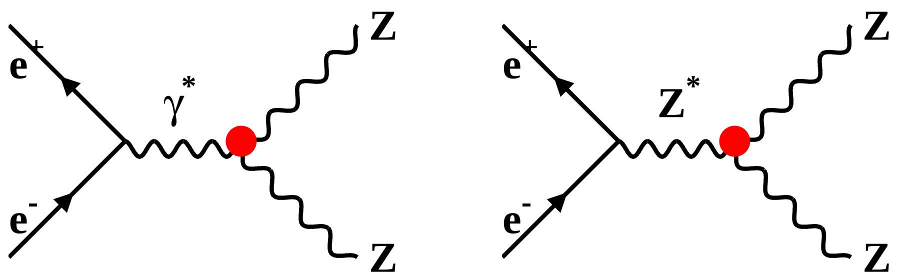

Figure 2.3: *Diagrams with vertices of three neutral gauge bosons, forbidden in the Standard Model at tree level*

2.4 Z boson pair production in e$^+$e$^-$ collisions

The production of pairs of real Z bosons occurs, in e$^+$e$^-$ collisions, through the Standard Model tree-level diagrams shown in Figure 2.4, the so-called Neutral Current, or $\mathcal{NC}02$, diagrams [18]. The process can occur at e$^+$e$^-$ center of mass energies above the threshold of ∼182 GeV, corresponding to twice the mass of the Z boson. Each of the Z bosons decays into one fermion-antifermion pair, so that the final state is a four-fermion state. The invariant masses of the two fermion-antifermion pairs peak at the Z mass $M_Z \simeq$91 GeV, and the angular distributions of the bosons and of the decay fermions in each boson's reference system preserve informations on the average polarisation of the Z boson. The Standard Model helicity amplitudes for the process $f\bar{f}$ →ZZ may be written as (see for example [11, 16]):

$$F^{\lambda}_{\tau_1\tau_2}(f\bar{f} \to ZZ; SM) = -e^2(g^Z_\lambda)^2 \frac{A^{\lambda}_{\tau_1\tau_2}}{4\beta^2 \sin\theta^* + \gamma^{-4}} \tag{2.21}$$

where τ_1, τ_2 indicate the helicities of the two Z bosons, $\lambda \equiv \lambda_1 - \lambda_2$ is the difference between the helicities of the two initial fermions[2], θ^* is the azimuthal angle of the Z bosons in their center of mass reference frame and:

$$\beta = \sqrt{1 - \tfrac{4m_Z^2}{s}} \qquad\qquad \gamma = \tfrac{1}{\sqrt{1-\beta^2}}.$$

The couplings g^Z_L and g^Z_R are those defined in the Standard Model Lagrangian involving a fermion with charge Q_f and third component of the weak isospin I^3_f:

$$g^Z_L = \tfrac{1}{\sin\theta_W \cos\theta_W}(I^3_f - Q_f \sin^2\theta_W), \qquad\qquad g^Z_R = \tfrac{1}{\sin\theta_W \cos\theta_W}(-Q_f \sin^2\theta_W)$$

The coefficients $A^{\lambda}_{\tau_1\tau_2}$ are given in table 2.2, from [16]

2.4.1 Signatures of anomalous γZZ and ZZZ couplings

The only non-vanishing helicity amplitudes introduced in the process $f\bar{f}$ →ZZ by the effective Lagrangian 2.20 are those where one Z is transverse ($\tau_1 \equiv \tau = \pm 1$) and the other longitudinal

[2] At collider energies, the mass of the initial fermions can be neglected, so the two possible values for λ are $\lambda = -1(+1)$ corresponding to an $f_{L(R)}$ fermion interacting with an $\bar{f}_{R(L)}$ antifermion respectively

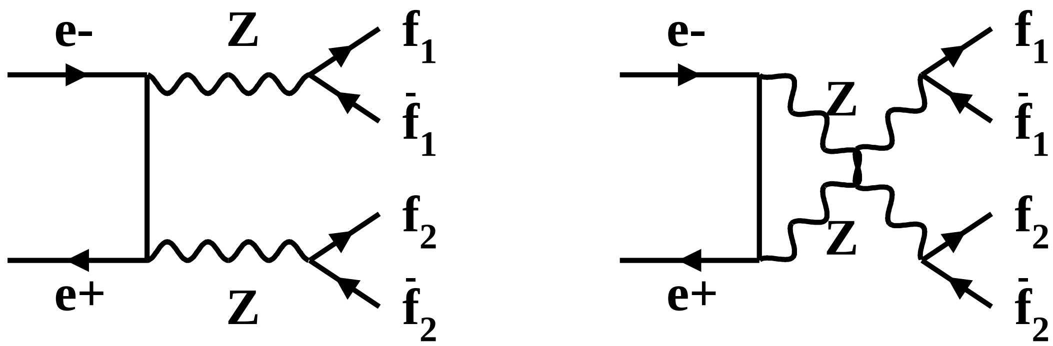

Figure 2.4: *Standard Model diagrams for Z boson pair production in* e^+e^- *collisions (NC02 diagrams).*

τ_1, τ_2	$A^{\lambda}_{\tau_1,\tau_2}$
$\tau_1\tau_2 \neq 0$	$A^{\lambda}_{\tau_1,\tau_2} = 2\sin\theta^*[2\lambda\cos\theta^*(\beta^2 - \tau_1\tau_2) - (1+\beta^2)(\tau_2 - \tau_1)]$
$\tau \neq 0$	$A^{\lambda}_{-\tau,0} = \frac{2\sqrt{2}}{\gamma}(1 - \lambda\tau\cos\theta^*)[\lambda\tau(1+\beta^2) + 2\cos\theta^*]$
$\tau_1 = \tau_2 = 0$	$A^{\lambda}_{0,0} = -\frac{4\lambda\sin(2\theta^*)}{\gamma^2}$

Table 2.2: *Helicity amplitudes for the process* $e^+e^- \to ZZ$

$(\tau_2 = 0)$. In this case the amplitudes are given by [16]:

$$F^{\lambda}_{\tau,0}(f\bar{f} \to \mathrm{ZZ}; NP) = F^{\lambda *}_{0,-\tau}(f\bar{f} \to \mathrm{ZZ}; NP) =$$
$$\frac{e^2 s^{3/2}\beta}{m_Z^3 2\sqrt{2}}(1 + \lambda\tau\cos\theta^*)[i(f_4^{\gamma}Q_f + f_4^Z g_{\lambda}^Z) - (f_5^{\gamma}Q_f + f_5^Z g_{\lambda}^Z)\beta\tau] \tag{2.22}$$

where the same definitions as in section 2.4 are used.

The CP-conserving couplings lead to real amplitudes interfering with the Standard Model ones, while the CP violating couplings lead to purely imaginary amplitudes which don't interfere with the Standard Model. The full helicity amplitudes for ZZ production are obtained by summing the SM amplitudes with the new physics (NP) ones given in eq. 2.22:

$$F^{\lambda}_{\tau_1\tau_2}(f\bar{f} \to \mathrm{ZZ}) = F^{\lambda}_{\tau_1\tau_2}(f\bar{f} \to \mathrm{ZZ}; SM) + F^{\lambda}_{\tau_1\tau_2}(f\bar{f} \to \mathrm{ZZ}; NP). \tag{2.23}$$

The amplitudes are normalised so that the differential cross section is given by:

$$\frac{d\sigma(f\bar{f} \to \mathrm{ZZ})}{d\cos\theta^*} = \frac{1}{128\pi s}\sqrt{1 - \frac{4M_Z^2}{s}} \sum_{\tau_1\tau_2}[|F^{\lambda=1}_{\tau_1\tau_2}|^2 + |F^{\lambda=-1}_{\tau_1\tau_2}|^2] \tag{2.24}$$

The observables affected by coupling values different from 0 are:

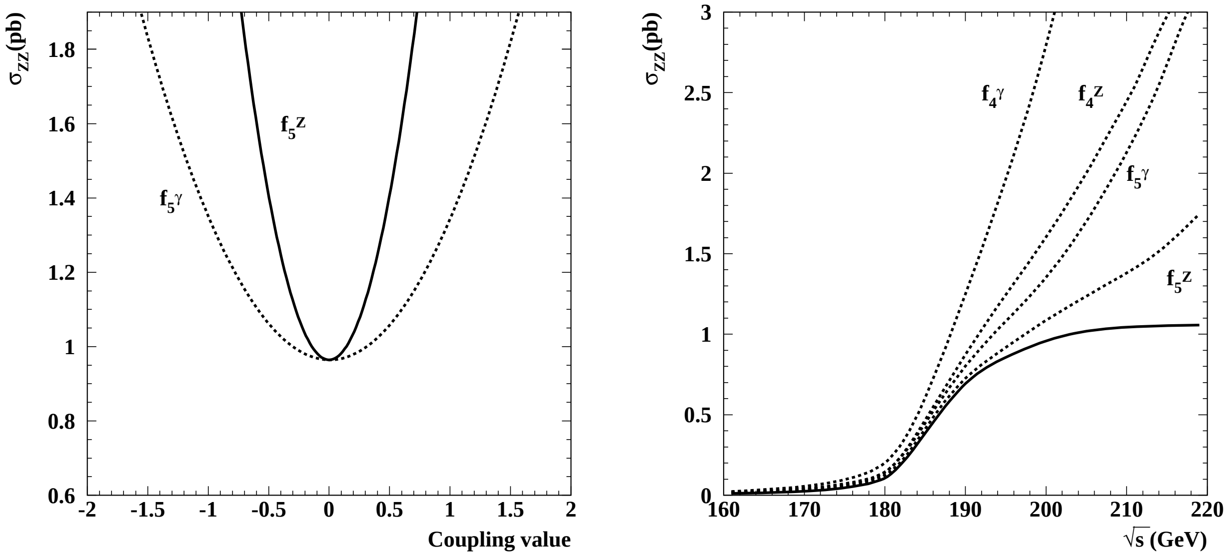

(a) (b)

Figure 2.5: *(a): total* e$^+$e$^-$ *$\rightarrow$ZZ cross section as a function of the anomalous couplings* f_5^{γ} *(full line) and* f_5^{Z} *(dashed line), at* $\sqrt{s} = 200$ *GeV. (b): total* e$^+$e$^-$ *$\rightarrow$ZZ cross section as a function of the center of mass energy, in the Standard Model (full line), and for anomalous triple couplings different from 0 (dashed lines). Each dashed line shows the cross section behaviour as a function of* $\sqrt{s}$*, when the coupling indicated in the plot is equal to 1.0*

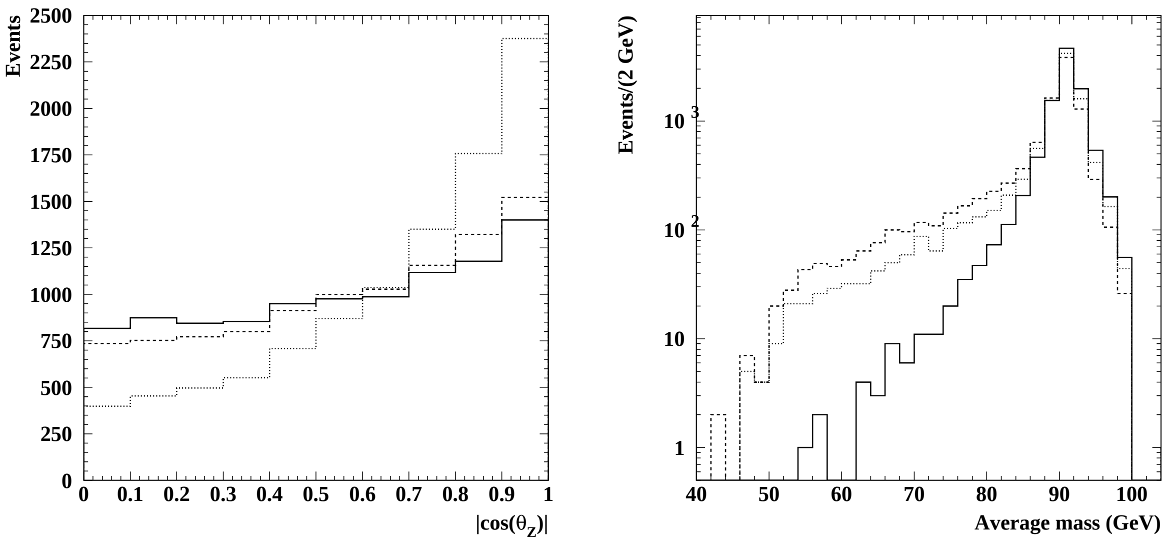

(a) (b)

Figure 2.6: *Distribution of the Z's polar production angle (a) and of the average Z's mass (b), in the case of the Standard Model (full line) and in the case of anomalous couplings different from 0. The dashed line histograms show the distributions for* $f_5^{\gamma} = 2.0$*, while the dotted line histograms show the distributions for* $f_5^{Z} = 2.0$.

- **The total cross section.** As the effective Lagrangian, and the corresponding helicity amplitudes, are linear in the anomalous couplings, the total cross section varies as a parabola as a function of the couplings. The CP-violating amplitudes (f_4^V couplings) don't interfere with the Standard Model, thus the cross section depends only quadratically on the f_4^V couplings, whereas the CP-conserving amplitudes produce interference patterns with the Standard Model contributions. In Figure 2.5.(a) the total $e^+e^- \to ZZ$ cross section as a function of the anomalous couplings is shown, at a center of mass energy $\sqrt{s}$=200 GeV. As the anomalous amplitudes 2.22 are proportional to $s^{3/2}$, the effects on the total cross section increase with the center of mass energy of the e^+e^- collisions (see Figure 2.5.(b)).
- **The angular distribution of the Z** As the anomalous amplitudes 2.22 depend on cosθ^*, i.e. on the Z's production azimuthal angle in the boson pair reference frame, they determine a change of the Z's azimuthal angular distributions. In figure 2.6.(a) the Z boson polar angle distribution in case of Standard Model couplings is compared to that expected for non-vanishing γZZ or ZZZ couplings.
- **The average polarisation of the Z bosons.** The anomalous amplitudes can only involve one transverse and one longitudinal Z. This feature induces a variation of the average polarisation of the bosons in presence of anomalous couplings. Observable effects are variations of the angular distributions of the Z's decay fermions in the center of mass frame of the $Z \to f\bar{f}$ decays.
- **The masses of the Z bosons.** Due to the β factor appearing in the anomalous amplitudes 2.22, events with Z bosons having smaller masses become more probable. This effect is more pronounced for the f_5^V couplings, due to the additional β factor present in the corresponding amplitudes. On the other hand, its importance decreases with the increase of the e^+e^- center of mass energy $\sqrt{s}$, becoming negligible for $\sqrt{s} \gg 2 \cdot M_Z$. A comparison of the Standard Model distribution of the average Z mass with the distribution expected for non-vanishing anomalous couplings is shown in figure 2.6.(b).

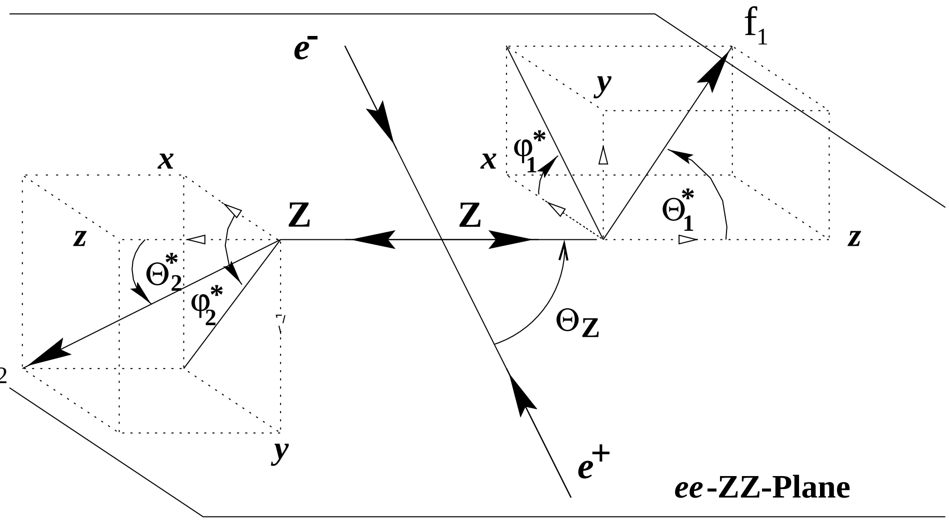

Figure 2.7: *The five angles which completely characterise the process* $e^+e^- \to ZZ \to f_1\bar{f}_1 f_2\bar{f}_2$. *The fermion angles* θ^* *and* ϕ^* *are measured in the reference system of each Z [19]. The plane shown is the plane formed by the* e^+e^- *and ZZ momenta.*

Thus, the angular distributions of the Z's and of the decay fermions allow, together with the measurement of the total cross section, a measurement of the triple gauge couplings. In an e$^+$e$^-$ →ZZ→ $f_1\bar{f}_1 f_2\bar{f}_2$ event, the measurement of 5 angles determines completely the final state; these angles are shown in Figure 2.7.

2.4.2 Standard Model contributions to the anomalous couplings

The γZZ and ZZZ couplings can only be induced, at the 1-loop level, by fermionic triangle diagrams of the type shown in figure 2.8, involving Standard Model or new Fermions. The contributions of these diagrams to the real and imaginary parts of the anomalous couplings have been calculated in [17]. When Standard Model vertices for the gauge boson interactions are used, and in particular no CP violation in the γ- and Z- couplings to the fermions is considered, then only CP conserving neutral gauge couplings can arise (f_5^V couplings). For scalars or W$^\pm$ bosons running around the loop in the diagram shown in Figure 2.8, the contribution to the CP conserving couplings is always vanishing [17].

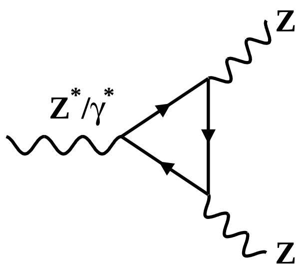

Figure 2.8: *The fermionic triangle which contributes to the γZZ and ZZZ couplings at 1-loop level*

The Standard Model contributions arise from the three families of leptons and quarks[3]. Only charged fermions contribute to the coupling f_5^γ, while f_5^Z receives contributions from the neutrinos as well. The couplings are complex, but the relative importance of the real and imaginary parts is strongly energy dependent. Below the $2m_t$ threshold, the imaginary part is negligible. In Table 2.3 the Standard Model contributions at LEP2 energy ($\sqrt{s}$ = 200 GeV) and at $\sqrt{s}$=500 GeV (from [17]) are shown.

$\sqrt{s}$ (GeV)	f_5^γ	f_5^Z
200	$2.05\text{-}0.15\cdot10^{-4}i$	$1.85\text{-}0.48\cdot10^{-4}i$
500	$0.25+0.62i$	$0.46+0.53i$

Table 2.3: *Standard Model contributions in units of* 10^{-4}

2.4.3 New physics contributions to the anomalous couplings

1-loop corrections in MSSM

As a first example of new physics effects, the one loop contributions arising in the Minimal Supersymmetric Standard Model (MSSM) can be taken into account, as in [17]. In this case the new fermions are charginos and neutralinos; the size of the contributions depends on the set of

[3] The contribution from each fermion family f arises once $\sqrt{s}$ gets above the threshold $2 \cdot m_f$.

MSSM parameters chosen, which influences the values of the chargino masses appearing in the triangle loop. In Table 2.4 the MSSM contributions to the anomalous couplings due to chargino loops are shown, for two different sets of MSSM parameters (defined in [17]).

Set	$\sqrt{s}$	f_5^γ	f_5^Z
5	200	0.29	0.49
5	500	-0.17+0.13i	-0.39+0.11i
6	200	0.43	0.70
6	500	-0.34+0.25i	-0.57+0.15i

Table 2.4: *Contributions to the anomalous couplings from chargino loops in units of* 10^{-4}

In addition there is a neutralino contribution to f_5^Z. The largest effects are obtained for a pair of neutralinos with masses (71,130) GeV, and they are, in units of 10^{-4}, $f_5^Z = -0.26 + 3.3i$ and $-0.32 - 0.22i$ at $\sqrt{s} = 200$ GeV and at $\sqrt{s} = 500$ GeV respectively.

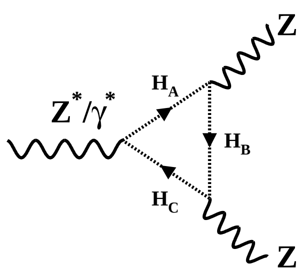

Figure 2.9: *Contribution from a triangle loop involving Higgs bosons in the Two-Higgs-Doublets model*

General 1-loop fermionic contributions

The contribution of a new fermion F can be considered in a model-independent way; new fermionic states arise in many extensions of the Standard Model, as for example in GUTS (Grand-Unified Theories) or TC (Technicolor). Assuming couplings of the electroweak size, and color-hypercolor factor $N_F = 1$ the resulting contributions of a general fermionic loop have the same size of the Standard Model and MSSM ones, so are of $\mathcal{O}(10^{-4})$. For $M_F \gg \sqrt{s}$ the resulting neutral couplings are purely real, and their dependence on M_F can be well approximated by the formula:

$$f_5^Z = 0.009 \cdot 10^{-4} \left(\frac{1\text{TeV}}{M_F}\right)^2 \tag{2.25}$$

For fermion masses of a few hundreds GeV, the contributions don't modify sizeably the Standard Model predictions. They may become relevant in case the new heavy fermions would have enhanced couplings to the γ or the Z, or in case of a large N_F factor.

1-loop bosonic contributions

CP-violating effects in triple neutral couplings may arise in the two-Higgs-doublets model (2HDM) [20], through triangle diagrams involving Higgs bosons in the loop, of the type shown in figure 2.9. To have CP-violation, three different Higgs bosons must appear in the loop. As in the 2HDM the γ coupling to the Higgses conserves the Higgs flavor, while the Z coupling violates it, only the f_4^Z coupling is affected by the loop correction. The effects on f_4^Z have been computed in [21], as a function of the Higgses mass, and are of $\mathcal{O}(10^{-6})$.

2.5 Quartic gauge couplings

2.5.1 Scattering of massive vector bosons

As shown in section 2.2.1, quartic couplings of the gauge bosons are foreseen in the Standard Model. Vertices of 4 vector bosons appear in the Lagrangian, provided that at least two of them are charged ($W^\pm$). Let's now consider the amplitudes for the process $VV \to VV$, where V generically denotes the particles $W^\pm, Z$. An example is the scattering of two W bosons, i.e. $W^+W^- \to W^+W^-$, which occurs, neglecting for the moment diagrams involving the Higgs boson, through the diagrams shown in figure 2.10.

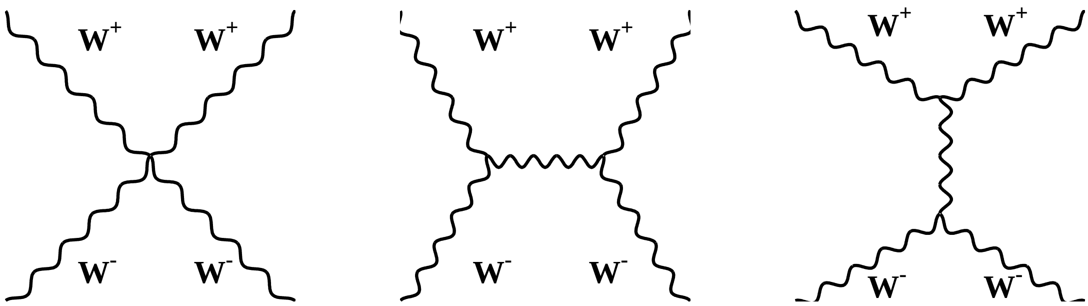

Figure 2.10: *Diagrams for W^+W^- scattering without Higgs boson exchange*

In section 2.2.2 it has been shown that the spontaneous symmetry breaking leads to the introduction of three massless scalar fields, which are "absorbed" by the gauge bosons. The $W^\pm$, Z bosons acquire in this way longitudinal degrees of freedom. In general, for a massive vector boson V the longitudinal component grows with energy [23]. In fact the polarisation vector ϵ_μ must satisfy the condition $\epsilon_\mu^V(p)P^\mu = 0$ [3], and for momenta $P_\mu = (E, 0, 0, p)$ the solution for ϵ_μ^V is:

$$\epsilon_\mu^V(p) = \frac{1}{m_V}(p, 0, 0, E) \simeq \frac{P_\mu}{m_V} + \mathcal{O}\left(\frac{m_W}{E}\right) \tag{2.26}$$

Therefore, if $\sqrt{s}$ is the center of mass energy of the two scattering bosons, each of the three diagrams in figure 2.10 has an amplitude growing as:

$$Amp \sim \frac{s^2}{m_W^4}, \tag{2.27}$$

when the four bosons are longitudinal. However, the sum of the three amplitudes grows linearly with s [3, 23]. Unitarity conservation requires each partial amplitude with angular momentum J to satisfy the relation: $\mathcal{R}e(A_J) \leq 1/2$. This means that sooner or later unitarity will be violated. The value of the critical energy $\sqrt{s_c}$ at which one of the partial waves violates unitarity varies according to the process and to the angular momenta. The S-wave scattering amplitude of longitudinally polarised W bosons, is given by (see for example [26]):

$$a_0^0 = \frac{\sqrt{2}G_F s}{16\pi} + \mathcal{O}(g^2) \tag{2.28}$$

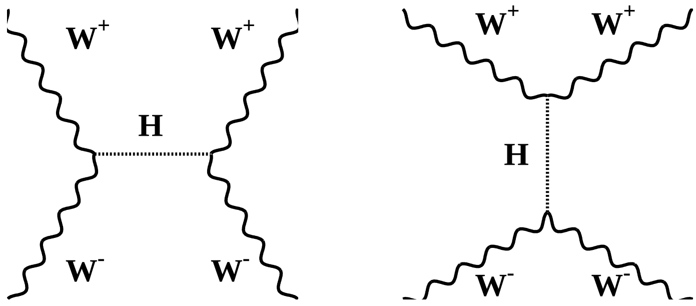

Figure 2.11: *Higgs boson exchange diagrams contributing to* $\mathrm{W^+W^-}$ *scattering*

where G_F is the Fermi coupling constant. So unitarity will be violated at a center of mass energy:

$$\sqrt{s_c} = \sqrt{\frac{4\pi\sqrt{2}}{G_F}} \simeq 1.2\mathrm{TeV} \tag{2.29}$$

In the Standard Model, the solution to this problem comes from the amplitudes with Higgs boson exchange, the diagrams in Figure 2.11. If the couplings of the Higgs to the gauge bosons are properly chosen, the additional contribution from these diagrams cancels the asymptotic rise of the WW scattering amplitudes and makes them converge towards an asymptotic value which depends on the Higgs mass.

2.5.2 Strong Electroweak Symmetry Breaking

In case a light Higgs boson is not realised in Nature, a second solution to the problem of unitarity violation exists. The upper bound of ~1 TeV can be seen as the scale up to which the Standard Model of the electroweak interaction can be extended before new phenomena due to new interactions become visible. At higher energies, to cancel the asymptotic rise of the scattering amplitudes, W and Z bosons must become strongly interacting. The new strong interaction of the gauge bosons can be traced back to a new fundamental strong interaction whose characteristic scale is of the order 1 TeV [29]. If the Lagrangian of the new interaction is chiral-invariant [30], the symmetry can be spontaneously broken to generate the masses and the longitudinal degrees of freedom of the bosons. The minimal way to realize this is via the breaking $SU(2) \otimes SU(2) \to SU(2)$, in such a way that the isospin group $SU(2)$ remains unbroken. In this case the Equivalence Theorem, whose first tree-level formulation is in [36], allows to predict the amplitudes for the scattering of longitudinal bosons for high energies below the scale at which new scalar resonances can be produced.

As seen in section 2.2.2, after the spontaneous breaking of the $SU(2)$ symmetry, the resulting Goldstone bosons are “absorbed” by the gauge bosons which acquire the additional longitudinal degree of freedom. The equivalence theorem asserts that for gauge boson energies much greater than $\mathrm{M_W}$, the following relation between the gauge bosons and the Goldstone bosons amplitudes holds [36, 24, 27]:

$$A(V_L^{a_1}, ..., V_L^{a_n}; \Phi_\alpha) = A(-i\pi^{a_1}, ..., -i\pi^{a_n}; \Phi_\alpha) + \mathcal{O}(M_\mathrm{W}/E), \tag{2.30}$$

where the π^a are the Goldstone bosons fields and Φ_α denotes other possible on-shell physical particles. For theories in which the chiral symmetry is broken spontaneously, it is possible to define effective Lagrangians for the associated Goldstone fields. They are written as expansions in the dimensions of the field operators, or equivalently, going to the momentum space, as expansions in the center of mass energy $\sqrt{s}$ [30, 31]. This expansion contains a parameter-free leading order interaction (plus higher order terms) which reflects the structure of the underlying strong interaction theory. As a first approach, it may be assumed that the symmetry breaking pattern of the new interaction is such that $SU(2) \otimes SU(2) \to SU(2)_c$, where $SU(2)_c$ denotes the so-called custodial $SU(2)$ symmetry, which leaves the parameter:

$$\rho \equiv \left(\frac{M_{\mathrm{W}}}{M_{\mathrm{Z}} \cos\theta_W} \right)^2 = 1 \tag{2.31}$$

unchanged up to small perturbative corrections. This condition is strongly supported by the electroweak precision data [38]. Under this assumptions, the kinetic terms and the first terms in the chiral Lagrangian, involving quartic interactions of the Goldstone fields are given by [26]:

$$\mathcal{L} = \mathcal{L}_g + \mathcal{L}_f + \mathcal{L}_0 + \sum_{i=1,14} \mathcal{L}_i \tag{2.32}$$

where $\mathcal{L}_g$ denotes the kinetic terms of the $\mathrm{W}^{\pm,3}$ and B fields, as in equation 2.12 and $\mathcal{L}_f$ denotes the Lagrangian coupling the gauge fields to the matter fields as in equation 2.10, through the usual covariant derivative:

$$D_\mu = \partial_\mu + ig\frac{\vec{\tau}}{2}\vec{W}_\mu + ig'\frac{Y_W}{2}B_\mu \tag{2.33}$$

already introduced in section 2.2. In general, the Goldstone fields $\vec{\pi}$ can be described by the unitary matrix:

$$U = exp(-i\vec{\pi} \cdot \vec{\tau}/F) \tag{2.34}$$

where the coefficient F parametrises the coupling between the Goldstone particles and the gauge fields W, B. The custodial-symmetric term $\mathcal{L}_0$ is given by:

$$\mathcal{L}_0 = \frac{F^2}{4}\mathrm{Tr}[(D_\mu U)^\dagger (D^\mu U)] \tag{2.35}$$

The value of $F = (\sqrt{2}G_F)^{-1/2} = 246$ GeV is fixed by the values of the W and Z masses which figure in $\mathcal{L}_0$:

$$\mathcal{L}_0 = M_{\mathrm{W}}^2 \mathrm{W}_\mu^+ \mathrm{W}^{-\mu} + \frac{1}{2} M_{\mathrm{Z}}^2 \mathrm{Z}_\mu \mathrm{Z}^\mu \tag{2.36}$$

In the Standard Model, F is replaced by the expectation value of the Higgs field in the ground state v (see section 2.2.2). Although the meaning of the two parameters is different in the two scenarios, as $F = v$ the symbol v is usually adopted, and will be adopted in the following, to characterise the weak-interaction scale.

As seen before, at the next order in the expansion, 14 operators can be defined [30] in the chiral Lagrangian. In the following, the treatment will be restricted to those which involve genuine quartic boson interactions, i.e. which do not have triple gauge boson vertices associated to the quartic couplings. This operators can be determined in the study of WW→WW scattering. To write the operators in terms of the W±,Z fields, a vector field can be defined starting from the Goldstone fields, as [24, 26]:

$$\mathrm{V}_\mu = U^\dagger D_\mu U. \tag{2.37}$$

The independent dimension-4 operators, which may be formed, are:

$$\mathcal{L}_4 = \frac{\alpha_4}{16\pi^2}\mathrm{Tr}[\mathrm{V}_\mu \mathrm{V}_\nu]\mathrm{Tr}[\mathrm{V}^\mu \mathrm{V}^\nu] \tag{2.38}$$

$$\mathcal{L}_5 = \frac{\alpha_5}{16\pi^2}\mathrm{Tr}[\mathrm{V}_\mu \mathrm{V}^\mu]\mathrm{Tr}[\mathrm{V}_\nu \mathrm{V}^\nu] \tag{2.39}$$

$-18.9 \leq \alpha_4 \leq +1.7$	$-3.2 \leq \alpha_6 \leq +0.28$
$-47.4 \leq \alpha_5 \leq +4.4$	$-3.0 \leq \alpha_7 \leq +0.28$
	$-3.3 \leq \alpha_{10} \leq +0.30$

Table 2.5: *Indirect bounds on the chiral Lagrangian coefficients from precision measurements at the Z-pole and at low energy. The limits are derived at 90% confidence level allowing only one parameter to be different from zero at a time.*

$$\mathcal{L}_6 = \frac{\alpha_6}{16\pi^2}\mathrm{Tr}[\mathrm{V}_\mu \mathrm{V}_\nu]\mathrm{Tr}[\mathcal{T}\mathrm{V}^\mu]\mathrm{Tr}[\mathcal{T}\mathrm{V}^\mu] \tag{2.40}$$

$$\mathcal{L}_7 = \frac{\alpha_7}{16\pi^2}\mathrm{Tr}[\mathrm{V}_\mu \mathrm{V}_\mu]\mathrm{Tr}[\mathcal{T}\mathrm{V}_\nu]\mathrm{Tr}[\mathcal{T}\mathrm{V}^\nu] \tag{2.41}$$

$$\mathcal{L}_{10} = \frac{\alpha_{10}}{16\pi^2}\frac{1}{2}(\mathrm{Tr}[\mathcal{T}\mathrm{V}^\mu][\mathcal{T}\mathrm{V}^\nu])^2, \tag{2.42}$$

where $\mathcal{T} = U\tau_3 U^\dagger$. The first two terms $\mathcal{L}_4, \mathcal{L}_5$ are $SU(2)_c$ custodial symmetric, i.e. they leave the value $\rho = 1$ unchanged[4]. The operators $\mathcal{L}_6$, $\mathcal{L}_7$, $\mathcal{L}_{10}$. due to the presence of $\mathcal{T}$, violate the custodial $SU(2)_c$ symmetry. Each of the $\mathcal{L}_i$ terms is proportional to a coupling α_i, whose value in the Standard Model is zero. From the magnitude of loop effects which carry a factor $1/16\pi^2$ together with an additional power of s/v^2 [24], the largest value of $\sqrt{s}$ for a chiral expansion to be valid may be estimated as [37] $\sqrt{s} \leq 4\pi v \sim 3$ TeV. If the coefficients α_i where required to be much bigger than 1, new resonances would have to be visible before the scale of 3 TeV. This means that the threshold for the production of resonances associated with the new strong interaction should be in this case between 1 and 3 TeV. In general, the coefficients α_i are then related to the scales of new physics Λ_i^* by dimensional analysis [37]:

$$\frac{\alpha_i}{16\pi^2} = \left(\frac{v}{\Lambda_i^*}\right)^2. \tag{2.43}$$

where v=246 GeV. In the absence of resonances lighter than $4\pi v$, from dimensional analysis one expects:

$$\Lambda_i^* \simeq 4\pi v \simeq 3\mathrm{TeV}, \tag{2.44}$$

and this corresponds to an order of magnitude for the coefficients of the chiral Lagrangian $\alpha_i \simeq \mathcal{O}(1)$.

2.5.3 Current bounds on Electroweak Chiral Lagrangian parameters

Indirect bounds from low-energy measurements

The coefficients $\alpha_{4,5}$ and $\alpha_{6,7,10}$ in the chiral Lagrangian can be indirectly constrained by low-energy experimental observables, to which they contribute through one-loop diagrams of the type shown in Figure 2.12. However, the loop divergences must be absorbed by the renormalization constant counter-terms, so the bounds obtained by keeping only the leading logarithmic terms should be considered only as a rough estimate, affected by large uncertainties. Since the ignored constant terms are of the same size of the logarithmic contributions, the size of these uncertainties could even be a factor 2 or 3 [24]. The 90% C.L. indirect bounds on the Chiral Lagrangian coefficients are shown in Table 2.5 (from [33]). Although the bounds on the ρ parameter severely constrain the $SU(2)_c$-violating parameters α_6, α_7 and α_{10}, they are still not constrained between values smaller than the natural size $\alpha_i \sim \mathcal{O}(1)$.

[4] The operators $\mathcal{L}_4, \mathcal{L}_5$ are explicitly $SU(2)_c$ invariant, but they do contribute to the renormalisation of a $SU(2)_c$ violating 2-dimensional operator. This induces a deviation of the ρ parameter at the loop level, which is anyway compatible with the electroweak precision measurements.

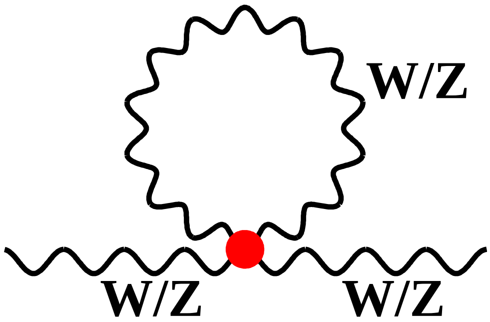

Figure 2.12: *One-loop corrections to the W and Z propagators, receiving contributions from anomalous quartic vertices*

Unitarity bounds

The weak isospin amplitudes $A^{(I)}$ $(I = 0, 1, 2)$ for WW scattering have been calculated in [26], assuming $SU(2)_C$ custodial symmetry (so keeping only the terms $\mathcal{L}_{4,5}$ of the chiral Lagrangian). The isospin amplitudes may be decomposed with respect to orbital angular momentum:

$$A^{(I)} = 32\pi \sum_{l=0}^{\infty} (2l+1) P_l(\cos\theta) a_l^I \tag{2.45}$$

All amplitudes with $I + l$ =odd vanish due to CP invariance, while angular momentum states with $l > 2$ are populated only by higher-order operators in the chiral Lagrangian. Unitarity requires $Re(a_I^l) \leq 1/2$; the strongest constraints come from the S-wave amplitudes for isospin 0 and 2 channels, which are given by:

$$a_0^0 = \frac{1}{64\pi}\left[+\frac{4s}{v^2} + \frac{16}{3}(7\alpha_4 + 11\alpha_5)\frac{s^2}{v^4}\right] \tag{2.46}$$

$$a_0^2 = \frac{1}{64\pi}\left[-\frac{2s}{v^2} + \frac{32}{3}(2\alpha_4 + \alpha_5)\frac{s^2}{v^4}\right] \tag{2.47}$$

The allowed α_4, α_5 values depend quite strongly on the WW scattering center of mass energy $\sqrt{s}$. In figure 2.13 the allowed regions in the (α_4, α_5) plane, calculated on the basis of the amplitudes 2.46, and 2.47, are shown, at $\sqrt{s} = 500$ GeV and $\sqrt{s}$=800 GeV.

2.5.4 Amplitudes for WW→WW scattering

The amplitudes for the processes of the type WW→WW, where V indicates a $W^{\pm}$ or a Z, can be calculated in the framework of the electroweak chiral Lagrangian, as in [26]. The leading contribution to the amplitudes is associated with longitudinal gauge bosons; their expression at asymptotic energies, at which the W,Z masses can be neglected $(|s|, |t|, |u| \gg M_{\mathrm{W}}^2)$, are given in table 2.6. Here s, t, u indicate the Mandelstam variables characterising the scattering process; e.g. in this case $\sqrt{s}$ is the center of mass energy of the scattering bosons. Elastic $W^+W^- \to W^+W^-$ scattering depends only on α_4, α_5, while the two processes $W^+W^- \to ZZ$ and $W^{\pm}Z \to W^{\pm}Z$ can be exploited to measure both the $SU(2)_c$ custodial coefficients α_4, α_5 and the $SU(2)_c$ custodial violating α_6, α_7. The process ZZ→ZZ is the only one which is sensitive to the coefficient α_{10}.

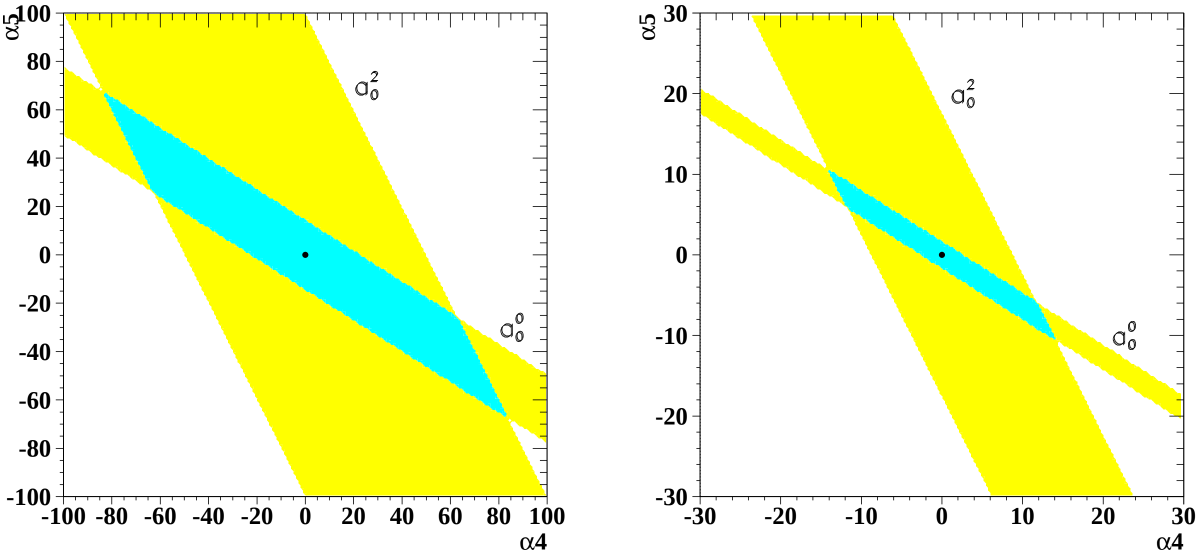

(a) (b)

Figure 2.13: *Unitarity bounds on the anomalous quartic couplings α_4, α_5. The gray shaded areas show the allowed regions for each of the S-wave isospin amplitudes a_0^0 and a_0^2, in the (α_4, α_5) plane. The Standard Model value of the couplings corresponds to the point (0,0). The allowed regions at a subprocess energy of 500 GeV (a) and 800 GeV (b) are shown.*

Process	Amplitude
$W^+W^- \to W^+W^-$	$A = -\frac{u}{v^2} + \frac{4(s^2+t^2+2u^2)}{v^4}\alpha_4 + \frac{8(s^2+t^2)}{v^4}\alpha_5$
$W^+W^- \to ZZ$	$A = +\frac{s}{v^2} + \frac{4(t^2+u^2)}{v^4}(\alpha_4+\alpha_6) + \frac{8s^2}{v^4}(\alpha_5+\alpha_7)$
$W^\pm Z \to W^\pm Z$	$A = +\frac{t}{v^2} + \frac{4(s^2+u^2)}{v^4}(\alpha_4+\alpha_6) + \frac{8t^2}{v^4}(\alpha_5+\alpha_7)$
$ZZ \to ZZ$	$A = \frac{8(s^2+t^2+u^2)}{v^4}[(\alpha_4+\alpha_5)+2(\alpha_6+\alpha_7+\alpha_{10})]$

Table 2.6: *Amplitudes for the scattering WW→WW of $W^\pm$ and Z bosons*

2.5.5 Signatures of SEWSB signals in e^+e^- collisions

At e^+e^- colliders, the scattering of $W^\pm$,Z bosons can be studied analysing processes of the type e^+e^- →6-fermion. The relevant final states, and the corresponding WW scattering subprocesses, are listed in Table 2.7. In particular, the subprocesses $W^+W^- \to W^+W^-$ and $W^+W^- \to ZZ$ lead to final states of the type $\nu\bar{\nu}f\bar{f}f\bar{f}$, while the subprocess $W^\pm Z \to W^\pm Z$ and $ZZ \to ZZ$ lead to $e\nu f\bar{f}f\bar{f}$ and $eef\bar{f}f\bar{f}$ final states respectively. $W^\pm$ bosons are radiated off electron/positrons with a probability $g^2/16\pi^2 \sim 3\cdot 10^{-3}$. On the other hand, the couplings of the Z bosons to electrons/positrons are smaller than those of the W's so the radiation of Z bosons is suppressed compared to W bosons[5] Hence, the W^+W^- scattering reactions are those having the highest sensitivity to the α_i couplings. The corresponding Feynman diagrams are shown in figure 2.14. Experimental observables influenced by the next-to-leading order terms of the chiral Lagrangian

[5] The neutral current coupling of the Z to e^+e^- is given by [3] $-i\frac{g}{\cos\theta_W}\gamma^\mu\frac{1}{2}(c_V^e - c_A^e\gamma^5)$ where the values of the vector and axial coupling for electrons are $c_V^e = -\frac{1}{2} + 2\sin^2\theta_W \simeq -0.03$ and$^1 c_A^e = \quad \frac{}{2}$ respectively.

Final state	Scattering processes	Couplings
$\nu\bar{\nu}f\bar{f}f\bar{f}$	$W^+W^- \to W^+W^-$ and $W^+W^- \to ZZ$	$\alpha_{4,5}$ and $\alpha_{4,5,6,7}$
$e\nu f\bar{f}f\bar{f}$	$W^\pm Z \to W^\pm Z$	$\alpha_{4,5,6,7}$
$ee f\bar{f}f\bar{f}$	$ZZ \to ZZ$	$\alpha_{4,5,6,7,10}$

Table 2.7: *6-fermion processes relevant for the study of WW scattering at* e^+e^- *colliders. The quartic couplings which each process is sensitive to are also shown.*

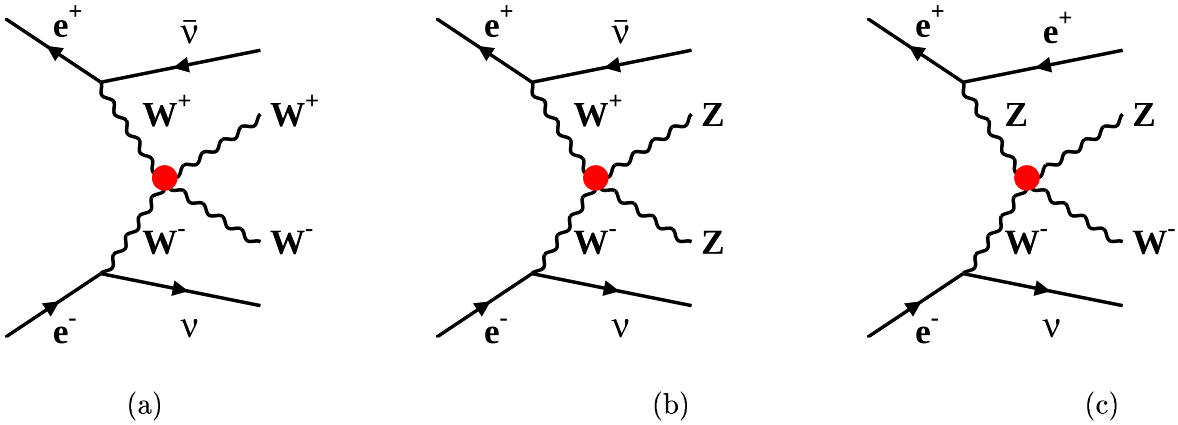

Figure 2.14: *WW scattering diagrams in* e^+e^- *collisions*

(i.e. by values of the α_i couplings different from 0), are:

- **The total cross section**. The $\mathcal{L}_i$ terms of the chiral Lagrangian are linear in the α_i couplings, hence the dependence of the total cross section on the couplings is parabolic. Besides, the additional quartic contributions introduced by the $\mathcal{L}_i$ terms are CP conserving, so an interference pattern is expected in the dependence of the total cross section on the couplings. The ratio of the total cross section to the Standard Model value for the processes $e^+e^- \to W^+W^-\nu\bar{\nu}$ and $e^+e^- \to ZZ\nu\bar{\nu}$, as a function of the quartic couplings α_4 and α_5, is shown in the figures 2.15.(a) and 2.15.(b)

- **The angular distributions**. The anomalous quartic couplings change the relative weight of each boson's polarisation state. This affects the angular distributions of the bosons, and those of their decay products. In figure 2.16.(a) the distribution of the cosine of the boson's polar angle is shown, in case of the Standard Model and for values of the coefficients α_i different from 0.

- **The boson-pair mass**. The impact of the strong interaction terms increases with the center of mass energy of the WW$\to$WW subprocess. In particular, the additional quartic contributions introduced by the $\mathcal{L}_i$ terms rise proportional to s^2, as can be seen in table 2.6. The maximal power of s is realised only for amplitudes in which all four bosons are longitudinally polarised. Replacing one longitudinal boson with a transverse one removes a factor $\sqrt{s}/v$. The invariant mass of the boson pair, i.e. of the four decay fermions is then sensitive to the couplings α_i. The distribution of the WW invariant mass is shown in Figure 2.16.(b). The distribution expected in the Standard Model ($\alpha_i \equiv 0$) is compared to the one expected in case one of the coefficients α_i is different from 0.

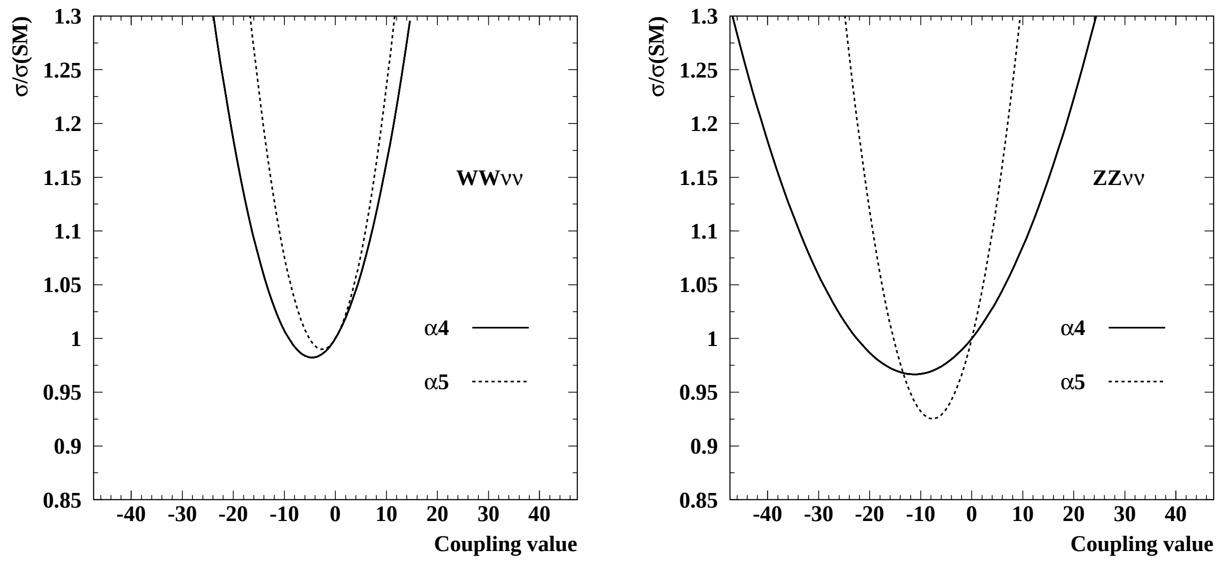

(a) (b)

Figure 2.15: *Ratio of the total $WW\nu\nu$ (a) and $ZZ\nu\nu$ (b) cross sections to the Standard Model value, as a function of the quartic couplings α_4 (full lines) and α_5 (dashed lines).*

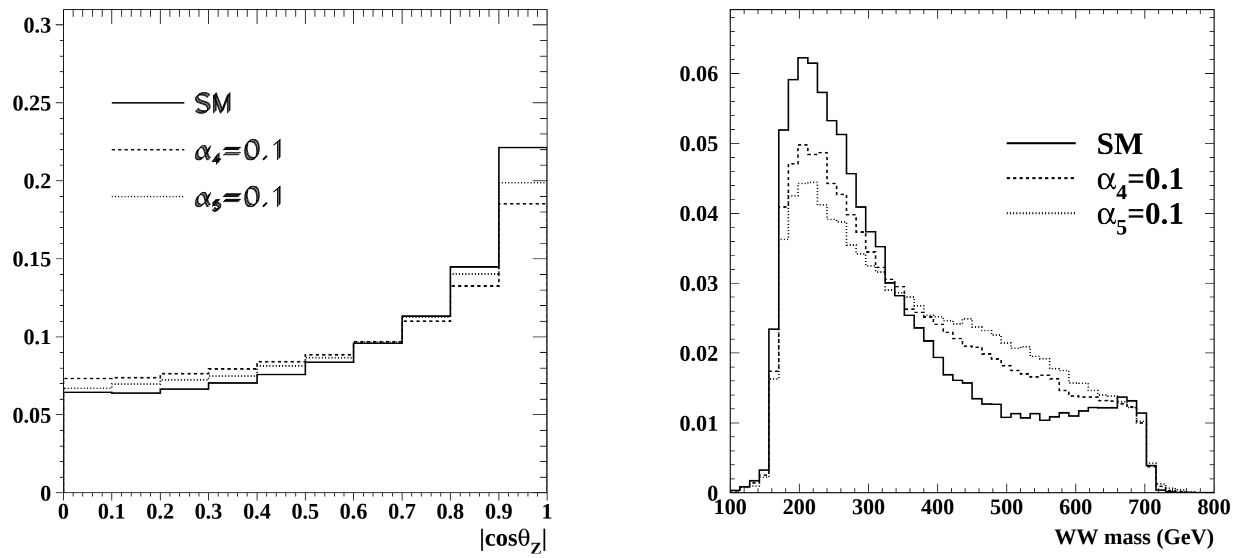

(a) (b)

Figure 2.16: *Distribution of the bosons polar angle in* $e^+e^- \to ZZ\nu\bar{\nu}$ *events, in case of the Standard Model ($\alpha_4 = \alpha_5 = 0$, full-line histogram) or in case of values of the quartic anomalous couplings different from 0 (dashed- and dotted-line histograms).*

2.6 Summary on the measurement of gauge boson couplings at e^+e^- colliders

As shown in the previous sections, the study of the process $e^+e^- \to ZZ$ allows the measurement of possible anomalous γZZ and ZZZ couplings. The study of this process is possible at e^+e^-

center of mass energies above the threshold of $\sim$182 GeV. In the following chapters the analysis of the data taken at the LEP collider in the years 1999 and 2000 at center of mass energies $192 \leq \sqrt{s} \leq 208$ GeV will be described.

The processes involving quartic vertices of massive bosons, of the type shown in Figure 2.7, cannot be studied at LEP. Although they are kinematically allowed, their cross section is negligible and the sensitivity to the coefficients of the chiral Lagrangian is correspondingly not significant. Future e^+e^- colliders, operating at center of mass energies reaching the TeV scale, will on the other hand provide the possibility of studying the scattering of massive vector bosons. As it will be shown in the second part of this thesis, an e^+e^- collider like TESLA [40], operating at a center of mass energy of 800 GeV, will provide the necessary statistics to measure with high sensitivity possible deviations from the Standard Model in the scattering of two massive bosons.

3. LEP and the OPAL experiment

This chapter will describe the OPAL experiment at the LEP e^+e^- collider. After a general description of the collider and of the OPAL detector, the characteristics of the physics processes relevant for the study of Z boson pair production in e^+e^- collisions will be introduced.

3.1 The LEP collider

The LEP (**L**arge **E**lectron **P**ositron collider) e^+e^- collider, at the European Organisation for Nuclear Research CERN, is an e^+e^- storage ring which has been operating from the year 1989 to the year 2000. The LEP ring has a circumference of 27 km; bunches of electrons and positrons circulate in the ring along opposite directions and collide in four points, where the detectors ALEPH, DELPHI, L3 and OPAL have been installed. Since the beginning of the data taking,

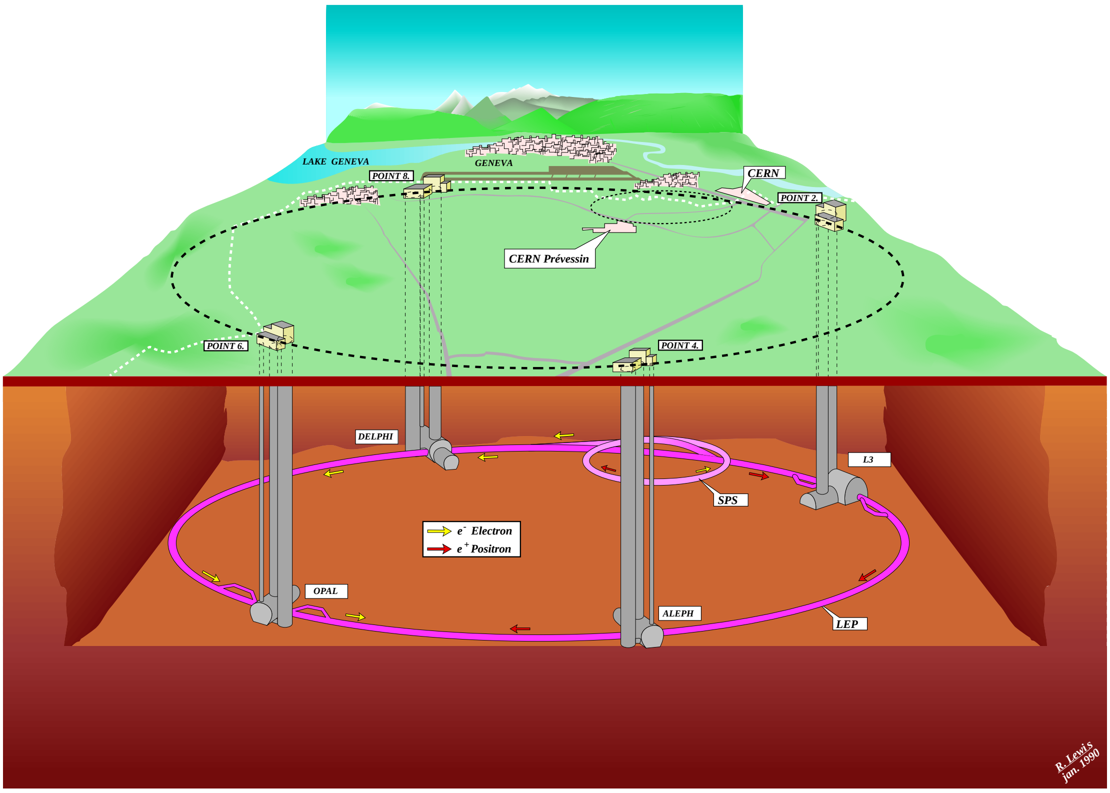

Figure 3.1: *The LEP storage ring at CERN, and the four experiments.*

in fall 1989, until the summer of 1995, the e^+e^- center of mass energy $\sqrt{s}$ was about 91 GeV, corresponding to the mass of the Z boson. Each experiment collected during this period an integrated luminosity of about 175 pb^{-1}, which corresponds to about 4.5 millions of hadronic Z decays. This has allowed to perform many precision tests of the Standard Model of the electroweak and strong interactions.

Since fall 1995 the electron and positron beam energy has been increased by successively adding superconduncting cavities along the ring (this second period of data taking is the so-called LEP2 period). LEP became then the world highest energy e^+e^- collider. The increase of the center of mass energy up to 208 GeV allowed to study e^+e^- processes in an energy range never reached before. Since the energy of 161 GeV was reached, in year 1996, the production of pairs of W bosons has been for the first time possible at an e^+e^- collider. When the energy of 183 GeV was reached, in the year 1997, also the production of pairs of Z bosons could be studied. A further central topic of the LEP2 physics program was the search for Higgs bosons and for new physics beyond the Standard Model, like for example supersymmetric particles.

In Table 3.1 a summary of the integrated luminosities $\mathcal{L}$ collected at LEP is shown. During the year 1999 data were taken at the four center of mass energies $\sqrt{s}$ =192 GeV, $\sqrt{s}$ =196 GeV, $\sqrt{s}$ =200 GeV and $\sqrt{s}$=202 GeV. During the year 2000, the last year of data taking, the goal of LEP was to take data at the highest energy possible. A different technique was used for the beam acceleration, consisting in adjusting and stabilising the beams at energies of about 200 GeV, and then increasing the energy in successive steps during the same fill (the so called mini-ramps). This led to a continuous energy spectrum. The resulting luminosity distribution for the year 2000 data is shown in figure 3.2. The next chapters will treat the study of Z boson pair production, and in particular the analysis of the OPAL data taken in the years 1999 and 2000,

Year	$\sqrt{s}$ (GeV)	$\mathcal{L}$ (pb^{-1})
1990-95	~91	165
1995	130/136	5
1996	161	10
1996	170/172	10
1997	183	55
1998	189	172
1999	192-202	213
2000	200-209	220

Table 3.1: *Integrated luminosities collected at LEP ordered according to the year of data taking and the* e^+e^- *center of mass energy.*

3.2 The Opal detector at LEP

The OPAL detector (**O**mni **P**urpose **A**pparatus for **L**EP), is one of the four detectors built in correspondence of the e^+e^- collision points to detect and identify the particles produced in the collisions, and to measure their 4-momenta. It is 12 m long, has a diameter of 10 m and a weight of about 3000 t. The geometrical acceptance covers 97% of the full solid angle. In the following, the different sections of the OPAL detector will be briefly described. A detailed description of the detector components can be found in [39]. The coordinate system is cylindrical, its $+z$ direction is given by the flight direction of the electrons, and its origin corresponds to the interaction point. The $+x$ direction points to the center of the storage ring. The polar angle θ is defined with respect to the $+z$ direction, while the azimuthal angle ϕ is defined with respect to the horizontal $+x$ direction.

The OPAL tracking system consists of a Silicon Microvertex Detector, which is the subdetector closest to the interaction point, and of a group of drift chambers (Vertex Chambers, Jet Chambers and z-Chambers) located inside a cylindrical pressurised vessel about 6 m long and

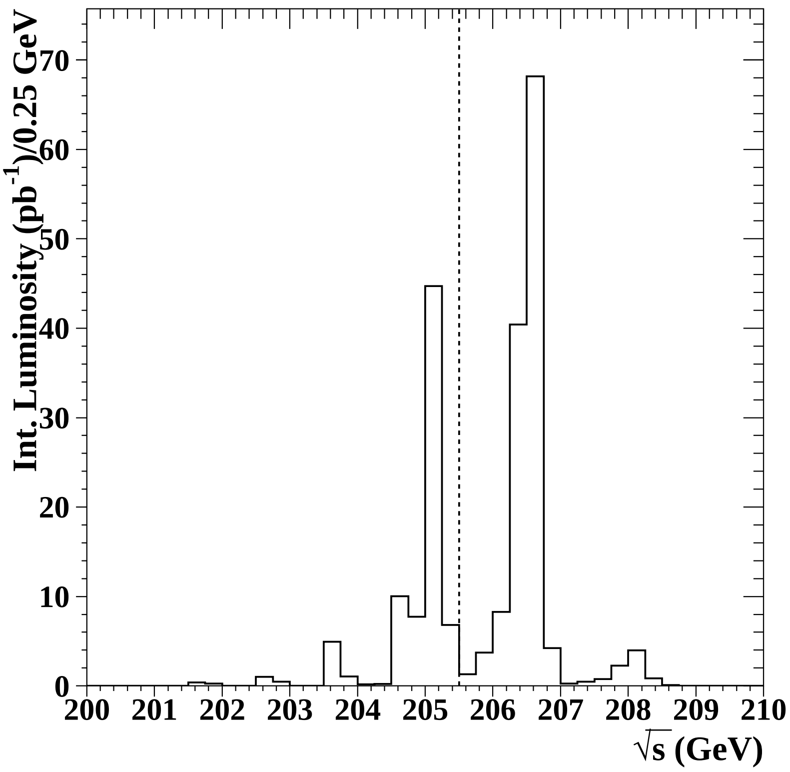

Figure 3.2: *Distribution of the integrated luminosities for the data collected during the year 2000 at LEP. The vertical dashed line in correspondence of $\sqrt{s} = 205.5$ GeV shows the point of separation between the two energy points considered for the analysis presented here, at $\sqrt{s} = 205$ GeV, and at $\sqrt{s} = 207$ GeV.*

with a diameter of about 4 meters. The vessel is surrounded by a normal conducting solonoidal coil, which produces an homogeneous magnetic field of 0.435 Tesla directed along the beam axis. The iron plates of the hadronic calorimeter work as return-joke.

The **Silicon Microvertex Detector (SI)** consists of two layers of silicon strips counters, which are cilidrically positioned around the beam axis at radii of 6.1 cm and 7.5 cm. After its third upgrade, in 1996, the detector covers the polar angle range up to $|\cos\theta| < 0.89$ (with hits in both layers), with respect to the LEP1 acceptance which was covering up to $|\cos\theta| < 0.77$. The two hits acceptance in the azimuthal plane direction has been similarly increased, via a larger number of strip detectors, from 80% to 97%. The track parameter resolution is 18 μm in the direction orthogonal to the beam axis ($r - \phi$ plane), and 24 μm in the z-direction. This precision plays a fundamental role in the identification of long-lived B hadrons. The **Central Vertex Chamber (CV)** is a cylindrical drift chamber divided into 36 sectors. Its length is 1 m, its inner radius is 8.8 cm and its outer radius is 23.5 cm. The 12 inner layers of the signal wires are parallel to the z axis, while the outer 6 layers are equipped with stereo wires having an angle of 4^o with the beam axis. The space resolution of the vertex chamber is 55 μm in the $r - \phi$ plane and 700 μm in the axial direction. This detector component is fundamental for the extrapolation of the tracks from the Jet-Chamber to the Silicon Microvertex Detector.

The **Central Jet-Chamber (CJ)** is a Jade-like drift chamber. It is subdivided into 24 azimuthal sectors each one having 159 signal wires separated by a distance of 1 cm. CJ covers

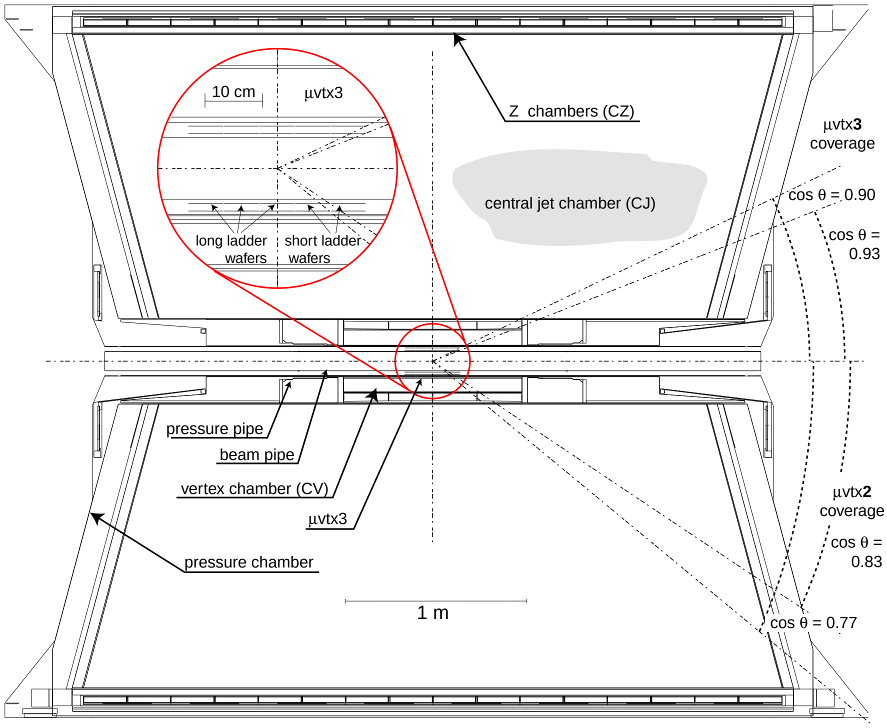

Figure 3.3: *The tracking system of the OPAL detector.*

the radial range from r = 25 cm up to r=183 cm, with an axial length of 4 m. The anode wires are slightly staggered to allow the solution of the left-right ambiguity in the track reconstruction. The hit positions of the charged tracks are determined from the wire positions, the drift times and the charge collected by the wires. The space resolution in the $r-\phi$ plane is 135 μm, in the z direction 6 cm. The double-track resolution is 2 mm. The particles momentum and charge is determined from the track curvature in the 0.435 T magnetic field. The relative resolution (of CJ alone) on the measurement of the transversal momentum is given by:

$$\frac{\sigma_{p_T}}{p_T} = \sqrt{(0.02)^2 + (0.0015\ (\mathrm{GeV})^{-1} \cdot p_T)^2} \tag{3.1}$$

The **z-chambers (CZ)** are the out-most completion of the tracking system. They consist of 24x8 planar drift chambers, each with 6 layers, whose signal wires are orthogonal to the CJ wires. This allows a precise measurement of the z coordinate with a resolution of σ_z = 300 μm inside the polar angle range $|\cos\theta| < 0.72$.

The **Time of flight system (TOF)** consists, in the barrel, of plastic scintillator strips with a time resolution of about 300 ps. Before the 1997 data taking the system has been extended to the end-cap (in the range $0.82 < |\cos\theta| < 0.95$), where the time resolution is 3ns. The TOF system is used mainly for triggering and to reject cosmic rays events.

The calorimeter system measures the amount of energy deposed by the particles, and the position of the energy deposits. It is constituted by the following parts:

the **Presampler** consists in the barrel of two cylindrical layers of streamer chambers, and in each of the two end-caps of 16 multi-wire proportional chambers. It is placed immediately before the electromagnetic calorimeter and measures the showering of particles in the pressure vessel and in the solenoid coil. The material before the electromagnetic calorimeter corresponds to 2 radiation lengths in the barrel and up to 7 radiation lengths in special sectors between the barrel and the end-caps. From the measured multiplicity in the presampler it is possible to measure the correction to be applied to the energy deposition measured in the electromagnetic calorimeter.

The **Electromagnetic calorimeter** is constituted, in the barrel, of 9940 lead-glass blocks each of 24.6 radiation lengths and a section of 10x10 cm^2. The barrel blocks are pointing in direction of the interaction point. In each of the end-caps consists of 1132 blocks with a section of 9.4x9.4 cm^2, with an average length of 22 radiation lengths. The blocks are parallel to the beam axis. Electrons, positrons and photons depose almost their total energy in the electromagnetic calorimeter. The energy is measured through the Cerenkov-light emitted by the particles in the electromagnetic showers, which is proportional to the deposed energy. The relative energy resolution, taking into account the energy loss in the material before the calorimeter, is given by:

$$\frac{\sigma_E}{E} = \sqrt{(0.03)^2 + (0.16)^2(\text{GeV})/E}. \tag{3.2}$$

The **hadronic calorimeter** is built of alternate layers of iron plates and stream tubes. It is constituted of a central component for the barrel, two end-caps and two pole-tips. In the calorimeter, the energy of hadrons is measured. Its radial width is more than 1.3 m, and this corresponds, considering also the electromagnetic calorimeter, to a total of at least 7 hadronic interaction lengths. Only 0.1% of the pions pass without showering the calorimeter system, which thus is a good muon filter.

The **muon chambers** are the outermost component of the OPAL detector. The 110 drift chambers mounted in the barrel region are 1.2 m long, and are disposed in four layers. The azimuthal and axial resolutions are 1.5 mm and 2 mm respectively. In each of the end-caps the muon detectors are constituted of two orthogonal layers of streamer tubes transversal to the beam axis. The single point space resolution of the end-cap chambers is 1 mm in both directions in the $r - \phi$ plane.

The hermeticity of the OPAL detector is granted by a group of subdetectors close to the beam axis, which detect particles produced at small polar angles:

the **forward detectors (FD)** are placed in the forward region and are a system of drift chambers, proportional counters and a lead-scintillator sandwich calorimeter.

The **gamma catcher (GC)** is a ring of lead-scintillator modules which have a width corresponding to 7 radiation lengths.

The **silicon-tungsten calorimeters (SW)** are built of alternate layers of tungsten plates and double-sided silicon strip counters. The counters have both radial and azimuthal strips. These components of the detector have been mounted in 1993, and together with the FD subdetectors they are used for the measurement of the luminosity.

The **MIP-plug** is a 2-layer subdetector of plastic scintillator with a width of 1 cm. It measures minimum ionising particles, in particular muons, at very small polar angles. The acceptance for MIPs is increased, through the MIP plug, from the limit of the hadron-poletip (200 mrad) to 43 mrad. This component has been added to the OPAL detector in 1997.

A view of the complete OPAL detector is shown in Figure 3.4, while the subdetectors under small polar angles are shown in Figure 3.5.

The tracks of the charged particles are bent in the axial magnetic field, and the helix corresponding to their trajectory can be univocally described by five independent parameters. At OPAL the following five quantities are used:

- $k = \frac{1}{2\rho}$: where ρ is the curvature radius of the track projection on the $r - \phi$ plane.
- ϕ_0: the azimuthal angle of the track tangent at the p.c.a.[1]
- d_0: the radial distance from the p.c.a. to the vertex.

[1] The point of closest approach (p.c.a.) denotes the point of the track closest to the interaction vertex, in the $r - \phi$ plane.

- z_0: the z-coordinate of the track at the p.c.a.
- $\tan\lambda = \cot\theta$: where θ is the polar angle of the track.

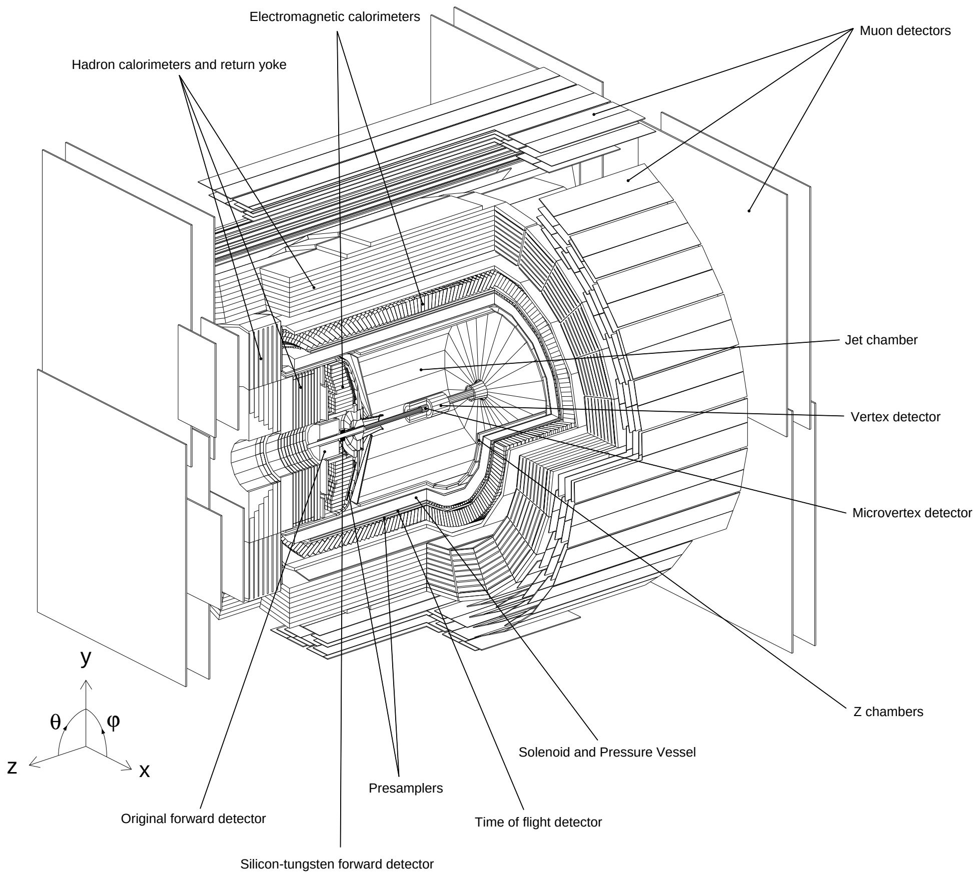

Figure 3.4: *An overview of the OPAL detector.*

3.3 Physics processes at LEP2

The LEP2 event classes relevant for the $e^+e^- \to ZZ$ analysis are presented in the following. Their experimental signature and their cross section are also discussed.

In general, leptons, quarks, and photons can be present in a final state, each particle leading to a different experimental signature. Charged leptons ($e^\pm$ and $\mu^\pm$) are reconstructed as single tracks in the central tracking detectors. The energy of the electrons is measured in the ECAL, while muons loose only part of their energy in the calorimeters via ionization, and are reconstructed using the muon chambers as well. The $\tau^\pm$ leptons decay immediately after their production; their decay channels involve different number of leptons or hadrons (e.g. π/K mesons), whose tracks are measured in the detector. Neutrinos can not be detected, and their signature is missing momentum and energy.

Quarks can not be directly observed in the detector, as they undergo the process of fragmentation immediately after they have been produced. Their experimental signature are bundles of particles, the so-called *jets*, which are mainly constituted by hadrons, but can also contain leptons and photons from hadron decays. The measure of the momentum of a jet allows the knowledge of the momentum of the corresponding primary quark, provided that all particles

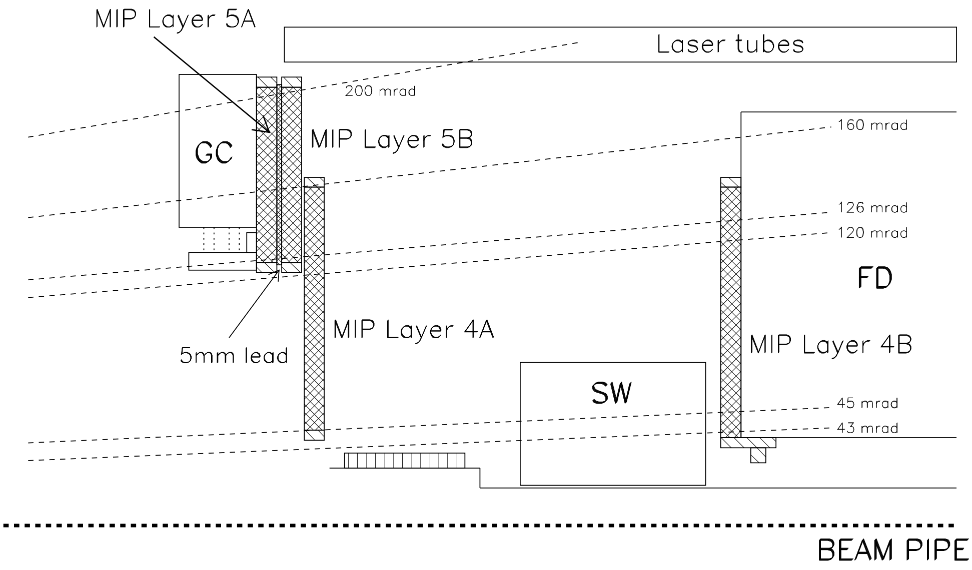

Figure 3.5: *OPAL subdetectors in the forward region*

are correctly assigned to the respective jets. The method used to reconstruct jets in the OPAL detector will be discussed in the following as well.

4-fermion processes

With the term "4-fermion events" we indicate all e^+e^- electroweak interactions leading to a final state with four fermions, with the exception of 2-photon (or *multiperipheral*) processes, which will be discussed in the next section. A selection of some of the most relevant 4-fermion diagrams is shown in Figure 3.6. The so-called double-resonant diagrams are W boson pair ones, also indicated as CC03 diagrams, and Z pair production, the NC02 diagrams already introduced in previous chapters (see Figure 2.4)[2].

Among the 4-fermion processes, W pair production is the one with the highest cross section. In fact the cross section for Z pair production is ~20 times smaller than that for W pair production. In both cases the two bosons decay in two fermion-antifermion pairs, the invariant mass distribution of the two pairs corresponding to the mass and the width of the bosons involved.

Other relevant 4-fermion diagrams are those for the production of a single W or a single Z (single-resonant diagrams), whose cross section is comparable with the $e^+e^- \to ZZ$ cross section.

The same 4-fermion final state may be produced by different diagrams. For example the process $e^+e^- \to e^+e^-\mu^+\mu^-$ may occur through the NC02 diagrams already shown Figure 2.4, or through the single-resonant diagram in Figure 3.6.(f).

In this analysis the signal corresponds to the NC02 diagrams, while all other 4-fermion processes are considered as background. Anyway the signal definition must take into account the interference between signal and background diagrams; this requires an appropriate treatment of the signal definition, which will be described in detail in Section 5.1.

The most relevant 4-fermion background for the selection of $e^+e^- \to ZZ \to q\bar{q}q\bar{q}$ events is constituted by W pairs, in particular $e^+e^- \to W^+W^- \to q\bar{q}q\bar{q}$ events. The mass resolution of the detector, i.e. angle and energy resolution in the measurement of jets, is crucial for the rejection of this background. The hadronic decays of the W bosons are dominated by the processes

[2] The denomination CC03 refers to the charged current involved in the 4-fermion production and to the fact that three diagrams are leading to W pair production. Similarly, the denomination NC02 refers to the 4-fermion production through neutral current, and to the number of corresponding diagrams, which is two.

$W^\pm \rightarrow u\bar{d}, \bar{u}d$ and $W^\pm \rightarrow c\bar{s}, \bar{c}s$. In fact the weak charged current couples up- and down-type quarks, i.e. quarks with third component of the weak isospin +1/2 and -1/2 respectively. The couplings can be parametrised by a 3×3 matrix, the so-called Cabibbo-Kobayashi-Maskawa (CKM) matrix [3]. The CKM matrix elements parametrising b-quark couplings to up-type quarks are dominated by the V_{tb} element, which is almost equal to one, while V_{cb} and V_{ub} are negligible. As the decays $W^+ \rightarrow t\bar{b}$ and $W^- \rightarrow \bar{t}b$ are kinematically not allowed, the decays involving b-quarks are strongly suppressed, having a branching ratio of ~ 0.2}.

On the contrary, the Branching Ratio for the decay $Z \rightarrow b\bar{b}$ is about 15%. This consideration suggests the development of a dedicated selection for the channel $ZZ \rightarrow q\bar{q}b\bar{b}$, where a least one Z is decaying in a $b\bar{b}$ pair, exploiting the identification of b-quarks to strongly reduce the WW background, as will be shown in detail in the following sections of this chapter.

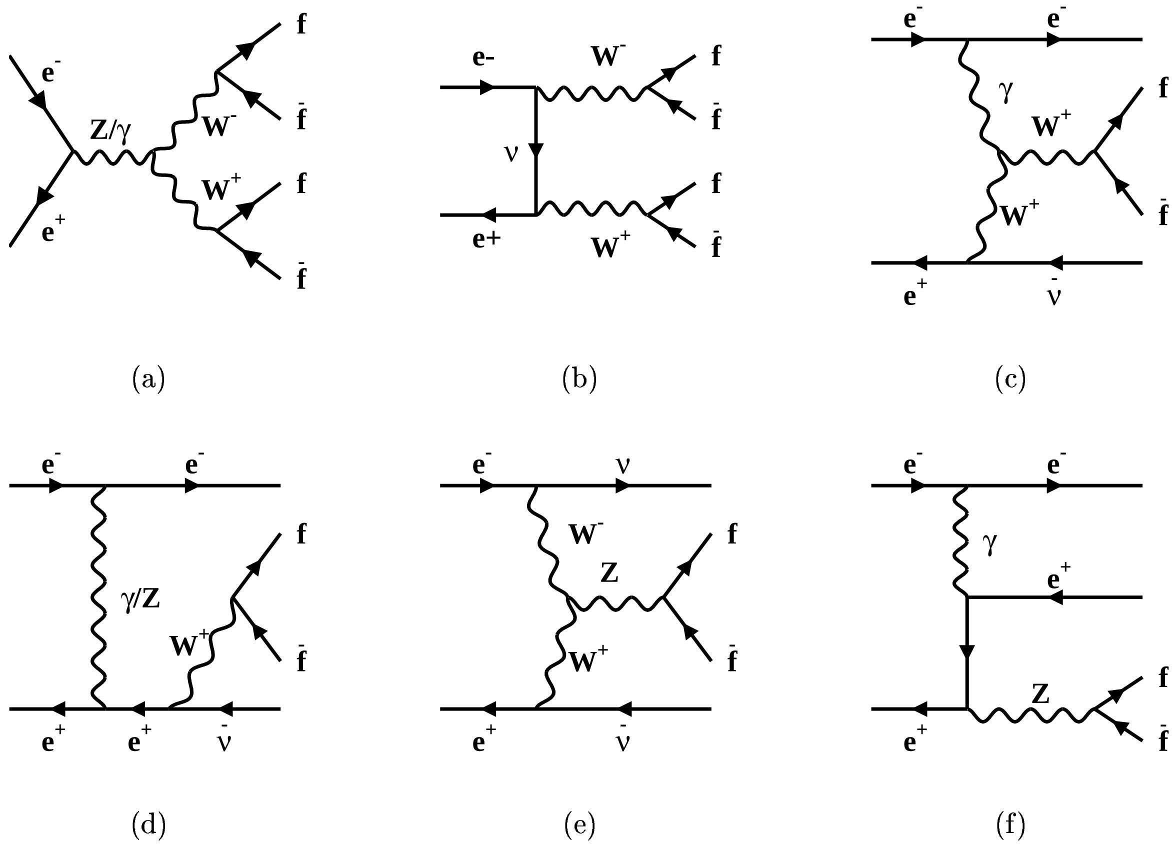

Figure 3.6: *Examples of 4-fermion diagrams, background to the NC02 signal diagrams. The diagrams (a) and (b) are the CC03 diagrams for W pair production (s- and t-channel respectively). The diagrams (c) and (d) are leading to single W production, while (e) and (f) lead to the production of a single Z.*

2-fermion processes

The production of pairs of fermions occurs through the diagrams in Figure 3.8, annihilations of the initial electron and positron into a γ or a Z, which in turn decay into a fermion-antifermion pair. In case the intermediate boson is a Z, the cross section for the process becomes significantly bigger as the effective e^+e^- center of mass energy comes closer to the Z mass. This happens after the radiation, in the initial state, of a photon with energy $E_\gamma = (s - M_Z^2)/(2\sqrt{s})$, a process called

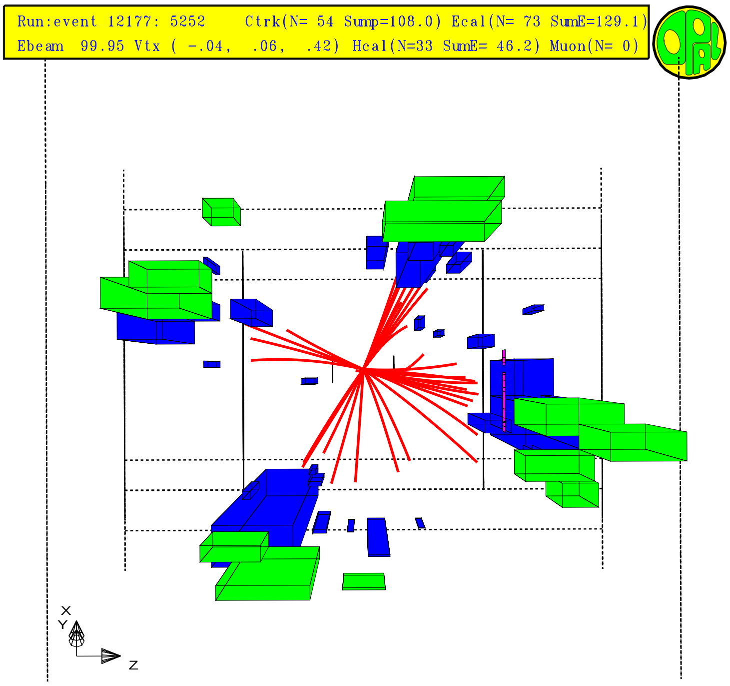

Figure 3.7: *A 4-fermion event, reconstructed in the OPAL detector. Shown is a* $\mathrm{e^+e^-} \to \mathrm{q\bar{q}q\bar{q}}$ *event in data taken at* $\sqrt{s} \simeq 200$ *GeV.*

Initial State Radiation (ISR), whose Feynman diagram is shown in Figure 3.8.(b). This kind of events, called "radiative return" to the Z, amount to about 90% of the whole $\mathrm{e^+e^-} \to \mathrm{Z} \to \mathrm{f\bar{f}}$ sample. If the radiated photon can not be measured in the detector, because it is produced almost collinearly with the beam, the total energy measured is less then the nominal $\mathrm{e^+e^-}$ center of mass energy: $\sqrt{s'} < \sqrt{s}$, where $\sqrt{s'}$ indicates the reconstructed center of mass energy of the $\mathrm{e^+e^-}$ interaction, after ISR. In this case the direction of the missing energy goes along the beam pipe, thus fermion and antifermion are approximately back to back only in the $r - \phi$ plane. If the photon can be measured in the detector, then $\sqrt{s'} = \sqrt{s}$. Also in case of no ISR it is $\sqrt{s'} = \sqrt{s}$; besides, the fermion and the antifermion are in this case collinear.

The 2-fermion background to the $\mathrm{e^+e^-} \to \mathrm{ZZ} \to \mathrm{q\bar{q}q\bar{q}}$ selection is exclusively constituted by $\mathrm{e^+e^-} \to \mathrm{Z}/\gamma \to \mathrm{q\bar{q}}$ events. Events with ISR can be easily rejected through a cut on the ratio $\sqrt{s'}/\sqrt{s}$. Events with $\sqrt{s'} \simeq \sqrt{s}$ are an important background to the $\mathrm{ZZ} \to \mathrm{q\bar{q}q\bar{q}}$ selection, especially when the event has a 4-jet shape. This may happen for example when one quark radiates a gluon, which then decays into a quark-antiquark pair (the *gluon splitting* $g \to \mathrm{q\bar{q}}$ process), as shown in the Feynman diagram in Figure 3.8.(c)[3]. In Figure 3.9 two $\mathrm{e^+e^-} \to \mathrm{q\bar{q}}$ events are shown, as they are reconstructed in the OPAL detector.

2-photon processes

The 2-photon process is the one having the highest cross section at LEP2 ($\sigma_{\gamma\gamma} \sim \mathcal{O}(10\mathrm{nb})$). The Feynman diagram (called *multiperipheral* diagram) for the process is shown in Figure 3.10; two photons are radiated off the electron and the positron and interact generating a fermion-antifermion pair. Thus, the process actually leads to a 4-fermion final state. Due to the peculiar experimental signature however, 2-photon processes are considered as a separate process. In

[3] Other subprocesses leading to a 4-jet like event are the radiation of a gluon followed by the process $g \to gg$, or the radiation of two gluons by the final-state quarks.

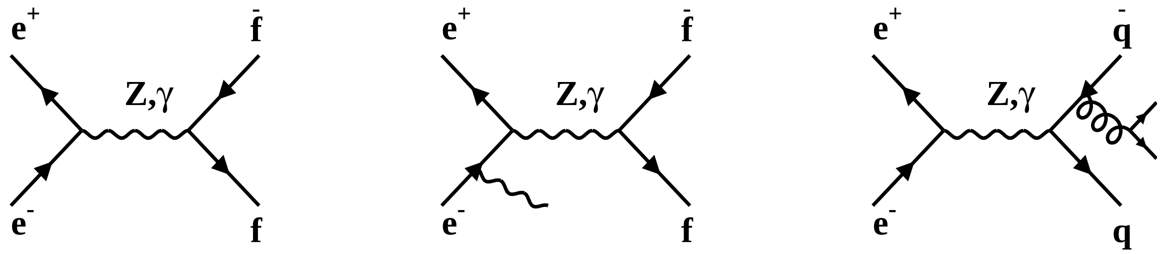

(a) (b) (c)

Figure 3.8: *2-fermion diagrams, at full center of mass energy (a), or after ISR (b). In (c) is also shown the diagram for* $\mathrm{q\bar{q}}$ *production associated with the radiation of a gluon in the final state (gluon splitting).*

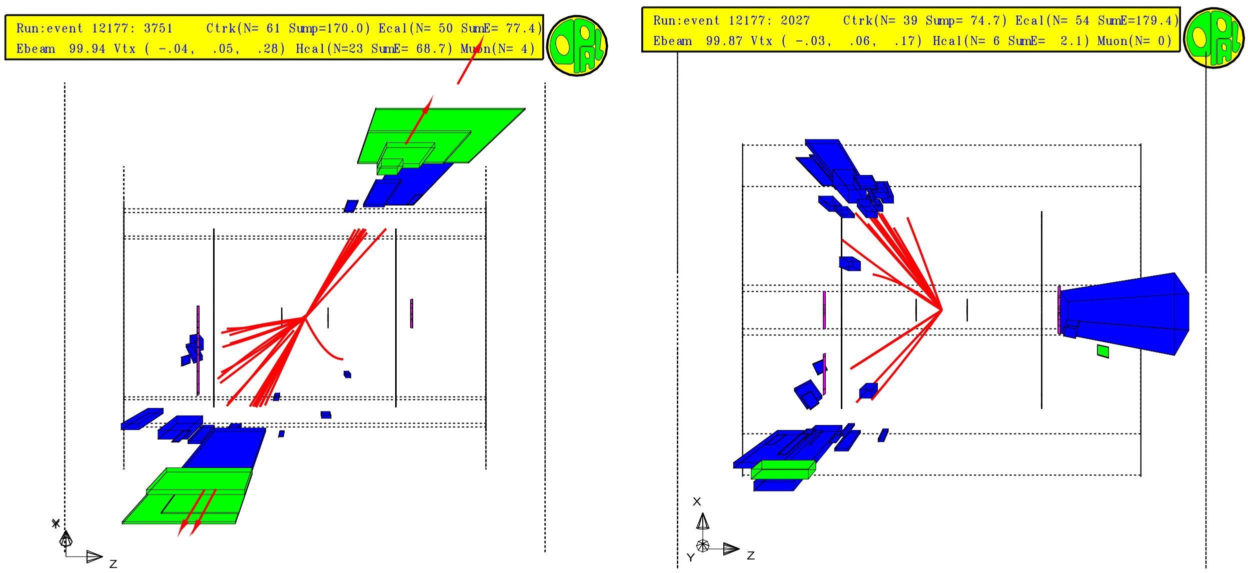

(a) (b)

Figure 3.9: (a): an event of the type $\mathrm{e^+e^-} \to \mathrm{q\bar{q}}$ in data taken at $\sqrt{s} \simeq$200 GeV, reconstructed in the OPAL detector. The event occurs at full center of mass energy, i.e. the amount of ISR is negligible, and the jets originated by the two quarks are back-to-back. (b): an $\mathrm{e^+e^-} \to \mathrm{q\bar{q}}\gamma$ event, where the quark pair production occurs after initial state radiation. In this case, the photon is detected in the forward ECAL, where the energy deposit is visible.

fact, after the radiation of a photon, the primary electron and positron are scattered under very small azimuthal angle, and in most cases remain unobserved along the beam-pipe. The fermion-antifermion pair is usually detected in the forward section of the detector. The experimental signature of the process is large missing energy, small transverse momentum and activity in the detector at small polar angles. Thus, in spite of the very high cross section, this background is very easy to reject in a selection of $\mathrm{e^+e^-} \to \mathrm{ZZ} \to \mathrm{q\bar{q}q\bar{q}}$ or $\mathrm{e^+e^-} \to \mathrm{ZZ} \to \mathrm{q\bar{q}b\bar{b}}$ events.

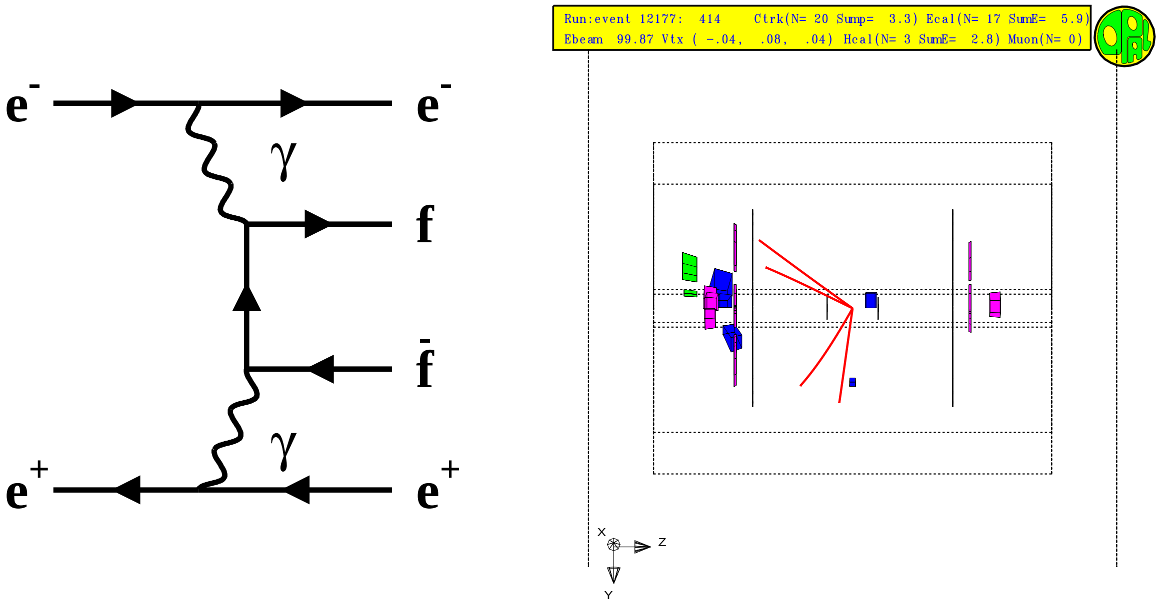

Figure 3.10: *(a): Feynman diagram of the 2-photon process. (b): a 2-photon event reconstructed in the OPAL detector; the electron and positron remain unobserved along the beam pipe.*

Cross sections

The cross sections for the processes discussed are shown in figure 3.11, as a function of the e^+e^- center of mass energy. In the figure, the cross section for the ZZ signal is shown, together with those for the main background processes to the fully hadronic channels, W pair production and $e^+e^- \rightarrow q\bar{q}$. The ZZ cross section is $\sim$1 pb at $\sqrt{s} \simeq$200 GeV, and it is overall a factor $\sim$20 smaller than that for WW production. W pair production represents therefore a relevant background for the measurement of the cross section for Z boson pair production.

The cross section for the process $e^+e^- \rightarrow q\bar{q}$ is, at $\sqrt{s} \simeq$200 GeV, $\sim$90 pb, so about 2 orders of magnitude bigger than the ZZ cross section. The $e^+e^- \rightarrow q\bar{q}$ cross section peaks at $\sqrt{s} \simeq$91 GeV, in correspondence of the mass of the Z resonance.

3.4 ZZ decay channels

The Standard Model branching ratios for the process $Z\rightarrow f\bar{f}$ are shown in Table 3.2 [12]. Consequently, the branching ratios for each channel of the process $ZZ \rightarrow f\bar{f}f\bar{f}$ can be easily calculated. They are shown in Table 3.3, where the branching ratio for the $ZZ \rightarrow q\bar{q}b\bar{b}$ channel, a subsample of the fully hadronic $ZZ \rightarrow q\bar{q}q\bar{q}$ channel is also indicated. The table shows also, as an example, the number of events expected for each channel, at $\sqrt{s}$ = 200 GeV and assuming an integrated luminosity $\mathcal{L}$=200 pb^{-1}. Each channel is characterised by a distinctive signature in

Channel	BR (%)
$Z \rightarrow q\bar{q}$	69.9
$Z\rightarrow l^+l^-$	10.1
$Z\rightarrow \nu\bar{\nu}$	20.0

Table 3.2: *Standard Model branching ratios for the process* $Z \rightarrow f\bar{f}$.

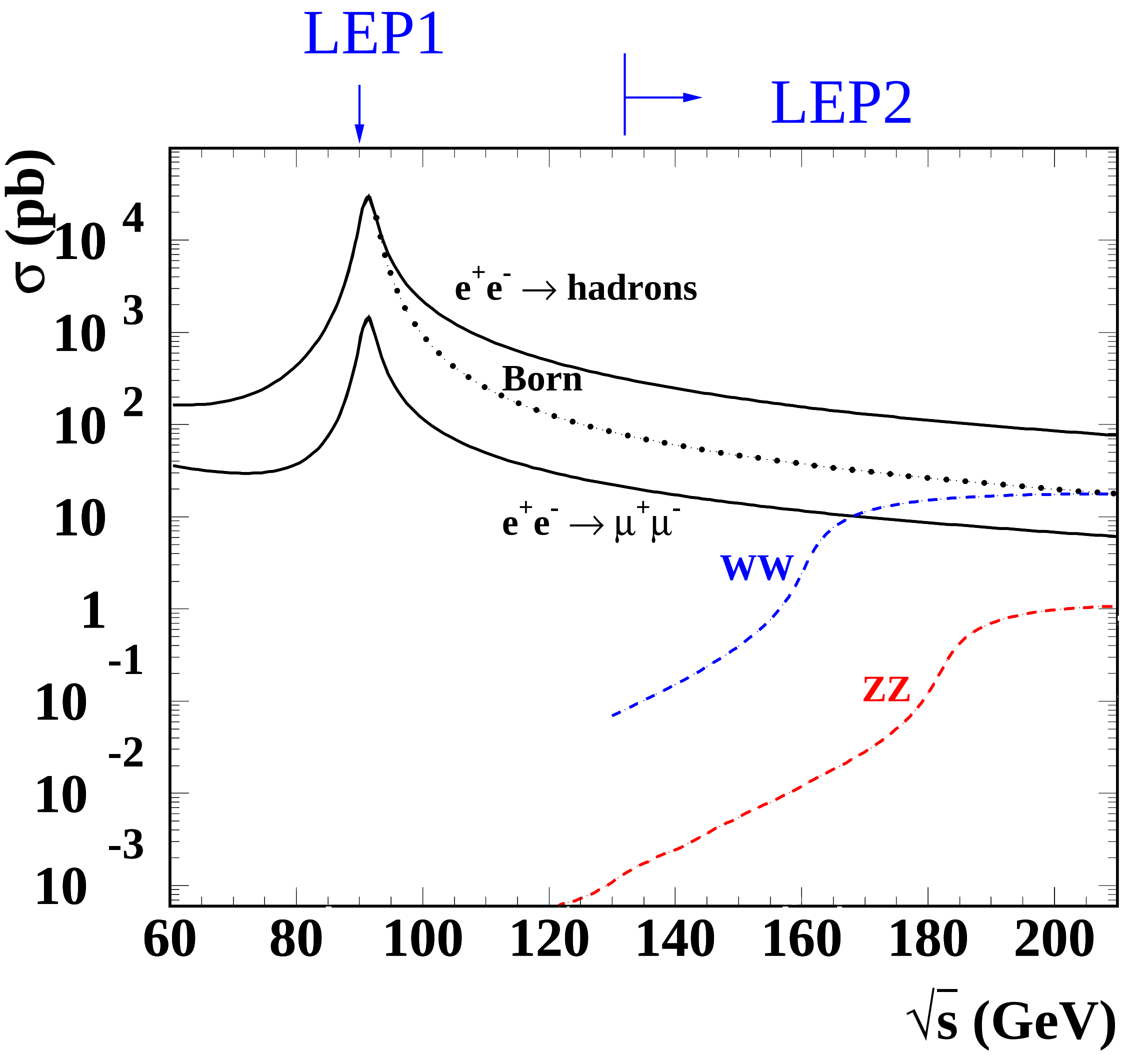

Figure 3.11: *Cross sections for the most relevant processes in* e^+e^- *collisions at LEP1 and LEP2, as a function of the center of mass energy* $\sqrt{s}$*. The 2-fermion processes (in the figure* $\sigma(e^+e^- \to \mu^+\mu^-)$ *and* $\sigma(e^+e^- \to$*hadrons) are shown) have the highest cross section. The dotted line shows the* $e^+e^- \to q\bar{q}$ *cross section computed at tree level, i.e. without including radiative corrections (Born approximation). The production of pairs of W and Z bosons leads to 4-fermion final states.*

the detector, according to the kind of fermions present in the final state. The masses of the two fermion-antifermion pairs peak at the value of $M_Z \simeq 91$ GeV. The quarks present in the final state undergo the process of fragmentation in jets of colourless hadrons. The charged leptons are detected or as single tracks (electrons and muons) or after their decay in channels involving different numbers of particles (τ leptons). The neutrinos are not detected (i.e. their signature is missing energy and momentum).

Channel	BR (%)	N. of expected signal events at $\sqrt{s}$ =206 GeV for $\mathcal{L}$=200 pb^{-1}
$ZZ \to l^+l^-l^+l^-$	1.0	2.1
$ZZ \to \nu\bar{\nu}\nu\bar{\nu}$	4.0	8.5
$ZZ \to l^+l^-\nu\bar{\nu}$	4.0	8.5
$ZZ \to q\bar{q}l^+l^-$	14.1	30.1
$ZZ \to q\bar{q}\nu\bar{\nu}$	28.0	59.8
$ZZ \to q\bar{q}q\bar{q}$	48.9	104.4
$\mathbf{ZZ \to q\bar{q}b\bar{b}}$	**18.4**	39.3

Table 3.3: *Branching ratios for the process* $ZZ \to f\bar{f}f\bar{f}$*. The* $ZZ \to q\bar{q}b\bar{b}$ *events are a subsample of the general fully hadronic channel* $ZZ \to q\bar{q}q\bar{q}$*. The third column of the table shows, as a reference example, the number of expected signal events assuming 100% selection efficiency.*

4. Event reconstruction at OPAL

This chapter will describe the simulation and reconstruction of the events in the OPAL detector, focusing in particular on events involving the production of quarks. Since the selection of $e^+e^- \to ZZ \to q\bar{q}b\bar{b}$ events exploits the identification of the *jets* originating from b-quarks, the OPAL b-tagging algorithm will be also described in detail in the chapter.

4.1 Simulation of the events

The development of an event selection for a given physics process, and the interpretation of the results, for example in terms of a cross-section measurement, require the simulation of the relevant signal and background events classes, i.e. of all the physics processes which are expected to play a role in the analysis. The comparison of the results of the data analysis with the results expected from the Monte-Carlo simulation allows to measure the parameters on which the simulation depends, like cross sections or couplings. The MC simulation of an event can be sub-divided in two steps, the event generation and the detector simulation.

Event generation

In this first phase of the simulation, the 4-vectors of the particles in the final state are generated, through programs (*event generators*) which calculate the probability of a given process for any point of the final state phase space, and generate the 4-vectors according to this probability. The probability is calculated on the basis of the differential amplitude for the process under exam. The integration of the differential cross section yields the total cross section for the process. If quarks are present in the final state, a second step follows the generation of the primary quarks 4-vectors: the simulation of the process of fragmentation in colourless hadrons, which can be measured in the detector. As a cross-check, and to compute systematic errors connected to the modelling of the physics process, different generators can be used to simulate the same process.

The event generators which have been used in this analysis are the following:

- **4-fermion processes:** GRC4F [41] is an event generator for 4-fermion processes. For a given 4-fermion final state, GRC4F generates events taking into account all lowest order diagrams leading to that final state, and the interference between them.

  The signal diagrams, i.e. the NC02 diagrams, are a subset of the 4-fermion diagrams included in GRC4F. For the simulation of the signal process, a dedicated generator including only NC02 diagrams has been used, the YFSZZ [44] generator.

  A cross check of the 4-fermion background simulation can be performed using KORALW [42], which includes only the CC03 diagrams for W pair production, or EXCALIBUR [43], which includes all 4-fermion diagrams.

- **2-fermion processes:** The 2-fermion processes relevant for the analysis presented in this work are those leading to a $q\bar{q}$ final state. They are shown in Figure 3.8, and have been discussed in Section 3.3, leading to a $q\bar{q}$ final state. The generators used to simulate these processes are KK2F [46], as reference generator, and PYHTIA [45] for systematic studies.

- **2-photon processes** To simulate the process shown in Figure 3.10 two generators have been combined: PYHTIA [45] (untagged electron), HERWIG (tagged electron) [48], where the two categories correspond to small or large Q^2 of the photon, respectively. Another generator, PHOJET [49] has been used for cross-check.

Fragmentation

QCD perturbation theory is valid at short distances. At long distances, QCD becomes strongly interacting, and perturbation theory breaks down. In this regime, the coloured partons (quarks or gluons) are transformed into colourless hadrons in the so-called fragmentation process. The process of fragmentation has yet to be understood from first principles, but many different phenomenological models have been developed. All models are of probabilistic and iterative nature, describing the fragmentation as a series of branching processes. The model implemented in JETSET[47], the program used to simulate the fragmentation in this analysis, is the string fragmentation, in particular the Lund string model.

To check the systematics connected with the modelling of the quark fragmentation, a second Monte-Carlo program, HERWIG [48], has been also used as a cross-check. HERWIG implements the cluster fragmentation algorithm.

Detector simulation.

The passage of the particles through the detector must be simulated in detail to have a good agreement between the simulated measurements and those performed on real data, in case no new physics occurs. The simulation of the OPAL detector is performed by the program GOPAL [50], which is based on the CERN program library GEANT3 [51].

The interactions of the particles with the material of the detector (for example energy loss by ionization, shower formation, multiple scattering or gas ionization in drift chambers) are simulated according to the real geometry and material structure of the detector. The response of the active parts of the detector is also simulated. This means that the formation of the electronic signals in the different parts of the detector, and their conversion in digital signals, are simulated in detail on the basis of the characteristics of the detector and in particular of its readout electronic.

4.2 Event reconstruction and energy correction

In the OPAL detector, the momentum of the charged particles is in most of the cases measured with best angular and momentum resolution using the central tracking devices (CT, see Section 3.2). The angular resolution of the calorimeters is limited by their granularity; only in the case of high energy electrons the calorimeter resolution is comparable with those of the central tracking devices [54]. The energy carried by neutral particles can only be measured in the calorimeters, however, to avoid double counting in the measurement of charged particles energy, the energy of the calorimeters clusters coming from charged tracks has to be removed. This could be naively done just counting only the clusters not associated to any track. However, due to the possible overlapping between the clusters from neutral and charged particles, this procedure can lead to wrong results. The correction algorithm used by OPAL is the *Matching Tracks (MT)* [54] algorithm. To find the matching between tracks and clusters, the tracks reconstructed in the CT are extrapolated to the ECAL and HCAL. Through the extrapolation it is possible to separate the energy depositions associated to tracks, from those which are not associated to any track. The latter clusters are treated as the energy depositions of photons with mass zero. For the clusters associated to tracks the energy is corrected with the following method: at first the average expected energy deposition is calculated, according to the momentum and the polar angle of the track. If the measured energy deposition is significantly greater than the expected, the measured energy is decreased to the expectation value, and the object is treated in the following as a photon. If the measured energy is smaller than the expected, the energy deposition is cancelled by the list of the objects, and the associated track is treated as a charged particle. After this procedure one obtains neutral particles with zero mass, and charged particles, for which the pion mass is assumed.

4.3 Jet finding

The primary quarks eventually present in the event topologies described in Section 3.3 produce, through the fragmentation process, bundles of particles in the detector, the so-called *jets*. Tracks and calorimeter clusters measured in the detector (in the following the denomination "objects" will be used for both of them) have to be grouped into jets to reconstruct the 4-momentum of the primary quarks. The algorithm which has been used in this work is a combination of the Durham [55] and JADE E0 [56] algorithms. The object association procedure consists of the following steps:

- For each pair (i, j) of objects the following quantity is calculated:

$$y_{ij}^D = \frac{2 \cdot \min(E_i^2, E_j^2) \cdot (1 - \cos\theta_{ij})}{E_{vis}^2} \tag{4.1}$$

  where E_i, E_j are the energies of the two objects, θ_{ij} is the angle between their directions, and E_{vis} is the total visible energy of the event. The quantity y_{ij}^D is the so-called "distance", or "jet-resolution" used by the Durham algorithm [55], as the superscript denotes. Neglecting the masses, the numerator corresponds to the invariant mass of the two objects scaled by the smaller of the energy ratios E_i/E_j and E_j/E_i. In the limit of small angles θ_{ij}, the numerator of y_{ij}^D corresponds to the relative transverse momentum of one object with respect to the other. The object pair with the minimum value of y_{ij}^D in the event is associated to form one new object, whose 4-momentum is the sum of the two objects 4-momenta: $p_\mu = (p_\mu^i + p_\mu^j)$.

- The previous step is iteratively repeated until the number of objects has reached a given value, or until the value of the minimal distance y_{ij}^D has become larger than a given threshold y_{cut}. While in the former case the number of final jets is obviously fixed, in the latter case this number is variable. In the analysis of the process $\mathrm{e^+e^-} \to \mathrm{ZZ} \to \mathrm{q\bar{q}q\bar{q}}$ we have chosen to fix the number of jets to 4, ending the iterative association procedure when this number of objects (jets) has been reached.

- The procedure described up to now can have limited performance when many low-energy objects, for example secondary tracks from particle decays or clusters from hadronic interactions in the ECAL, are reconstructed in the event. In fact the jet-finding, combining objects which have the smallest distance according to 4.1, tends to start from small momentum tracks or clusters. The cross-talk between the reconstructed jets may be affected by these association scheme for the small energy objects. Thus, after the previous iterative procedure has determined the 4-momenta p_μ^{jet} of 4 reference jet, a second re-association iteration follows, in which each object is reassigned to the jet whose distance to the object is minimal. During this second iteration the 4-momenta of the reference jets are kept constant. They are recalculated at the end of the re-association procedure, when all objects have been reassigned to the reference jets. Different ways to calculate this re-association distance have been tested [57]. The performance has been evaluated in terms of jets angular resolution and mass resolution, for example in $\mathrm{e^+e^-} \to \mathrm{WW} \to \mathrm{q\bar{q}q\bar{q}}$ events. The best performance has been obtained when using the JADE E0 distance [56]:

$$y^J_{ij} = \frac{2 \cdot E^{jet}_i \cdot E^{object}_j \cdot (1 - \cos\theta_{ij})}{E^2_{vis}} \tag{4.2}$$

where now E^{jet}_i is the reference jet energy ($i = 1, 4$), E^{object}_j is the energy of the j-th object, and θ_{ij} is the angle between the reference jet and the object. E_{vis} is again the total visible energy of the event.

4.4 Kinematic fits

The jet energy and angular resolution, and thus the primary boson mass resolution, can be further improved performing constrained kinematic fits of the jet momenta. In kinematic fits, the jet momenta reconstructed by the jet finding algorithm are corrected, varying them inside the range of their experimental errors in such a way, that particular constraints coming from physics assumptions are fulfilled. The 3-vectors $\vec{p}$ of the jets are corrected in the fit, while the jet energies are re-calculated on the basis of the jet masses. The method used to perform the fits is that of Lagrange multipliers (see for example [58]), which consists of minimising a χ^2 defined as:

$$\chi^2 = (\vec{p}\,' - \vec{p})^T V^{-1}(\vec{p})(\vec{p}\,' - \vec{p}) + 2\vec{\lambda}^T \vec{f}(\vec{p}\,') \tag{4.3}$$

where $\vec{p}$ is a vector containing the measured 3-vectors of the 4 jets, $\vec{p}\,'$ contains the fitted 3-vectors (thus both $\vec{p}$ and $\vec{p}\,'$ are 12-dimensional vectors in case of 4 jet events), $\vec{f}(p\,') = 0$ is a set of K constraint equations depending on the fitted 3-vectors $\vec{p}\,'$ and $\vec{\lambda}$ is a K-dimensional vector of additional fit parameters, the Lagrange multipliers, introduced to implement the constraints in the fit. The minimisation problem can be solved iteratively, by using a Taylor expansion of the constraint equations, as shown for example in [58].

The number of degrees of freedom of the fit is given by:

$$N_{DOF} = N_{meas} - N_{fit} + K. \tag{4.4}$$

where N_{fit} is the number of fitted quantities, N_{meas} is the number of measured quantities, and K is the number of constraint equations. For most of the fits used in the analysis presented here, $N_{fit} = N_{meas}$, so the number of degrees of freedom is given by the number of constraints K.

The kinematic fits, which are relevant for the $e^+e^- \to ZZ \to q\bar{q}q\bar{q}$ analysis, are the following:

- **4C-fit** Energy and momentum conservation are required to be fulfilled. This means that the constraint equations are given by:

$$\sum_{i=1}^{4} E_i = \sqrt{s} \qquad \text{and} \qquad \sum_{i=1}^{4} \vec{p}_i = \vec{0} \tag{4.5}$$

  and $N_{DOF} = 4$.

- $\sqrt{s'}$ **fit.** The hypothesis, that a photon is emitted along the z-axis before the e^+e^- interaction (Initial State Radiation) is tested. An additional unmeasured quantity p^{γ}_z figures in the fit together with the measured jet 3-vectors. As the energy and momentum conservation constraints are required to be fulfilled, the number of degrees of freedom is 3. The invariant mass of the fitted jets is called $\sqrt{s'}$. It corresponds to the effective center of mass energy of the e^+e^- interaction, and can be used to reject the "radiative returns" described in Section 3.3.

- **5C-fit** To test the hypothesis of the production of a pair of bosons with the same mass, the requirement that the two di-jet masses are equal is added to the energy and momentum conservation constraints. So in this case the constraint equations are the same of the 4C-fit, plus the additional one:

$$M(jet1, jet2) = M(jet3, jet4) \tag{4.6}$$

and $N_{DOF} = 5$. In this case, there are 3 possible ways of combining the 4 jets in pairs. The fit is performed for all 3 combinations, and the best one is chosen with a statistical method which will be described in the following sections.

- **6C-fit** To test the hypothesis of production of a pair of W bosons, the following constraint is added to the 5C-fit:

$$M(jet1, jet2) = M(jet3, jet4) = M_{\rm W}. \tag{4.7}$$

In this case both di-jet masses are required to be equal to the W mass. The number of possible di-jet combinations in this case is also 3. This kind of fit can be used for example as a veto against W pairs.

The improvement of the mass resolution provided by the kinematic fits is shown in Figure 4.1, where the mass reconstructed in $e^+e^- \to ZZ \to q\bar{q}q\bar{q}$ events without performing any kinematic fit (just after the correction of the jet energies), is compared to the masses reconstructed after 4C and 5C kinematic fits.

The χ^2 resulting from the kinematic fits represents a test of the goodness of the hypothesis under which the fit was performed.

4.5 Identification of b-quarks

The identification of b-quarks is a fundamental tool to reject WW background. In fact, while the branching ratio of the decay $Z \to b\bar{b}$ is about 15%, the branching ratio of the decay of a W boson in a quark-antiquark pair containing a b-quark is about 0.2%.

In the fragmentation process of a b-quark, b-hadrons are produced, which have an average lifetime $\tau \simeq 10^{-12}$s. At LEP2 energies this lifetime corresponds to a mean path $\lambda = c\beta\gamma\tau \simeq$ 2mm. Thus the identification of jets originated by b-quarks is based on the search for decay vertices displaced from the primary interaction vertex; this search is mainly relying on the precise reconstruction of the track hits in the Silicon Microvertex Detector, the OPAL subdetector closest to the e^+e^- interaction point.

Another characteristic of the b-quark jets is that the b-hadrons decay semileptonically, i.e. as $B \to l\nu X$ with $l = e$ or μ, with a branching ratio of about 21%. Thus, high-P_t lepton tagging can be also exploited to identify b-quarks jets. Besides, b-hadrons tend to produce high-multiplicity and high mass jet topologies. These features are almost independent from the b-hadron lifetime, so they can be separately exploited, in particular to reduce the background from long-lived c-hadrons, and then combined with the lifetime tagging. In the following the OPAL b-tagging algorithm will be described. The algorithm, exploited in the selection of the events in which at least one Z is decaying in a $b\bar{b}$ pair, is a jet-wise algorithm, i.e. the reconstructed objects in an event are forced in a pre-defined number of jets, and the b-tagging is applied to each jet. A more general and detailed description of the OPAL b-tagging can be found in [59, 60].

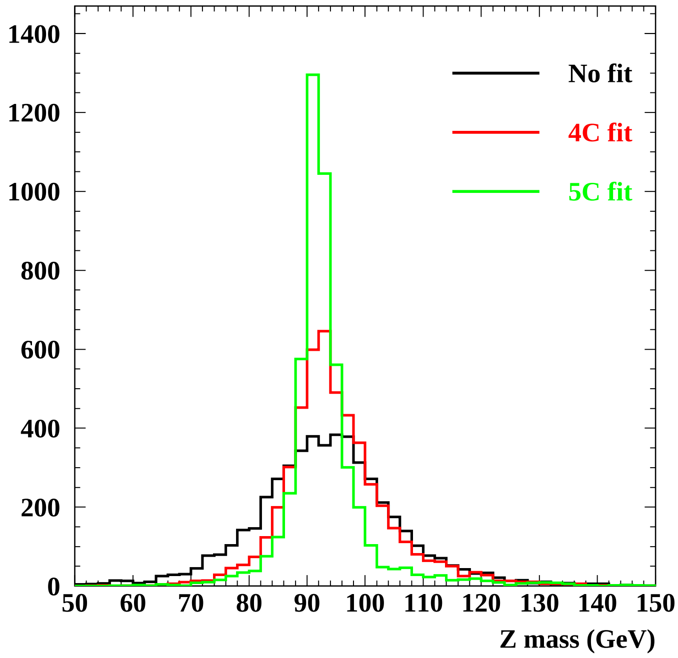

Figure 4.1: *Reconstructed mass in* $e^+e^- \to ZZ \to q\bar{q}q\bar{q}$ *events, without kinematic fits (continuous line), after the 4C-fit (dashed line), and after the 5C-fit (dotted line). For the mass reconstructed without any fit and the 4C-fit mass, the average of the two Z masses is plotted.*

4.5.1 Lifetime tagging

Secondary vertex tagging

The relevant quantity in the tagging of secondary vertices is the decay length significance l/σ_l, defined as the distance l between the secondary vertex and the primary interaction vertex, divided by its error σ_l. In the calculation of the error σ_l both errors on the primary and on the secondary vertex measurement are taken into account. A combination of two algorithms is exploited to tag secondary vertices. These are the so-called *Tear-down* and *Build-up* algorithm:

- **Tear-down algorithm:** a vertex is fitted using all tracks of a given jet. The track giving the largest contribution to the χ^2 is then excluded from the fit and the fit is repeated. The procedure is repeated until the χ^2 has become less than 4 or the number of the remaining tracks is two. The key point of the tear-down algorithm is the high multiplicity from the secondary vertex; but, if the track multiplicity of the primary vertex is higher than that of the secondary, the algorithm tends to tag the primary vertex and fails to tag the secondary. To reduce the number of primary tracks and increase the relative rate of secondary tracks in the jets, sub-jets are formed inside each jet, using the CONE algorithm [61]. The CONE algorithm consists in summing the energy of the objects contained inside a cone around each track of the jet. The cone is defined by:

$$\sqrt{\Delta\phi^2 + \Delta\eta^2} < R \tag{4.8}$$

  where R is a parameter which can be tuned (in this work $R = 0.50$ was chosen). If the total energy of the objects (tracks and ECAL clusters) inside a cone is greater than $\epsilon = 7$ GeV, then a sub-jet is formed out of the objects.

- **Build-up algorithm:** here a scheme opposite to the tear-down algorithm is followed. The tracks with high impact parameter significance d/σ_d in the $r-\phi$ plane are considered as seed-tracks. Each pair of crossing seed tracks in a jet is considered as a seed vertex. The combination of each track in the jet with each of the seed vertices is then tested, and the three-tracks combination giving the best χ^2 is taken as a new seed vertex, if the χ^2 probability is bigger than 1%. The procedure is repeated until there are no more tracks in the jet, or until no combination with a χ^2 probability greater than 1% is found.

Sub-jet formation with the CONE algorithm is introduced to reduce the number of tracks from the primary vertices and keep most of those coming from b-hadron decays. In order to further separate the tracks likely to come from b-hadrons, a track-by-track discriminator is built, to define the priority of the tracks in a given sub-jet. Only tracks having high priority in a given sub-jet are used in the secondary vertex fitting. The priority of each track in a sub-jet is calculated using an Artificial Neural Network (ANN), whose input variables are:

- the absolute value of the impact parameters both in the $r-\phi$ and $r-z$ planes;
- the track momentum;
- the track transverse momentum with respect to the sub-jet axis;
- the track direction with respect to the beam axis

The output of the priority-ANN is shown in Figure 4.2, together with a schematic description of successive vertex finding algorithm, which can be described as follows: the tracks of a sub-jet are then ordered according to the priority P_{ANN}, calculated using the ANN. Using the first 6 tracks (or all the tracks of the sub-jet if they are less than 6) a vertex candidate (seed vertex) is formed with the tear-down algorithm. The tracks used to form the seed vertex are called seed tracks; the choice of using the first 6 tracks comes from the results of optimisation studies. Using this procedure, only one seed vertex per sub-jet is formed.

The next step uses the possible residual tracks: they are sorted according to the distance to the seed vertex, then the vertex fit is repeated adding the residual tracks one by one starting with the nearest one. If the new vertex has a small enough χ^2, the new vertex replaces the original seed vertex; the procedure is iteratively repeated like in the build-up algorithm.

The vertex significance $s = l/\sigma_l$, where l is the distance of the vertex from the primary vertex and σ_l is its error, is translated into a secondary vertex likelihood $\mathcal{L}_{SV}$, which is calculated depending on the vertex multiplicity and on the direction of the sub-jet. The probability densities f for b-, c- and uds-quarks as a function of the significance s and of the vertex multiplicity are calculated in three zones of the detector: $|\cos\theta| < 0.75$, $0.75 < |\cos\theta| < 0.9$ and $|\cos\theta| > 0.9$, where θ indicates the polar angle of the sub-jet direction. In fact the forward region of the detector has a worse reconstruction performance than the central region. The secondary vertex likelihood is then calculated as:

$$\mathcal{L}_{SV} = \frac{f_b^{n,i}(s)}{f_b^{n,i}(s) + f_c^{n,i}(s) + f_{uds}^{n,i}(s)} \tag{4.9}$$

where $f_b^{n,i}$ is the b-flavour probability density for the vertex multiplicity n in the detector region i, with significance s. If in a jet more than one secondary vertex is found, the one with the highest $\mathcal{L}_{SV}$ is chosen. The distribution of $\mathcal{L}_{SV}$ is shown in Figure 4.4.(a) for data and Monte Carlo, where the Monte Carlo sample has been subdivided according to the quark flavour to evidentiate the discriminating power of $\mathcal{L}_{SV}$.

A second discriminating variable is calculated to improve the robustness of the secondary vertex tagging. This variable is the reduced secondary vertex likelihood $\mathcal{R}_{SV}$ which is calculated

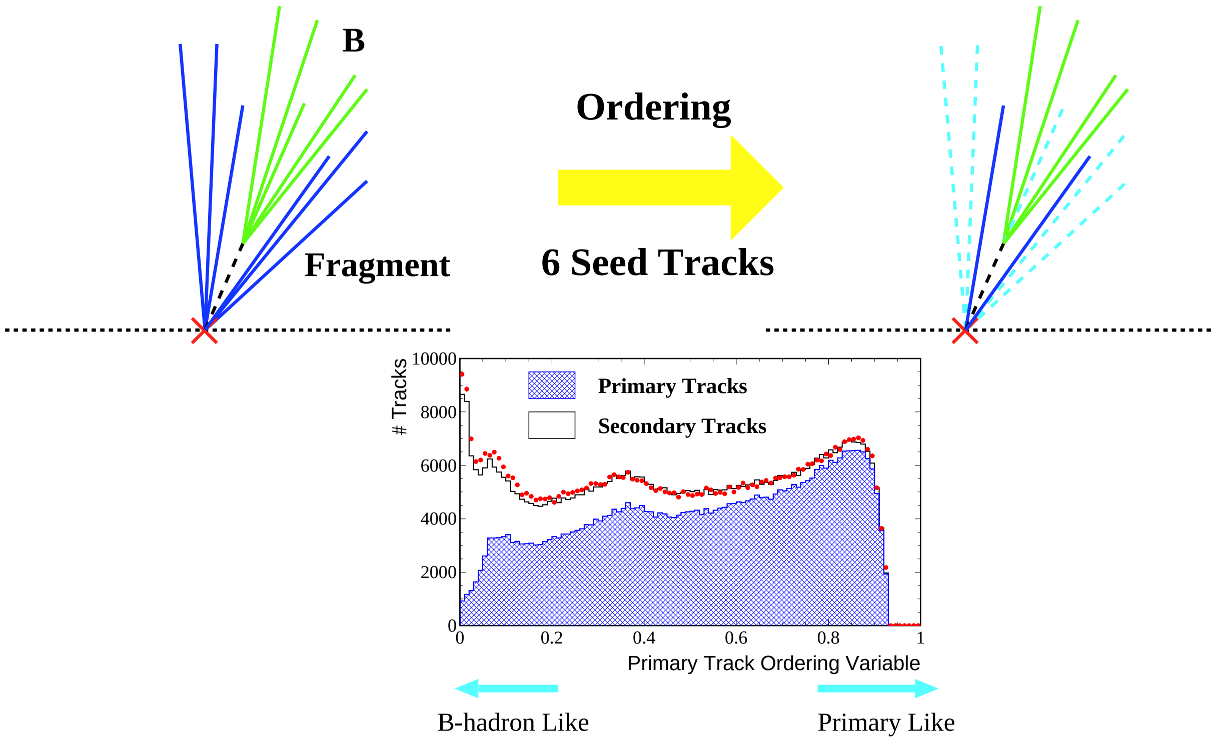

Figure 4.2: *Schematic view of the secondary vertex tagging, through the ordering of the cone tracks. The bottom plot shows the distribution of the priority-ANN*

as follows: from the vertex used for the calculation of $\mathcal{L}_{SV}$ the track with the highest impact parameter significance d/σ_d is removed, and the vertex is fitted again. $\mathcal{R}_{SV}$ is then calculated in the same way as $\mathcal{L}_{SV}$. For b-hadrons, this so-called reduced vertex is expected to have about the same decay length significance of the secondary vertex previously found; in the case of light quarks, a single wrongly reconstructed track may lead to a fake high decay length significance. The reduced likelihood $\mathcal{R}_{SV}$ would be in such a case not affected. The distribution of $\mathcal{R}_{SV}$ is shown in figure 4.4.(b) for data and Monte Carlo.

Impact parameter tagging

The tagging based on the track impact parameters is very important to increase the efficiency of the lifetime tagging for those jets in which no secondary vertex can be reconstructed. The impact parameter tagging constructs a single-track likelihood from the probability density function (p.d.f.) of the impact parameter significance $S = d/\sigma_d$ for different quark flavors. While for the priority-ANN used for the vertex tag the absolute value of the impact parameter was used as an input, in this case the impact parameter is considered with its sign. If the track point of closest approach to the primary vertex is in the hemisphere, where also the jet axis is, then the impact parameter is positive, otherwise is negative. The distribution of the impact parameter significance in the plane $r - \phi$ is shown in Figure 4.3 for data and Monte Carlo.

Both the impact parameters in the $r - \phi$ and $r - z$ plane are used [1].

[1] The use of the 3-dimensional impact parameter has been tested to give worse performance than the use of the two projected impact parameters.

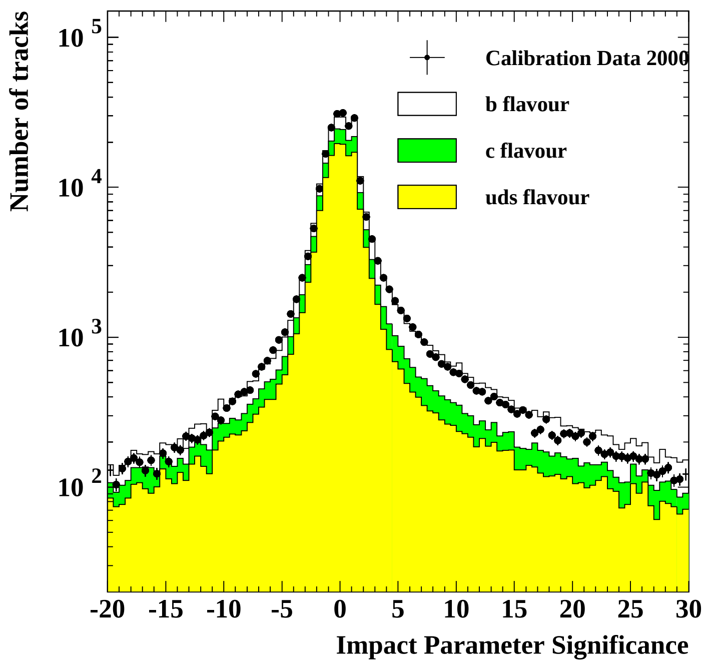

Figure 4.3: *Distribution of the impact parameter significance for the calibration data at* $\sqrt{s} = M_Z$ *taken in the year 2000. The points are the OPAL data, the histograms are the* $\mathrm{Z} \to \mathrm{q\bar{q}}$ *MC, where the double-hatched histogram refers to uds-quarks, the hatched histogram to c-quarks, and the open histogram to b-quarks.*

The combination of the two informations is done according to the formula:

$$F_{\mathrm{q}} = \prod_{i=1}^{N_{r\phi}} f_{\mathrm{q}}^{r\phi}(S_i^{r\phi}) \cdot \prod_{i=1}^{N_{rz}} f_{\mathrm{q}}^{rz}(S_i^{rz}) \tag{4.10}$$

where q=uds, c or b denotes the quark flavour, $f_{\mathrm{q}}^{r\phi}$ and f_{q}^{rz} are the p.d.f., of the impact parameter significances $S_i^{r\phi}$ and S_i^{rz} in the plane $r\phi$ and rz respectively, for the flavour q. The $S_i^{r\phi}$ and S_i^{rz} are the impact parameter significances in the $r\phi$ and rz plane respectively. The first product runs over all tracks having good track quality in the $r\phi$ plane, $N_{r\phi}$, while the second runs over all tracks having good track quality in the rz plane, N_{rz}; for the definition of the track quality criteria see Appendix A, Section A.1 and A.2.

The resulting F_{q} is the relative likelihood for the quark flavour q. The final impact parameter likelihood $\mathcal{L}_{IP}$ is calculated as:

$$\mathcal{L}_{IP} = \frac{R_{\mathrm{b}} F_{\mathrm{b}}}{R_{\mathrm{b}} F_{\mathrm{b}} + R_{\mathrm{c}} F_{\mathrm{c}} + R_{\mathrm{uds}} F_{\mathrm{uds}}} \tag{4.11}$$

Where the R_{q} are the relative branching ratios of the hadronic Z decays $R_{\mathrm{q}} = \frac{\Gamma(\mathrm{Z}\to\mathrm{q\bar{q}})}{\Gamma(\mathrm{Z}\to\mathrm{hadrons})}$. The distribution of $\mathcal{L}_{IP}$ is shown in Figure 4.4.(c).

As for the secondary vertex likelihood, a reduced impact parameter likelihood is calculated, to avoid that a single track with high impact parameter significance, due to wrong reconstruction, could lead to a fake b identification. The reduced impact parameter likelihood $\mathcal{R}_{IP}$ is calculated as $\mathcal{L}_{IP}$, but excluding the track having the highest impact parameter significance. The distribution of $\mathcal{R}_{IP}$ is shown in Figure 4.4.(d).

Lifetime Artificial Neural Network

The secondary vertex likelihoods and the impact parameter likelihoods are combined in a single lifetime discriminant, through an Artificial Neural Network. The input variables for the Lifetime-ANN are the following:

1. $\mathcal{L}_{SV}$: secondary vertex likelihood
2. $\mathcal{R}_{SV}$: reduced secondary vertex likelihood
3. $\mathcal{L}_{IP}$: Impact Parameter likelihood
4. $\mathcal{R}_{IP}$: reduced impact parameter likelihood

The distribution of the four input likelihoods are shown in Figure 4.4, while the resulting output of the lifetime-ANN is shown in Figure 4.5.

4.5.2 Lepton tagging

A powerful variable to discriminate b-quarks from c-quarks is the transversal momentum p_t of the leptons (electrons or muons) from semi-leptonic decays of b- and c-mesons. The lepton p_t is calculated with respect to the direction of the sub-jet which contains the lepton track. Leptons which do not belong to any sub-jet are not used. The p_t spectra of tagged electrons and muons are shown in Figure 4.6 for data and Monte Carlo.

Although the efficiency is in this case limited by the semileptonic branching ratio (which is about 21%), the combination of the lepton tag with the lifetime tag helps in improving the purity of the tagging.

The OPAL lepton ID is described in [62]; besides those of the lepton ID, additional requirements imposed are:

- the lepton track must have at least two hits in SI;
- the track momentum must be greater than 2 GeV (electrons) or 3 GeV (muons).

4.5.3 Jet kinematic tagging

Because of the higher multiplicity of b-hadron decays and of the high mass of the b-hadrons, the jets originating from the fragmentation of b-quarks have in average a more spherical shape than those originating from the other quarks. The shape of a jet (or, more in general, of an event) can be characterised through the eigenvalues of the normalised energy-momentum tensor, which is defined as:

$$\theta_{ij} = \frac{\sum_{\alpha=1}^{N} p_i^\alpha p_j^\alpha / |\vec{p}_\alpha|}{\sum_{\alpha=1}^{N} |\vec{p}_\alpha|} \qquad \text{with} \quad i,j = 1,2,3, \tag{4.12}$$

where the sum runs over all jet tracks and energy clusters of the jet, and the three-momenta are calculated in the jet's reference system. If λ_i (with $i = 1,2,3$ and $\lambda_1 \leq \lambda_2 \leq \lambda_3$) are the eigenvalues of the tensor θ, then the so-called C-parameter is defined as [63]:

$$C = 3(\lambda_1 \cdot \lambda_2 + \lambda_2 \cdot \lambda_3 + \lambda_1 \cdot \lambda_3) \tag{4.13}$$

The value of the C-parameter, which is ranging from 0 to 1, tends to be larger for jets which are more spherical. The eigenvector corresponding to the eigenvalue λ_3 is the so-called sphericity-axis of the jet.

Three discriminating quantities are combined in a jet kinematic tagging Artificial Neural Network. These quantities are:

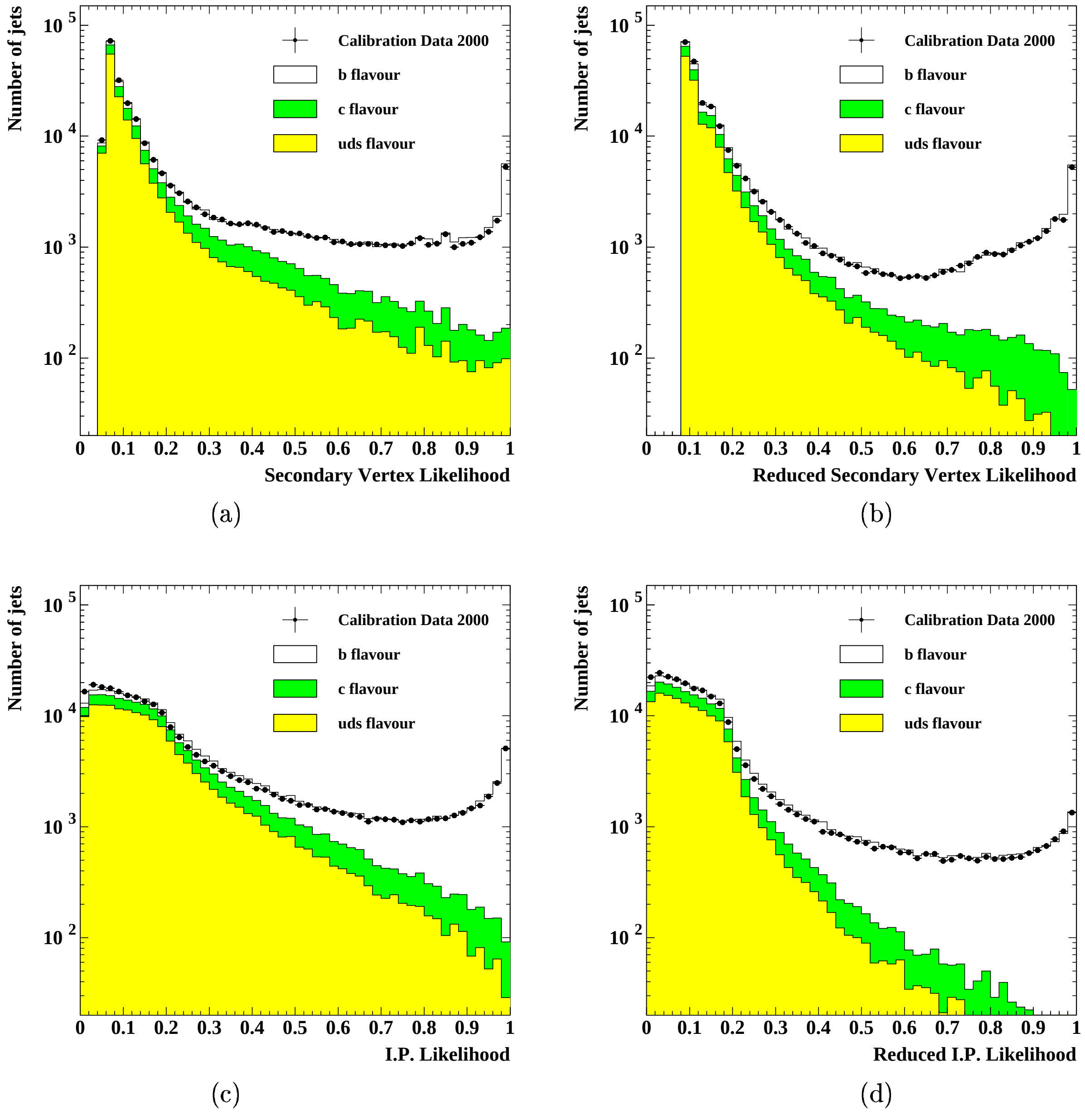

Figure 4.4: *Summary of the four likelihoods used as input for the lifetime-ANN; (a): secondary vertex likelihood; (b): reduced secondary vertex likelihood; (c): impact parameter likelihood; (d): reduced impact parameter likelihood. The light-grey histograms show the MC distributions for uds-quarks, the dark-grey histograms show the MC distributions for c-quarks, while the open histograms show the MC distribution for b-quarks. The points are the OPAL calibration data taken in the year 2000 at* $\sqrt{s} = M_{\mathrm{Z}}$.

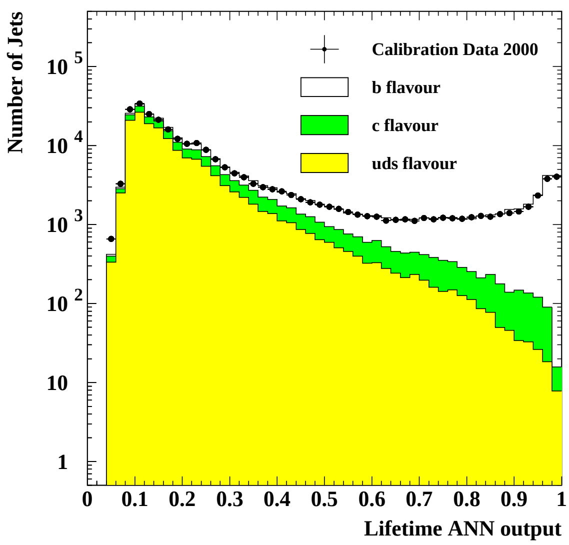

Figure 4.5: *The distribution of the lifetime-ANN. The light-grey histogram shows the MC distribution for uds-quarks, the dark-grey histogram shows that for c-quarks, while the open histogram shows the distribution for b-quarks. The points are the OPAL calibration data of the year 2000.*

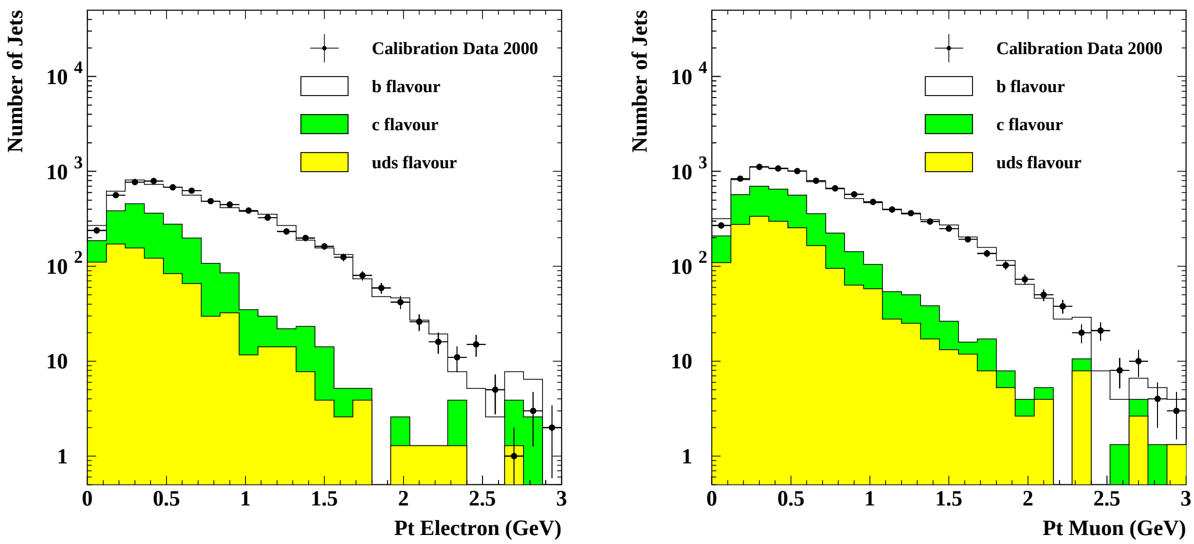

Figure 4.6: *Distribution of the transversal momentum, with respect to the sub-jet direction, of the identified electrons (left) and muons (right). Shown is a comparison of the* $\mathrm{Z} \rightarrow \mathrm{q\bar{q}}$ *MC with the calibration data taken in the year 2000: light-grey histogram for uds-quarks, dark-grey histogram for c-quarks, open histogram for b-quarks, while the points are the OPAL data.*

1. the number of tracks and energy clusters in the central part of the jet. All tracks and energy clusters contained in a 0.4 rad cone around the jet axis are counted.

2. The angle between the jet axis in the laboratory system and the jet sphericity axis in the jet reference system.

3. The C-parameter of the jet, calculated using all the tracks and energy clusters contained inside a 1.5 rad cone around the jet axis.

4.5.4 b-tagging discriminant

The three rather independent tagging variables lifetime ANN, lepton-p_t and jet-kinematic ANN are combined in a single b-tagging discriminant, using an unbinned likelihood method. The final b-tagging output $\mathcal{L}_{jet}$ for a single jet, combining the b-tagging quantities is given by:

$$\mathcal{L}_{jet} = \frac{R_{\mathrm{b}} \cdot f_{\mathrm{b}}^{t} \cdot f_{\mathrm{b}}^{l} \cdot f_{\mathrm{b}}^{k}}{R_{\mathrm{b}} \cdot f_{\mathrm{b}}^{t} \cdot f_{\mathrm{b}}^{l} \cdot f_{\mathrm{b}}^{k} + R_{\mathrm{c}} \cdot f_{\mathrm{c}}^{t} \cdot f_{\mathrm{c}}^{l} \cdot f_{\mathrm{c}}^{k} + R_{\mathrm{uds}} \cdot f_{\mathrm{uds}}^{t} \cdot f_{\mathrm{uds}}^{l} \cdot f_{\mathrm{uds}}^{k}} \tag{4.14}$$

where R_{q} is the Z branching ratio to the flavour q as already defined in section 4.5.1, and $f_{\mathrm{q}}^{t,l,k}$ are the probability densities for each of the three quantities (lifetime, lepton and jet kinematic tag) corresponding to the flavour q (where q=b,c,uds). The result of the combination is shown in Figure 4.7 for data and Monte Carlo.

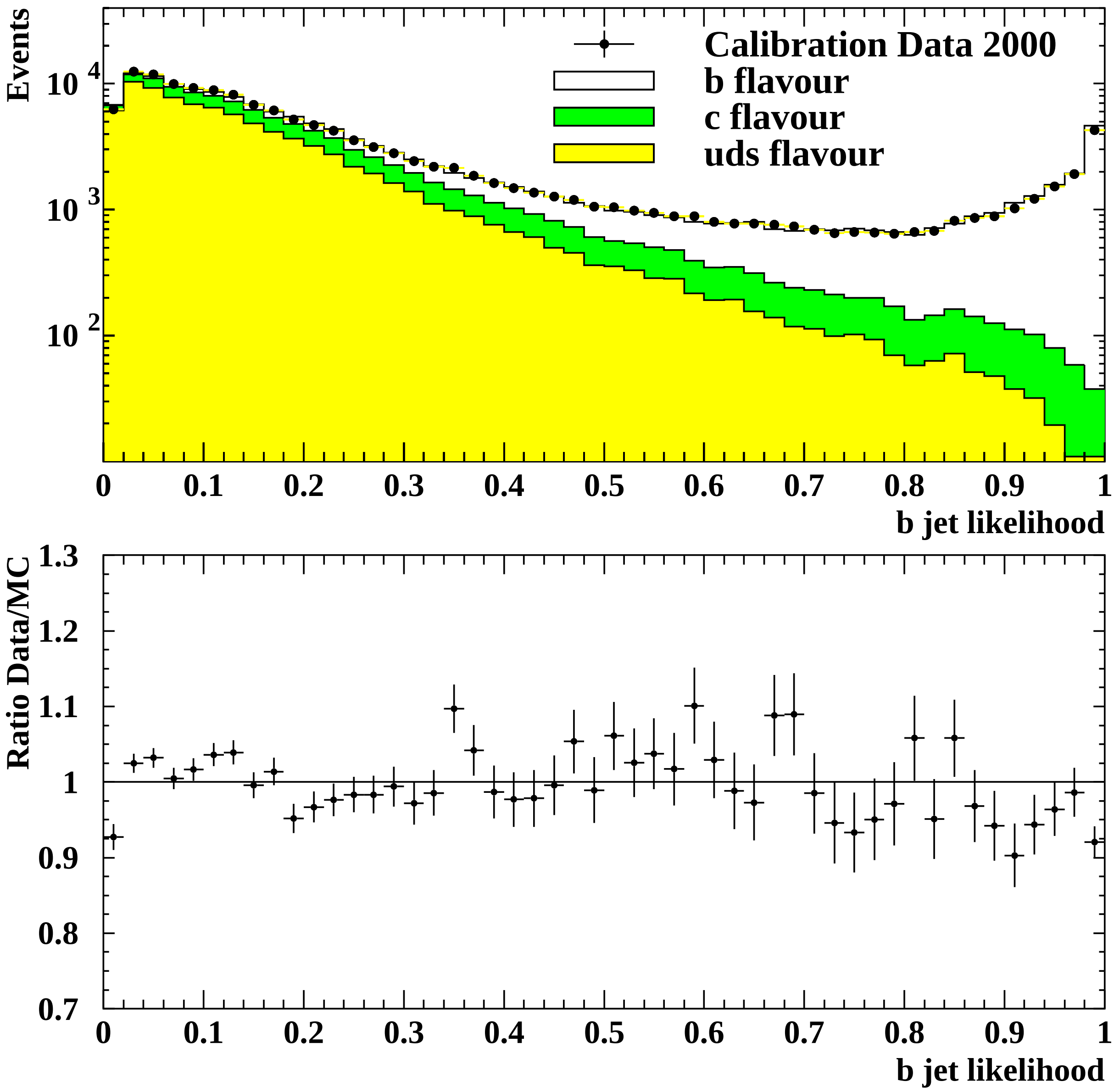

Figure 4.7: *Output of the combined b-tagging likelihood. In the upper plot, the light grey histogram shows the distribution of the likelihood for uds-quarks, the dark grey histogram shows the distribution for c-quarks, and the open histogram shows that for b-quarks. The points are the OPAL calibration data taken in the year 2000 at $\sqrt{s} = M_Z$. The lower plot shows the ratio between data and MC as a function of the likelihood value.*

5. Measurement of the $e^+e^- \to$ZZ cross section at OPAL.

This chapter will describe in particular the selection of the fully hadronic ZZ events. The selection of the ZZ $\to$ q$\bar{\text{q}}$b$\bar{\text{b}}$ events, which exploits the identification of b-quarks, will be discussed in more detail. The combination of the ZZ $\to$ q$\bar{\text{q}}$b$\bar{\text{b}}$ with the flavour independent ZZ $\to$ q$\bar{\text{q}}$q$\bar{\text{q}}$ selection, and the combination of the two fully hadronic selections with the results of the other decay channels selections, for the measurement of the $e^+e^- \to$ZZ cross section will be also described.

5.1 Signal definition

The ZZ cross section is defined as the contribution to the total 4-fermion cross section from the NC02 Z-pair diagrams. All efficiencies and other results which will be given in the following are with respect to these Z-pair processes. Contribution from all other 4-fermion states, including the interference with NC02 diagrams, are considered as background. When using generators which include all 4-fermion diagrams, like for example grc4f, an event weighting method has to be used to define whether a generated event belongs to the signal or to the background. The method used is based on the probability, for each event, of the that the event has been originated by the NC02 diagrams. This probability is defined as:

$$W_{NC02} = \frac{|\mathcal{M}_{NC02}|^2}{|\mathcal{M}_{\text{4fermion}}|^2} \tag{5.1}$$

where $\mathcal{M}_{NC02}$ is the NC02 matrix element, while $\mathcal{M}_{\text{4fermion}}$ is the matrix element calculated using the full set of 4-fermion diagrams. Thus, the signal is defined by reweighting each 4-fermion event by the factor W_{NC02}, while the 4-fermion background is defined by the re-weighting factor $1-W_{NC02}$ [1]. The set of libraries described in [53], based on the grc4f matrix elements, has been used in this analysis for the calculation of the event weights.

In case event generators which include only a particular subset of diagrams are used (for example YFSZZ, which includes only the NC02 diagrams), no event reweighting is usually necessary to define signal and background.

5.2 Analysis strategy

The process $e^+e^- \to$ ZZ $\to$ q$\bar{\text{q}}$q$\bar{\text{q}}$ leads to a 4-jet final state. An example of an event, as reconstructed in the OPAL detector, is shown in Figure 5.1, where a ZZ $\to$ q$\bar{\text{q}}$q$\bar{\text{q}}$ Monte Carlo event at $\sqrt{s}$=200 GeV is shown. The relevant background classes are 4-fermion events, in particular the process $e^+e^- \to$ WW $\to$ q$\bar{\text{q}}$q$\bar{\text{q}}$, and 2-fermion events of the type $e^+e^- \to (\text{Z}/\gamma)^* \to$ q$\bar{\text{q}}$. As seen in Section 3.3, the signal cross section is much smaller than the background cross sections. This requires the development of a selection based on a statistical method (i.e. a likelihood selection), rather than a cut-based selection.

[1] The interference between the NC02 and the other 4-fermion diagrams can be calculated as the difference between $1 - W_{NC02}$ and the weight relative to all 4-fermion but the NC02 ones.

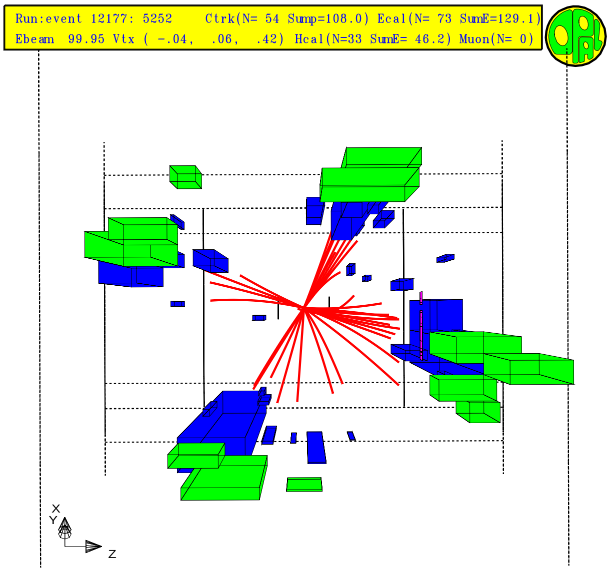

Figure 5.1: *A* $e^+e^- \to ZZ \to q\bar{q}q\bar{q}$ *event reconstructed in the OPAL detector. The event is a Monte Carlo event at* $\sqrt{s} = 200$ *GeV*

The event characteristics which can be exploited to discriminate the signal from the background are the following:

- **Rejection of W pairs.** The flavour-independent selection can only exploit the difference between the invariant masses of the quark-antiquark pairs, which in case of W pair production peak at $M_W \simeq 80.4$ GeV, while in case of Z pair production peak at $M_Z \simeq 91.2$ GeV. Due to the mass resolution of the detector, and to the natural widths of the W and Z bosons (which are ~ 2.0 and ~ 2.4 GeV respectively), the discrimination between WW and ZZ events is particularly difficult, and W pairs represent the main background for the flavour independent $ZZ \to q\bar{q}q\bar{q}$ selection.

  On the other hand, the branching ratio for the decay of the W boson in a pair of quarks, one of which is a b-quark, is $\sim 0.2\%$. On the contrary the Branching Ratio for the decay $Z \to b\bar{b}$ is about 15% [12]. Thus, the identification of b-quarks (the b-tagging algorithm described in Section 4.5) allows to reduce significantly the W pair background for the signal events of the type $ZZ \to q\bar{q}b\bar{b}$. This consideration suggests the development of a dedicated selection for this decay channel.

- **$q\bar{q}$ rejection.** The events of the type $e^+e^- \to q\bar{q}(n\gamma)$ $(n \geq 1)$, the so-called radiative returns to the Z (see Section 3.3) can be easily rejected through a cut on the effective e^+e^- center of mass energy. If the process occurs without initial state radiation, the final state quark and anti-quark are produced back to back; the event is then a two-jet event, and can be rejected exploiting the distributions of variables sensitive to the shape of the event (the so-called event-shape variables, which will be described in the following).

  The $e^+e^- \to q\bar{q}$ events followed by the radiation of one or more gluons by the final state quarks (for example the so-called gluon-splitting, see in Figure 3.8.(c)), lead to event topologies more similar to the 4-jet signal. Such events can also be rejected by the use of event-shape variables in the selection.

5.3 Preselection

A set of preselection cuts, common to both the ZZ $\rightarrow$ q$\bar{\text{q}}$q$\bar{\text{q}}$ and ZZ $\rightarrow$ q$\bar{\text{q}}$b$\bar{\text{b}}$ selections, is performed to remove the background event topologies which have very small similarities with the signal. This allows a better rejection power for the background topologies which more similar to the signal, by using a likelihood selection following the preselection. The preselection consists of a series of cuts on kinematical and event shape variables, and is designed to have a high efficiency for the ZZ $\rightarrow$ q$\bar{\text{q}}$q$\bar{\text{q}}$ events, while reducing significantly the number of events from the main background classes and from the other ZZ decay channels. The following cuts are performed as preselection for the 4-jet channels:

1. **Hadronic final state.** The event must be classified as an hadronic final state (see Appendix B, for the details of the classification). The cuts on the number of energy objects and on the total and polar angle-balanced energy, allow to remove almost completely the fully leptonic final states and the two-photon events.

2. **Effective center of mass energy $\sqrt{s'} > 0.7 \cdot \sqrt{s}$.** The process $(\mathrm{Z}/\gamma)^* \rightarrow$ q$\bar{\text{q}}$ takes place, for about 3/4 of the events, after the radiation of a photon in the initial state. The production of a q$\bar{\text{q}}$ pair after initial state radiation, leading to a center of mass energy closer to the Z-pole (the so-called radiative return to the Z) has in fact a much larger cross section than the full-energy process (by a factor $\simeq$6).

   In case of initial state radiation, the effective center of mass energy of the $q\bar{q}$ system, denoted as $\sqrt{s'}$ is significantly less than the actual $\mathrm{e^+e^-}$ center of mass energy. It is possible to determine $\sqrt{s'}$ in two ways. In the first method the biggest energy deposition in the electromagnetic calorimeter not associated to any track is assumed to be the radiated photon, and the effective center of mass energy is calculated as $\sqrt{s'} = ((\sqrt{s}-E_\gamma)^2 - \vec{P}_\gamma^2)^{1/2}$. In the second method, it is assumed that the photon is emitted along the direction of the beam-pipe and can't be observed in the detector. The effective center of mass energy $\sqrt{s'}$ is then determined by the kinematic fit described in Section 4.4. Both methods are applied to each event, and the smallest of the two $\sqrt{s'}$ values is used to perform the preselection cut $\sqrt{s'} > 0.7 \cdot \sqrt{s}$.

3. **4-jet final state: $Y_{43} > 0.003$.** To remove 3-jet-like events, mainly coming from q$\bar{\text{q}}$ production followed by gluon radiation, a cut on the jet-resolution parameter y_{43} is applied. Y_{43} is calculated according to the DURHAM algorithm, as described in Section 4.3. y_{43} represents the DURHAM "distance" between the two closest jets after the event has been constrained in 4 jets. So its value it's expected to be smaller for events which have a topology more similar to a 3-jet event than to a 4-jet one.

4. **C-parameter: $C > 0.27$.** The C parameter, calculated as shown in Section 4.5.3, Equation 4.13 [2] gives an estimate of the sphericity of the event, i.e. of the uniformity of the distribution of the reconstructed objects over the full solid angle. A 2-jet event with two almost collinear jets has a value of the C parameter close to zero, while a 4-jet event tends to have higher values of C.

5. **At least two good tracks per jet.** This cut is performed to reject the events in which a jet is constituted by a single photon or by a single lepton track. The cut is mostly effective against semileptonic decays of W pairs, i.e. WW$\rightarrow qql^{\pm}\nu$.

[2] In Section 4.5.3 the C parameter was calculated using tracks and clusters of a single jet only, but its definition is the same when referring to a whole event, with the only difference that the energy and momentum tensor 4.12 is calculated using all the objects of the event.

6. **$P(\chi^2)$ of the kinematic fits.** The hypothesis of energy and momentum conservation is tested through the 4C and 5C kinematic fits, which have been described in Section 4.4 The 4C fit is required to converge, and is required to have $P(\chi^2) > 10^{-10}$. The $e^+e^- \to ZZ$ hypothesis is tested performing the 5C fit, where in addition to energy and momentum conservation the masses of the two jet pairs are required to be equal. The fit is applied in turn to all three possible combinations of the four jets, and is required to have $P(\chi^2) > 10^{-10}$ for at least one combination.

A comparison between data and Monte Carlo for the preselection variables is shown in the Figures 5.5 and 5.6; the two figures contain the distributions at center of mass energies of 200 and 205 GeV, respectively[3]. The data distributions are compared with the distributions obtained from Monte Carlo events generated at the center of mass energy corresponding to the data. The number of events selected in data, the total expected number of events, and the number of events expected from each event class, are summarised in the Tables 5.1 and 5.2. The agreement between data and Monte Carlo is in general good and the differences are compatible with the statistical errors. The efficiency of the preselection for the $ZZ \to q\bar{q}q\bar{q}$ signal events is about 85%, while the 4-fermion and 2-fermion backgrounds are reduced to ~30% and ~2% of their initial amount, respectively.

5.4 Jet pairing

In 4-jet events, under the hypothesis that the four jets are originated by a pair of Z bosons, there are three possible combinations for associating the four jets to the two bosons. Finding the correct association between jets is essential to determine correctly the four momenta of the primary bosons. The method used in the 4-jet ZZ analysis is a likelihood method. A jet-pairing likelihood is calculated on the basis of reference variables which are sensitive to the correct pairing of the Z. The likelihood developed for this analysis is flavour-independent: this means that no b-tagging information is used for the pairing; due to this choice, the likelihood pairing can be used both by the flavour-independent analysis and by the $ZZ \to q\bar{q}b\bar{b}$ analysis.

The variables used as reference for the jet-pairing likelihood are:

- The mass resulting from the 5C fit, the kinematic fit where the two jet pairs are constrained to have the same mass (see section 4.1)
- The χ^2 probability of the 5C fit
- The difference between the two di-jet invariant masses, calculated using the jet momenta resulting from the 4C fit.

The reference distributions of the pairing likelihood variables are shown in figure 5.4. They are generated using $e^+e^- \to ZZ \to q\bar{q}q\bar{q}$ Monte Carlo events which are passing the preselection. For each of the three combinations, the likelihood is calculated as:

$$\mathcal{L}_{\text{pairing}} = \frac{\prod_{i=1,3} P^i_{\text{correct}}}{\prod_{i=1,3} P_{\text{correct}} + \prod_{i=1,3} P_{\text{wrong}}} \tag{5.2}$$

where the products run over the three reference variables, and P^i_{correct} and P^i_{wrong} are the probabilities, calculated from the reference distributions in figure 5.4, that the combination is correct or wrong respectively.

[3] The data sets used for the plots are subsets of the data taken in the years 1999 and 2000, when e^+e^- the center of mass energy was increased from 192 to 208 GeV.

$\sqrt{s} = 192$ GeV $\mathcal{L} = 29.1\text{pb}^{-1}$							
Cut	Data	Total MC	4-fermion	$q\bar{q}$	ZZ not $q\bar{q}q\bar{q}$	ZZ $\to q\bar{q}q\bar{q}$	Efficiency (%)
1	3008	2924.5	535.9	2368.2	9.1	11.3	99.8
2	1051	1012.2	318.6	677.4	5.1	11.1	97.4
3	325	315.7	219.8	83.5	2.1	10.4	91.3
4	321	309.1	219.4	77.3	2.1	10.3	90.8
5	273	261.8	191.8	59.2	0.7	10.0	89.0
6	269	253.0	188.4	54.0	0.7	9.9	87.3
$\sqrt{s} = 196$ GeV $\mathcal{L} = 75.4\text{pb}^{-1}$							
Cut	Data	Total MC	4-fermion	$q\bar{q}$	ZZ not $q\bar{q}q\bar{q}$	ZZ $\to q\bar{q}q\bar{q}$	Efficiency (%)
1	6954	7212.8	1401.2	5751.1	26.9	33.6	99.8
2	2465	2554.6	832.7	1675.4	13.6	32.9	97.6
3	859	816.0	570.2	209.1	6.0	30.8	91.3
4	845	799.5	569.4	193.5	5.9	30.7	91.0
5	731	678.1	497.7	148.6	2.0	29.8	89.4
6	707	653.9	489.3	133.2	1.9	29.5	87.5
$\sqrt{s} = 200$ GeV $\mathcal{L} = 77.7\text{pb}^{-1}$							
Cut	Data	Total MC	4-fermion	$q\bar{q}$	ZZ not $q\bar{q}q\bar{q}$	ZZ $\to q\bar{q}q\bar{q}$	Efficiency (%)
1	7111	7134.1	1457.9	5608.3	30.2	37.6	99.8
2	2529	2551.5	860.1	1639.9	14.8	36.7	97.3
3	849	830.0	587.2	202.2	6.5	34.1	90.3
4	841	815.0	586.3	188.4	6.4	34.0	90.1
5	716	693.1	512.2	145.8	2.1	33.0	88.4
6	682	669.9	502.8	132.4	1.9	32.7	86.6
$\sqrt{s} = 202$ GeV $\mathcal{L} = 36.6\text{pb}^{-1}$							
Cut	Data	Total MC	4-fermion	$q\bar{q}$	ZZ not $q\bar{q}q\bar{q}$	ZZ $\to q\bar{q}q\bar{q}$	Efficiency (%)
1	3384	3282.5	686.1	2563.6	14.5	18.2	99.8
2	1213	1179.9	404.8	750.3	7.1	17.7	97.2
3	396	389.8	276.3	94.0	3.2	16.4	89.7
4	394	382.7	275.9	87.3	3.1	16.3	89.5
5	349	323.0	240.7	65.6	1.0	15.8	87.7
6	339	312.4	236.2	59.6	0.9	15.6	85.7

Table 5.1: *The table refers to the analysis of the data taken in the year 1999, and shows the number of events after each preselection cut, at the different* e^+e^- *center of mass energies analysed. The expected number of events is derived from the Monte Carlo simulation, and is normalised to the integrated luminosity in data. The last column shows the efficiency for* ZZ $\to q\bar{q}q\bar{q}$ *events.*

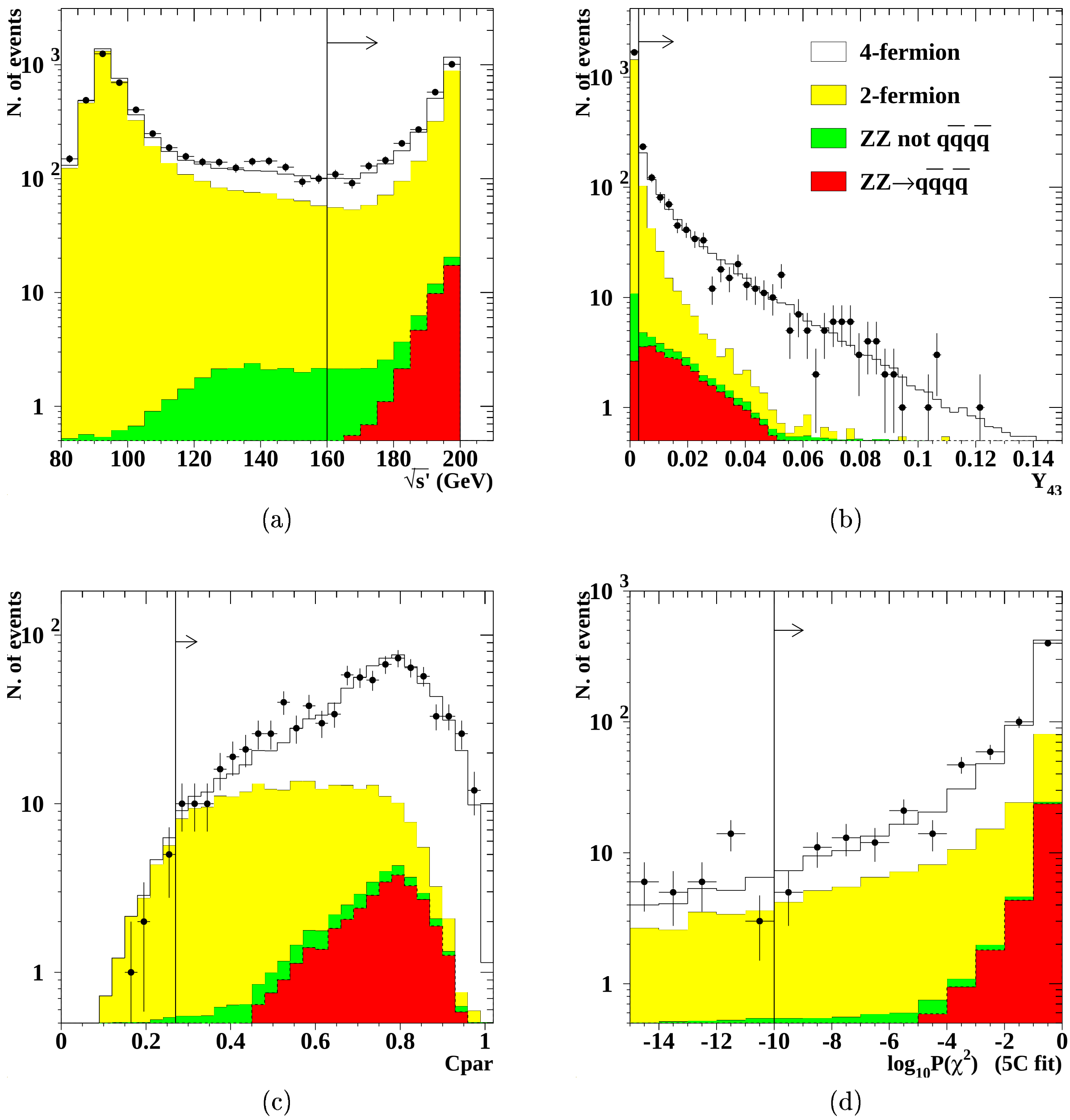

Figure 5.2: *The preselection variables at* $\sqrt{s} = 200$ *GeV. (a):* $\sqrt{s'}$*; (b):* Y_{43}*; (c): the C-parameter; (d): the* χ^2 *probability for the 5-C kinematic fit, constraining energy and momentum conservation, and the two di-jet masses to be equal. The dark-grey histograms show the distributions for* ZZ $\rightarrow$ q$\bar{\text{q}}$q$\bar{\text{q}}$ *events, the grey histograms for ZZ not decaying in four quarks; the light-grey histograms show the distributions of* q$\bar{\text{q}}$ *background events, while the open histograms those of 4-fermion background events. The points are the OPAL data, and the error bars indicate the statistical error.*

Out of the three possible combinations, the one which is giving the highest likelihood value is chosen to be the correct one. The rate of correct pairings obtained with this method is slightly depending on the center of mass energy; the differences are mainly due to the Lorentz-boost of the Z bosons, which is increasing as $\sqrt{s}$ increases.

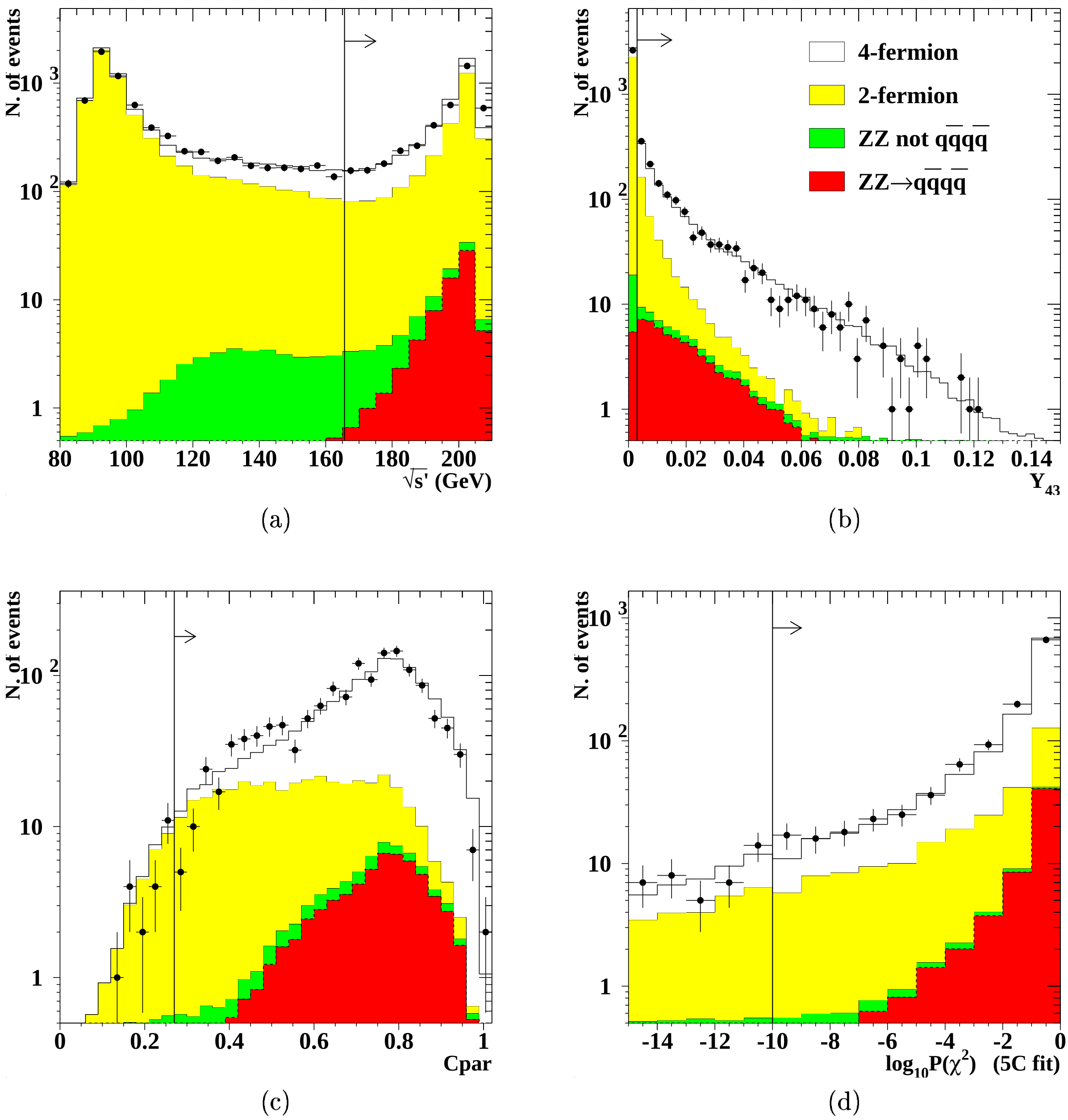

Figure 5.3: *The preselection variables at $\sqrt{s}$ = 207 GeV. (a): $\sqrt{s'}$; (b): Y_{43}; (c): the C-parameter; (d): the χ^2 probability for the 4-C kinematic fit, constraining energy and momentum conservation. The Monte Carlo histograms are divided in subsamples as in Figure 5.2. The points are the OPAL data, and the bars indicate the statistical error.*

An alternative method to determine the correct pairing would be to choose the combination which gives the highest χ^2 probability. The likelihood method results anyway, as it exploits also the mass information, in a higher rate of correct pairings. The results at each center of mass energy are summarised in Table 5.3, for the likelihood pairing and for the χ^2 probability pairing. In the analysis presented here, the likelihood method, giving a better performance, has been used.

As the reference distributions include only ZZ $\rightarrow$ q$\bar{\text{q}}$q$\bar{\text{q}}$ events, the pairing efficiency is opti-

$\sqrt{s} = 205$ GeV $\mathcal{L} = 80.2\mathrm{pb}^{-1}$							
Cut	Data	Total MC	4-fermion	$q\bar{q}$	ZZ not $q\bar{q}q\bar{q}$	ZZ $\to q\bar{q}q\bar{q}$	Efficiency (%)
1	7061	6868.0	1510.3	5282.6	33.4	41.7	99.8
2	2528	2533.6	893.6	1583.6	15.8	40.6	97.1
3	855	838.9	598.8	195.5	7.3	37.3	89.2
4	836	823.9	597.9	181.6	7.3	37.2	89.0
5	727	697.0	520.5	138.4	2.1	36.0	87.2
6	702	672.5	509.3	125.6	2.0	35.6	85.3
$\sqrt{s} = 207$ GeV $\mathcal{L} = 133.3\mathrm{pb}^{-1}$							
Cut	Data	Total MC	4-fermion	$q\bar{q}$	ZZ not $q\bar{q}q\bar{q}$	ZZ $\to q\bar{q}q\bar{q}$	Efficiency (%)
1	11185	11415.4	2510.2	8780.4	55.5	69.3	99.8
2	4049	4159.4	1461.4	2605.3	25.4	67.2	96.8
3	1416	1380.7	986.5	320.5	11.9	61.8	88.9
4	1394	1355.7	984.9	297.4	11.8	61.6	88.8
5	1196	1153.2	861.7	228.4	3.4	59.7	86.9
6	1155	1113.5	843.7	207.4	3.2	59.1	85.1

Table 5.2: *The table refers to the analysis of the data taken in the year 2000, and shows the number of events after each preselection cut, at the different e^+e^- center of mass energies analysed. The expected number of events is derived from the Monte Carlo simulation, and is normalised to the integrated luminosity in data. The last column shows the efficiency for the ZZ $\to q\bar{q}q\bar{q}$ events.*

$\sqrt{s}$	Correct pairings (%)	
	Likelihood method	$P(\chi^2)$ method
192	81.8±0.4	66.4±0.5
196	80.3±0.4	66.2±0.5
200	79.5±0.4	66.1±0.5
202	78.5±0.4	65.9±0.5
206	78.1±0.4	66.1±0.5

Table 5.3: *Rate of correct pairings for the different center of mass energies examined in this analysis. The results of the likelihood method are compared to those of the maximum-$P(\chi^2)$ method.*

mised for the signal, and not for the background; thus, the output value of the pairing likelihood can be also used as a signal discriminating variable.

5.5 Event selections

In order to maximise the sensitivity to the Z pair production cross section, the fully-hadronic selection is split into two channels: an inclusive selection which accepts all final state quark flavours and which is based mainly on the di-jet mass information; a second selection specialised for $e^+e^- \to ZZ \to q\bar{q}b\bar{b}$ events exploits the identification of b-quarks in the final state (b-tagging, see in Section 4.5) along with more relaxed kinematic selection criteria. The ZZ $\to q\bar{q}b\bar{b}$ selection will be described in more detail, while the flavour-independent selection will be shortly discussed in Section 5.8.

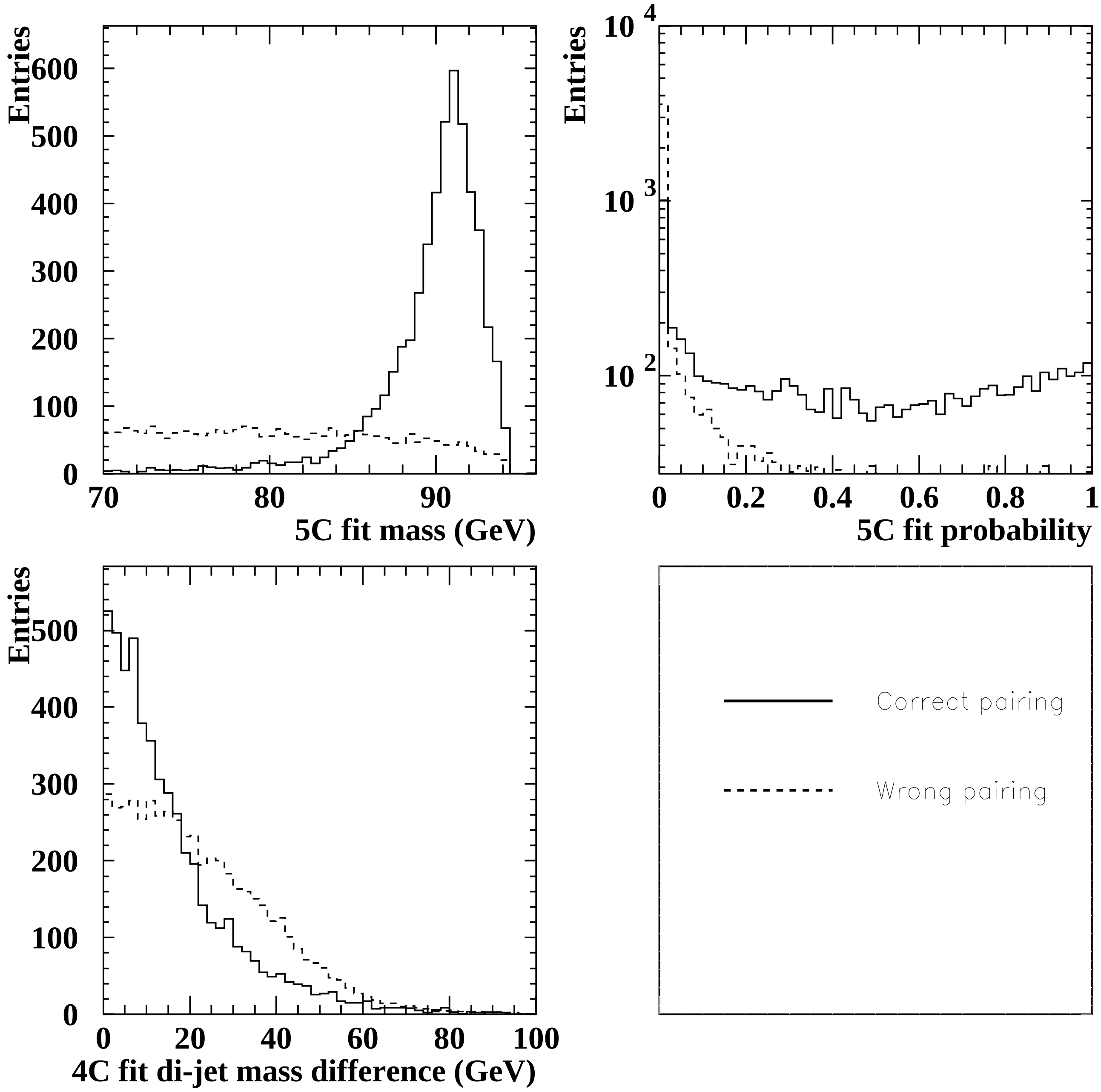

Figure 5.4: *Reference distribution of the variables used for the calculation of the ZZ jet-pairing likelihood. The histograms are computed using* $e^+e^- \to ZZ \to q\bar{q}q\bar{q}$ *Monte Carlo events. The full-line histograms show the distributions in case the correct pairing is chosen. The dashed-line histograms shows the distributions in case of the wrong pairings. Each of the two wrong pairings is entering the histogram with weight 0.5, such that the number of entries in the reference distribution is the same in the case of correct and wrong pairings.*

5.6 $e^+e^- \rightarrow ZZ \rightarrow q\bar{q}b\bar{b}$ Likelihood selection

A likelihood method (see Appendix C), is applied in order to classify the events remaining after the preselection as background events from $Z/\gamma^* \rightarrow q\bar{q}$, or four-fermion processes, or $ZZ \rightarrow q\bar{q}b\bar{b}$ signal events. To select signal events, eight quantities which provide a good separation between the three event classes, are used. The background reference distributions for $q\bar{q}$ events were generated by PYHTIA [45], while for the 4-fermion background events produced with grc4f with pure hadronic decays were used. The signal reference distributions included $ZZ \rightarrow q\bar{q}b\bar{b}$ events generated by YFSZZ[44]. For the analysis at each value of the e^+e^- center of mass energy, the reference distributions are generated using Monte Carlo samples at that energy.

The first two likelihood variables exploit the possibility of identifying the b-quarks in a $ZZ \rightarrow q\bar{q}b\bar{b}$ event. They are calculated in the same way as the jet-wise b-tagging discriminant described in Section 4.5: the probability $\mathcal{B}_i$ that the jet i originated from a primary b-quark, modified by the weight factors for the different flavour composition of the background, is given by:

$$\mathcal{B}_i = \frac{w_b P_b^i}{w_{uds} P_{uds}^i + w_c P_c^i + w_b P_b^i}. \tag{5.3}$$

where P_b^i, P_c^i and P_{uds}^i are the probabilities that the jet i comes from a b-quark, c-quark or uds-quark respectively. The weight factors w have been set, in this analysis, to $w_b = w_c = w_{uds} = 1$. Out of the four $\mathcal{B}_i$ values, the two highest, ordered by jet energy, are used as likelihood variables (in the following they will be denoted by $\mathcal{B}_1$ and $\mathcal{B}_2$). The other six likelihood variables exploit the different kinematics and event-shape of each event class.

In detail, the eight quantities input to the likelihood are:

1. The b-tagging discriminant $\mathcal{B}_1$.

2. The b-tagging discriminant $\mathcal{B}_2$.

3. The logarithm of Y_{43}, the jet resolution parameter, calculated according to the DURHAM algorithm. A cut on this variable has been already applied in the preselection (see Section 5.3)

4. The C-parameter. Also on this variable a preselection cut is applied.

5. The output of the jet pairing likelihood, as described in Section 5.4: the largest likelihood value of the three possible jet combinations in the event. As for the reference distributions just ZZ events are used, its value is a good discriminating variable against both 4-fermion and $q\bar{q}$ background. It should be noticed that among the reference variables for the pairing likelihood there is the output of the 5C fit. This is therefore not used in the likelihood for the event selection.

6. The logarithm of the χ^2 probability of the 6C-fit, in which in addition to energy an momentum conservation, both di-jet masses are constrained to be equal to the W mass. Signal events, failing the W mass constraint, are expected to result in an higher χ^2 (smaller $P(\chi^2)$) for the 6C fit, than W pair events. This variable is thus intended as a veto against 4-jet events from W-pairs.

7. The total multiplicity of charged tracks in the event. Jets from b-quarks tend in fact to have an higher multiplicity than the jets from light quarks (see Section 4.5.3)

8. The variable $|cos\theta_{bb} - cos\theta_{qq}|$, where θ_{bb} is the opening angle between the two jets with highest b-tagging discriminants $\mathcal{B}$, and θ_{qq} is the opening angle between the remaining two jets. In the case of the $ZZ \rightarrow q\bar{q}b\bar{b}$ signal, this variable is expected to have values

$\sqrt{s}$ (GeV)	Data	Total MC	Background 4-fermion	2-fermion ($q\bar{q}$)	Signal $ZZ \to q\bar{q}b\bar{b}$	Efficiency (%)
192	3	2.6	0.3	0.6	1.6	36.5
196	12	7.8	1.0	1.6	4.7	36.8
200	8	8.5	1.0	1.7	5.3	37.7
202	2	4.0	0.5	0.8	2.4	34.8
205	7	7.3	0.8	1.5	5.0	33.4
207	13	12.2	2.3	2.5	8.4	33.4

Table 5.4: *Results of the $ZZ \to q\bar{q}b\bar{b}$ selection at $\sqrt{s}$ from 192 to 207 GeV. The statistical and systematic errors on these results will be discussed in the following, and given in Table 5.6.*

closer to zero than in case of the background. In ZZ events, the two angles are expected to be similar as both di-quark pairs come from a Z. In case of the $q\bar{q}(g)$ background, two b-quarks may eventually be originated by the gluon splitting $g \to b\bar{b}$, leading thus to a different distribution of the opening angle between the two b-quarks.

The first two likelihood variables (the C-parameter and y_{43}) are the same used for the preselection, and their distributions are shown in Figures 5.2 and 5.3. The distributions of the other likelihood variables are shown in the Figures 5.5 and 5.6, for data and Monte Carlo at $\sqrt{s}$ =200 GeV and $\sqrt{s}$ =207 GeV respectively. The distributions for the other center of mass energies are similar to these, and are not shown.

The likelihood output distributions of the $ZZ \to q\bar{q}b\bar{b}$ selection are shown in Figure 5.7 and 5.8, for year 1999 and year 2000 data, respectively, where again data and Monte Carlo are compared. Events with a likelihood greater than 0.8 are selected. The value of the cut has been chosen in such a way that the product of the efficiency ϵ times the purity p is maximal[4]. The contribution of a single channel selection to the statistical error on the the total cross section is in fact proportional to $1/\sqrt{\epsilon \cdot p}$.

The mass distribution of the events selected after the likelihood cut is shown in Figure 5.9. The plots show the mass resulting from the 5C-fit, where the pairing has been chosen using the likelihood method described in Section 5.4. The results of the $ZZ \to q\bar{q}b\bar{b}$ selection are summarised in Table 5.4 for the different values of $\sqrt{s}$ for which the analysis has been performed.

After the likelihood cut, the number of 4-fermion background events of the type $e^+e^- \to q\bar{q}q\bar{q}$ is reduced by a factor ~100; the 4-fermion background of the type $e^+e^- \to q\bar{q}ll$ is even more significantly reduced (by a factor ~500), and contributes to about 20% of the total 4-fermion background.

As can be seen in Table 5.4, the most important contribution to the background after the likelihood cut comes from $q\bar{q}$ events, even if only ~0.04% of those events are passing the likelihood cut. Other 2-fermion contributions are negligible.

5.7 Systematic uncertainties

A series of checks have been performed in order to assess the systematic uncertainties of the measurement; they are listed in the following.

The efficiencies of the selections and the expected number of background events are inferred from the Monte Carlo simulation; thus, eventual systematic errors may come from differences

[4] The purity of the selection is defined as $p = N_s/(N_s+N_b)$, where N_s (N_b) is the number of signal (background) events after the likelihood cut

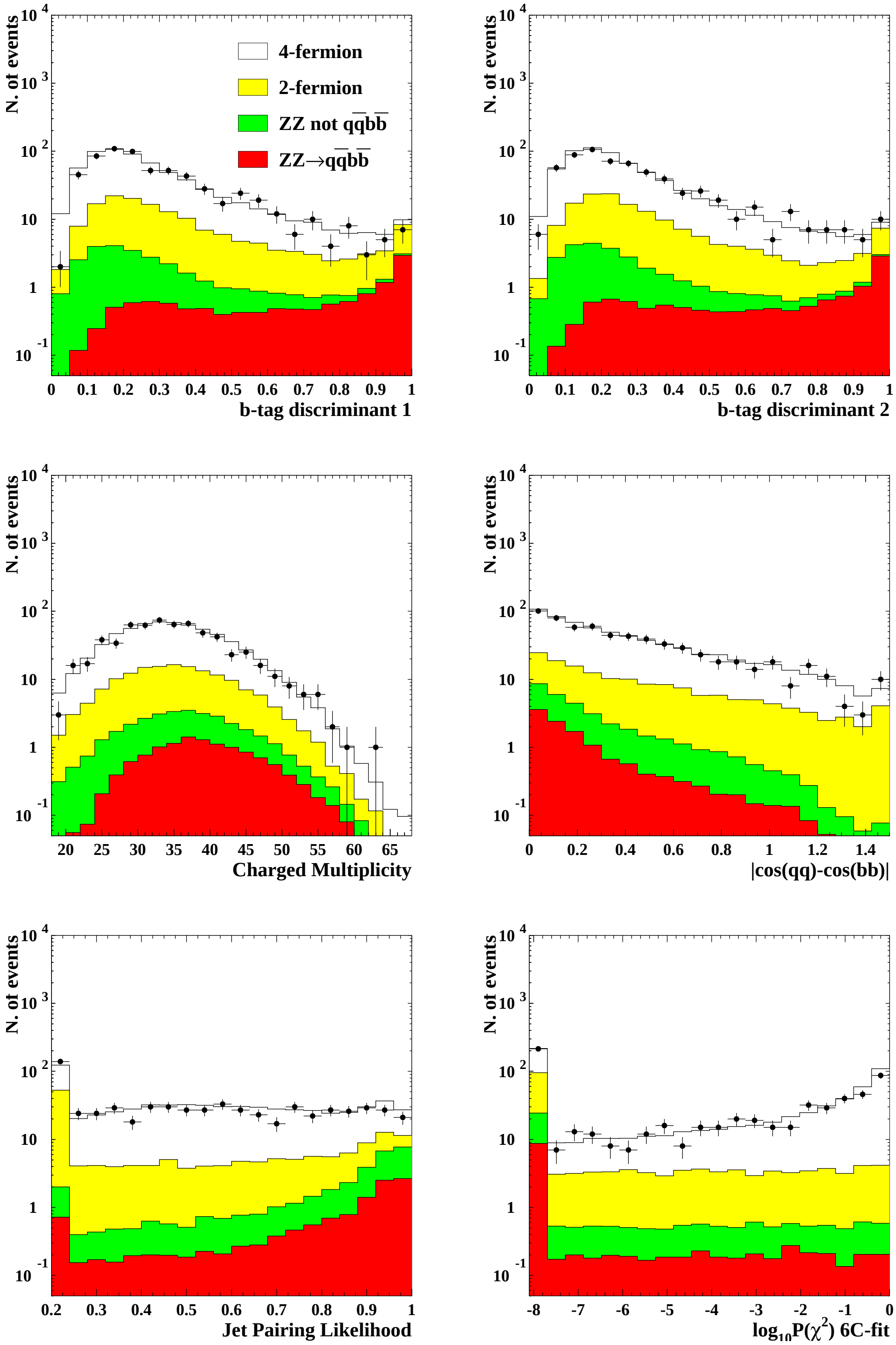

Figure 5.5: *Likelihood variables for the* ZZ → q$\bar{\text{q}}$b$\bar{\text{b}}$ *selection at* $\sqrt{s}$*=200 GeV. The points are the data, the dark-grey histograms are the* ZZ → q$\bar{\text{q}}$b$\bar{\text{b}}$ *signal events, the gray histograms are the ZZ events except* ZZ → q$\bar{\text{q}}$b$\bar{\text{b}}$*, the light-gray histograms are the* q$\bar{\text{q}}$ *background events, while the open histograms are the 4-fermion background events.*

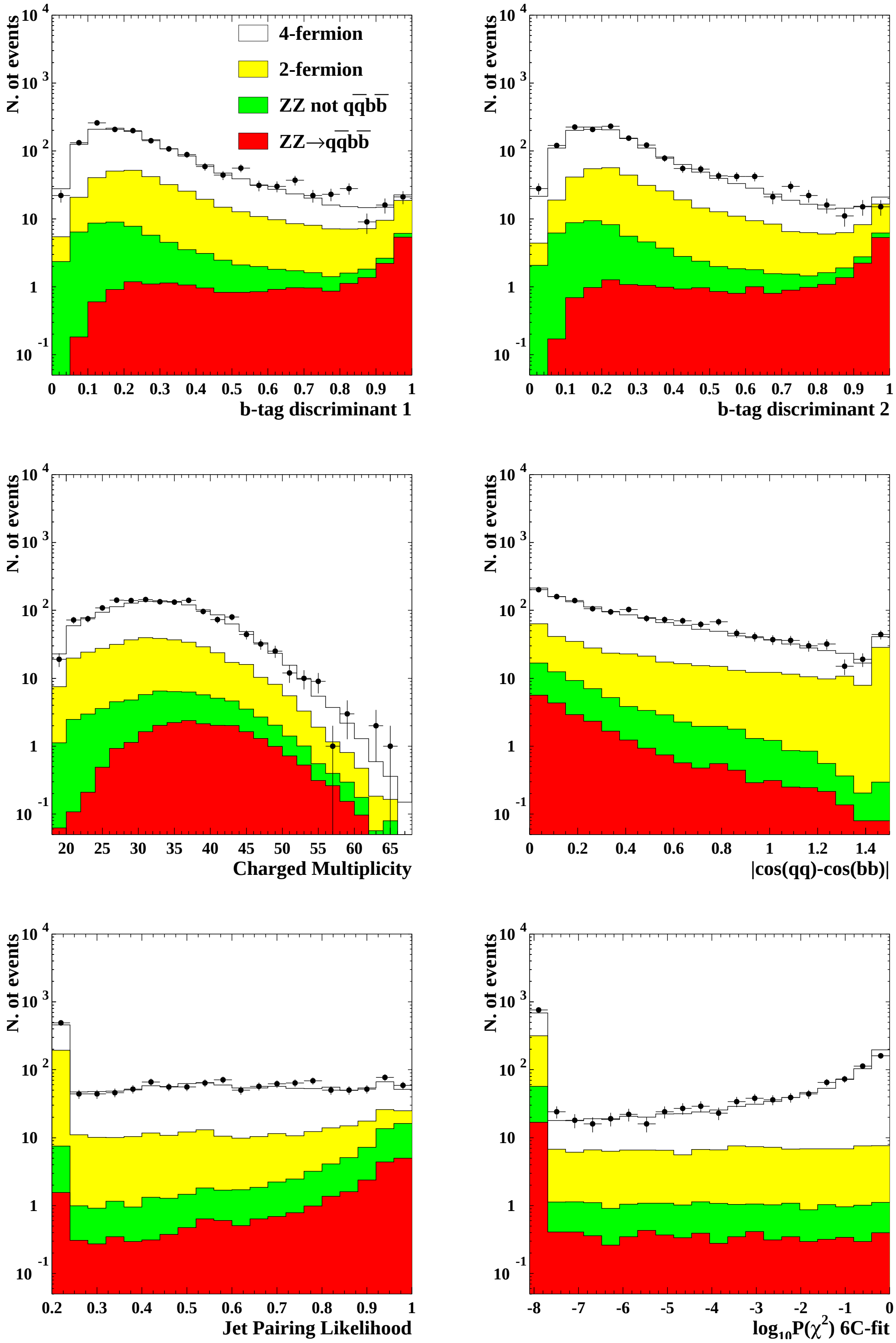

Figure 5.6: *Likelihood variables for the* $ZZ \to q\bar{q}b\bar{b}$ *selection at* $\sqrt{s}$*=207 GeV. The points are the data, the dark-grey histograms are the* $ZZ \to q\bar{q}b\bar{b}$ *signal events, the gray histograms are the ZZ events except* $ZZ \to q\bar{q}b\bar{b}$*, the light-gray histograms are the* $q\bar{q}$ *background events, while the open histograms are the 4-fermion background events.*

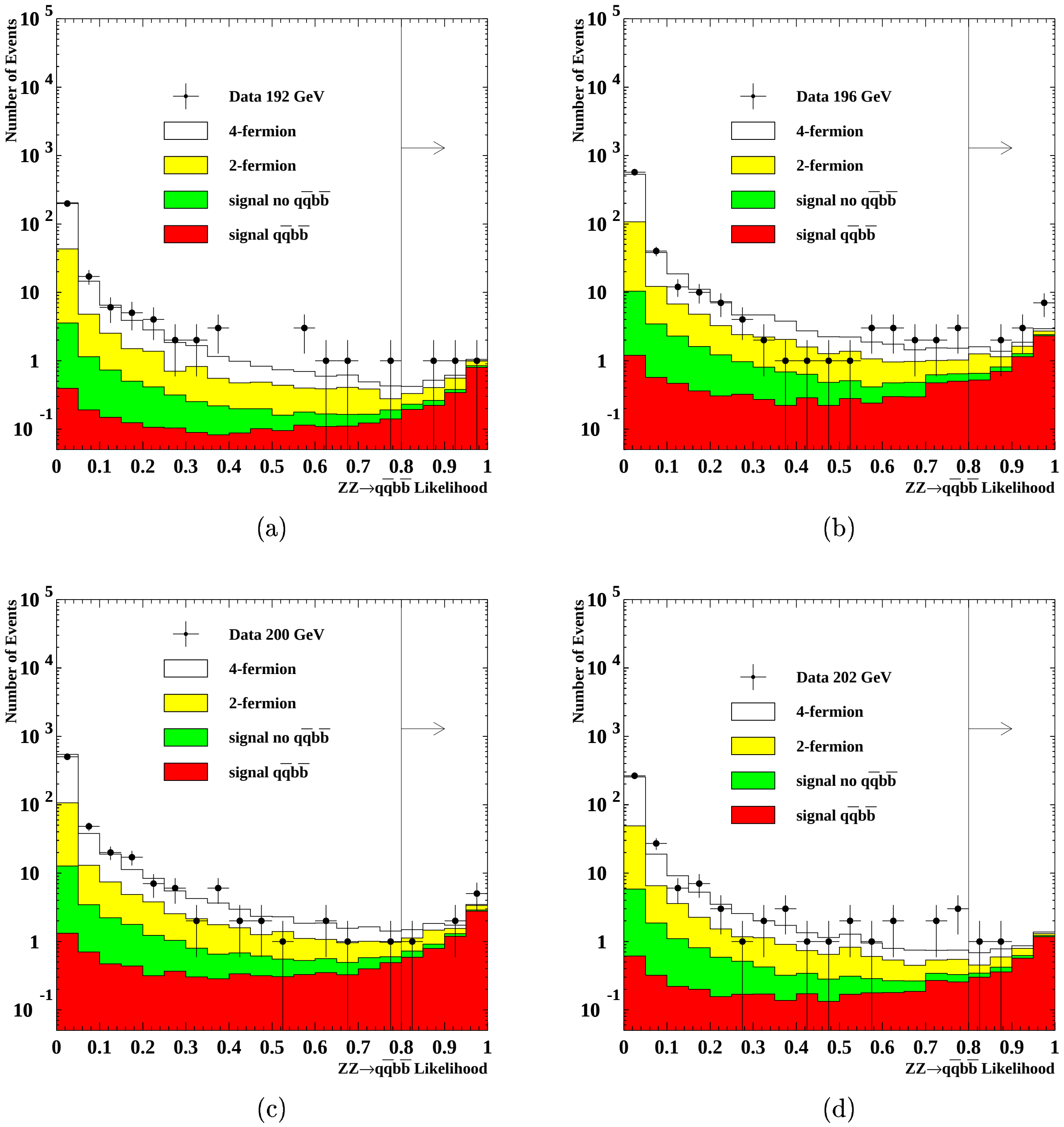

Figure 5.7: *The distributions of the likelihood discriminants for the selection of* $ZZ \to q\bar{q}b\bar{b}$ *events; (a):* $\sqrt{s}$ *=192 GeV; (b):* $\sqrt{s}$ *=196 GeV; (c):* $\sqrt{s}$*=200 GeV; (d):* $\sqrt{s}$ *=202 GeV. The points are the data, while the histograms show the Monte Carlo expectations, normalised to the integrated luminosity of the data. The vertical line and the arrow show the position of the likelihood cut applied to select* $ZZ \to q\bar{q}b\bar{b}$ *events.*

between the data and the Monte Carlo modelling of the physical process and of the detector resolution. The method to determine the systematic uncertainties of the measurement, consists, in general, in varying the modelling of the Monte Carlo simulation, and taking the corresponding variation of the results of the selection as systematic error. The variation of each parameter is done inside a range roughly corresponding to the experimental resolution on the parameter. In this way, the systematic error on the signal efficiency and on the number of expected background

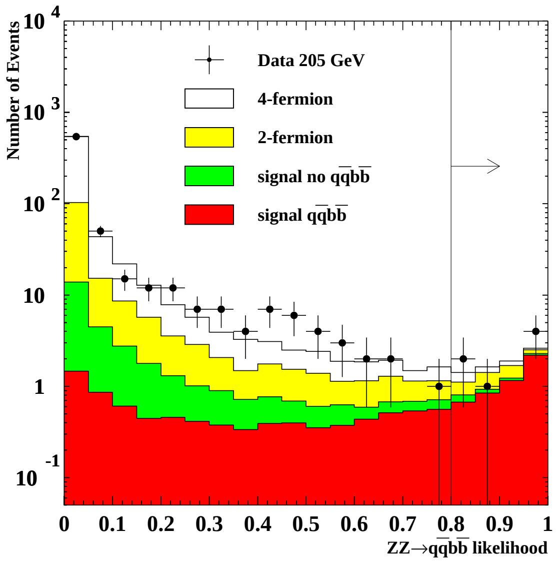

Figure 5.8: *The distributions of the likelihood discriminants for the selection of* $ZZ \to q\bar{q}b\bar{b}$ *events; (a): data and Monte Carlo at* $\sqrt{s}$ *=205 GeV; (b): data and Monte Carlo at 207 GeV. The points are the data, the histograms show the Monte Carlo expectations, normalised to the integrated luminosity of the data. The vertical line and the arrow show the position of the likelihood cut applied to select* $ZZ \to q\bar{q}b\bar{b}$ *events.*

events is determined.

The relevant effects which have been studied and quantified are the following:

Kinematic fits

The Monte Carlo description of the jet energy and angular resolutions influences the distribution of the χ^2 probability resulting from the kinematic fits, and thus the event selections.

The influence of possible mismodelings in the Monte Carlo parametrisation of the jet energy resolution has been estimated by applying an additional gaussian smearing of all simulated jet energies by 5%. This smearing corresponds to about 60% of the actual jet energy resolution.

Similarly, the dependence on the parametrisation of the angular resolution of the jets has been verified by smearing both polar and azimuthal angles of all simulated jets by 1^o, corresponding to about 70% of the jet angular resolution of the OPAL detector.

Model dependence of signal and background simulation

This effect can be estimated choosing alternative models for the generation of signal and background events. Differences between the Monte Carlo models used could for example be originated by differences in the treatment of the radiative corrections to the process under examination (e.g. the description of initial state radiation).

The set of generators which have been used in this analysis, as reference and as alternative model, has been described in Section 4.1. For each class of events, the selection results obtained using alternative generators are compared to the reference one, and the difference is assumed as systematic error on the number of selected events for the class.

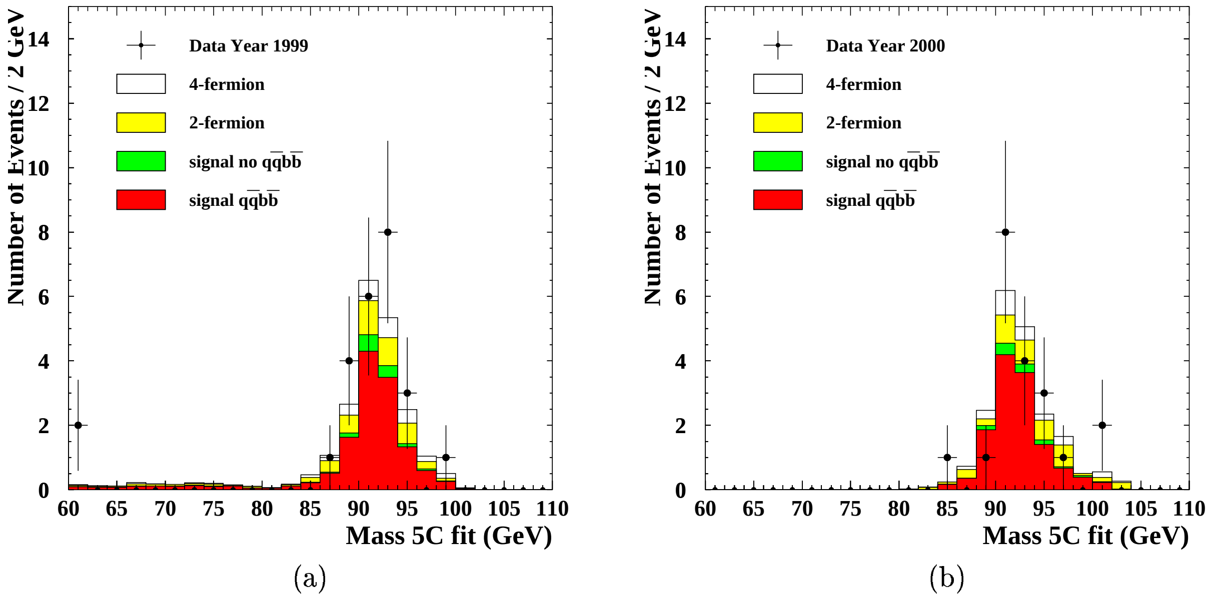

Figure 5.9: *Mass distributions of the events selected by the* $ZZ \to q\bar{q}b\bar{b}$ *selection. Shown is the mass resulting from the 5C-fit. Figure (a) and Figure (b) show the distribution for the data taken in the year 1999 (at* $\sqrt{s}$*=192-202 GeV) and in the year 2000 (at* $\sqrt{s}$*=202-209 GeV) respectively. The data are compared to the distributions from the Monte Carlo simulation; the Monte Carlo samples at each value of* $\sqrt{s}$ *are normalised to the integrated luminosity in the data.*

Fragmentation scheme

The quark fragmentation model used for the generation of the reference samples is the Lund string fragmentation as implemented in PYHTIA/JETSET[45]. As alternative was used the cluster fragmentation model as implemented in HERWIG[48]. To assess the systematic error introduced by the fragmentation model alone, the comparison was done between samples of each event class having the same sets of primary quarks 4-vectors; in this case the only differences between the reference and the alternative samples are caused by the fragmentation model.

Track resolution and secondary vertex tagging

The description of the track resolution in the Monte Carlo simulation is of fundamental importance for the correct modelling of the b-tagging performance in the simulation. The comparison of the Monte Carlo simulation with the high-statistic calibration data samples (at $\sqrt{s} \simeq M_Z$) taken in the years 1999 and 2000, shows that the resolution for the track parameters k, ϕ_0, d_0, $\tan\lambda$ and z_0[5] is better than 5%. Thus the systematic uncertainty is determined by smearing the track parameters by $\pm 5\%$. The smearing is performed at the same time for k and ϕ_0, and for d_0, $\tan\lambda$ and z_0[6]. The smearing of the first set of parameters corresponds to the smearing of the track impact parameter in the $r-\phi$ plane, while smearing the second set corresponds to smearing the impact parameter in the $r-z$ plane.

[5] The definition of the track parameters in OPAL has been discussed in Section 3.2.

[6] The smearing is actually performed by increasing (or decreasing) by 5% the difference between the reconstructed and the generated track parameters.

The bigger of the variations induced by the two smearings of $\pm 5\%$ is taken as systematic error on the measurement of the impact parameter on each of the two planes, $r-\phi$ and $r-z$.

Microvertex detector efficiency

The Silicon Microvertex Detector is the OPAL subdetector which is most relevant for the identification of b-quarks. Systematic effects arising from the modelling of possible inefficiencies of the detector were assessed by randomly dropping, before the track reconstruction in the Monte Carlo simulation, 1% of the hits on the $r-\phi$ plane and 3% of the hits on the $r-z$ plane.

b and c quark fragmentation functions

The fragmentation functions of the b and c quarks describe the energy spectrum of the hadrons originating by the primary quark. This spectrum has a direct influence on the output of the b-likelihood described in Chapter 3, as hadrons with higher energy decay on average after a longer path (the mean path is $\lambda = c\beta\gamma\tau$, τ being the lifetime of the hadron), thus making easier the identification of a secondary vertex. The modelling of the b and c fragmentation functions affects only the $ZZ \to q\bar{q}b\bar{b}$ selection, which is exploiting the b-tagging information.

To assess the uncertainty, the simulated events are reweighted according to the measured energy of the hadrons. The weights vary the energy of the hadrons by $\pm 1.1\%$ and $\pm 1.7\%$ in average, for b and c jets respectively [66, 67]. The energy of the hadrons was varied in both directions, and the biggest of the two corresponding variations induced on the analysis results was taken as systematic error.

Charged particle multiplicity of b jets

The average B-multiplicity, i.e. the number of charged particles that on average come from the decay of a B-hadron, has been measured to be $n_{\mathrm{B}} = 4.955 \pm 0.062$ [66]. To check the systematic error arising from the knowledge of n_{B}, the events are reweighted in such a way that the value of n_{B} is varied inside its experimental error. As for the fragmentation functions, the variation is done in both directions, and the biggest effect is taken as systematic error.

The contributions to the systematic error on the efficiency and on the expected background are summarised in Table 5.5, for the two values of the center of mass energy $\sqrt{s}$=200 GeV and $\sqrt{s}$=206 GeV.

As can be seen from the table, the most important contributions to the total systematic error come from the b-tagging and the Monte Carlo modelling, while the contribution of the jet resolution is relatively small.

5.8 The flavour independent selection

Here the flavour independent selection will be briefly described, while the description of its combination with the $ZZ \to q\bar{q}b\bar{b}$ selection will be described with more detail in the following sections.

The first step of the event selection consists of the preselection cuts already described in Section 5.3. Then, as for the $ZZ \to q\bar{q}b\bar{b}$ selection a likelihood discriminant is calculated. The variables used as reference for the likelihood are based exclusively on the reconstructed di-quark masses and the event shape:

1. The output value of the jet pairing likelihood described above in Section 5.4.

2. The difference between the smallest and the largest jet energy after the 4C kinematic fit.

Systematic errors at $\sqrt{s}$=200 GeV

Effect	Efficiency	Background
Monte Carlo Statistic	1.9	6.9
$r-\phi$ smearing	0.8	4.7
$r-z$ smearing	1.4	3.3
$r-\phi$ hit drop	1.6	0.7
$r-z$ hit drop	1.5	1.5
B multiplicity	0.6	0.3
B fragmentation	3.4	1.6
C fragmentation	0.6	0.7
Total b-tagging	4.4	6.3
Jet angle smearing	0.2	1.1
Jet energy smearing	1.7	1.8
Total jet resolution	1.7	2.1
Monte Carlo model	3.0	8.1
Total error	5.6	10.5

Systematic errors at $\sqrt{s}$=206 GeV

Effect	Efficiency	Background
Monte Carlo Statistic	2.1	7.9
$r-\phi$ smearing	1.9	7.7
$r-z$ smearing	1.4	2.2
$r-\phi$ hit drop	0.6	6.9
$r-z$ hit drop	0.4	2.4
B multiplicity	0.8	1.4
B fragmentation	2.1	1.7
C fragmentation	0.5	1.1
Total b-tagging	3.4	11.1
Jet angle smearing	0.7	0.8
Jet energy smearing	1.1	0.1
Total jet resolution	1.3	0.8
Monte Carlo model	2.5	11.6
Total error	4.4	16.1

Table 5.5: *Summary of the contributions, in %, to the systematic error on the signal efficiency and on the number of background events. The contributions studied are subdivided into those affecting the b-tagging performance, those connected to the jet resolution, and those coming from the Monte Carlo modelling of the physics processes.*

3. The matrix element at leading order for the QCD process $Z/\gamma^* \rightarrow \mathrm{q\bar{q}gg}$ for the most probable jet-parton assignment, i.e. the combination which is resulting in the biggest value of the matrix element.

4. The corresponding matrix element for the process WW→ $\mathrm{q\bar{q}q\bar{q}}$.

5. The visible center of mass energy $\sqrt{s'}$.

6. The angular variable $j_{ang} = E_4(1 - \cos\theta_{12}\cos\theta_{13}\cos\theta_{23})/E_{CM}$ where E_4 is the smallest of the four jet energies, and θ_{ij} are the opening angles between jets i and j, with the jets ordered by energy.

7. The smallest difference between the obtained 5C-fit mass and the PDG mass of the W boson, for the two jet pairings with the smallest mass differences between the two jet pairs.

8. The absolute value of the sum of the cosines of the polar angles of the four jets, which tends to be large for events with unobserved particles along the beam direction.

The performance of the flavour independent selection is mainly limited by the WW background, which can't be easily rejected exploiting the b-tagging, as in case of the ZZ → $\mathrm{q\bar{q}b\bar{b}}$ selection. The efficiency of the selection is about 32%, while the purity is about 30%. The agreement between the observed and the expected number of events is in general good, at the various values of $\sqrt{s}$ at which the analysis has been performed.

For the analysis of the year 2000 data (i.e. at $\sqrt{s}$ ≃205 GeV and $\sqrt{s}$ ≃207 GeV), the cut on the likelihood discriminant has been modified in order to increase the purity of the selection, slightly decreasing the efficiency.

5.9 Combinations of the selections

The two selection algorithms described above lead to two overlapping event samples. In order to calculate the cross section, the samples are splitted into three non-overlapping subsamples, defined as follows:

1. The *exclusive* $\mathrm{q\bar{q}q\bar{q}}$ sample, which contains events which are selected by the ZZ → $\mathrm{q\bar{q}q\bar{q}}$ selection, but not from the ZZ → $\mathrm{q\bar{q}b\bar{b}}$ one.

2. The *exclusive* $\mathrm{q\bar{q}b\bar{b}}$ sample, which contains events which are selected by the ZZ → $\mathrm{q\bar{q}b\bar{b}}$ selection but not from the ZZ → $\mathrm{q\bar{q}q\bar{q}}$ one.

3. The *overlap* sample, which contains the events which are accepted by both selections.

The number of events selected in data and Monte Carlo, at the different values of $\sqrt{s}$, is summarised in Table 5.6, for the three fully-hadronic subchannels. The contribution of each event class to the total number of expected events is also shown in the table.

5.10 Fit of the e^+e^- →ZZ cross section

The results from all ZZ decay channels are combined in a likelihood fit to the total cross section. The number of expected events μ_e is calculated according to the formula:

$$\mu_{\mathrm{e}} = \sigma_{\mathrm{ZZ}} \cdot B_{\mathrm{ZZ}} \cdot \mathcal{L}_{\mathrm{int}} \cdot \epsilon_{\mathrm{chan}} + n_{\mathrm{back}} \tag{5.4}$$

where σ_{ZZ} is a common cross section for all channels, B_{ZZ} is the Standard Model Branching Ratio of ZZ to the channel under consideration, $\mathcal{L}_{\mathrm{int}}$ is the integrated luminosity in data, ϵ_{chan} is the

$\sqrt{s}$=192 GeV						
Selection	N_{obs}	N_{SM}	N_{ZZ}	Tot. bgnd.	4-fermion	$q\bar{q}$
$q\bar{q}q\bar{q}$ and $\overline{q\bar{q}b\bar{b}}$	27	17.6±1.4	3.8±0.2	13.8±1.4	9.0	4.8
$q\bar{q}b\bar{b}$ and $\overline{q\bar{q}q\bar{q}}$	2	0.93±0.11	0.52±0.03	0.42±0.10	0.17	0.25
$q\bar{q}b\bar{b}$ and $q\bar{q}q\bar{q}$	1	1.68±0.12	1.21±0.05	0.47±0.11	0.16	0.31

$\sqrt{s}$=196 GeV						
Selection	N_{obs}	N_{SM}	N_{ZZ}	Tot. bgnd.	4-fermion	$q\bar{q}$
$q\bar{q}q\bar{q}$ and $\overline{q\bar{q}b\bar{b}}$	38	42.1±3.3	10.3±0.5	31.8±3.3	21.5	10.3
$q\bar{q}b\bar{b}$ and $\overline{q\bar{q}q\bar{q}}$	4	3.13±0.32	1.89±0.11	1.24±0.30	0.45	0.79
$q\bar{q}b\bar{b}$ and $q\bar{q}q\bar{q}$	8	4.69±0.35	3.31±0.14	1.38±0.32	0.59	0.79

$\sqrt{s}$=200 GeV						
Selection	N_{obs}	N_{SM}	N_{ZZ}	Tot. bgnd.	4-fermion	$q\bar{q}$
$q\bar{q}q\bar{q}$ and $\overline{q\bar{q}b\bar{b}}$	26	32.4±2.5	9.1±0.5	23.3±2.4	16.5	6.8
$q\bar{q}b\bar{b}$ and $\overline{q\bar{q}q\bar{q}}$	6	4.33±0.39	2.73±0.13	1.60±0.37	0.65	0.95
$q\bar{q}b\bar{b}$ and $q\bar{q}q\bar{q}$	2	4.26±0.29	3.16±0.12	1.10±0.26	0.37	0.73

$\sqrt{s}$=202 GeV						
Selection	N_{obs}	N_{SM}	N_{ZZ}	Tot. bgnd.	4-fermion	$q\bar{q}$
$q\bar{q}q\bar{q}$ and $\overline{q\bar{q}b\bar{b}}$	22	21.5±1.7	5.4±0.3	16.1±1.7	10.3	5.8
$q\bar{q}b\bar{b}$ and $\overline{q\bar{q}q\bar{q}}$	2	1.54±0.14	1.03±0.06	0.51±0.12	0.30	0.21
$q\bar{q}b\bar{b}$ and $q\bar{q}q\bar{q}$	0	2.21±0.15	1.63±0.07	0.59±0.14	0.25	0.33

$\sqrt{s}$=205 GeV						
Selection	N_{obs}	N_{SM}	N_{ZZ}	Tot. bgnd.	4-fermion	$q\bar{q}$
$q\bar{q}q\bar{q}$ and $\overline{q\bar{q}b\bar{b}}$	36	24.8±2.0	7.9±0.4	16.8±1.7	11.4	5.4
$q\bar{q}b\bar{b}$ and $\overline{q\bar{q}q\bar{q}}$	3	4.21±0.38	2.61±0.12	1.60±0.36	0.48	1.12
$q\bar{q}b\bar{b}$ and $q\bar{q}q\bar{q}$	4	3.11±0.21	2.44±0.11	0.67±0.16	0.31	0.36

$\sqrt{s}$=207 GeV						
Selection	N_{obs}	N_{SM}	N_{ZZ}	Tot. bgnd.	4-fermion	$q\bar{q}$
$q\bar{q}q\bar{q}$ and $\overline{q\bar{q}b\bar{b}}$	36	41.2±3.3	13.2±0.7	28.0±3.0	19.0	9.0
$q\bar{q}b\bar{b}$ and $\overline{q\bar{q}q\bar{q}}$	7	7.00±0.64	4.35±0.25	2.65±0.62	0.79	1.86
$q\bar{q}b\bar{b}$ and $q\bar{q}q\bar{q}$	6	5.17±0.35	4.06±0.17	1.11±0.26	0.52	0.59

Table 5.6: *The table shows the results of the ZZ event selections for the fully hadronic channels. N_{obs} is the number of events selected in data, N_{SM} is the number of events expected in the Standard Model, derived by the Monte Carlo simulation. N_{ZZ} is the number of expected ZZ events, while $N_{\rm back}$ is the total number of expected background events. The last two columns show the composition of the background. The errors include contributions from the common systematic errors.*

efficiency for the decay channel. The efficiency and the number of expected events are derived from the Monte Carlo simulation, while the luminosity is measured as described in Section 3.2.

The expected number of events is modelled by a Poisson distribution, i.e. the probability to observe n_{obs} events is given by:

$$P(n_{\text{obs}}, \mu_{\text{e}}) = e^{-\mu_{\text{e}}} \cdot \frac{\mu_{\text{e}}^{n_{\text{obs}}}}{n_{\text{obs}}!} \tag{5.5}$$

The Poisson distribution is then convolved with Gaussian distributions to account for uncertainties in the efficiencies and the expected background. A summary of the results for all ZZ decay channels, in terms of selected number of events in data and expected number of events from the Monte Carlo simulation can be found in [52].

The results of the cross section measurement are shown in Figure 5.10. The measured values of the cross section, with their statistical and systematic errors, are the following:

$$\sigma_{\text{ZZ}}(192\text{ GeV}) = 1.13^{+0.46}_{-0.39}(\text{stat.})^{+0.13}_{-0.09}(\text{syst.})\text{ pb} \tag{5.6}$$
$$\sigma_{\text{ZZ}}(196\text{ GeV}) = 1.19^{+0.27}_{-0.24}(\text{stat.})^{+0.10}_{-0.08}(\text{syst.})\text{ pb} \tag{5.7}$$
$$\sigma_{\text{ZZ}}(200\text{ GeV}) = 1.09^{+0.25}_{-0.23}(\text{stat.})^{+0.09}_{-0.07}(\text{syst.})\text{ pb} \tag{5.8}$$
$$\sigma_{\text{ZZ}}(202\text{ GeV}) = 0.94^{+0.37}_{-0.32}(\text{stat.})^{+0.09}_{-0.06}(\text{syst.})\text{ pb} \tag{5.9}$$
$$\sigma_{\text{ZZ}}(205\text{ GeV}) = 1.07^{+0.26}_{-0.24}(\text{stat.})^{+0.10}_{-0.08}(\text{syst.})\text{ pb} \tag{5.10}$$
$$\sigma_{\text{ZZ}}(207\text{ GeV}) = 1.07^{+0.20}_{-0.19}(\text{stat.})^{+0.09}_{-0.07}(\text{syst.})\text{ pb} \tag{5.11}$$

The measurements are in good agreement with the Standard Model expectation, and at each center of mass energy, the error is dominated by the statistical component. In order to check the consistency of the results with the Standard Model, one can allow the branching ratio of Z bosons to b quarks, BR(Z$\rightarrow$ b$\bar{\text{b}}$, to be a free parameter of the fit at each of the energy points. The results are shown in Figure 5.11, where the results are compared to the measured value from LEP1 data. Combining all energies, the average value is 0.196$\pm$0.032, which is in agreement with the the LEP1 measurement of 0.151$\pm$0.001 [12].

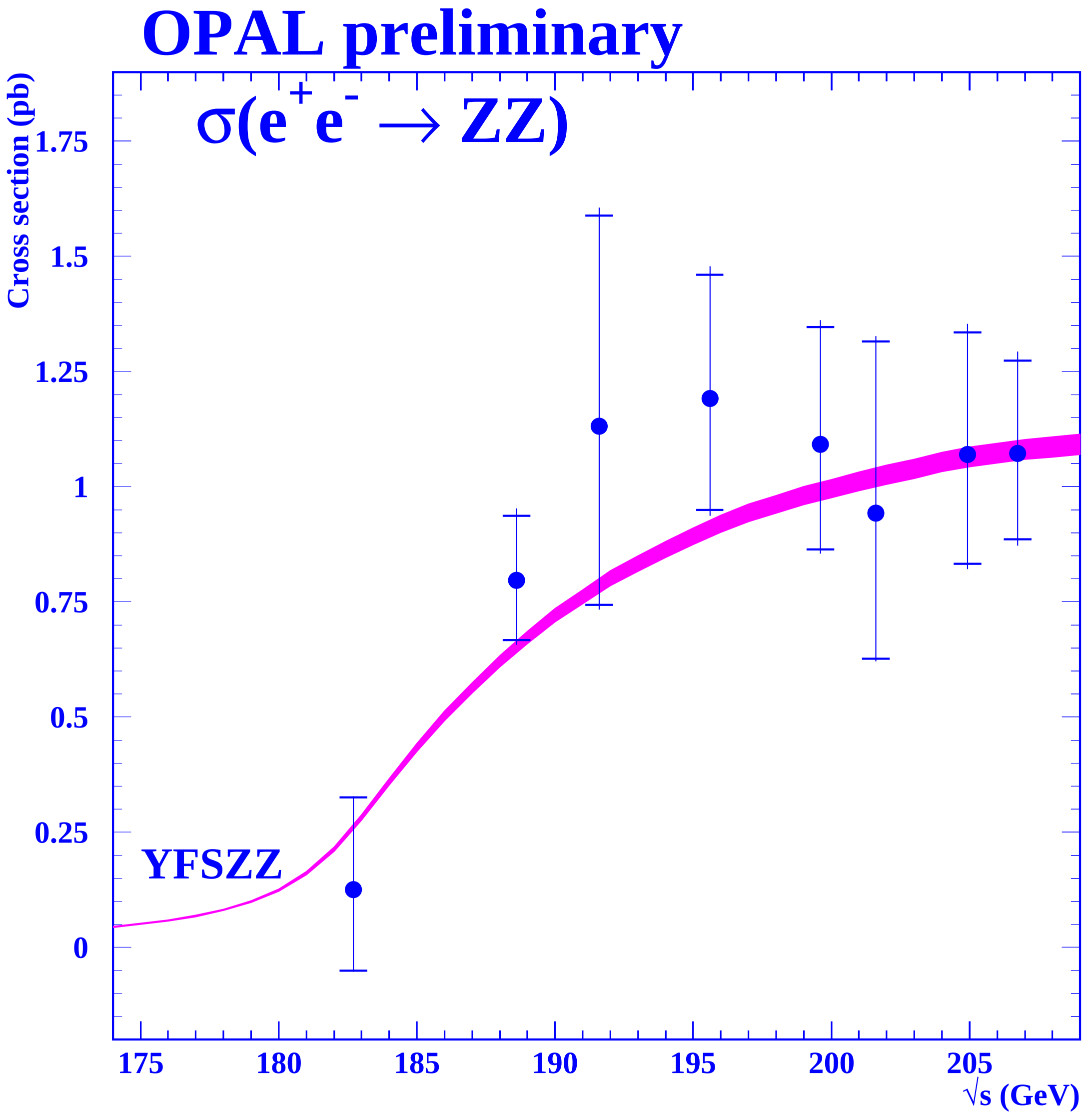

Figure 5.10: *The results of the ZZ cross section measurements. The dark grey band shows the prediction of the* YFSZZ*[44] Monte Carlo; the width of the band represents the theoretical uncertainty of $\sim 2\%$. The points are the preliminary OPAL measurements; the error bars show the total error, while the horizontal segments identify the statistical error.*

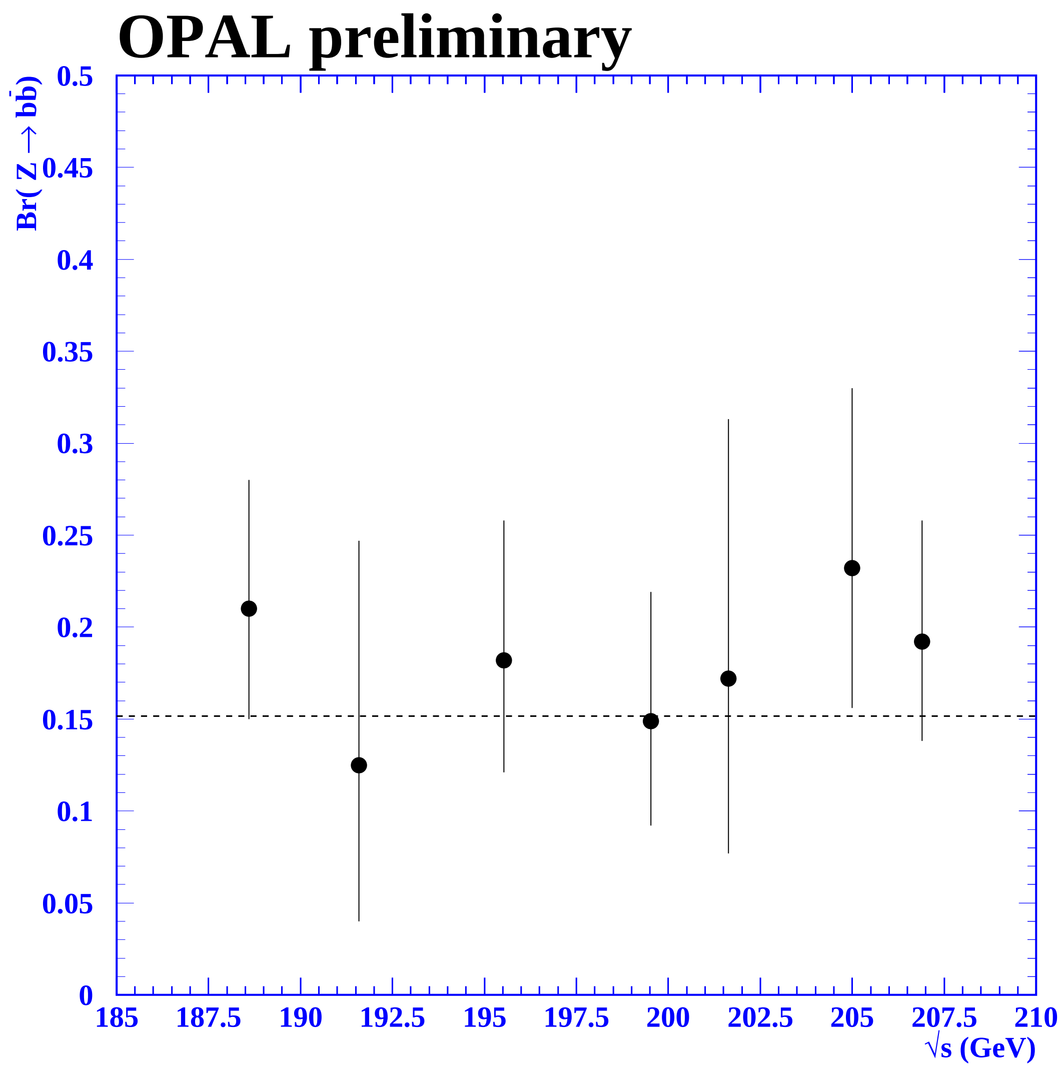

Figure 5.11: *Determination of BR(Z→ b$\bar{b}$) from ZZ events. The line shows the measured value from LEP1 data. Only statistical errors are shown. At 183 GeV the ZZ samples were too small to allow a meaningful measurement to be obtained.*

6. Fit of the anomalous neutral triple gauge couplings

In this chapter the fit of the neutral triple gauge couplings, using the selected ZZ events, will be described. As described in Chapter 2, the anomalous γZZ and ZZZ couplings induce variations of the total $e^+e^- \to$ZZ cross section and of the kinematics of the final state. The kinematics is completely described by the five angles shown in Figure 2.7, and by the invariant masses of the two Z's. The couplings could be thus determined, for example, through a binned maximum likelihood fit of the distributions of these quantities. A fit of a 7-dimensional distribution would be however very difficult, as it would require the generation of a huge number of reference Monte Carlo events, and an accurate study of the selection efficiencies all over the phase-space. In the first analysis of the $e^+e^- \to$ZZ process at OPAL [68], where data at $\sqrt{s}$ =183 GeV and $\sqrt{s}$=189 GeV had been analysed, a binned maximum likelihood fit of the differential cross section $d\sigma/d(\cos\theta_Z)$ was performed to derive limits on the anomalous couplings; in the analysis of the data at $\sqrt{s}$ $\geq$192 GeV (i.e. the data collected during the years 1999 and 2000) the method of optimal observables, which allows to fully exploit the kinematic information of an event, has been used. The fit method and the results will be described in this chapter.

As seen in Section 2.4.3, possible new physics would show up, at LEP2 energies, as a deviation mainly of the real part of the anomalous couplings from the expected zero value. The effects of new physics on the imaginary part of the couplings are at these energies negligible. For this reason, only the results relative to fit of the real part of the couplings will be described in this chapter.

6.1 Optimal observables

The effective Lagrangian introduced in Section 2.3.2, Equation 2.20, is linear in the anomalous couplings f_4^V, f_5^V (where $V \equiv \gamma$ or Z). Thus, the differential cross section $d\sigma/d\Omega$ is parabolic in the anomalous couplings at any point of the phase space Ω (where the phase space point is defined by the 4-momenta of the four fermions in the final state), i.e. the differential cross section can be written as [69]:

$$\frac{d\sigma}{d\Omega}(\Omega, \vec{\alpha}) = S^{(0)}(\Omega) + \sum_{i=1}^{4} \alpha_i S_i^{(1)}(\Omega) + \sum_{i,j=1}^{4} \alpha_i \alpha_j S_{ij}^{(2)}(\Omega) \tag{6.1}$$

where $\vec{\alpha}$ corresponds in this case to the set of 4 couplings $f_{4,5}^{\gamma,Z}$, while $S^{(0)}$, $S^{(1)}$ and $S^{(2)}$ are function of the phase space only. If one assumes that only one coupling α_i is different from 0, the 6.1 becomes:

$$\frac{d\sigma}{d\Omega}(\Omega, \alpha_i) = S^{(0)}(\Omega) + \alpha_i S_i^{(1)}(\Omega) + \alpha_i^2 S_i^{(2)}(\Omega) \tag{6.2}$$

Denoting with $\mathcal{M}_{SM}$ the Standard Model matrix element for the $e^+e^- \to$ZZ process, and with $\mathcal{M}_{NP}$ the New Physics matrix element (see in Section 2.3.2), for the functions $S^{(0)}(\Omega)$, $S^{(1)}(\Omega)$ and $S^{(2)}(\Omega)$ one can write:

$$S^{(0)}(\Omega) \propto |\mathcal{M}_{SM}|^2 \quad S^{(1)}(\Omega) \propto 2 \cdot Re(\mathcal{M}_{SM} \cdot \mathcal{M}_{NP}^*) \quad S^{(2)}(\Omega) \propto |\mathcal{M}_{NP}|^2$$

where the proportionality factor is a phase-space factor common to the three functions.

The so-called first and second order optimal observables $\mathcal{O}_1$, $\mathcal{O}_2$ are then defined as:

$$\mathcal{O}_i^{(1)}(\Omega) \equiv S_i^{(1)}(\Omega)/S^{(0)}(\Omega) \quad (6.3)$$

$$\mathcal{O}_i^{(2)}(\Omega) \equiv S_i^{(2)}(\Omega)/S^{(0)}(\Omega) \quad (6.4)$$

and the differential cross section 6.2 can be rewritten as:

$$\frac{d\sigma}{d\Omega}(\Omega, \alpha_i) = S^{(0)}(\Omega) \cdot \left(1 + \alpha_i \cdot \frac{S_i^{(1)}(\Omega)}{S^{(0)}(\Omega)} + \alpha_i^2 \cdot \frac{S_{ii}^{(2)}(\Omega)}{S^{(0)}(\Omega)}\right) = \quad (6.5)$$

$$= S^{(0)}(\Omega) \cdot \left(1 + \alpha_i \cdot \mathcal{O}_i^{(1)}(\Omega) + \alpha_i^2 \cdot \mathcal{O}_i^{(2)}(\Omega)\right) \quad (6.6)$$

The factor $S^{(0)}(\Omega)$ (i.e. the Standard Model differential cross section) does not depend on the anomalous couplings. The differential cross section as a function of the anomalous couplings can be thus parametrised through the optimal observables. For each event, the optimal observables contain already the full kinematic information on the couplings. It is then possible to use them instead of the seven phase-space variables necessary to describe a ZZ final state (see in Chapter 2).

This can be shown as follows, for the case in which only one coupling α is assumed to be non-zero: having determined the set of phase-space variables Ω for each event of a set of data events N_{Data}, the most likely value of the couplings α is the one that maximises the *Maximum Likelihood Function*:

$$L(\alpha_i) = \prod_k^{N_{Data}} (S^{(0)}(\Omega_k) + \alpha_i S_i^{(1)}(\Omega_k) + \alpha_i^2 S_i^{(2)}(\Omega_k)). \quad (6.7)$$

The value α_0 that maximises the function $L(\alpha)$ can be easily calculated from the differentiation of the logarithm of the Likelihood Function:

$$\frac{d\log L}{d\alpha}|_{\alpha=\alpha_0} = \sum_k^{N_{Data}} \frac{S^{(1)}(\Omega_k) + 2\alpha_0 S^{(2)}(\Omega_k)}{S^{(0)}(\Omega_k) + \alpha_0 S^{(1)}(\Omega_k) + \alpha_0^2 S^{(2)}(\Omega_k)} = \quad (6.8)$$

$$= \sum_k^{N_{Data}} \frac{\mathcal{O}^{(1)}(\Omega_k) + 2\alpha_0 \mathcal{O}^{(2)}(\Omega_k)}{1 + \alpha_0 \mathcal{O}^{(1)}(\Omega_k) + \alpha_0^2 \mathcal{O}^{(2)}(\Omega_k)} \stackrel{!}{=} 0. \quad (6.9)$$

This expression depends only on the optimal observables, which thus contain already the complete information on the couplings. A maximum likelihood fit of their distributions would than provide the same sensitivity as a maximum likelihood fit of the 7 phase-space variables.

Already the mean values of the optimal observables are functions of the anomalous couplings, and can be used, for small deviations of α_i from zero, to fit them in a way simpler than a maximum likelihood fit. This can be shown as follows: Equation 6.8 can be expanded in a Taylor series around the value $\alpha = 0$, obtaining thus the following relation:

$$\overline{\mathcal{O}}^{(1)} - \alpha_0 \cdot (\overline{\mathcal{O}}^{(1)^2} - 2 \cdot \overline{\mathcal{O}}^{(2)}) + \alpha_0^2 \cdot ... \stackrel{!}{=} 0. \quad (6.10)$$

For small values of the couplings the higher order terms can be neglected.

Instead of determining the value α_0 from the Equation 6.10, i.e. through the measurement of the mean values $\overline{\mathcal{O}}^{(1)}$ and $\overline{\mathcal{O}}^{(2)}$, the expected mean values of the observables as a function of the anomalous couplings can be inferred from the Monte Carlo simulation. The functions $E[\mathcal{O}^{(1)}](\alpha)$ and $E[\mathcal{O}^{(2)}](\alpha)$, which in the following will be called *Calibration Curves*, allow the determination of the value α_0 through the solution of equations of this kind:

$$\overline{\mathcal{O}}^{(1)} - E[\overline{\mathcal{O}}^{(1)}](\alpha_0) \stackrel{!}{=} 0. \quad (6.11)$$

Technically, the solution to this equation is found by minimising the a χ^2 function of the form:

$$\chi^2(\alpha) = \sum_{k}^{N_{Data}} \frac{(\overline{\mathcal{O}}^{(1)}(\Omega_k) - E[\overline{\mathcal{O}}^{(1)}(\Omega_k)](\alpha))^2}{\sigma^2} \tag{6.12}$$

where σ represents the error on the mean value $\overline{\mathcal{O}}$. This point will be discussed in more detail in the rest of this chapter.

To calculate the optimal observables, the e$^+$e$^-$ $\to$ZZ differential cross section is computed using the matrix element of the YFSZZ [44] generator[1]. From the matrix element the functions $S^{(0)}$, $S_i^{(1)}$ and $S_{ij}^{(2)}$ can be calculated. In case of the fully hadronic channel, it is not possible to distinguish between fermion and anti-fermion; thus, the three functions are averaged over all the possible combinations. For the calculation of the matrix element, the jets 4-vectors resulting from the 4C-fit (see Section 4.4) are used.

An example of the distributions of the first and second order optimal observables is shown in Figure 6.1, for ZZ signal events selected by the ZZ $\to$ q$\bar{\text{q}}$q$\bar{\text{q}}$ exclusive event selection. In the figure, the distributions of the observables for non-zero values of the coupling f_5^Z are shown, for two different values of the coupling. In the following section the calculation of the observables, and of their mean values as a function of the anomalous couplings will be described in more detail.

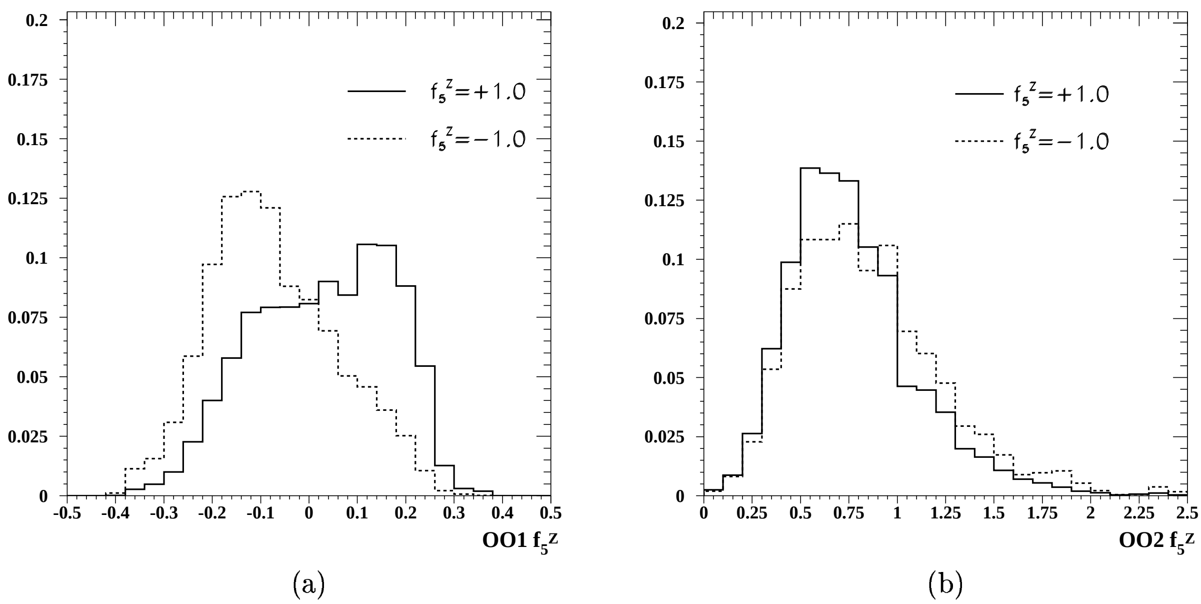

Figure 6.1: *Distributions of the first order (a) and second order (b) optimal observables relative to the coupling f_5^Z, at $\sqrt{s}$ = 207 GeV. The solid line histograms show the distributions for $f_5^Z = +1.0$, while the dashed line histograms show the distributions for $f_5^Z = -1.0$. In the plots, the histograms are normalised such that their integral is 1.*

[1] The YFSZZ event generator provides, given the four vectors of the four fermions in the final state, the e$^+$e$^-$ $\to$ZZ matrix element at Born level.

6.2 Calibration Curves

The expected mean values as a function of the anomalous couplings (the so-called *calibration curves*), can be obtained from the Monte Carlo simulation, by reweighting the events:

$$\overline{\mathcal{O}}^{(N)}_{i(expected)}(\alpha_i) = \frac{\sum_{Events} w(\Omega, \alpha_i)\mathcal{O}^{(N)}_i(\Omega)}{\sum_{Events} w(\Omega, \alpha_i)} = \frac{f(\alpha_i)}{g(\alpha_i)} \tag{6.13}$$

where the sums run over the selected events in the signal and background samples.

The weights $w(\Omega, \alpha_i)$ contain a factor which reweights the Monte Carlo statistic to the statistic in the data. This factor is given by the ratio of the integrated luminosities of the data and the Monte Carlo sample considered: $\mathcal{L}_{DATA}/\mathcal{L}_{MC}$. For the signal sample, a second factor is then needed to reweight the distributions of the optimal observables to the distributions corresponding to a given value of the coupling α_i. If the signal sample has been generated with Standard Model couplings ($\alpha_i \equiv 0$), this factor is given by $|\mathcal{M}(\Omega, \alpha_i)|^2/|\mathcal{M}_{SM}(\Omega)|^2$, where $\mathcal{M}(\Omega, \alpha_i)$ is the matrix element including the anomalous interaction, and $\mathcal{M}_{SM}(\Omega)$ is the Standard Model matrix element. As the background doesn't depend on the anomalous couplings, this second factor is equal to 1 for the background samples[2].

Thus, since the event weights are either constant (in case of background), or parabolas as function of the α_i (in case of signal), the functions $f(\alpha_i)$ and $g(\alpha_i)$ in the 6.13 are parabolas as function of α_i. To get an analytic expression of the calibration curves, it is sufficient to evaluate these functions at three different points.

The calibration curves obtained using the ZZ $\rightarrow$ q$\bar{\text{q}}$b$\bar{\text{b}}$ selected events, at $\sqrt{s} = 207$ GeV are shown, as an example, in figure 6.2. The observed mean value in data is also shown for each of the observables, together with its statistical error.

6.3 Cuts on optimal observables

As discussed in the previous sections, the calibration curves are calculated using only Standard Model Monte Carlo samples. As signal samples are reweighted to the values of the anomalous couplings, this could result in large statistical uncertainties for the events belonging to sparsely populated regions of the phase-space. For example, events with one of the Z's in the low-mass region are enhanced for non-zero values of the anomalous couplings; this phase-space region is sparsely populated by Standard Model signal events. Events belonging to it (eventually because of mis-reconstruction of the boson 4-momenta) get high statistical importance when reweighted using matrix elements including non-zero anomalous couplings. An example of this effect is shown in Figure 6.3, referring to the second-order optimal observables. It should be noticed in addition, that in general the ZZ event selections are optimized to select events in which both Z's are on-shell. Thus, the efficiency for events with one or both Z's in the off-shell (low-mass) region is quite poor.

Another reason to apply cuts on the optimal observables distributions is, that the reliability of χ^2 fits is only granted in case of Gaussian, or approximately Gaussian distributions. To avoid being affected by eventual tails, one can set some loose cuts on the OO's values.

A first criterium to choose the cut values can be the optimization of the sensitivity. The expected limits on the anomalous couplings, obtained using different cuts are compared, and those giving the best results can be choosen.

Another criterium, which was used in this analysis, is to check which values of the observables correspond to the sparsely populated regions of the phase space. The cuts are placed accordingly, taking care that the fraction of events cut doesn't exceed a certain value ($\sim$3%).

[2] For the 4-fermion background sample, the weight $w(\Omega, \alpha_i)$ in the Equation 6.13 must be multiplied by the reweighting factor discussed in Section 4.1, needed for the signal definition.

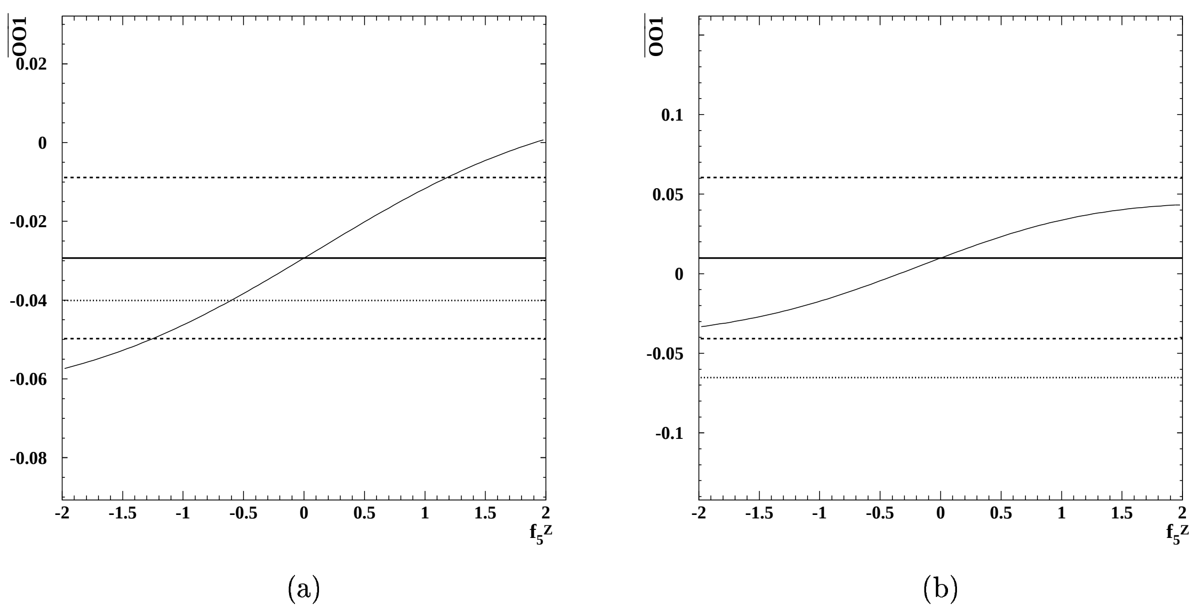

Figure 6.2: *Calibration curves at $\sqrt{s} = 207$ GeV, for the coupling f_5^Z. Shown are the calibration curves for the first order observables. (a): exclusive* $ZZ \to q\bar{q}q\bar{q}$ *channel, (b): exclusive* $ZZ \to q\bar{q}b\bar{b}$ *channel. The horizontal solid line shows the expected mean value, the dashed lines the expected $\pm 1\ \sigma$ bounds, while the dotted lines show the observed mean value in the data.*

6.4 Correction for the center of mass energy

The Monte Carlo samples used to calculate the calibration curves don't have the same center of mass energy as the data. For the 1999 data, the measured center of mass energy is about 400 MeV smaller than the energy set in the simulation (the exact values are reported in Table 6.1)[3]. In a similar way, the calibration curves for the fit of the year 2000 data have been calculated using Monte Carlo samples at $\sqrt{s} = 206$ GeV, while the two luminosity-weighted energies in data are $\sqrt{s} = 204.9$ GeV and $\sqrt{s} = 206.6$ GeV.

On the other hand, as shown in Figure 6.4 the calibration curves depend on the center of mass energy (in fact, as described in Section 2.3.2, the anomalous amplitudes are proportional to $s^{3/2}$).

It is thus necessary to apply a correction to the calibration curves to take into account the $\sqrt{s}$ difference between data and Monte Carlo. The correction is performed on the basis of the expected mean values of the optimal observables for vanishing anomalous couplings. The dependence of the mean values on the center of mass energy can be described by a parabola in $\sqrt{s}$ (see in [69]), i.e. by an equation of the form:

$$\xi(\sqrt{s}) = a + b \cdot \sqrt{s} + c \cdot (\sqrt{s})^2. \tag{6.14}$$

The parameters of the parabola are determined, for each coupling, by a fit to the expected mean values[4]. The calibration curves can be consequently corrected by the constant amount:

$$\zeta = \xi(\sqrt{s}_{measured}) - \xi(\sqrt{s}_{MC}). \tag{6.15}$$

[3] In fact the Monte Carlo samples were generated before the data were taken, thus before the actual beam energy was exactly known

[4] The comparison between the mean values at different center of mass energy can be performed under the constraint that the cuts on the optimal observables are the same at each $\sqrt{s}$.

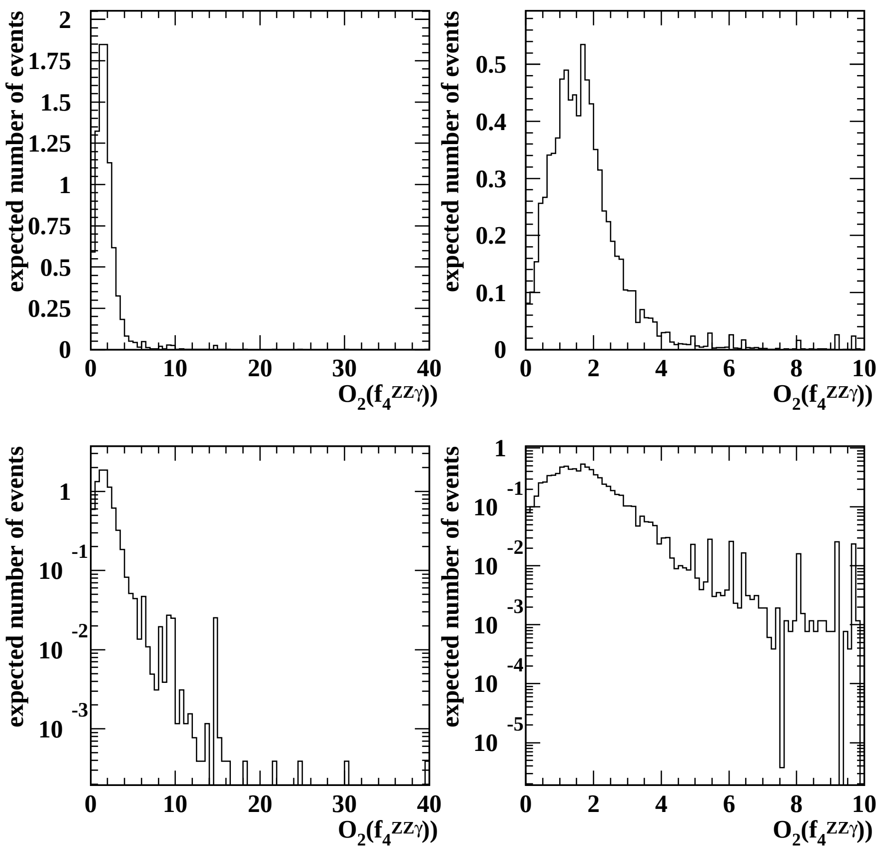

Figure 6.3: *Distributions of the second order optimal observables, for the coupling f_4^γ. The two upper plots show the distributions in linear scale, the lower two in logarithmic scale.*

As an example, for the optimal observable measuring f_5^Z, the parabolic fit to the mean values as a function of $\sqrt{s}$ is shown in Figure 6.5.

As can be seen in Figure 6.4, not only the expected mean value of the observables at Standard Model couplings, but also the shape of the calibration curves depends on $\sqrt{s}$. In fact the sensitivity to the anomalous couplings, as already seen in Chapter 2, increases with the increasing e^+e^- center of mass energy.

Thus, the correction applied should vary as a function of each coupling. As shown in [69], this effect is very small, and it is taken into account in the determination of the systematic uncertainties.

6.5 Fit of the anomalous couplings

Using the calibration curves obtained from the Monte Carlo simulation and the measured mean values of the optimal observables in data, a χ^2 variable can be constructed:

$$\chi^2(\alpha_i) = \sum_{k=1}^{2}\sum_{l=1}^{2} \left(\overline{\mathcal{O}}^{(k)}_{i(obs)} - \overline{\mathcal{O}}^{(k)}_{i(exp)}(\alpha_i)\right) (V^{-1})_{kl} \left(\overline{\mathcal{O}}^{(l)}_{i(obs)} - \overline{\mathcal{O}}^{(l)}_{i(exp)}(\alpha_i)\right) \tag{6.16}$$

Measured $\sqrt{s}$ (GeV)	$\sqrt{s}$ in Monte Carlo (GeV)
Year 1999	
191.59±0.04	192
195.53±0.04	196
199.52±0.04	200
201.63±0.04	202
Year 2000	
204.9±0.1	205
206.6±0.1	207

Table 6.1: *Measured center of mass energies (first column), and center of mass energies used in the Monte Carlo simulation of the signal and background processes. For the analysis of the data collected during the year 2000, only Monte Carlo Samples generated at $\sqrt{s}$=206 GeV were used, while the two values reported in the table represent the labels which will identify the two energy points in the following of the chapter.*

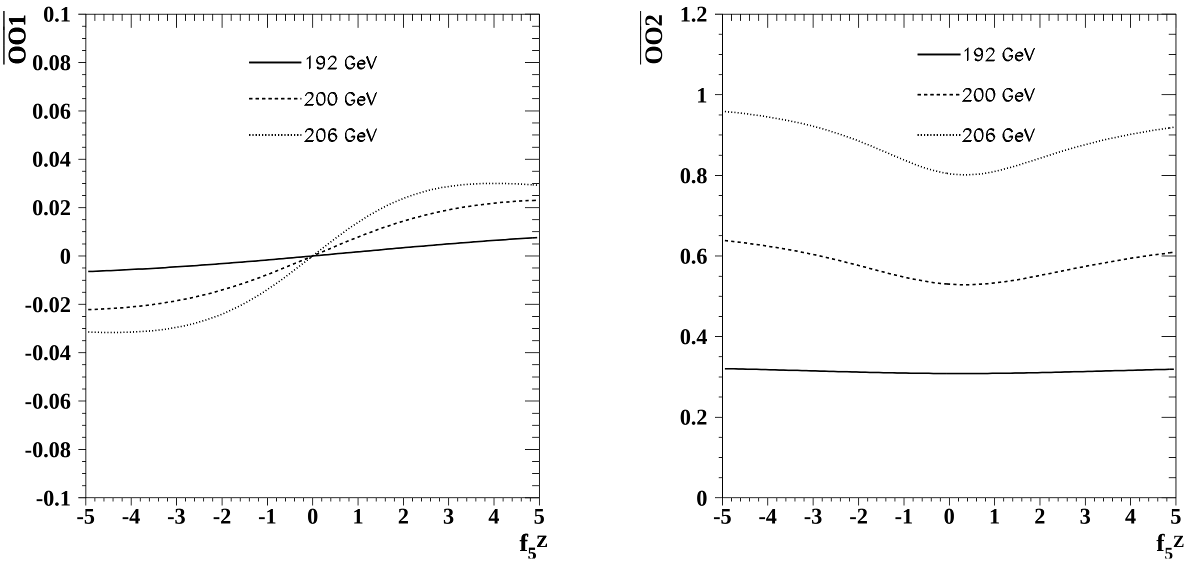

(a) (b)

Figure 6.4: *The calibration curves for the exclusive* $q\bar{q}b\bar{b}$ *channel, for three different center of mass energies. In Figure (a) the first order calibration curves are shown, in Figure (b) the second order ones.*

where the subscripts (obs) and (exp) denote the observed and expected mean values, while (k) and (l) are the order of the optimal observables. The matrix V is, for a single channel at a single center of mass energy, the 2×2 covariance matrix which describes the statistical and systematical uncertainties on the mean values:

$$V = V_{stat} + V_{syst} \tag{6.17}$$

Minimising the χ^2 in Equation 6.16 gives the measured value of the anomalous coupling α_i.

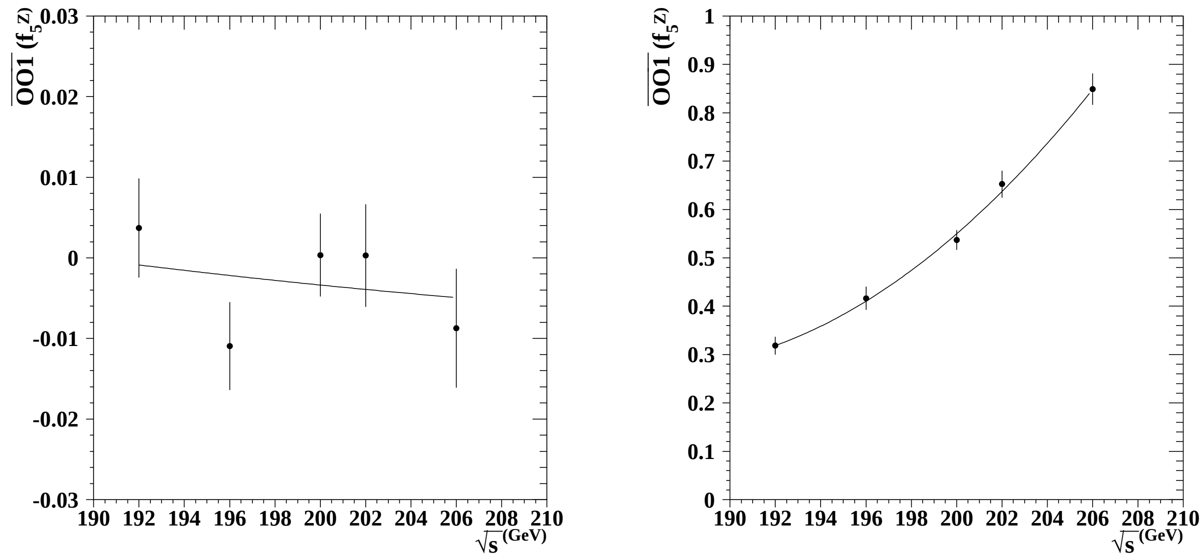

(a) (b)

Figure 6.5: *The mean values of the optimal observables of first order (a) and second order (b), as a function of the center of mass energy $\sqrt{s}$, for Standard Model couplings. The points are the mean values from the Monte Carlo, the error bars show the statistical error on the mean values, while the curves show the parabolic functions used for the correction of the calibration curves. The plots refer to the observables for the coupling f_5^Z.*

The statistical covariance matrix

The statistical covariance matrix V_{stat} could be in principle determined using the values of the optimal observables in data. Due to the low statistics resulting from ZZ event selections, the elements of the covariance matrix would in this case suffer from large statistical fluctuations. To avoid this, the expected covariance matrix can be used, calculated from the events selected in the high-statistics Monte Carlo samples, and rescaled to the number of selected events in the data. In principle, the covariance matrix depends on the anomalous couplings. However, it has been shown in studies of the process $e^+e^- \rightarrow W^+W^-$ that using a coupling-dependent covariance matrix can lead to biases, especially in case of low-statistic samples [69, 19]. In this analysis, the covariance matrix was calculated for the expected Standard Model couplings (i.e. for vanishing anomalous couplings).

The form of the statistical covariant matrix elements, rescaled to the data statistics, is:

$$(V_{stat})_{kl} = \frac{1}{N_{data}} \left(\frac{1}{\sum w_i} \left(\sum w_i \mathcal{O}_i^{(k)} \mathcal{O}_i^{(l)} - \frac{1}{\sum w_i} \left(\sum w_i \mathcal{O}_i^{(k)} \sum w_j \mathcal{O}_j^{(l)} \right) \right) \right), \tag{6.18}$$

where N_{data} indicates the number of events in data and the w_i are the reweighting factors described in Section 6.2.

The systematical covariance matrix

The systematic covariance matrix V_{syst} can be determined by comparing the calibration curves obtained after systematic variations with the reference ones. The differences in the mean values of the observables at Standard Model couplings (i.e. vanishing anomalous couplings) are taken as estimates of the systematic error originating from each effect, and the resulting errors are summed in quadrature to get the total error. More in detail, if $\overline{\mathcal{O}}^{(N)}_{i(ref)}(\alpha_i)$ is the reference calibration curve for the N-th order observable for the coupling α_i, and $\overline{\mathcal{O}}^{(N)}_{i(var)}(\alpha_i)$ is the one where a systematic variation has been applied to the Monte Carlo, the systematic error, related to a single effect, on the expected mean value is given by:

$$\Delta\overline{\mathcal{O}}^{(k)}_i(0) = \left|\overline{\mathcal{O}}^{(k)}_{i(ref)}(0) - \overline{\mathcal{O}}^{(k)}_{i(var)}(0)\right| \tag{6.19}$$

The elements of the covariance matrix are then given, assuming 100% correlation among the first and second order observables, by:

$$(V_{syst})_{kl} = \sum_{\text{syst. effects}} \Delta\overline{\mathcal{O}}^{(k)}_i(0) \cdot \Delta\overline{\mathcal{O}}^{(l)}_i(0). \tag{6.20}$$

The systematical variations which have been examinated for the hadronic channels are those described in Section 5.7; an extensive study on all effects for the ZZ $\to$ q$\bar{\text{q}}$b$\bar{\text{b}}$ channel has been carried out in [69]. The relevant effects, which have been finally taken into account for the fully hadronic channels and for their combination with the other channels are the following:

- The jet energy and angular resolution. The optimal observables are calculated on the basis of the event kinematic, i.e. of the 4-momenta of the reconstructed jets, in particular the 4-momenta resulting from the 4C-fit (see Section 4.4). Thus, a possible source of systematic effects could be the jet energy and angular resolution assumed in the kinematic fits. As already discussed in Section 5.7, to assess this systematic effect, the jet energy is smeared by 5%, and the jet angles are smeared by 1 degree, both in θ and ϕ, and the kinematic fits are performed again[5].
- The systematic effect arising from the Monte Carlo modelling of signal and background has been evaluated comparing the reference Monte Carlo samples with those generated using alternative models, as already discussed in Section 5.7.

Similar effects were studied for the channel involving leptons, and the systematic errors connected to the modelling of the detector resolution and to the Monte Carlo modelling of the physics processes were also taken into account (see in [52]).

6.6 Simultaneous fit of two couplings

In case two anomalous couplings α_i and α_j are assumed to be simultaneously non-zero, then the differential cross section is given by:

$$\begin{aligned}
\frac{\mathrm{d}\sigma}{\mathrm{d}\Omega}(\Omega,\alpha_i,\alpha_j) &= S^{(0)}(\Omega) \\
&\quad +\alpha_i \cdot S^{(1)}_i(\Omega) + \alpha_j \cdot S^{(1)}_j(\Omega) \\
&\quad +\alpha_i^2 \cdot S^{(2)}_{ii}(\Omega) + \alpha_j^2 \cdot S^{(2)}_{jj}(\Omega) + \alpha_i\alpha_j \cdot S^{(2)}_{ij}(\Omega) \\
&= S^{(0)}(\Omega) \cdot [1 + \alpha_i\mathcal{O}^{(1)}_i(\Omega) + \alpha_j\mathcal{O}^{(1)}_j(\Omega) \\
&\quad +\alpha_i^2 \cdot \mathcal{O}^{(2)}_i(\Omega) + \alpha_j^2 \cdot \mathcal{O}^{(2)}_j(\Omega) + \alpha_i\alpha_j \cdot \mathcal{O}^{(2)}_{ij}(\Omega)]
\end{aligned} \tag{6.21}$$

So in this case, besides the two observables relative to each of the couplings, another observable $\mathcal{O}^{ij}_2$ appears in the differential cross section. This observable is originating from the interference

[5] The energy smearing corresponds to about 60% of the energy resolution, while the angular smearing corresponds to about 70% of the angular resolution.

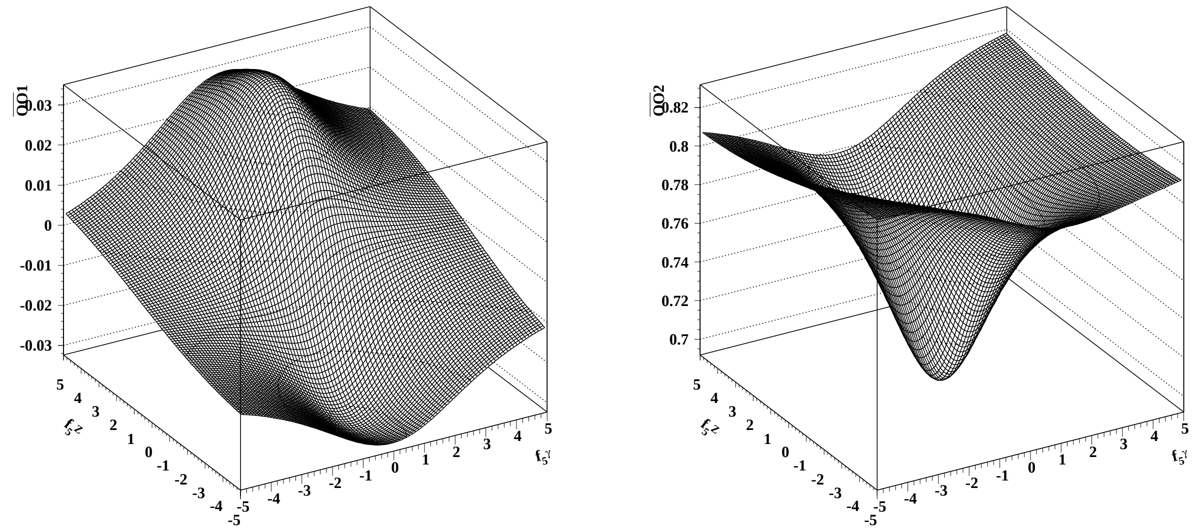

(a) (b)

Figure 6.6: *Calibration surfaces for the exclusive* $\mathrm{q\bar{q}b\bar{b}}$ *channel at* $\sqrt{s} = 207$ *GeV. The first (a) and second (b) order observables relative to the pair of couplings* (f_5^γ, f_5^Z) *are shown.*

between the anomalous amplitudes corresponding to the two couplings α_i and α_j. However, the 2-dimensional fits which will be presented in this work study only the pairs of couplings (f_4^γ, f_4^Z) and (f_5^γ, f_5^Z) i.e. pairs of couplings with the same behaviour under CP transformation[6]. In this case the observables of same order are fully correlated, as they differ just by a constant factor [69]:

$$\mathcal{O}_1^i(\Omega) = c_1 \mathcal{O}_1^j(\Omega) \qquad \mathcal{O}_2^i(\Omega) = c_2 \mathcal{O}_2^j(\Omega) = c_3 \mathcal{O}_2^{ij}(\Omega). \tag{6.22}$$

This can be explained by looking at the helicity amplitudes introduced in Section 2.4.1, and shown in Equation 2.22.

In case the fit is performed assuming that two couplings may vary at the same time, calibration surfaces in the space of the two couplings have to be determined, instead of the calibration curves of the 1-dimensional case. The reweighting of the events to get the calibration surfaces is done in a way similar to the 1-dimensional case (Equation 6.13), but now the mean value of the observables will depend on two couplings:

$$\overline{\mathcal{O}}^{(N)}_{i(expected)}(\alpha_i, \alpha_j) = \frac{\sum_{Events} w(\Omega, \alpha_i, \alpha_j) \mathcal{O}_i^{(N)}(\Omega)}{\sum_{Events} w(\Omega, \alpha_i, \alpha_j)} = \frac{f(\alpha_i, \alpha_j)}{g(\alpha_i, \alpha_j)}. \tag{6.23}$$

The functions $f(\alpha_i, \alpha_j)$ and $g(\alpha_i, \alpha_j)$ are now two-dimensional paraboloids, and they have to be evaluated at six different points to get an analytic expression.

In Figure 6.6 two examples of calibration surfaces are shown. They are the calibration surfaces for the first and second order observables for the pairs of couplings (f_5^γ, f_5^Z), at $\sqrt{s} = 207$ GeV, for the exclusive $\mathrm{q\bar{q}b\bar{b}}$ channel. The χ^2 fit is performed in a way similar to the 1-dimensional case; the χ^2 is now given by:

$$\chi^2(\alpha_i, \alpha_j) = \sum_{k=1}^{2} \sum_{l=1}^{2} \left(\overline{\mathcal{O}}^{(k)}_{i(obs)} - \overline{\mathcal{O}}^{(k)}_{i(exp)}(\alpha_i, \alpha_j) \right) (V^{-1})_{kl} \left(\overline{\mathcal{O}}^{(l)}_{i(obs)} - \overline{\mathcal{O}}^{(l)}_{i(exp)}(\alpha_i, \alpha_j) \right) \tag{6.24}$$

[6] As for the 1-dimensional case, the fit is limited to the real part of the couplings.

Where V is the covariance matrix including both statistical and systematical errors. As two observables for each coupling are fitted, the covariance matrix has in this case dimensions 4×4.

6.7 Combination with the event rate likelihood

The optimal observables are only sensitive to the event kinematic, while the information from the total event rate is not taken into account in the χ^2 fit to the mean values. Thus, the result of the fit must be combined with the information contained in the number of observed events in data N_{data}. To do this, a likelihood function is calculated, corresponding to the probability of observing N_{data} events when the number of expected events is $N_{exp}(\vec{\alpha})$, calculated assuming a Poisson distribution for the total number of events:

$$L(\vec{\alpha}) = \frac{N_{exp}(\vec{\alpha})^{N_{data}} \cdot e^{-N_{exp}(\vec{\alpha})}}{N_{data}!}, \tag{6.25}$$

where the number of expected events $N_{exp}(\vec{\alpha})$ depends on the anomalous couplings. The combination with the χ^2 resulting from the optimal observables fit can be done as follows [58]:

$$\chi^2_{tot}(\vec{\alpha}) = \chi^2(\vec{\alpha}) - 2 \cdot \ln L(\vec{\alpha}). \tag{6.26}$$

where a single combined χ^2 is calculated. This χ^2 can be easily turned in a log likelihood: $\ln L_{tot} = \frac{1}{2} \cdot \chi^2_{tot}$.

6.8 Optimal observables for the fully hadronic channels

As discussed in Chapter 5, the events satisfying the two selections $\mathrm{ZZ} \to \mathrm{q\bar{q}q\bar{q}}$ and $\mathrm{ZZ} \to \mathrm{q\bar{q}b\bar{b}}$ are divided into three non-overlapping classes: the exclusive $\mathrm{ZZ} \to \mathrm{q\bar{q}q\bar{q}}$, the exclusive $\mathrm{ZZ} \to \mathrm{q\bar{q}b\bar{b}}$, and the overlap i.e. the class containing the events satisfying both selections.

Examples of the distributions of the first and second order optimal observables for the coupling f_5^Z are shown in Figures 6.7 and 6.8. The calibration curves are calculated separately for the three classes; the Figures 6.7 and 6.8 show the distributions of the first and second order optimal observables, for the two exclusive channels, at $\sqrt{s} = 207$ GeV. As can be seen in the plots, and as discussed in Chapter 5, the exclusive $\mathrm{ZZ} \to \mathrm{q\bar{q}q\bar{q}}$ channel is affected by a much bigger amount of background than the exclusive $\mathrm{ZZ} \to \mathrm{q\bar{q}b\bar{b}}$.

In Figure 6.2, examples of the calibration curves obtained from the events passing the fully hadronic selections are shown. In the figure, the expected Standard Model mean value is also shown for each observable, together with the observed mean value in the data, which is then used to perform the fit.

6.9 Systematic uncertainties

The χ^2 calculated as in Equation 6.16 and 6.24, where the covariance matrix V includes both statistical and systematic uncertainties, can be extended to the case of N_{chan} channels and N_{cms} center of mass energies. In this case, the covariance matrix is given by a $N \times N$ matrix, with $N = 2 \cdot N_{chan} \cdot N_{cms}$, as 2 observables (first and second order) are entering the fit for each channel at each center of mass energy. The covariance matrix is computed as described in the previous sections, and the systematic errors are assumed to be fully correlated between channels and energies.

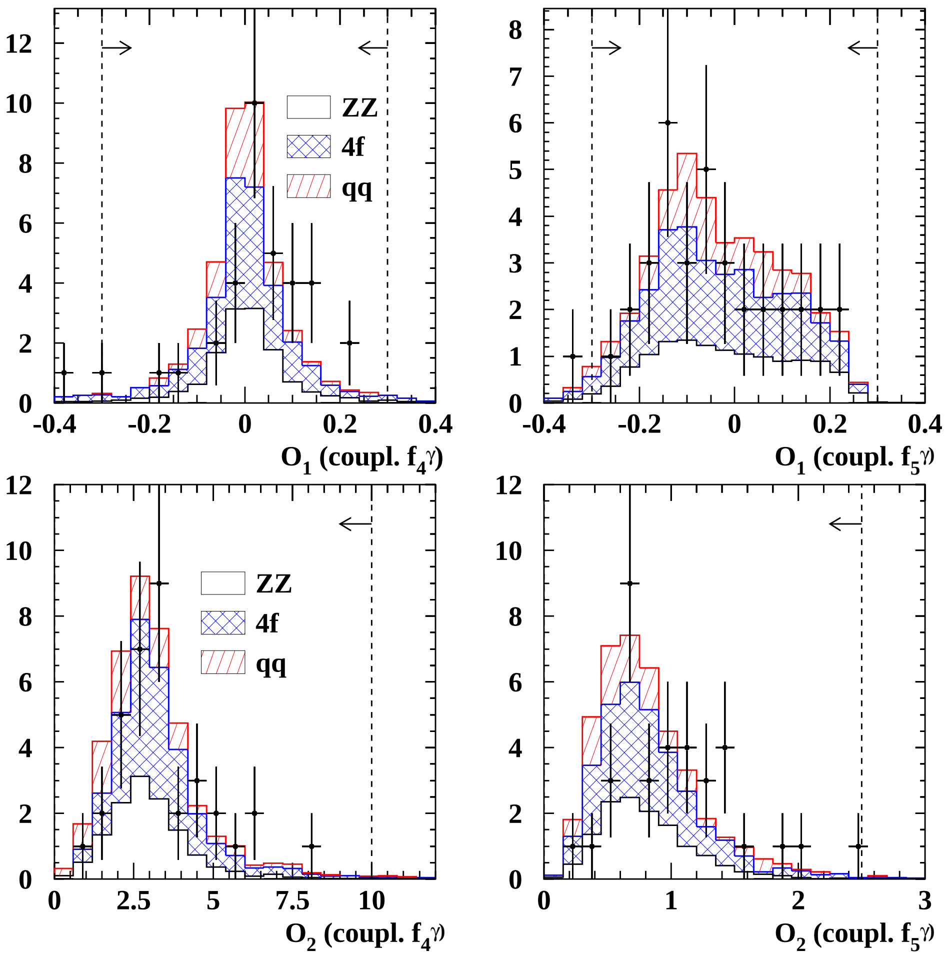

Figure 6.7: *Distributions of the optimal observables for the events passing the exclusive* $ZZ \to q\bar{q}q\bar{q}$ *selection, at* $\sqrt{s} = 207$ *GeV. The two upper plots show the first-order observables and the two lower plots the second order observables, for the two couplings* f_4^γ *and* f_5^γ *respectively.*

6.10 Fit results

The results of the 1-dimensional fit combining all ZZ decay channels, after the combination of the optimal observables with the event rate likelihood, are shown in Table 6.2. In this case, only one coupling at a time is assumed to be non-vanishing.

The table shows, for each coupling, the 95% confidence level lower and upper limit, corresponding to a change in the log likelihood of 1.92 from the minimum value. The results have been obtained combining all ZZ decay channels and all center of mass energies. The fit using the optimal observables was applied only to the data collected in the years 1999 and 2000 (i.e. at $\sqrt{s}$ from 192 to 208 GeV). For the data at $\sqrt{s} = 183$ GeV and $\sqrt{s} = 189$ GeV, a binned maximum likelihood fit to the differential cross section was used instead of the optimal observables fit, as described in [68].

The likelihood curves are shown in Figure 6.9 for the four real parts of the anomalous

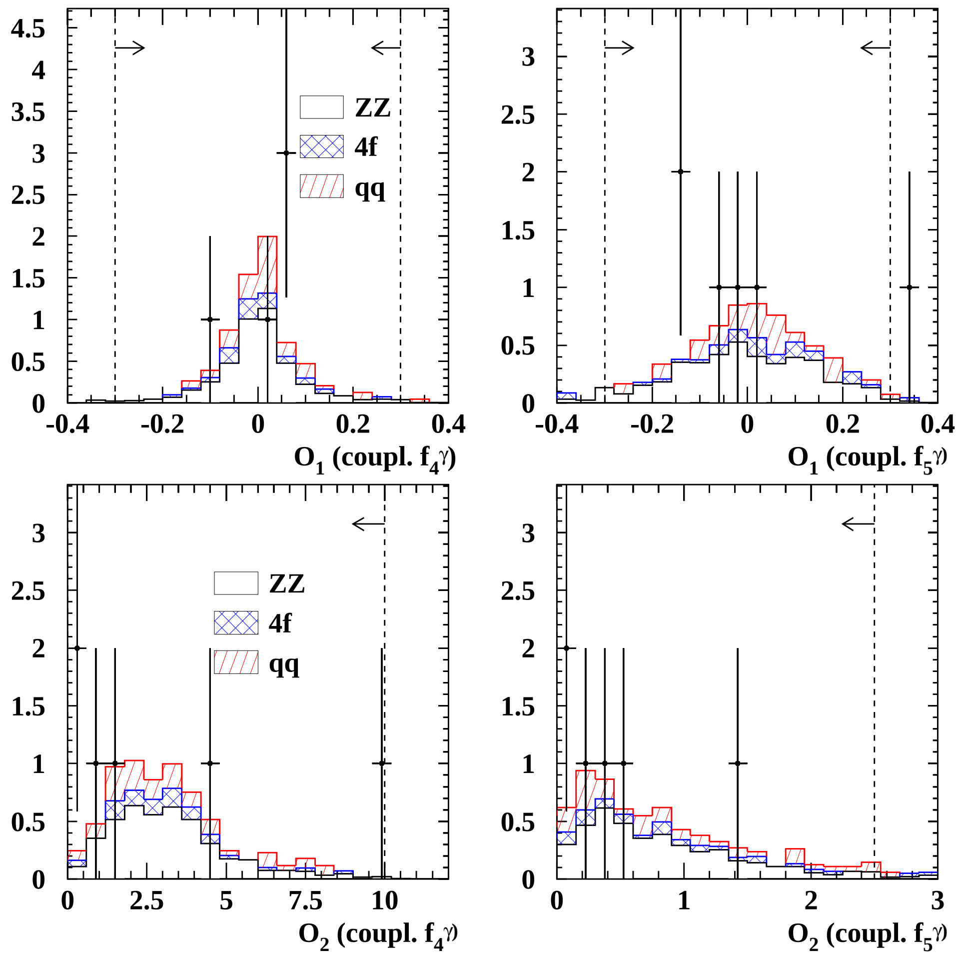

Figure 6.8: *Distributions of the optimal observables for the events passing the exclusive* $ZZ \to q\bar{q}b\bar{b}$ *selection, at* $\sqrt{s} = 207$ *GeV. The two upper plots show the first-order observables and the two lower plots show the second-order observables, for the two couplings* f_4^γ *and* f_5^γ*, respectively.*

Coupling	95% C.L. lower limit	95% C.L. upper limit
f_4^γ	-0.55	0.64
f_5^γ	-0.97	0.31
f_4^Z	-0.36	0.36
f_5^Z	-0.36	0.36

Table 6.2: *The table shows the 95% confidence level limits on the anomalous neutral triple gauge couplings. These results include all ZZ decay channels and all center of mass energies. For* $\sqrt{s} = 183$ *GeV and* $\sqrt{s} = 189$ *GeV the binned maximum likelihood fit described in [68] was used instead of the optimal observables method.*

couplings. The figure shows the log likelihood (i.e. 1/2 times the χ^2) resulting from the optimal observables fit and the log likelihood from the event rate information. The solid line is the sum of the two log likelihoods.

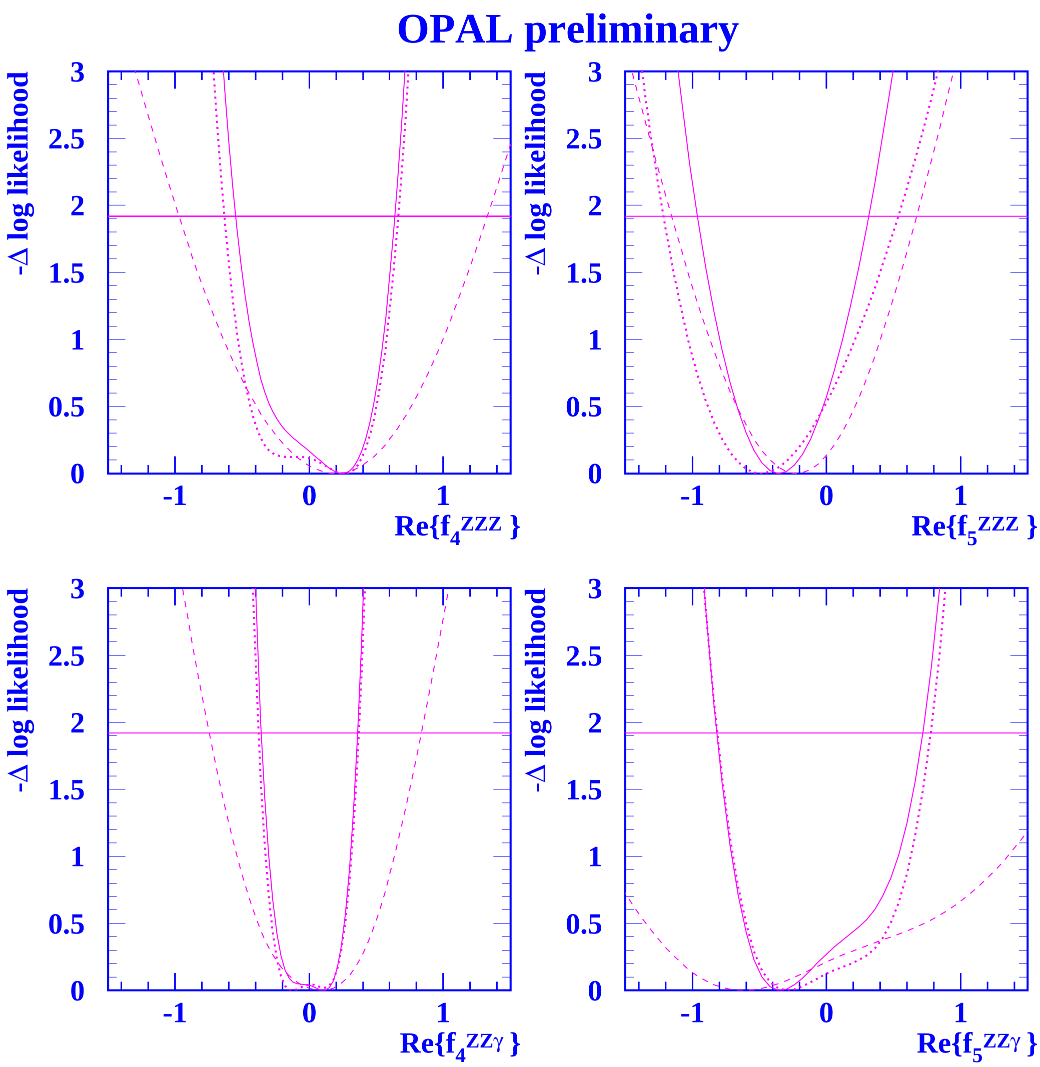

Figure 6.9: *The negative log likelihood as a function of the four anomalous couplings. The dotted line is the log likelihood from the cross section information, the dashed line is the one from the optimal observables analysis, and the solid line is the sum of the two. The 95% confidence level limits correspond to a change in the log likelihood of 1.92 from the minimum value.*

The fit can be extended to the case of two non-vanishing couplings, as described in Section 6.6, and limits can be derived on pairs of couplings. The constraint from the event rate can be calculated for two non-zero couplings as well. The resulting 95% confidence level contours in the f_4 and f_5 plane, including both optimal observables and cross section constraints, are shown in Figure 6.10.

The results of the fit agree with the Standard Model expectation, which corresponds to vanishing anomalous couplings. The 95% confidence level limits obtained are O(10^{-1}).

The OPAL results have been also combined with the results obtained by the other three

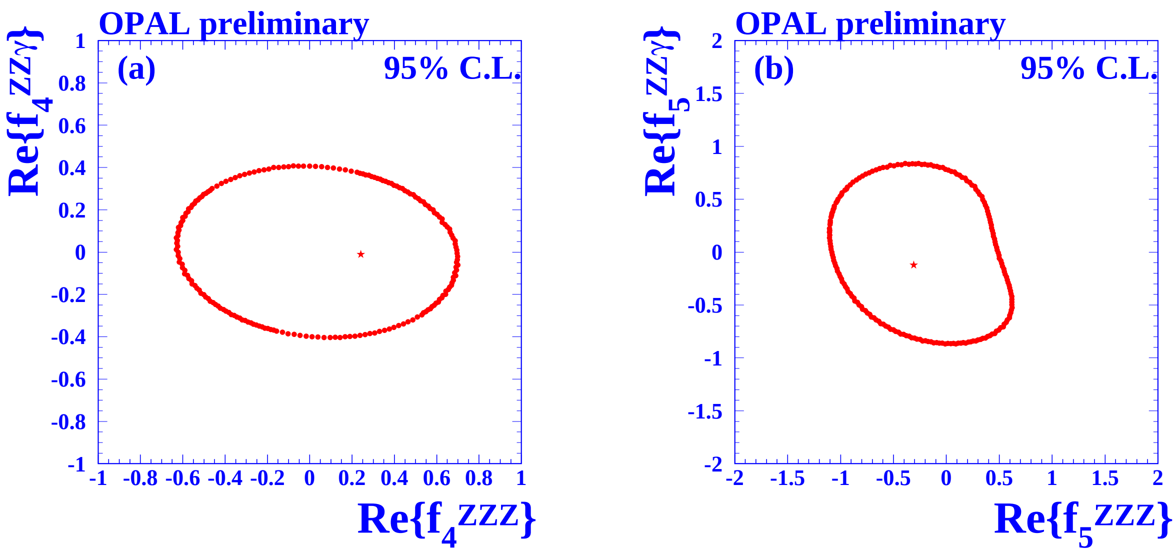

(a) (b)

Figure 6.10: *The 95% Confidence Level contours, corresponding to a change of 3.0 in the log likelihood from the minimum, for (a): the* $f_4^Z - f_4^\gamma$ *plane and (b): the* $f_4^Z - f_4^\gamma$ *plane. The expected Standard Model value is located at (0,0), while the star shows the location of the minimum. The results are obtained including all the ZZ decay channels and all the energies, and including also the OPAL data taken at* $\sqrt{s} = 183$ *GeV and at* $\sqrt{s}$*=189 GeV [68].*

LEP experiments; the results of the combination are also in agreement with the Standard Model expectations. A detailed description of the combination and the results can be found in [70].

7. The TESLA Linear Collider

This chapter will give a general description of the projected future Linear Collider TESLA, and of the planned detector layout. Then the physics processes which are relevant for an analysis of the scattering of massive vector bosons will be introduced. The Monte Carlo generators and the detector simulation used to perform the analysis will be also presented.

7.1 Introduction

Due to synchrotron radiation, the idea of a circular e^+e^- storage ring of the kind of LEP can not be extended to build an accelerator of this type able to operate in the TeV range. In a storage ring in fact, the energy loss per turn is proportional to the fourth power of $\gamma = E/m$, and linear in $1/r$.

The energy region beyond the reach of LEP2 can thus only be explored by linear colliders.

TESLA (**T**eV **E**nergy **S**uperconducting **L**inear **A**ccelerator) is a project for a linear electron-positron collider; a proposed site for its construction is DESY-Hamburg (**D**eutsches **E**lektronen-**Sy**nchrotron). In Figure 7.1 the design of the project is shown. The collider is designed to be 33 Km long, and it consists of two accelerating branches for electrons and positrons respectively, with a collision point in the center. The electrons produced by the source (on the left side of the picture) are pre-accelerated and cooled in the damping ring. The electrons, packed in bunches, are then driven to the main linear accelerator branch. The electrons needed for the XFEL[1] are extracted at the point of the accelerator where they have an energy of about 50 GeV, while the remaining electrons are accelerated up to the final energy. The electron beam is also used for the production of the positron beam, which is at its turn pre-accelerated, damped, and then driven to the linear accelerator. The accelerating cavities are superconducting, in order to limit the energy consumption of the system. The beams can reach an energy of up to 400 GeV, thus leading to an e^+e^- center of mass energy of 800 GeV. The main parameters of TESLA are summarised in Table 7.1, for $\sqrt{s}$ = 500 GeV and $\sqrt{s}$ = 800 GeV, and compared to the corresponding LEP2 parameters.

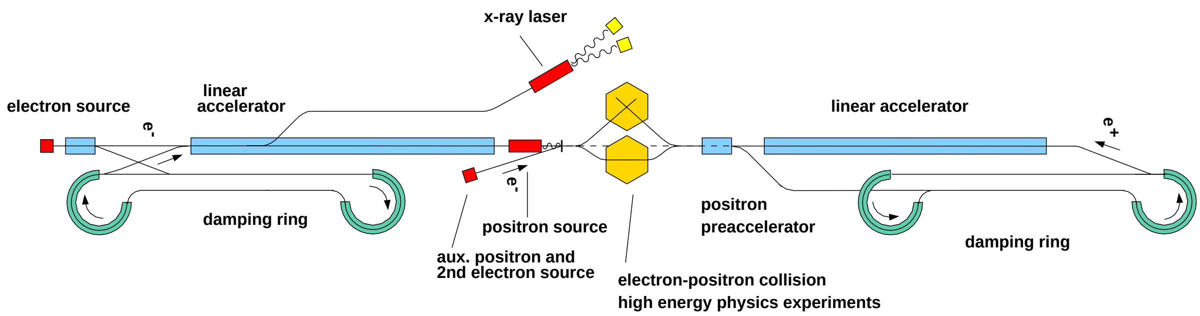

Figure 7.1: *Design of the TESLA Linear Collider. The full length of the accelerator is 33 Km.*

[1] The XFEL (**X**-ray **F**ree **E**lectron **L**aser) is a coherent X-ray source which exploits the syncrotron radiation of the beam extracted from the TESLA accelerator. The XFEL can perform a wide range of researches in natural sciences, like for example atomic and molecular physics, plasma and condensed matter physics, or materials science.

Parameter	TESLA 500	TESLA 800	LEP2
C.o.m. Energy (GeV)	500	800	200
Luminosity ($\mathrm{cm}^{-2}\mathrm{s}^{-1}$)	$3 \cdot 10^{34}$	$5 \cdot 10^{34}$	$6 \cdot 10^{31}$
Beam size x,y (nm)	553 , 5	391 , 2	$3 \cdot 10^5$, $8 \cdot 10^3$
Bunch spacing (ns)	337	187	22000
Bunch length (mm)	0.3	0.3	10
$\mathrm{N_e}$/bunch	$2 \cdot 10^{10}$	$1.4 \cdot 10^{10}$	$4.5 \cdot 10^{10}$

Table 7.1: *Some of the operating parameters for TESLA at 500 GeV and 800 GeV, compared to the corresponding parameters of LEP2.*

7.2 The TESLA detector

The TESLA detector will have to deal with a large dynamic range in particle energy, complexity of final states and signal-to-background ratio. The physics requirements affect four main detector benchmarks which must be substantially better than at LEP: i) track momentum resolution, ii) jet flavour tagging, iii) energy flow measurement, iv) hermeticity. The detector design for e^+e^- physics up to ~1 TeV has been evolving during two series of workshops; large detector, lower magnetic field and small detector, higher magnetic field options were compared, and the large version was found to have better overall performance because the tracking can be more precise and efficient, the effective calorimeter granularity is better being further away from the interaction point, both electromagnetic and hadronic calorimeters can be inside the magnet coil, and the sensitivity to long-lived particles is increased. Figure 7.2 shows the detector layout. The detector is described in detail in [40]; here its components will be briefly presented.

The **Tracking System** must satisfy the requirements of optimal momentum resolution ($\Delta(1/p_t) = 5 \cdot 10^{-5}(\mathrm{GeV})^{-1}$ in the central region), very high b- and c-tagging capabilities, very good pattern recognition capabilities and minimal amount of material. The layout of the tracking system is shown in Figure 7.3, and its components are the following:

The **Vertex Detector** is the subdetector closest to the interaction point. For the vertex detector there are three proposals among which the detector technology has to be chosen: a CCD (**C**harge-**C**oupled **D**evice), CMOS pixels and hybrid pixel sensors. The design of both CCD and CMOS options foresees a first cylindrical layer as close as possible to the interaction point (the radius of ~15 mm is defined by the machine), followed by 4 additional layers. The 4 outer layers can reconstruct the tracks in a stand-alone way, while the hits in the inner layer are used to refine the track extrapolation to the interaction point. The inner three layers extend to $|\cos\theta|$=0.96, with 5-layer coverage to $|\cos\theta|$=0.9. The design of the hybrid pixel sensor option foresees, due to the higher thickness of a single layer, a 3-layer cylindrical detector, complemented by forward layer and disks extending the polar acceptance to small angles. The three-hit coverage extends up to $|\cos\theta| = 0.995$.

The **Time Projection Chamber (TPC)** is the main tracking detector. The TPC is made of a gas-filled drift volume with the readout electronic placed at the end-caps. As the drift gas is the only material of the detector, the multiple scattering contribution to the resolution is negligible. In addition, the TPC allows the measurement of the specific ionization dE/dx which is used for particle identification. The outer radius of the TPC is 1.7 m; the length of 5 m allows a good reconstruction of tracks produced with small polar angles. The single-point resolution is 160 μm in the $r - \phi$ plane and 1 mm in the z-direction.

The **Forward Chambers (FCH)**. Particles produced at small polar angles do not cross the TPC in its full radial length, leading to a worse momentum resolution. To compensate this

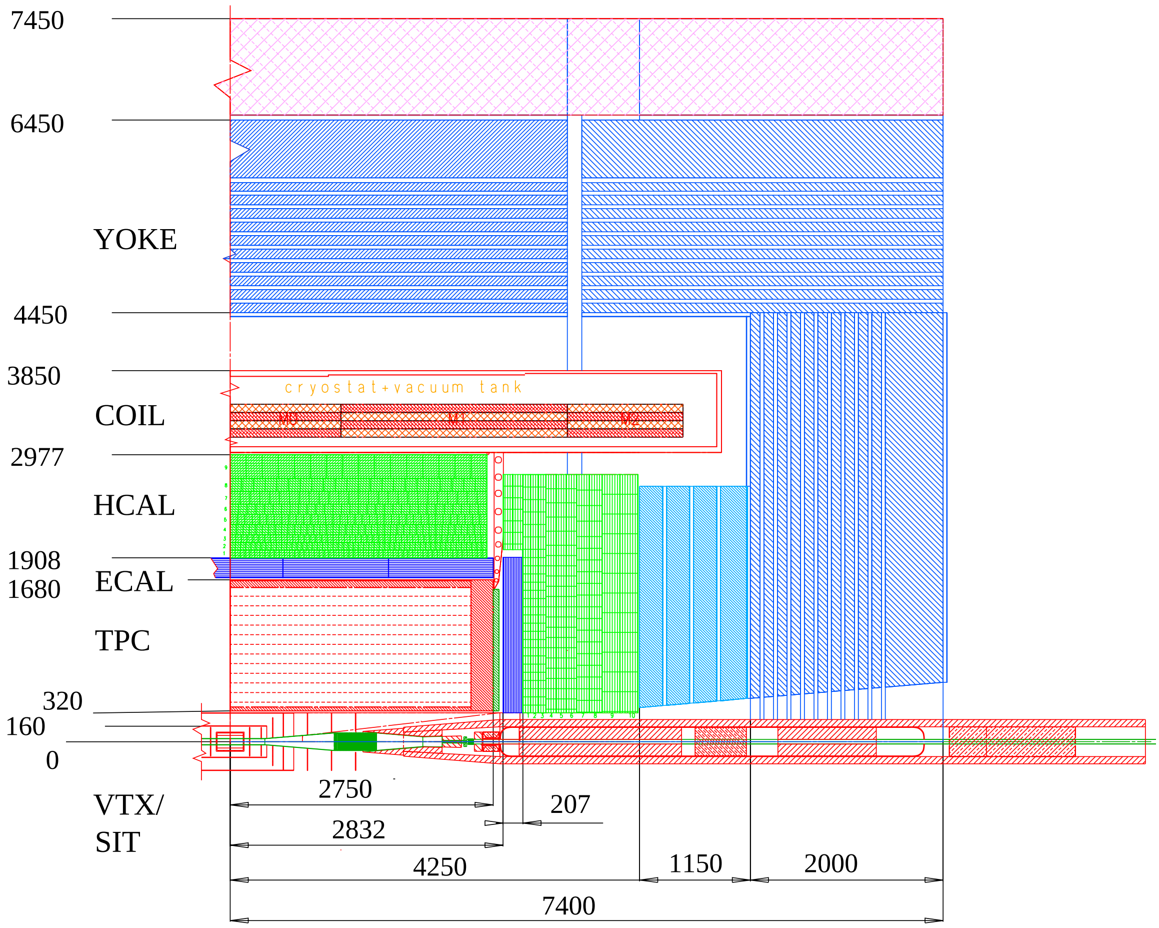

Figure 7.2: *View of one quadrant of the TESLA Detector. Dimensions are in mm*

effect, two tracking detectors with high resolution (50 μm) are placed in correspondence of the TPC end-caps, implemented as 6 layers of straw-tubes chambers. These forward detectors, are also designed to measure showers originating between the tracking system and the calorimeters, in particular in the TPC end-caps.

The **Silicon Intermediate Tracker (SIT)** is placed between the vertex detector and the TPC. It consists of two silicon-strips detectors with spatial resolution of $\sim$ 10 μm, which are placed at radial distances from the interaction point of 16 cm and 30 cm. The purpose of this subdetector is to reconstruct decay vertices of long-lived particles which decay between the Vertex Detector and the TPC, and to generally improve the momentum resolution.

The **Forward Tracking Disks (FTD)** are also placed inside the TPC inner radius, on both sides of the Vertex Detector. Each of them is built of seven disks. The FTD improves the track reconstruction in the small polar angle zone. The four inner disks are Silicon-Pixel-Detectors, while the outer three are Silicon-Strips. Their resolution is about 25 μm.

The **Calorimeter System** must ensure the reconstruction of jet (parton) four-momenta with high resolution, to be able to cope with the many physics signatures which will show up as complex hadronic final states. The system must be hermetic down to small polar angles, have an excellent energy and angular resolution, and have a good time resolution to avoid event pile-up. This strategy is best realized in a dense and hermetic sampling calorimeter with a very high granularity, where it is possible to separate the contributions of the different particles in a jet and measure their four-momenta. The calorimeter system consists of the following subdetectors:

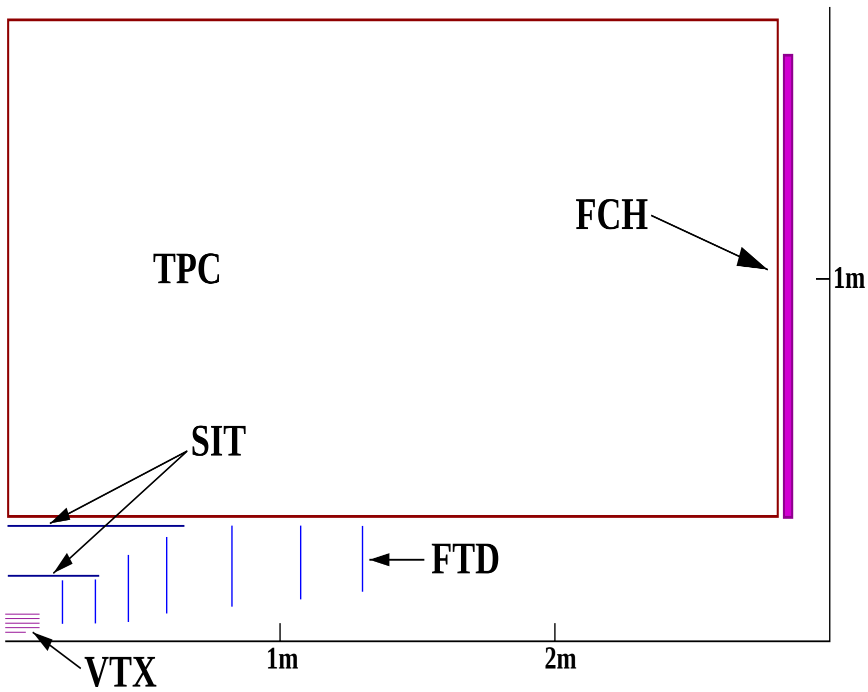

Figure 7.3: *The layout of the TESLA tracking system. In the figure, one quadrant of the system is shown.*

The **Electromagnetic Calorimeter (ECAL)** for which two possible solutions are foreseen: a very high granularity 3D calorimeter, based on tungsten absorbers and silicon pads, transversely segmented into readout cells of approximately 1 cm^2, or a so-called *shashlik* sampling calorimeter, equipped with lead and scintillator plates and with a transversal segmentation of about 3x3 cm^2. The ECAL resolution assumed in the physics studies which will be presented in this work is:

$$\frac{\sigma(E)}{E} = \frac{10\%}{\sqrt{E(\mathrm{GeV})}} + 0.6\% \tag{7.1}$$

as resulting from prototypes tests and simulation studies.

The **Hadronic Calorimeter (HCAL)** is placed behind the ECAL, inside the superconducting coil generating the 4 T magnetic field. Also for the HCAL two approaches have been studied, a tile sampling calorimeter of moderate segmentation (5x5 cm^2 in the inner layers increasing to 25x25 cm^2 at the outer radius), with stainless steel and scintillator plates, or a highly segmented calorimeter with digital readout and with cells of approximately 1 cm^2. The latter solutions foresees stainless steel plates as absorber, while the detecting medium can be made of resistive plate chambers or wire chambers. The HCAL energy resolution which has been assumed in this work, and which comes from simulations of hadronic showers and detector response is:

$$\frac{\sigma(E)}{E} = \frac{40\%}{\sqrt{E(\mathrm{GeV})}} + 4\% \tag{7.2}$$

As already pointed out, excellent hermeticity of the detector is needed for many physics studies. The acceptance of the ECAL+HCAL system reaches a polar angle of about 80 mrad. The calorimetric coverage is completed by two devices in the very forward region on both sides of the interaction point. Both devices are at the same time a part of a masking system shielding the detector from backgrounds, the **Instrumented Mask** whose layout is shown in Figure 7.4.

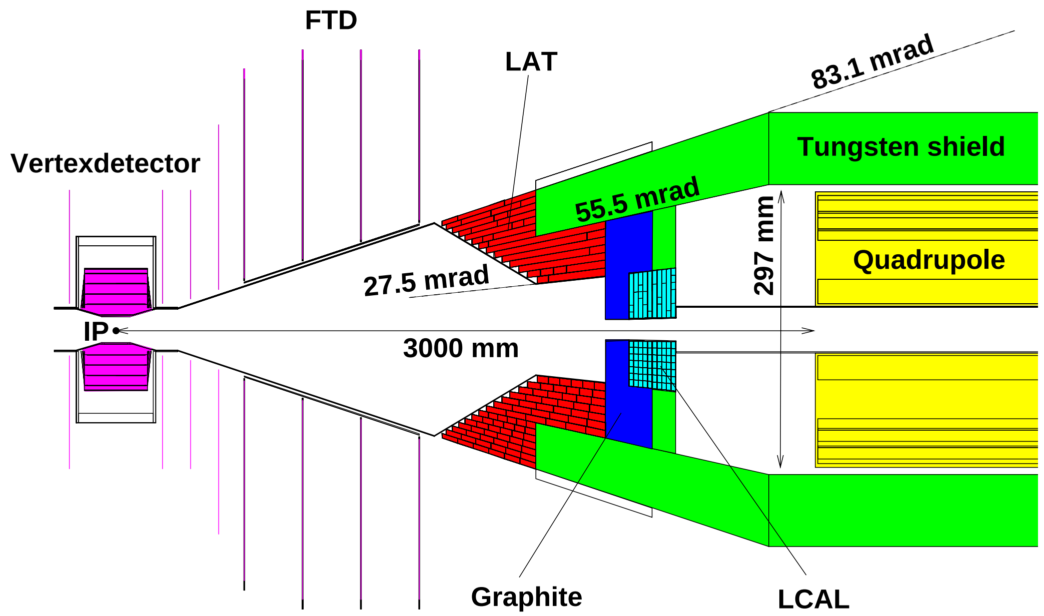

Figure 7.4: *The design of the instrumented mask, with the forward angle calorimeters. The LAT and LCAL calorimeters are integrated into the tungsten shield of the mask.*

The two devices placed in the Instrumented Mask are:

The **Low Angle Tagger (LAT)**, designed to provide an accurate measurement of electrons up to the nominal beam energy of 400 GeV. Its design foresees a tungsten sampling calorimeter, with silicon detectors as active elements. The beamsstrahlung background (e^+e^- pairs originating from the beams) is relatively small, the typically deposited energy per bunch crossing being of the order of a few GeV. The detector covers the polar angle region between 23 mrad and 83 mrad.

The **Luminosity Calorimeter (LCAL)**, serving both as fast luminosity monitor and as low angle calorimeter. It will be placed at a distance of 220 cm on both sides of the interaction point, between radii of 1.2 cm and 6.2 cm from the beam line. As a luminosity monitor, the detector will measure the amount of beam induced background particles. About $2 \cdot 10^4$ e^+e^- pairs on each side, corresponding to over 20 TeV of energy per bunch crossing, hit the LCAL. As a calorimeter, the LCAL will measure electrons in the region between 5 mrad and 28 mrad. Due to the measurement uncertainties connected with to the subtraction of the large background, which are still under study, the conservative choice of not including the LCAL in the simulation studies presented here was taken.

7.3 Physics processes at the TESLA Linear Collider

The TESLA Linear Collider will have the possibility of operating over a wide range of center of mass energies, from $\sqrt{s} \simeq 90$ GeV up to $\sqrt{s} = 800$ GeV. TESLA will be in fact able to make dedicated runs with high luminosity at low energies, close to the Z resonance (the so-called GigaZ mode) and above the threshold for W^+W^- production, i.e. the same energies of the LEP1 and LEP2 physics programs. This will allow to measure the electroweak mixing angle and the W boson mass with much higher precision than at previous colliders.

On the other hand, one of the main aims of the TESLA physics program is to firmly establish the electroweak symmetry breaking as mechanism for the generation of the masses. If a Higgs bosons exists, TESLA will be able to measure its properties with high precision, and check whether the observed Higgs boson has the profile predicted by the Standard Model. At TESLA it will be possible to measure with high precision the Higgs mass, the production cross section, the branching ratios to quarks, leptons and bosons and the Yukawa coupling to the top quark. A precision of 50(70) MeV on the mass of a 120(200) GeV Higgs will be for example achievable, while the branching ratios will be measured with a precision of a few percent [40].

However, at high center of mass energies, some alternative new physics beyond the Standard Model may emerge, ranging from supersymmetric theories to theories in which the symmetry breaking is generated by new strong interactions. The latter alternative model, which foresees a new strong interaction between the W and Z bosons at high energies, has been described in Chapter 2. An experimental study of this scenario will be treated in the following of this work.

The signal and background processes which are relevant for an analysis of the scattering of W and Z bosons will be presented in the following of this chapter, together with a description of the Monte Carlo generators and of the detector simulation tools which have been used to perform the study.

7.4 $VV \to VV$ scattering processes

The scattering subprocesses $VV \to VV$ occur, in e^+e^- collisions, through the Feynman diagrams which have been introduced in Section 2.5.5 (see also in Figure 2.14).

Each of the two bosons decays into a fermion-antifermion pair, so the final state is a 6-fermion final state. Only the final states in which the two bosons are decaying each to a quark-antiquark pair have been taken into account in the analyses presented in this work. This means that the final states for the signal processes are involving four quarks and two leptons. The corresponding 6-fermion final states branching ratios are the following:

$$\mathrm{BR}(\mathrm{W^+W^-}\nu\bar{\nu} \to \mathrm{q\bar{q}q\bar{q}}\nu\bar{\nu}) = 46.9\% \tag{7.3}$$
$$\mathrm{BR}(\mathrm{ZZ}\nu\bar{\nu} \to \mathrm{q\bar{q}q\bar{q}}\nu\bar{\nu}) = 48.9\% \tag{7.4}$$
$$\tag{7.5}$$

The signature in the detector is therefore 4-jet plus missing energy and transverse momentum, due to the two neutrinos, with the invariant masses of the two jet pairs peaking in correspondence of the W or Z boson mass, according to the process.

7.5 Signal definition

In the analyses presented here, the signal is constituted by the doubly-resonant diagrams shown in Figure 7.5, where the denomination "doubly-resonant" denotes the fact that the two di-quark pairs are both originating from the decay of a W or a Z boson. Other diagrams leading to the same 6-fermion final states are considered as background; a set of examples of such background diagrams is shown in Figure 7.6.

The study of 6-fermion processes requires the use of a dedicated generator, able to deal with the huge number of diagrams leading to the given final state, and with the complexity of the phase-space. As an example, the total number of diagrams corresponding to the process $e^+e^- \to \nu\bar{\nu}\mathrm{u\bar{d}c\bar{s}}$ is 212.

The generator used in this analysis to simulate 6-fermion events is WHIZARD [71], which generates $e^+e^- \to$6-fermion events taking into account, for the matrix element calculation, all the Feynman diagrams leading to a given final state, and their interference. The signal processes have thus to be defined applying, at generator level, the following cuts on the $e^+e^- \to \mathrm{q\bar{q}q\bar{q}}\nu\nu$ phase space:

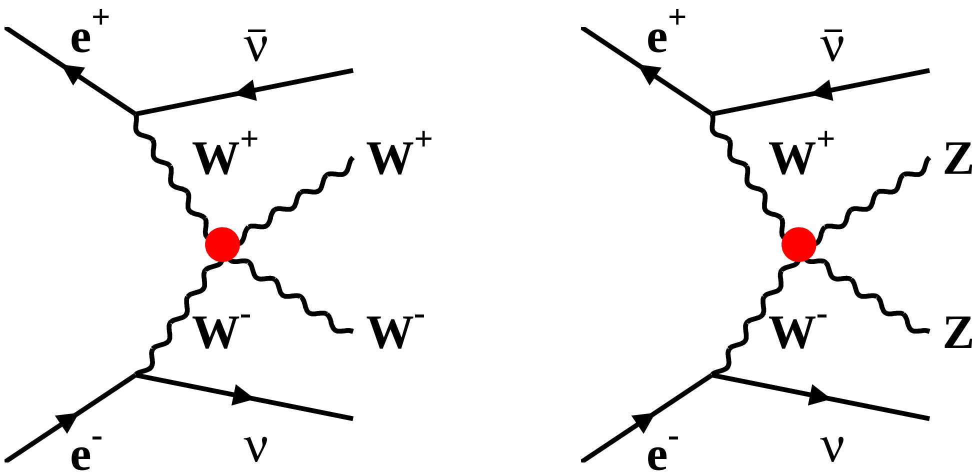

(a) (b)

Figure 7.5: *Feynman diagrams for the two signal processes involving the scattering subprocesses WW→WW and WW→ZZ. The two bosons present in the WW$\nu\nu$ and ZZ$\nu\nu$ final states decay in two fermion-antifermion pairs, so the final state is a 6-fermion final state.*

$$2m_V - 12 \text{ GeV } \leq m^1_{qq} + m^2_{qq} \leq 2m_V + 12 \text{ GeV}$$

$$|m^1_{qq} - m^2_{qq}| \leq 20 \text{ GeV}$$

$$m_{\nu\nu} \geq 100 \text{ GeV}$$

where V denotes a boson, m^1_{qq} and m^2_{qq} are the invariant masses of the two quark-antiquark pairs. The mass $m_{\nu\nu}$ is the invariant mass of the two neutrinos; the cut on $m_{\nu\nu}$ is applied to remove the contribution of diagrams involving the production of a Z boson followed by the decay Z→ $\nu\bar{\nu}$.

Figure 7.7 shows the distribution, at generator level, of $m_{\nu\nu}$, obtained after having applied the first two cuts. The Z peak is evident and not contributing to boson-boson scattering processes. As can be seen in Figure 7.7.(a), after the mass cuts defining the $WW\nu\nu$ signal the peak is more pronounced. In fact the cross section for the process $e^+e^- \to W^+W^-Z$, is higher than the one for the process $e^+e^- \to ZZZ$, due to the higher probability for the radiation of W boson off an electron, and to the vertex $\gamma/Z \to W^+W^-Z$, which is allowed in the Standard Model. On the contrary, vertices of four neutral gauge bosons are forbidden in the Standard Model, as explained in Chapter 2.

7.6 Background processes

The relevant background classes can be subdivided into three main classes of events:

- **6-fermion events.** To this background class belong all processes leading to a 6-fermion final state, and in particular to states of the type $q\bar{q}q\bar{q}\nu\bar{\nu}$, $q\bar{q}q\bar{q}e\nu$ and $q\bar{q}q\bar{q}ee$ excluding the $VV \to VV$ scattering process defined as signal. Thus a huge number of diagrams contributes to the production of 6-fermion events; some examples of such diagrams have been shown in Figure 7.6.

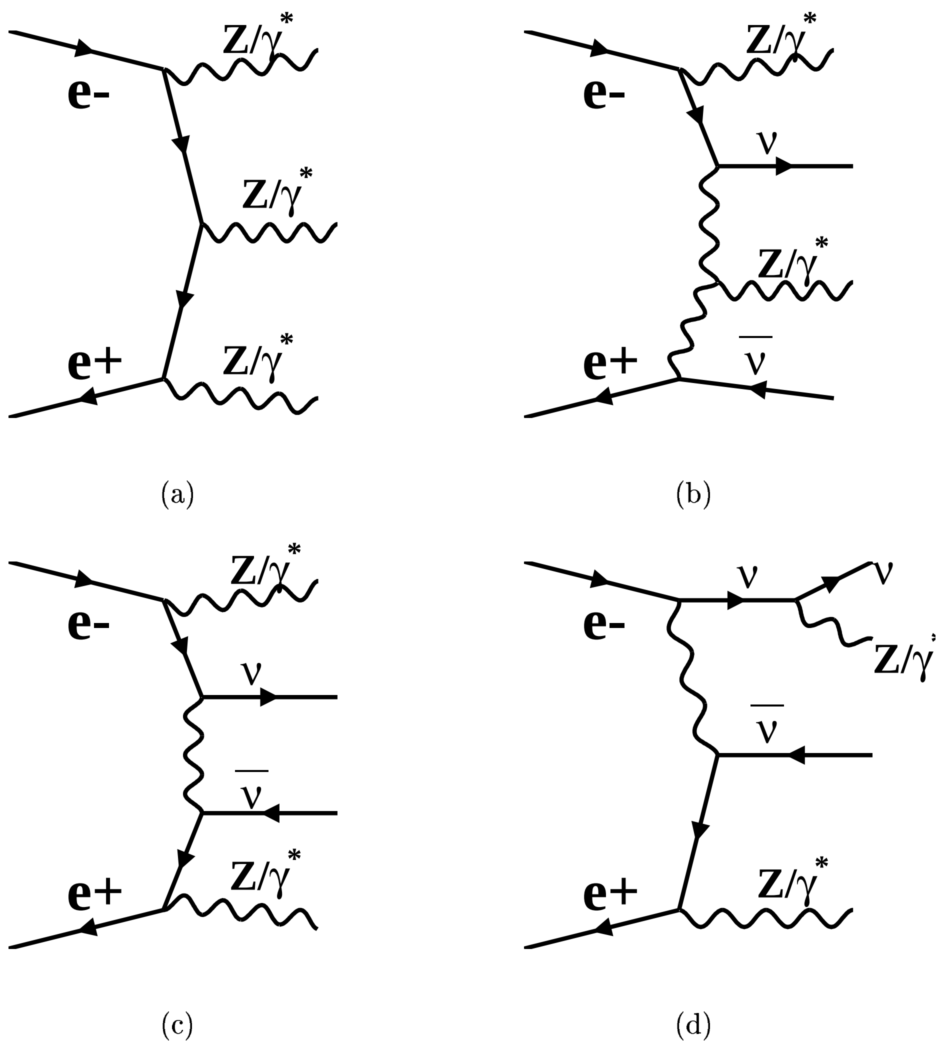

Figure 7.6: *The figure shows some of the 6-fermion processes which lead to* $q\bar{q}q\bar{q}\nu\bar{\nu}$ *final states and which constitute a background for the signal processes shown in Figure 7.5. Only processes involving hadronic decays of the bosons present in the event have been taken into account.*

The events of the class $q\bar{q}q\bar{q}e\nu$ are produced mainly through γW fusion diagrams shown in Figure 7.8.(a); here the scattering $\gamma W \rightarrow ZW$ leads to a 4-jet plus missing energy signature, similar to the signal topology. The incoming electron (or positron) radiates off a photon and is thus scattered with a very small azimuthal angle. Thus, as it will be shown in the following, the forward coverage of the detector is a fundamental issue for the identification and rejection of this event class.

The same considerations apply to the $q\bar{q}q\bar{q}ee$ background events, which are mainly produced through the Feynman diagram shown in Figure 7.8.(b). In this case both electron and positron radiate off a photon and are scattered in the very forward direction.

Together with the forward coverage of the detector, another fundamental issue for the rejection of the 6-fermion background is the detector resolution in the reconstruction of the boson masses; an optimal resolution allows in fact to separate W from Z bosons and thus identify the class which the event is belonging to.

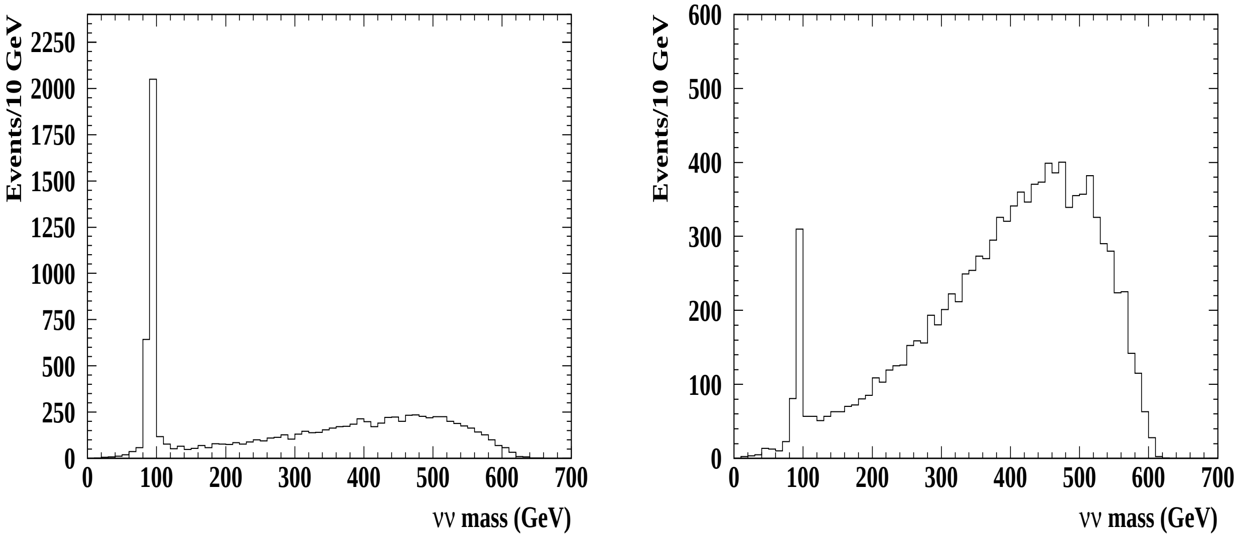

(a) (b)

Figure 7.7: *Distribution of the $\nu\bar{\nu}$ invariant mass in* $\mathrm{q\bar{q}q\bar{q}}\nu\bar{\nu}$ *events after the mass cuts defining the* $\mathrm{W^+W^-}\nu\bar{\nu}$ *(a) and the* $\mathrm{ZZ}\nu\bar{\nu}$ *phase space regions. The normalisation of the vertical scale is arbitrary.*

- **4-fermion events.** This event class has been already presented in Section 3.3, as it is one of the most relevant physics event classes at LEP2. The dominant contributions come from the production of W and Z pairs (the CC03 and NC02 diagrams introduced in Chapter 3). As it will be discussed in the following, the cross sections for these processes are some order of magnitudes bigger than the signal cross sections; in particular, the fully hadronic decay channels of the WW and ZZ events may constitute a potentially relevant background. These events however are characterised by having a vanishing missing momentum, thus being easily rejectable through cuts on the visible energy and momentum. In case the 4-quarks are generated through WW and ZZ production after Initial State Radiation, the missing momentum is not vanishing, but it's mostly pointing in the forward direction. The forward coverage of the detector becomes then an important issue for the rejection of this background.

- **2-fermion events.** Also the 2-fermion event class has been already described in Section 3.3, when discussing the LEP2 physics events. The cross section for the process $\mathrm{e^+e^-} \to \mathrm{q\bar{q}}$ is also some orders of magnitude bigger than that for the signal. Anyway, as for the 4-fermion background, the eventual missing momentum due to Initial State Radiation is directed along the beam pipe. This allows to easily reject the 2-fermion background through cuts on the visible energy and on the direction of the missing momentum.

- **$\mathrm{t\bar{t}}$ events**. At the TESLA Linear Collider operating at $\sqrt{s}$=800 GeV, the production of top-antitop pairs will be kinematically allowed (the mass of the top quark is $m_t = 174.3$ GeV [12]). The top-quark decays in a b-quark plus two other fermions, as shown in Figure 7.9. Therefore, the process $\mathrm{e^+e^-} \to \mathrm{t\bar{t}}$ is actually leading to a 6-fermion final state of the type $\mathrm{b\bar{b}f_1\bar{f}_2f_3\bar{f}_4}$. The decay channel which constitutes a relevant background for the $\mathrm{q\bar{q}q\bar{q}}\nu\bar{\nu}$ and $\mathrm{q\bar{q}q\bar{q}e}\nu$ signals is the channel $\mathrm{t\bar{t}} \to \mathrm{b\bar{b}q\bar{q}'}l\nu$, as the event topology resembles in this case the 4-jets plus missing energy signal. Due to the high cross section, the rejection of

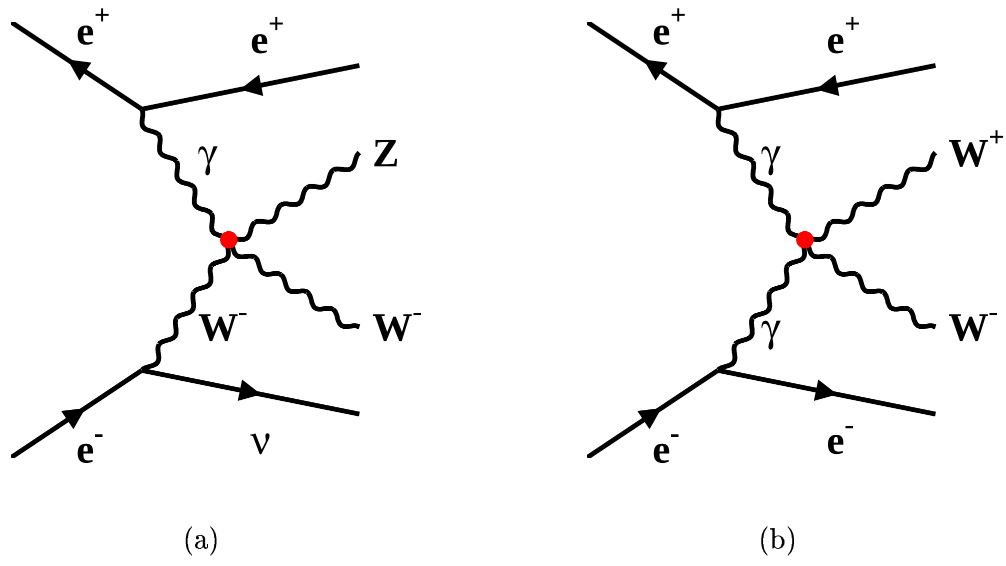

Figure 7.8: *Two of the most important processes contributing to the 6-fermion background. (a): Feynman diagram for the process* $\mathrm{e^+e^-} \rightarrow \mathrm{W^\pm Ze}\nu \rightarrow \mathrm{q\bar{q}q\bar{q}e^\mp}\nu$ *through* $\gamma\mathrm{W}$ *fusion; (b): Feynman diagram for the process* $\mathrm{e^+e^-} \rightarrow \mathrm{W^+W^-e^+e^-} \rightarrow \mathrm{q\bar{q}q\bar{q}e^+e^-}$ *(note that the decay of the two bosons in quark-antiquark pairs is not represented in the diagrams).*

this background process has to be carefully optimised. The characteristic of the $\mathrm{t\bar{t}}$ events, which can be exploited in the $\mathrm{e^+e^-} \rightarrow \mathrm{W^+W^-}\nu\bar{\nu} \rightarrow \mathrm{q\bar{q}q\bar{q}}\nu\bar{\nu}$ event selection, is the presence of two b-quarks in the final state. Thus, the tagging of the jets originating from b-quarks may be used, in case of the $\mathrm{e^+e^-} \rightarrow \mathrm{W^+W^-}\nu\bar{\nu} \rightarrow \mathrm{q\bar{q}q\bar{q}}\nu\bar{\nu}$ selection, as a veto against the $\mathrm{t\bar{t}}$ background. As the Z boson decays into a $\mathrm{b\bar{b}}$ pair with a branching ratio of about 15%, the same veto can not be applied in case of the $\mathrm{e^+e^-} \rightarrow \mathrm{ZZ}\nu\bar{\nu} \rightarrow \mathrm{q\bar{q}q\bar{q}}\nu\bar{\nu}$ selection. In this case however, another characteristic of the $\mathrm{t\bar{t}}$ events, which can be exploited as a veto, is the presence of an isolated lepton in the event.

7.7 Beam Polarisation

As discussed in Section 7.2, at the TESLA Linear Collider it will be possible to operate with polarised electron and positron beams. The foreseen polarisations are $P_- = 80\%$ for electrons and $P_+ = 40\%$ for positrons, where the polarisations are defined as follows:

$$P_- \equiv \frac{N^L_{e^-} - N^R_{e^-}}{N^L_{e^-} + N^R_{e^-}} \qquad\qquad P_+ \equiv \frac{N^R_{e^+} - N^L_{e^+}}{N^L_{e^+} + N^R_{e^+}}.$$

In these definitions, $N^{L(R)}_{e^-}$ is the number of left- (right-) handed electrons, and $N^{L(R)}_{e^+}$ is the number of left- (right-) handed positrons. As W bosons are coupling to left-handed electrons and right-handed positrons, a process involving one $e^- \rightarrow \mathrm{W^-}\nu$ vertex will be enhanced, with respect to the case of unpolarised beams, by the factor:

$$f = 2 \cdot \left(\frac{N^L_{e^-}}{N^L_{e^-} + N^R_{e^-}} \right) = 1 + \frac{N^L_{e^-} - N^R_{e^-}}{N^L_{e^-} + N^R_{e^-}} = 1 + P_-. \qquad (7.6)$$

This factor is the ratio between the probability $N^L_{e^-}/(N^L_{e^-} + N^R_{e^-})$ of having a left-handed electron in case the beam is polarised, and the probability 1/2 of having a left-handed electron in case

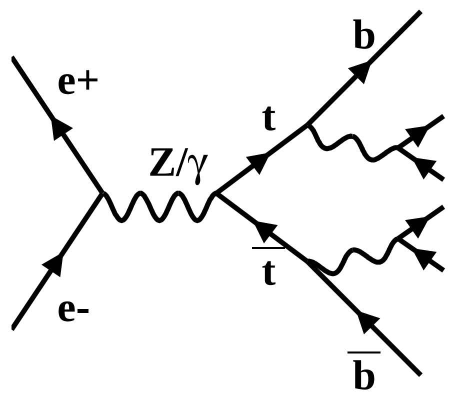

Figure 7.9: *Feynman diagram for the production of a* $t\bar{t}$ *pair, and its decay into 6 fermions.*

the beam is not polarised. The same consideration applies to the radiation of a W^+ boson off a positron, thus if also a $e^+ \to W^+\bar{\nu}$ vertex is involved in the Feynman diagram for the process the total enhancement factor is given by:

$$f = (1 + P_-) \cdot (1 + P_+) \tag{7.7}$$

This is the case of the two signal processes $e^+e^- \to W^+W^-\nu\bar{\nu} \to q\bar{q}q\bar{q}\nu\bar{\nu}$ and $e^+e^- \to ZZ\nu\bar{\nu} \to q\bar{q}q\bar{q}\nu\bar{\nu}$. For the $e^+e^- \to W^\pm Ze\nu \to q\bar{q}q\bar{q}e^\mp\nu$ process, which is dominated by the γW fusion subprocess, shown in the diagram in Figure 7.8.(a), the enhancement factor is $f_- = (1+P_-)$ for the diagram with a positron in the final state (the W^- is radiated off the electron) and $f_+ = (1 + P_+)$ for the diagram with an electron in the final state (where on the contrary a W^+ is radiated off a positron).

A smaller contribution to the $e^+e^- \to W^\pm Ze\nu \to q\bar{q}q\bar{q}e^\mp\nu$ process comes from the ZW $\to$ ZW scattering subprocess, where, instead of a γ, a Z is radiated off the electron or the positron. The vector and axial couplings of the Z to electrons are:

$$c_V = I^3 - 2\sin^2\theta_W Q_e = -\frac{1}{2} + 2\sin^2\theta_W \simeq -0.014 \tag{7.8}$$

$$c_A = I^3 = -\frac{1}{2} \tag{7.9}$$

thus the coupling is almost of purely axial type. This means that the same scaling factor as for the γW fusion diagrams holds for the diagrams with ZW $\to$ ZW scattering.

Thus the enhancement factor for the $q\bar{q}q\bar{q}e\nu$ cross section will be:

$$f \simeq \frac{1+P_-}{2} + \frac{1+P_+}{2} = 1 + \frac{P_- + P_+}{2} \tag{7.10}$$

The $q\bar{q}q\bar{q}ee$ background is almost not modified by polarisation. The contribution of the $e^+e^- \to W^+W^-e^+e^- \to q\bar{q}q\bar{q}e^+e^-$ diagram in Figure 7.8.(b), which corresponds to the subprocess $\gamma\gamma \to W^+W^-$, and which is largely dominating the other diagrams, is not modified. There are diagrams, leading to the $q\bar{q}q\bar{q}ee$ final state however, in which the W's both originate from the same fermion line. The contribution from this kind of diagrams increases by the factor

$1 + (P_- + P_+)/2$, but the effect on the total $\mathrm{q\bar{q}q\bar{q}ee}$ cross section is rather small (see in the following, in Table 7.2).

The same kind of considerations can be repeated to derive the scaling factors of the 4-fermion, $\mathrm{t\bar{t}}$ and $\mathrm{q\bar{q}}$ cross sections. The cross sections, calculated using the set of Monte Carlo generators discussed in the following Section 7.8, will be listed in the following Table 7.2.

7.8 Monte Carlo generators

The following set of Monte Carlo generators has been used for the simulation of the physics processes:

- **6-fermion**: when considering all tree-level Feynman diagrams contributing to the amplitude of an $\mathrm{e^+e^-} \to$6-fermion process, and their interference, the matrix elements may become very complicated (as in general up to $\mathcal{O}(10^3)$ diagrams may contribute), and the structure of the final state phase-space very difficult to handle. The event generator WHIZARD[71], combines known packages for generating matrix elements with a program which is able to sample a generic phase space, integrate the cross section and generate events. The matrix element generator used in this analysis is O'Mega [72], which can deal with final states with six particles, and which includes the terms of the Electroweak Chiral Lagrangian describing the $VV \to VV$ scattering in the matrix element calculation. The phase-space integration and the event generation are performed by WHIZARD[2].

  Besides that, WHIZARDcan generate events assuming polarised $e^\pm$ beams.

- **4-fermion, $\mathbf{t\bar{t}}$, $\mathbf{q\bar{q}}$**: the events of these classes have been generated using PYHTIA [45]. For $\mathrm{t\bar{t}}$ events, PYHTIA simulates also the decay of the $\mathrm{t\bar{t}}$ pair in six fermions.

For all event classes, the fragmentation and hadronization were simulated using JETSET [47], implementing the Lund string fragmentation model (see also Section 4.1).

7.9 Cross sections

The cross sections calculated using the Monte Carlo generators described in the previous section are shown in Table 7.2. The table shows the cross sections for the two signal classes and for the background classes[3], with no beam polarisation and with the beam polarisations foreseen at TESLA. As can be seen in the table, the 6-fermion processes which have the highest cross section are those leading to $\mathrm{q\bar{q}q\bar{q}e}\nu$ and $\mathrm{q\bar{q}q\bar{q}ee}$ final states. The dominating contributions to these final states come from the process $\mathrm{e^+e^-} \to \mathrm{W^\pm Ze}\nu \to \mathrm{q\bar{q}q\bar{q}e^\mp}\nu$ and $\mathrm{e^+e^-} \to \mathrm{W^+W^-e^+e^-} \to \mathrm{q\bar{q}q\bar{q}e^+e^-}$ respectively.

The cross sections for the other background processes, i.e. $\mathrm{t\bar{t}}$, 2-fermion and 4-fermion are some order of magnitudes higher than the signal ones. However, the event topologies of these background processes, discussed in the previous sections, and the optimal detector resolution allow to reject these background classes almost completely, as will be shown in the following chapter.

7.10 Detector simulation

To simulate the response of the TESLA detector, a parametric Monte Carlo has been used, SIMDET V3.1 [74]. This means that the reconstructed objects (tracks and energy clusters) are

[2] For the phase-space sampling and integration, WHIZARD makes use of the VAMP [73] integration program.

[3] Each of the two signal classes represents a background for the other one.

Channel	σ_{SM} (fb) no polarisation	σ_{SM} (fb) $P_{e^-} = 80\%$ $P_{e^+} = 40\%$
Signals		
$e^+e^- \to W^+W^-\nu\bar{\nu} \to q\bar{q}q\bar{q}\nu\bar{\nu}$	3.4	8.6
$e^+e^- \to ZZ\nu\bar{\nu} \to q\bar{q}q\bar{q}\nu\bar{\nu}$	1.7	4.3
6-fermion background		
$e^+e^- \to q\bar{q}q\bar{q}\nu\bar{\nu}$ (background)	3.5	5.5
$q\bar{q}q\bar{q}e\nu$	24.5	39.2
$q\bar{q}q\bar{q}ee$	225	286
$e^+e^- \to t\bar{t} \to X$	344	619
4-fermion and 2-fermion background		
$e^+e^- \to ZZ \to q\bar{q}q\bar{q}$	168	302
$e^+e^- \to W^+W^- \to q\bar{q}q\bar{q}$	2340	5900
$e^+e^- \to q\bar{q}$	5100	9180

Table 7.2: *Standard Model cross sections of signal and background processes at $\sqrt{s}$=800 GeV. The signal processes are defined through the phase-space cuts described in Section 7.5. The second column shows the cross sections for unpolarised beams, while the cross sections in the third column are calculated assuming a 80% e^- polarisation (left-handed) and a 40% e^+ polarisation (right-handed). The $q\bar{q}$ background doesn't include the $e^+e^- \to t\bar{t}$ class, whose cross sections are separately reported in the table.*

not derived from a full simulation of the detector, but are computed by smearing the generated 4-momenta of the objects in the event. The smearing parameters have been derived by a full GEANT [51] simulation of the TESLA detector (the package BRAHMS [75]), and are functions of the particles 4-momenta. The setup of the detector is the one presented in Section 7.2, and is the one which has been used for the set of physics performance studies presented in the TESLA Technical Design Report [40].

As discussed in the previous sections, the detector issues which are particularly relevant for the VV scattering analyses are the mass resolution (i.e. the jet energy and momentum resolution) and the forward detector coverage. The detector performance with respect to the mass resolution can be estimated in terms of the separation power of W bosons from Z bosons, using $e^+e^- \to W^+W^-\nu\bar{\nu} \to q\bar{q}q\bar{q}\nu\bar{\nu}$ and $e^+e^- \to ZZ\nu\bar{\nu} \to q\bar{q}q\bar{q}\nu\bar{\nu}$ events at $\sqrt{s}$=800 GeV (after applying the signal definition cuts to remove the non-resonant 6-fermion background contributions). In Figure 7.10 the reconstructed masses after the detector simulation are shown, for the two classes of events. The plot shows the excellent separation of the two contributions; the resolution for the invariant $q\bar{q}$ mass is about 4%.

The forward coverage of the detector is another important issue for the measurement of the missing momentum and for the tagging of forward electrons, for example in $q\bar{q}q\bar{q}e\nu$ and $q\bar{q}q\bar{q}ee$ events. As seen in Section 7.2, the very forward coverage of the TESLA detector is guaranteed by the Instrumented Mask, which includes the Low Angle Tagger (LAT) and the Lumi Calorimeter (LCAL), covering up to a polar angle $\theta = 5$ mrad. In this study however the conservative choice of using detector instrumentation up to 23.5 mrad (so only the LAT) was adopted, thus avoiding the results to be affected by uncertainties on the machine background. The acceptance of the LAT and of the LCAL for $q\bar{q}q\bar{q}ee$ events is shown in Table 7.3.

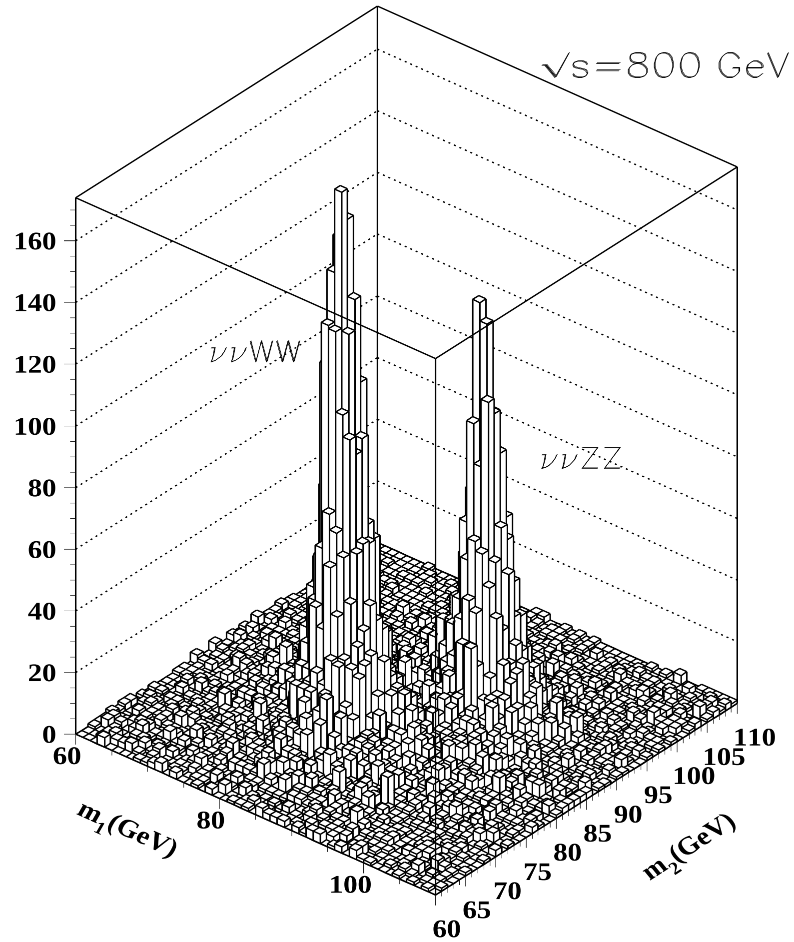

Figure 7.10: *Reconstructed* q$\bar{\text{q}}$ *invariant masses after the detector simulation. In the histogram the two* q$\bar{\text{q}}$ *masses are plotted versus each other, for $WW\nu\nu$ and $ZZ\nu\nu$ events which satisfy the signal definition described in Section 7.5*

N. of tagged e	Event fraction (%)		
	w/o Mask	+LAT	+LAT+LCAL
0	63	49	36
≥1	37	51	64
2	6	11	19

Table 7.3: *The table shows the fraction of* q$\bar{\text{q}}$q$\bar{\text{q}}$ee *events in which 0, 1 or 2 electrons can tagged, without the instrumented mask (second column), including the instrumented mask with the LAT only (third column), and including the instrumented mask with both LAT and LCAL. The fractions are computed assuming 100% tagging efficiency.*

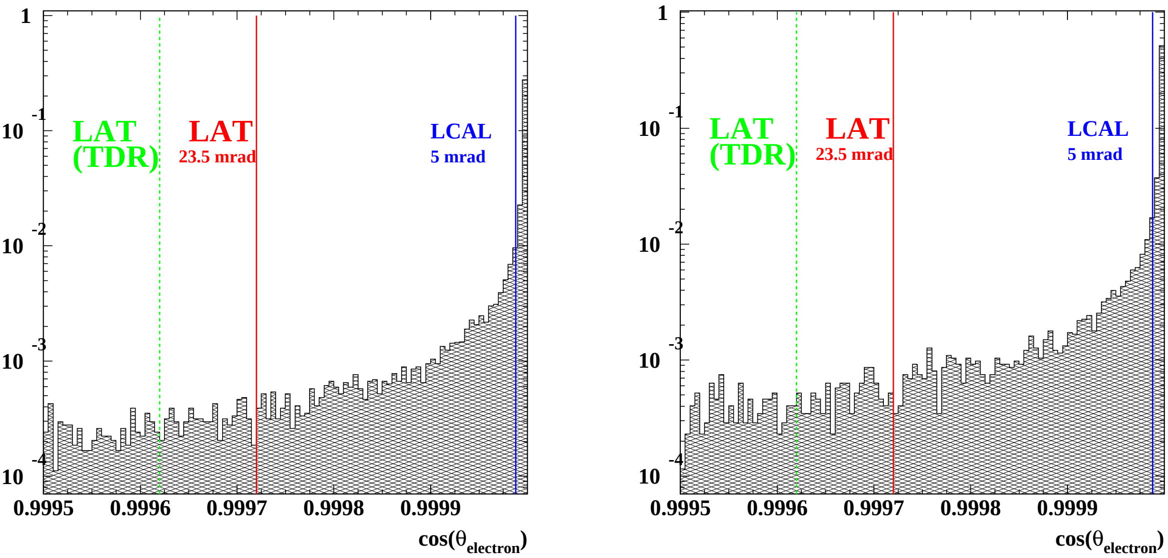

Figure 7.11: *Distribution of the electron polar angle in case of (a):* $q\bar{q}q\bar{q}e\nu$ *events and (b):* $q\bar{q}q\bar{q}ee$ *events. The distribution in the very forward section of the detector is shown in the plots. The vertical lines indicate the position of the inner borders of the detectors of the Instrumented Mask: the Low Angle Tagger (LAT) and the Lumi Calorimeter (LCAL). Concerning the LAT, two different lines show the detector border assumed in this study (23.5 mrad) and the detector border foreseen in the final TESLA detector design (27 mrad) [40].*

8. Strong Electroweak Symmetry Breaking and Quartic Couplings at TESLA

8.1 Introduction

In this chapter an experimental study of the sensitivity of the TESLA Linear Collider to signals of Strong Electroweak Symmetry breaking will be presented. The TESLA detector, and the physics processes relevant for an analysis of the scattering of W and Z bosons, have been introduced in Chapter 7. This chapter will describe a Monte Carlo study of the analyses of the processes $e^+e^- \to W^+W^-\nu\bar{\nu} \to q\bar{q}q\bar{q}\nu\bar{\nu}$ and $e^+e^- \to ZZ\nu\bar{\nu} \to q\bar{q}q\bar{q}\nu\bar{\nu}$, for a center of mass energy $\sqrt{s} = 800$ GeV and with beam polarisations 80% and 40% for the electron and positron beam, respectively. The event generators used, and the cross sections for the single event classes, have been already discussed in the previous chapter.

The first part of this chapter will describe the two event selections, giving in particular more details on the $e^+e^- \to ZZ\nu\bar{\nu} \to q\bar{q}q\bar{q}\nu\bar{\nu}$ selection. All the relevant background processes, discussed in Section 7.6, have been taken into account, and the expected error on the cross section measurement has been optimised.

The second part of the chapter will treat the estimate of the expected sensitivity to the coefficients of the Electroweak Chiral Lagrangian (see in Section 2.5.2). The sensitivity was evaluated through an extended maximum likelihood fit of the differential distributions resulting from the event selections. The expected limits on the coefficients α_i can be translated into the expected TESLA sensitivity to new physics scales connected to the Strong Electroweak Symmetry Breaking.

8.2 Analysis strategy

The strategy of the analysis is similar for the two selections of the $e^+e^- \to W^+W^-\nu\bar{\nu} \to q\bar{q}q\bar{q}\nu\bar{\nu}$ and $e^+e^- \to ZZ\nu\bar{\nu} \to q\bar{q}q\bar{q}\nu\bar{\nu}$ events. Due to the smaller cross-section, a likelihood-based selection has been developed for the $ZZ\nu\nu$ channel, while the $WW\nu\nu$ selection is a cut-based one. The $ZZ\nu\nu$ selection will be described in more detail here, while a summary of the main $WW\nu\nu$ selection cuts will be given.

8.3 $e^+e^- \to ZZ\nu\bar{\nu} \to q\bar{q}q\bar{q}\nu\bar{\nu}$ Event selection

Event reconstruction and preselection

The selection of the $e^+e^- \to ZZ\nu\bar{\nu} \to q\bar{q}q\bar{q}\nu\bar{\nu}$ events can be outlined as follows:

- The first step of the selection consists of forcing the tracks and clusters of the event in four jets, using the Durham algorithm [55] (see also in Section 4.3 for a description of the algorithm).

- The $ZZ\nu\nu$ hypothesis is then tested via a kinematic fit to the jet 4-vectors, forcing the two jet pairs to have the same mass. As this is the only constraint applied, the fit is called 1C-fit (due to the presence of the two neutrinos in the final state in fact, the energy and momentum conservation constraints can not be applied). The kinematic fit is in this case not as crucial as for the OPAL experiment (see in Section 4.4) to improve the mass resolution. Since the Z bosons can decay as $\mathrm{Z} \to \mathrm{b\bar{b}}$, and the B-hadrons may decay semileptonicallly, neutrinos may be present in the jets which are originated from the b-quarks. In this case, the kinematic fit can compensate the loss in resolution deriving from the unmeasured momentum of the neutrinos.

- As in case of the OPAL ZZ analysis (see in Section 5.4), the pairing of the four jets has to be chosen out of 3 possible combinations. The method used is a likelihood method similar to the one described in Section 5.4. For each combination a likelihood probability is calculated, whose inputs are the mass resulting from the 1C-fit, the χ^2 probability of the fit, and the difference between the two reconstructed di-jet masses. The reference distributions are filled using $\mathrm{ZZ}\nu\nu$ signal events, and the two classes are given by the right and the wrong combinations, respectively.

  The combination giving the highest value of the likelihood is chosen to be the correct one. This method gives a rate of correct pairings of 93%. The much better performance of the likelihood pairing with respect to the results of similar the OPAL analysis (where the pairing is correct for ~80% of the events), is due mainly to the much better resolution of the TESLA detector.

A preselection is applied, consisting of a series of cuts mainly aiming to significantly reduce the 4-fermion, $\mathrm{q\bar{q}}$ and $\mathrm{t\bar{t}}$ background classes. The preselection cuts are the following:

- $200< E_{miss} <650$ GeV: E_{miss} denotes in this case the event missing energy. This cut selects the range of values of the missing energy expected from the signal events. It is mostly effective against the 4-fermion and the $\mathrm{q\bar{q}}$ background classes, from which no missing energy is expected. The visible energy for events of these background classes may actually be smaller than the $\mathrm{e^+e^-}$ center of mass energy, in case the interaction takes place after initial state radiation. To cut these events another preselection cut on the direction of the missing momentum is applied.

- $|\cos(\theta_{P_{miss}})| < 0.99$: a cut on the cosine of the polar angle of the missing momentum is applied to remove 4-fermion and $\mathrm{q\bar{q}}$ events which take place after the radiation of a photon by one of the initial state particles, with the photon going unobserved along the beam-pipe (i.e. being produced at a polar angle smaller than 23.5 mrad)

- $|\cos(\theta_{P_{Emax}})| < 0.99$: a cut on the cosine of the polar angle of the most energetic charged track is applied in order to remove events with high energetic electrons in the very forward direction. Thus, this cut removes mainly the events of the $\mathrm{q\bar{q}q\bar{q}e}\nu$ and $\mathrm{q\bar{q}q\bar{q}ee}$ background classes, for which the electron can be tagged in the detector (see in Table 7.3).

- at least two charged tracks in each jet are required: this cut is mainly intended to reject events with leptons, like for example those in which the W or Z bosons decay leptonically, or $\mathrm{e^+e^-} \to \mathrm{t\bar{t}}$ background events, followed by the decay $\mathrm{t\bar{t}} \to \mathrm{b\bar{b}q\bar{q}}l\nu$.

- in order to further reduce the $\mathrm{t\bar{t}} \to \mathrm{b\bar{b}q\bar{q}}l\nu$ background, an event is rejected if one of the four most energetic charged tracks is isolated. A charged track is considered to be isolated if the sum of the energies of the objects (tracks and clusters) in a 10 degrees cone around the track is less than 2 GeV.

Likelihood selection

After the preselection cuts, a likelihood discriminant is calculated, out of the following input variables:

1. The mass resulting from the 1C-fit described above.
2. The jet pairing likelihood described in the previous section. In fact, the reference distributions for the jet pairing likelihood are built using only signal events, so the likelihood value can be used also as a sensitive variable for the separation of the signal from the background.
3. M_{recoil}: the recoil mass, which is defined as $M_{recoil} = \sqrt{E^2_{miss} - P^2_{miss}}$, where E_{miss} and P_{miss} are the event missing energy and momentum.
4. $|\cos(\theta_{P_{miss}})|$: the cosine of the polar angle of the missing momentum.
5. $|\cos(\theta_{P_{Emax}})|$: the cosine of the polar angle of the most energetic charged track in the event.
6. E_{max}: the energy of the most energetic charged track in the event.

The distributions of the variables used as input for the likelihood calculation are shown in Figure 8.1 for the different classes of events. The distribution of the likelihood discriminant for the different event classes is shown in Figure 8.2; the events with a likelihood value greater than 0.84 are selected. The cut has been optimised in such a way that the product of the efficiency times the purity is maximal, i.e. such that the error on the cross section measurement is minimal. The mass distribution of the selected events is shown in Figure 8.3. The figure shows the reconstructed mass of the two $q\bar{q}$ pair (thus, the plot is filled with two entries per event), where the pairing has been chosen with the likelihood method. For the signal events which are passing the likelihood cut, the rate of correct pairings increases to ~99%.

In order to increase the purity of the selection, a further cut on the two di-quark reconstructed masses can be applied. The two masses are required to satisfy the condition:

$$85 \text{ GeV} < M_{q\bar{q}} < 100 \text{ GeV} \tag{8.1}$$

The results of the $ZZ\nu\nu$ selection are summarised in Table 8.1. The table shows the number of expected events after all cuts for each of the examined classes, assuming $\sqrt{s} = 800$ GeV, 1000 fb^{-1} of integrated luminosity and e^- and e^+ beam polarisations of 80% and 40%, respectively. This value of the integrated luminosity corresponds to approximately 2 years of data taking at TESLA. The expected relative error on the cross section measurement $\Delta\sigma/\sigma$ is 2.8%. This result can be compared with the expected error in case of no polarisation of the beams, for the same integrated luminosity: in this case the expected error would be $\Delta\sigma/\sigma = 3.2\%$ [76].

8.4 $e^+e^- \to W^+W^-\nu\bar{\nu} \to q\bar{q}q\bar{q}\nu\bar{\nu}$ Event selection

The $e^+e^- \to W^+W^-\nu\bar{\nu} \to q\bar{q}q\bar{q}\nu\bar{\nu}$ event selection will be here only shortly described, more details can be found in [76].

The jets are reconstructed using the LUCLUS algorithm [45]. The scheme of this algorithm is similar to the DURHAM scheme described in section 4.3 and in [55] but the distance measure between the objects i and j is in this case given by:

$$d^2_{ij} = \frac{4|\vec{p}_i|^2|\vec{p}_j|^2\sin^2(\theta_{ij}/2)}{(|\vec{p}_i| + |\vec{p}_j|)^2} \tag{8.2}$$

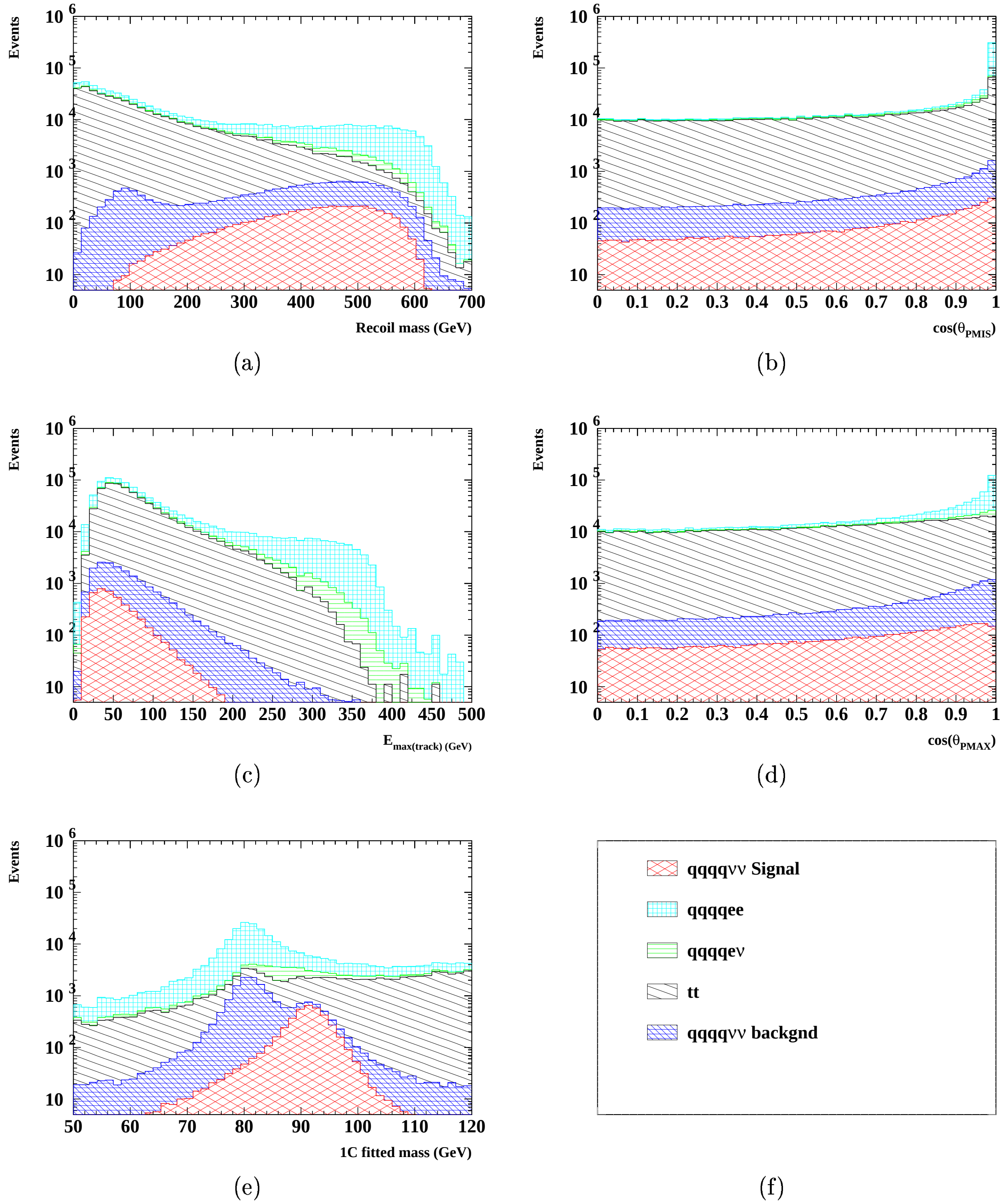

Figure 8.1: *Distributions of the likelihood variables used as input for the calculation of the $ZZ\nu\nu$ likelihood. The events which are used to fill the distributions are those passing the preselection cuts.*

where the $\vec{p}_i$, $\vec{p}_j$ are the momenta of the two objects, and θ_{ij} is the angle between them. The two objects with the smallest relative distance d_{ij} are joined to one (i.e. their 4-momenta are added) if d_{ij} is smaller than a parameter d_{join}. The parameter d_{join} was set to 7 GeV. Only

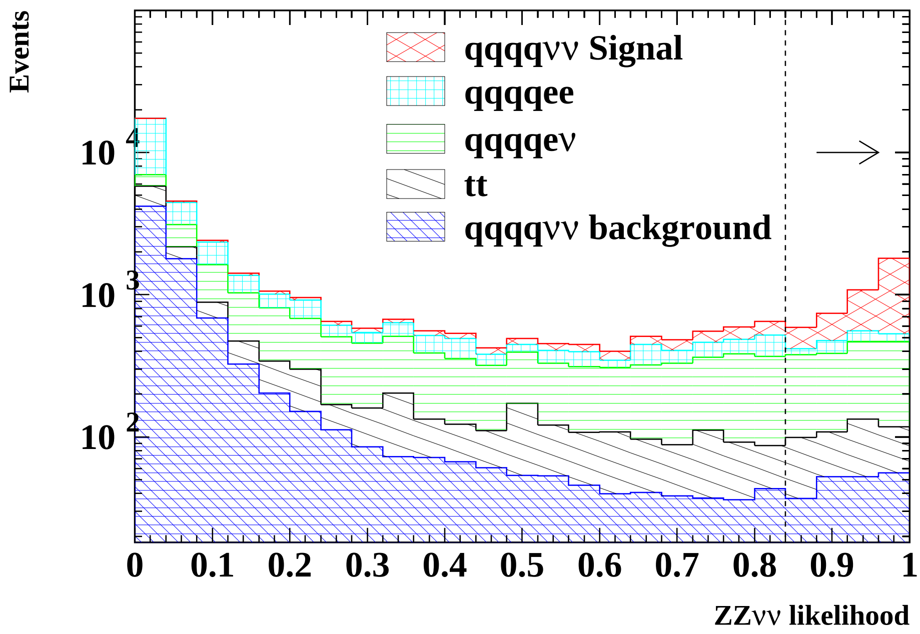

Figure 8.2: *Distribution of the likelihood discriminant for the ZZ$\nu\nu$ selection. The distributions for signal and background events are shown in the plot. The vertical line shows the position of the cut on the likelihood value. All events with a likelihood greater than 0.84 are selected.*

Event Class	Number of events	Efficiency (%)
Signal		
$e^+e^- \to ZZ\nu\bar{\nu} \to q\bar{q}q\bar{q}\nu\bar{\nu}$	2168 ± 10	50.7
Background		
$q\bar{q}q\bar{q}\nu\bar{\nu}$	174 ± 5	1.3
$q\bar{q}q\bar{q}e\nu$	993 ± 20	2.5
$q\bar{q}q\bar{q}ee$	250 ± 60	$9\cdot10^{-2}$
$e^+e^- \to WW, ZZ \to q\bar{q}q\bar{q}$	negligible	$< 10^{-3}$
$e^+e^- \to t\bar{t} \to X$	143 ± 20	$2\cdot10^{-2}$
$e^+e^- \to q\bar{q}$	negligible	$< 10^{-3}$

Table 8.1: *Results of the selection of* $e^+e^- \to ZZ\nu\bar{\nu} \to q\bar{q}q\bar{q}\nu\bar{\nu}$ *events. The table shows the numbers of events expected from each channel, at* $\sqrt{s}$ = 800 *GeV, and assuming 1000 fb*$^{-1}$ *of integrated luminosity. The last column shows, for signal and background processes, the fraction of events which are passing the selection.*

events with three, four or five jets are selected. Each event is then forced in four jets, and the jet-pairing is chosen, out of the three possible combinations, in such a way that the product $|M_{ij}-M_{\mathrm{W}}|\cdot|M_{kl}-M_{\mathrm{W}}|$ is minimal, where M_{ij} and M_{kl} are the di-jet invariant masses resulting from each combination, and M_W is the mass of the W boson. To suppress two- and four-fermion background and contamination from ZWW events with the Z decaying invisibly, the transverse energy in the event E_{trans} is required to be between 150 GeV and 600 GeV and the recoil mass, defined as described in Section 8.3, to be above 200 GeV. To reduce background classes leading

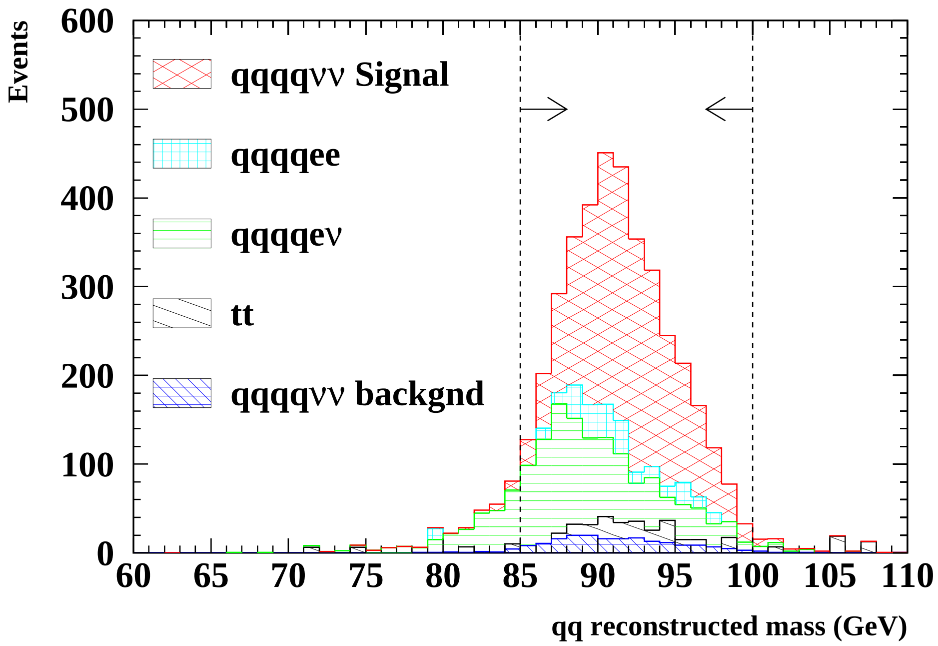

Figure 8.3: *Distribution of the* $q\bar{q}$ *masses for the events passing the cut on the likelihood discriminant of the ZZνν selection. Both reconstructed masses are filling the histogram, which has thus two entries per event. The two vertical lines show the position of the final mass cuts. All events with both di-jet masses included in the range between 85 and 100 GeV are selected.*

to isolated leptons, in particular $t\bar{t}$, the number of charged tracks per jet is required to be greater than 2.

The $t\bar{t}$ background class is also strongly reduced by rejecting the events with more than 1 tagged b-jet. In fact, the main part of the $t\bar{t}$ background comes from the events in which the $t\bar{t}$ pair is decaying as: $t\bar{t} \to b\bar{b}q\bar{q}l\nu$. The purity of the b-tagging has been parametrised as a function of the jet energy according to the parametrisation described in [77], The efficiency is fixed at 80%, and for the vertex detector a 2 cm CCD option is chosen. This cut, rejecting events with more than 1 tagged b-jet, is also effective for the rejection of 6-fermion events involving the production and decay of at least a Z boson, i.e. $ZZ\nu\nu$ and $WZe\nu$ events[1].

To remove the background events coming from other 6-fermion final states, in particular those from WWee and $WZe\nu$ processes, a cut on the missing momentum is necessary. As already discussed for the $ZZ\nu\nu$ selection, the characteristics of these background classes is the missing momentum from the electrons, which are mostly lost in the beam pipe. Thanks to the excellent hermeticity of the TESLA detector, these background classes can be strongly reduced by a cut requiring $P_T^{WW} > 40$ GeV, where P_T^{WW} denotes the transverse momentum of the boson pair (i.e. the event transverse momentum).

A further cut to remove combinatorial background and events with Z bosons requires both reconstructed boson masses to be above 60 GeV and below 88 GeV. Two of the selection variables on which cuts are applied, namely the recoil mass and P_T^{WW}, are shown in Figure 8.4. The results of the analysis are shown in Table 8.2, in terms of expected number of events (for an integrated luminosity of 1000 pb^{-1}) and efficiency. The expected relative error on the cross

[1] The Branching Ratio of the decay $Z \to b\bar{b}$ is in fact about 15% [12]

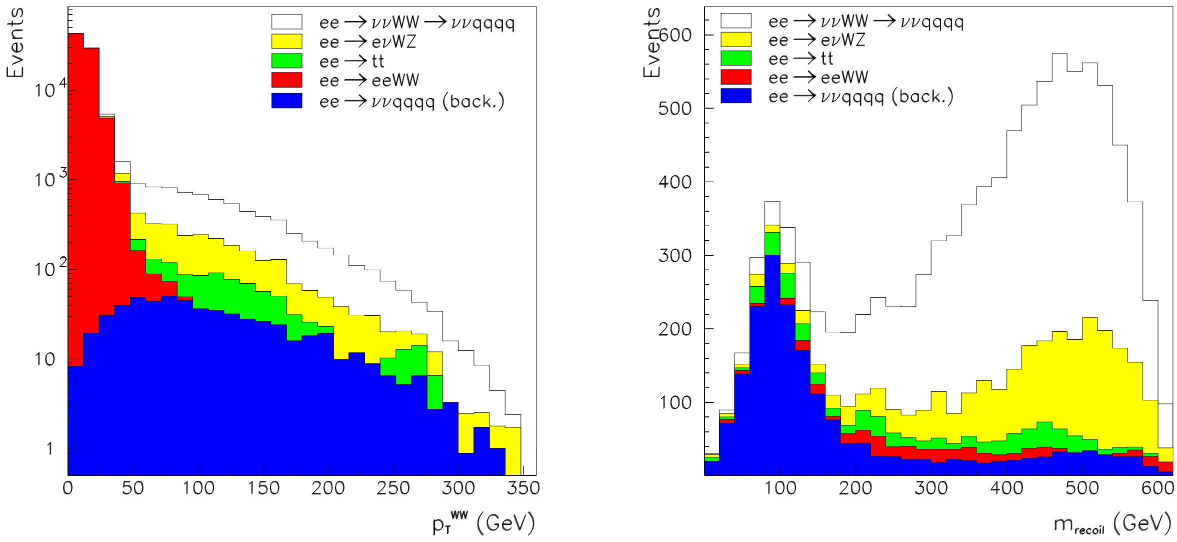

(a) (b)

Figure 8.4: *Distributions of two of the variables used for the* $e^+e^- \to W^+W^-\nu\bar{\nu} \to q\bar{q}q\bar{q}\nu\bar{\nu}$ *selection, for signal and background event classes. Figure (a) shows* P_T^{WW}*, the event transverse momentum, while Figure (b) shows the event recoil mass. Only the events passing the cut* $P_T^{WW} > 40$ *GeV are used to fill the histograms in Figure (b).*

section measurement $\Delta\sigma/\sigma$ is 1.7%. As for the $ZZ\nu\nu$ selection, this result can be compared with the expected error in case of no polarisation of the beams, for the same integrated luminosity: in this case the expected error would be $\Delta\sigma/\sigma = 2.0\%$ [76].

Event Class	Number of events	Efficiency (%)
Signal		
$e^+e^- \to W^+W^-\nu\bar{\nu} \to q\bar{q}q\bar{q}\nu\bar{\nu}$	5077±23	58.8
Background		
$q\bar{q}q\bar{q}\nu\bar{\nu}$	509±8	5.2
$q\bar{q}q\bar{q}e\nu$	1728±34	4.4
$q\bar{q}q\bar{q}ee$	257±57	$9 \cdot 10^{-2}$
$e^+e^- \to WW, ZZ \to q\bar{q}q\bar{q}$	negligible	$< 10^{-3}$
$e^+e^- \to t\bar{t} \to X$	444±75	$6 \cdot 10^{-2}$
$e^+e^- \to q\bar{q}$	negligible	$< 10^{-3}$

Table 8.2: *Results of the selection of* $e^+e^- \to W^+W^-\nu\bar{\nu} \to q\bar{q}q\bar{q}\nu\bar{\nu}$ *events. The table shows the number of events expected from each channel, at* $\sqrt{s} = 800$ *GeV, and assuming 1000* fb^{-1} *of integrated luminosity. The last column shows, for signal and background processes, the fraction of events which are passing the selection.*

8.5 Fit of the $SU(2)_c$ custodial couplings

As discussed in Chapter 2, the processes

$$e^+e^- \to ZZ\nu\bar{\nu} \to q\bar{q}q\bar{q}\nu\bar{\nu} \quad \text{and} \quad e^+e^- \to W^+W^-\nu\bar{\nu} \to q\bar{q}q\bar{q}\nu\bar{\nu} \tag{8.3}$$

(corresponding to the scattering subprocesses WW→ZZ and WW→WW) are sensitive to values of the coefficients α_4 and α_5 of the Electroweak Chiral Lagrangian different from the expected Standard Model value of zero, and thus to possible signals of SEWSB. The signatures of strong interactions of the W and Z have been described in Section 2.5.5. They are, in general, changes of the total cross section and of the average polarisation of the final state bosons with respect to the Standard Model expectation. This means that the angular distributions of the bosons and of their decay products vary, for non-zero values of the couplings, with respect to their Standard Model expectations. Besides, the impact of the strong interaction terms rises with the center of mass energy of the $VV \to VV$ scattering subprocess. Thus, the distribution of the invariant mass of the two bosons in the final state is also sensitive to the coefficients α_4 and α_5.

The sensitivity to the anomalous couplings α_4 and α_5 is determined by using the total cross section and the differential distributions of the following kinematic variables:

1. $|\cos\theta_{W,Z}|$: where $\theta_{W,Z}$ is the production polar angle of the two bosons.
2. $|\cos\theta^*_{decay}|$: where θ^*_{decay} is the polar angle of the decay products in the reference frame of each boson. No discrimination between quarks and anti-quarks has been done in this analysis.
3. M_{VV}: the invariant mass of the two bosons.

Thus, two entries per event, one for each of the reconstructed bosons, fill the fitted distributions.

The sensitivity is determined through an Extended Maximum Likelihood fit to the distributions expected from a 1000 fb^{-1} Standard Model sample with $\alpha_4 = \alpha_5 = 0$. For each bin, the likelihood probability associated to a given point in the (α_4, α_5) space is given by the Poisson probability of observing N_{ijk}^{SM} events if $N_{ijk}(\alpha_4, \alpha_5)$ are expected (where the indices ijk denote the bin in the 3-dimensional differential distributions):

$$P_{ijk}(\alpha_4, \alpha_5) = \frac{N_{ijk}(\alpha_4, \alpha_5)^{N_{ijk}^{SM}}}{N_{ijk}^{SM}!} e^{-N_{ijk}(\alpha_4,\alpha_5)} \tag{8.4}$$

The likelihood probability as a function of the couplings is then given by the product over all bins of the probabilities $P_{ijk}(\alpha_4, \alpha_5)$:

$$L(\alpha_4, \alpha_5) = \prod_{ijk} P_{ijk}(\alpha_4, \alpha_5) \tag{8.5}$$

The number of expected events, includes both signal and background events which are passing the event selection.

As the Electroweak Chiral Lagrangian is linear in the couplings α_i (see Section 2.5.2), the total cross section, like the differential cross section at any given point of the 6-fermion phase space is given by an hyper-paraboloid in the (α_4, α_5) space. Thus, to determine the number of signal events expected in any bin of the differential distributions, it is sufficient to generate Monte Carlo samples for six different values of the couplings and then fit the number of events in each bin with an hyper-paraboloid in the (α_4, α_5) space. Thus $N_{ijk}(\alpha_4, \alpha_5)$ can be in such a way analytically calculated.

The point in the (α_4, α_5) space where the likelihood reaches its maximum value, corresponds to the fitted value of the parameters. The sensitivity of the coupling measurement can be estimated calculating the 68% and 90% confidence level limits on the parameters, corresponding to $-\Delta\log L = 1.15$ and $-\Delta\log L = 2.3$, where $\Delta\log L$ is the negative variation of the logarithm of the likelihood with respect to the maximum value.

It can be interesting to study the improvement of the sensitivity obtained by including each of the differential distributions in the likelihood fit. Figure 8.5 shows the results of the fit applied to the events selected by the WW$\nu\nu$ and ZZ$\nu\nu$ selections, when using only the total event rate, and when successively including the differential distributions. As can be seen, fitting also the distributions of the three kinematical variables permits to exclude the second intersection between the allowed regions, which appears when looking just at the total cross section. The results of the fit for the two analyses, and their combination, are shown in Figure 8.6. The combination is performed summing the two logL distributions; possible correlated systematics between the two analysis have not been taken into account at the moment.

The following section will summarise the results of the fit in terms of the sensitivity to the Electroweak Chiral Lagrangian coefficients and to the scales of new physics.

Strong Electroweak Symmetry Breaking Scales

The limits obtained by the combination of the results of the $e^+e^- \to W^+W^-\nu\bar{\nu} \to q\bar{q}q\bar{q}\nu\bar{\nu}$ and $e^+e^- \to ZZ\nu\bar{\nu} \to q\bar{q}q\bar{q}\nu\bar{\nu}$ analysis are shown in Table 8.3. The table shows the expected limits obtained assuming that only one coupling is non-vanishing. The limit values correspond to the 68% confidence level intervals, i.e. to the value $\Delta\chi^2 = 1$.

As seen in Section 2.5.2, the coefficients of the Electroweak Chiral Lagrangian are related to the scales of new physics through the relation:

$$\frac{\alpha_i}{16\pi^2} = \left(\frac{v}{\Lambda_i^*}\right)^2. \tag{8.6}$$

where v=246 GeV is the Fermi scale. The expected sensitivity to the couplings α_i can thus be translated into the sensitivity to scales of new physics (i.e. strong interactions of the W and Z bosons). The results are also shown in Table 8.3.

TESLA Results 1000 fb^{-1}, $P_{e^-} = 80\%, P_{e^+} = 40\%$			
Coupling	Lower limit	Upper limit	New physics scales
α_4	-1.1	+0.8	Λ_4^*=2.9 TeV
α_5	-0.4	+0.3	Λ_5^*=4.9 TeV
LHC Results [33] 100 fb^{-1}			
Coupling	Lower limit	Upper limit	New physics scales
α_4	-0.2	+1.7	Λ_4^*=2.3 TeV
α_5	-0.4	+1.2	Λ_5^*=2.8 TeV

Table 8.3: *One dimensional expected lower and upper limits limits, at 68% confidence level, on the Strong Electroweak Symmetry Breaking parameters α_4 and α_5, and the corresponding expected sensitivities to new physics scales. The table compares the results of this work, i.e. the limits expected at the TESLA Linear Collider, with the results expected at LHC for an integrated luminosity of 100 fb^{-1} [33]. The TESLA limits are computed assuming an integrated luminosity of 1000 fb$^-1$ at $\sqrt{s}$=800 GeV, with beam polarisation of 80% and 40% for the electron and positron beam, respectively.*

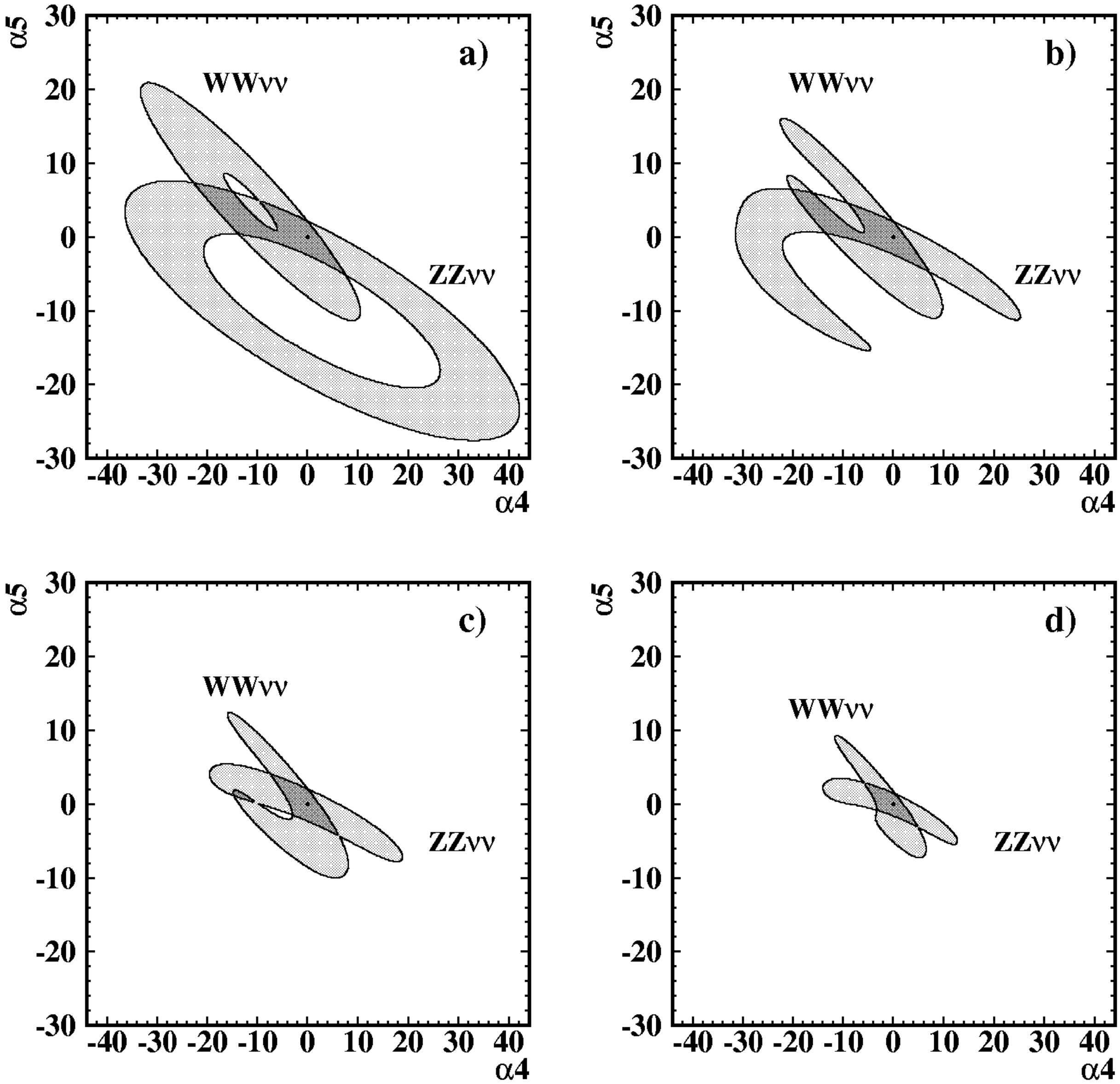

Figure 8.5: *Expected 90% confidence level limit contours on the couplings α_4 and α_5, obtained by using in the fit: (a) the total cross section alone, (b) including the differential distribution in the bosons polar angle (c) including the differential distribution in the bosons and the decay fermions polar angles (d) including also the differential distribution in the invariant mass M_{VV}. The shaded areas represent the allowed region, the rest of the (α_4, α_5) space is excluded at 90% confidence level.*

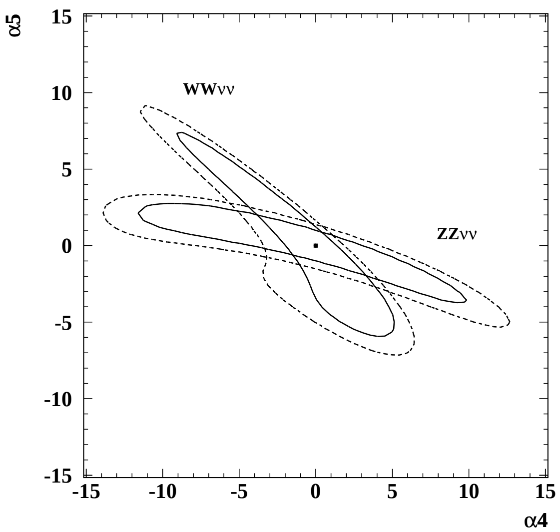

(a)

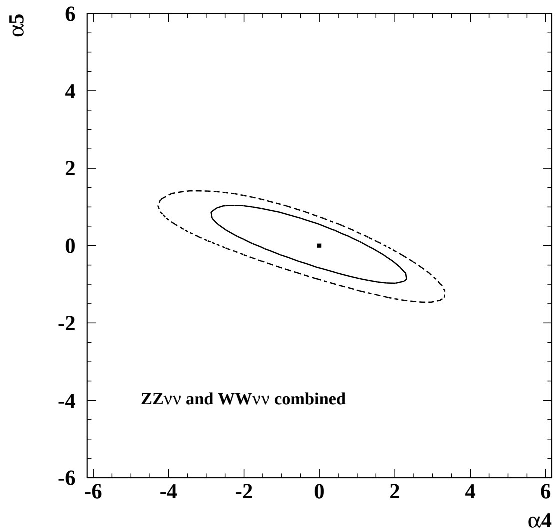

(b)

Figure 8.6: *Expected limit contours in the (α_4, α_5) plane, obtained by the two analyses. Figure (a) shows the results of the two analyses separately, while figure (b) shows their combination. The continuous lines represent the 68% confidence level contours (corresponding to $-\Delta\log L = 1.15$), while the dashed lines are the 90% confidence level limit contours (corresponding to $-\Delta\log L = 2.3$).*

The table also compares the results of this work with those expected at the LHC proton-proton collider [33]. The LHC results are those expected from the analysis of 100 fb^{-1} of data. The integrated luminosity of 1000 fb^{-1} considered in this work corresponds to approximately two years of TESLA data taking at $\sqrt{s}$ =800 GeV.

The expected limits on α_4 and α_5 can be compared with the indirect limits obtained from precision measurements at the Z-pole and at low energy, reported in Table 2.5. As can be seen comparing the values, the direct measurement allows to put much stronger constraints than the indirect ones.

As seen in Chapter 2, Section 2.5.2, the largest value of the new physics scales Λ for the chiral expansion to be valid is $\sim$3 TeV, corresponding to values of O(1) of the Chiral Lagrangian coefficients. The sensitivity of the TESLA linear collider is thus sufficient to reveal possible Strong Electroweak Symmetry Breaking signals.

It should also be noticed that the results have been obtained by looking only at the fully hadronic channels. The combination with all other boson decay channels would improve the statistics of about a factor two. Besides that, the limits scale with the integrated luminosity approximately as $\propto 1/\sqrt{\mathcal{L}}$.

9. Summary

In the first part of this thesis, the study of Z boson pair production in e^+e^- collisions with the OPAL detector at LEP has been presented. The data analysed have been taken in the years 1999 and 2000, at center of mass energies ranging from 192 to 208 GeV. The event selection for the fully hadronic decay channel, i.e. for events of the type $e^+e^- \to ZZ \to q\bar{q}q\bar{q}$ has been outlined. In particular, the selection of events of the type $e^+e^- \to ZZ \to q\bar{q}b\bar{b}$ has been described in more detail. This selection exploits the identification of the b-quarks to reduce significantly the amount of background from WW events.

The measured cross sections, combined for all ZZ decay channels, are in agreement with the Standard Model expectation, and read:

$$\begin{aligned}
\sigma_{ZZ}(192\ \mathrm{GeV}) &= 1.13^{+0.46}_{-0.39}(\mathrm{stat.})^{+0.13}_{-0.09}(\mathrm{syst.})\ \mathrm{pb}\\
\sigma_{ZZ}(196\ \mathrm{GeV}) &= 1.19^{+0.27}_{-0.24}(\mathrm{stat.})^{+0.10}_{-0.08}(\mathrm{syst.})\ \mathrm{pb}\\
\sigma_{ZZ}(200\ \mathrm{GeV}) &= 1.09^{+0.25}_{-0.23}(\mathrm{stat.})^{+0.09}_{-0.07}(\mathrm{syst.})\ \mathrm{pb}\\
\sigma_{ZZ}(202\ \mathrm{GeV}) &= 0.94^{+0.37}_{-0.32}(\mathrm{stat.})^{+0.09}_{-0.06}(\mathrm{syst.})\ \mathrm{pb}\\
\sigma_{ZZ}(205\ \mathrm{GeV}) &= 1.07^{+0.26}_{-0.24}(\mathrm{stat.})^{+0.10}_{-0.08}(\mathrm{syst.})\ \mathrm{pb}\\
\sigma_{ZZ}(207\ \mathrm{GeV}) &= 1.07^{+0.20}_{-0.19}(\mathrm{stat.})^{+0.09}_{-0.07}(\mathrm{syst.})\ \mathrm{pb}
\end{aligned}$$

The method of optimal observables, which allows to combine the full kinematic of each reconstructed event in a set of observables with optimal sensitivity, has been used to fit the γZZ and ZZZ anomalous couplings, on the basis of the selected $e^+e^- \to$ZZ events. The Standard Model forbids γZZ and ZZZ couplings at tree level. As no deviation from the Standard Model expectation (i.e. vanishing anomalous couplings) was observed, limits on the couplings have been set. The 95% Confidence Level limits, obtained by combining the results of all ZZ decay channels, are the following:

Coupling	95% C.L. lower limit	95% C.L. upper limit
f_4^γ	-0.55	0.64
f_5^γ	-0.97	0.31
f_4^Z	-0.36	0.36
f_5^Z	-0.36	0.36

The second part of this work was dedicated to an experimental study of WW scattering at the planned e^+e^- Linear Collider TESLA. In case no Higgs with a mass smaller than ~800 GeV is found, the study of the scattering of massive vector bosons assumes central relevance in studying how the breaking of the $SU(2)_L \otimes U(1)_Y$ symmetry is realized. The TESLA sensitivity to Strong Electroweak Symmetry Breaking signals in WW→WW and WW→ZZ scattering processes has been estimated. An experimental analysis of the process $e^+e^- \to ZZ\nu\bar{\nu} \to q\bar{q}q\bar{q}\nu\bar{\nu}$, including the simulation of the detector response and of all relevant background processes, has been developed, and has been described in detail in this work. A similar analysis for the process $e^+e^- \to W^+W^-\nu\bar{\nu} \to q\bar{q}q\bar{q}\nu\bar{\nu}$ has been also presented. Assuming 1000 fb^{-1} of integrated luminosity, corresponding to approximately 2 years at TESLA, and e^-,e^+ beam polarisations of 80% and 40% respectively, the expected errors on the cross section measurement for the two processes are:

$$\frac{\Delta\sigma}{\sigma}(\mathrm{e^+e^-} \to \mathrm{ZZ}\nu\bar{\nu} \to \mathrm{q\bar{q}q\bar{q}}\nu\bar{\nu}) = 2.8\%$$
$$\frac{\Delta\sigma}{\sigma}(\mathrm{e^+e^-} \to \mathrm{W^+W^-}\nu\bar{\nu} \to \mathrm{q\bar{q}q\bar{q}}\nu\bar{\nu}) = 1.7\%$$

WW scattering at low energies can be effectively described by the electroweak chiral Lagrangian, containing the Standard Model gauge interactions plus five additional 4-dimensional terms. Expected limits on the coefficients of the chiral Lagrangian have been derived from the results of a binned maximum likelihood fit of the differential distributions of the selected $\mathrm{e^+e^-} \to \mathrm{ZZ}\nu\bar{\nu} \to \mathrm{q\bar{q}q\bar{q}}\nu\bar{\nu}$ and $\mathrm{e^+e^-} \to \mathrm{W^+W^-}\nu\bar{\nu} \to \mathrm{q\bar{q}q\bar{q}}\nu\bar{\nu}$ events. The limits on the α_4, α_5 coefficients, and the corresponding new physics scales which the TESLA Linear Collider is expected to be sensitive to, are listed in the following table: These limits scale approximately as $\propto 1/\sqrt{\mathcal{L}}$, and have been

TESLA Results
1000 fb^{-1}, $P_{e^-} = 80\%, P_{e^+} = 40\%$

Coupling	Lower limit	Upper limit	New physics scales
α_4	-1.1	+0.8	Λ_4^*=2.9 TeV
α_5	-0.4	+0.3	Λ_5^*=4.9 TeV

obtained considering only the hadronic decay channels of the W and Z bosons. Including the other decay channels would improve the statistics by about a factor of two.
As seen in the first chapter of this work, in absence of resonances which are lighter than ~3 TeV, one expects from dimensional analysis, in a strongly interacting symmetry breaking sector: $\Lambda_i^* \simeq$3 TeV. So this work shows with realistic simulations, that the TESLA experiment can probe the parameters of a strong electroweak symmetry breaking sector.

Bibliography

[1] S. L. Glashow, Nucl. Phys. 22 (1961) 579.
S. Weinberg, Phys. Rev. Lett. 19 (1967) 1264.
A. Salam, in *Elementary Particle Theory.* N Svartholm ed. (1968)

[2] LEP Higgs Working Group, *Search for the Standard Model Higgs Boson at LEP*, LHWG Note/2002-01, July 2002.
ALEPH 2002-024 CONF 2002-013. DELPHI 2002-088-CONF-621. L3 Note 2766. OPAL Technical Note TN721.

[3] F. Halzen, A. D. Martin, *Quarks & Leptons*, Wiley & Sons 1984

[4] A. Pich, *The Standard Model of Electroweak Interactions*, hep-ph/9412274 (1994)

[5] P. W. Higgs, Phys. Lett. 12 (1964) 132 Phys. Rev. Lett. 13 (1964) 585

[6] J. Goldstone, Nuov. Cim. 19 (1961) 154

[7] G. 't Hooft, Nucl. Phys. B33 (1971) 173

[8] M. Herrero, *The Standard Model*, hep-ph/9812242 (1998);
M. Herrero, *Introduction to the symmetry breaking sector*, hep-ph/9601286 (1996)

[9] H. Georgi, Nucl. Phys. B361 (1991) 339

[10] K. J. F. Gaemers and G. J. Gounaris, Z. f. Phys. C1 (1979) 259

[11] K. Hagiwara, R. D. Peccei and D. Zeppenfeld, Nucl. Phys. B282 (1987) 253

[12] Particle Data Group, D.E. Groom et al., Eur. Phys. J. C15 (2000) 1.

[13] E. Fermi, Nuovo Cim. 11 (1934) 1.

[14] G. Arnison et al. (UA1 Collaboration), Phys. Lett. B122 (1983) 103,
G. Arnison et al. (UA1 Collaboration), Phys. Lett. B126 (1983) 398,
M. Banner et at. (UA2 Collaboration), Phys. Lett. B122 (1983) 476.

[15] G. Gounaris, D. Schildknecht, Phys. Lett. B263 (1991) 291.
A. De Rujula, M. B. Gavela, O. Pène, F. J. Vegas, Nucl. Phys. B357 (1991) 311.

[16] G. J. Gounaris, J. Layssac and F. M. Renard hep-ph/9910395

[17] G. J. Gounaris, J. Layssac and F. M. Renard hep-ph/9910395

[18] R. W. Brown, K. O. Mikaelian, Phys. Rev. D19 (1979) 922.

[19] H. Voss, *Messung der Drei-Eichboson-Kopplungen in $W^+W^- \to \mathrm{q\bar{q}}l\bar{\nu}_l$ Ereignissen mit optimalen Observablen bei OPAL*, PhD. Thesis, BONN-IR-2000-04, Bonn University April 2000.

[20] A. Méndez and A. Pomarol, Phys. Lett. B272 (1991) 313

[21] D. Chang, W. Keung, and P. B. Pal, Phys. Rev. D51 (1995) 1326

[22] K. Agashe, N. G. Deshpande, Phys. Lett. B456 (1999) 60.

[23] V. Novikov, *Field Theory and the Standard Model*, in Proceedings of the 1998 European School of High-Energy Physics, CERN 99-04 (1999)

[24] H. He, Y. Kuang, C. Yuan, hep-ph/9704276 (1997)

[25] T. L. Barklow et al., in *Snowmass 1996. New directions for high-energy physics*, and hep-ph/9704217

[26] E. Boos, H. He, W. Kilian, A. Pukhov, C Yuan and P. Zerwas, Phys. Rev. D61 (2000) 077901; Phys. Rev. D57 (1998) 1553

[27] M. Chanowitz, M. Golden, H. Georgi, *Universal scattering theorems for strongly interacting W's and Z's* LBL-22119 (1986)

[28] B. Lee, C. Quigg and H. Tacker, Phys. Rev. Lett. 38 (1977) 883; Phys. Rev. D16 (1977) 1519;
D. Dicus and V. Mathur, Phys. Rev. D7 (1973) 3111.

[29] S. Weinberg, Phys. Rev. D13 (1976) 974; Phys. Rev. D19 (1979) 1277;
L. Susskind, Phys. Rev. D20, (1979) 2619.

[30] T. Appelquist and C. Bernard, Phys. Rev. D22 (1980) 200;
A. C. Longhitano, Phys. Rev. D22 (1980) 1166; Nucl. Phys. B188 (1981) 118;
T Appelquist and G. Wu, Phys. Rev. D51 (1995) 240.

[31] J. Gasser, H. Leutwyler, Ann. Phys. (N.Y.) 158 (1984) 142; Nucl. Phys. B250 (1985) 465.

[32] A. Brunstein, O.J.P. Éboli, M.C. Gonzalez-Garcia, Phys. Lett. B375 (1996) 233

[33] A. S. Bekyaev et al., Phys. Rev. D59 (1998) 015022

[34] G. Azuelos et al., *Electroweak Physics*, hep-ph/003275

[35] J. D. Bjorken, S. D. Drell, *Relativistic quantum mechanics* McGraw-Hill (1964)

[36] J. M. Cornwall, D. N. Levin, G. Tiktopoulos, Phys. Rev. D10 (1974) 1145;
C. E. Vayonakis, Lett. Nuovo Cimento 17 (1976) 383;
B. W. Lee, C. Quigg, H. Thacker, Phys. Rev. D16 (1977) 1519.

[37] S. Weinberg, Physica A96:327 (1979);
A. Manohar, H. Georgi, Nucl. Phys. B234 (1984) 189;
H. Georgi, L. Randall, Nucl. Phys. B276 (1986) 241.

[38] The LEP Collaborations ALEPH, DELPHI, L3, OPAL, the LEP Electroweak Working Group and the SLD Heavy Flavour and Electroweak Groups, *A Combination of Preliminary Electroweak Measurements and Constraints on the Standard Model*, CERN-EP/2001-098 and LEPEWWG/2001-02.

[39] The OPAL Collaboration, K. Ahmet et al., Nucl. Instrum. Meth. A305 (1991) 275;
S. Anderson et al., Nucl. Instrum. Meth. A403 (1998) 326;
B.E. Anderson et al., IEEE Trans. Nucl. Sci. 41 (1994) 845;
M. Arignon et al., Nucl. Instrum. Meth. 313 (1992) 103;
M. Arignon et al., Nucl. Instrum. Meth. 333 (1993) 330;
J.T. Baines et al., Nucl. Instrum. Meth. A325 (1993) 271;
D.G. Charlton, F. Meijers, T.J. Smith, and P.S. Wells, Nucl. Instrum. Meth. A325 (1993) 129.

[40] *TESLA. The Superconducting Electron-Positron Linear Collider with an Integrated X-Ray Laser Laboratory.* Technical Design Report. DESY 2001-011, ECFA 2001-209, TESLA Report 2001-23, TESLA-FEL 2001-05.

[41] J. Fujimoto et al., Comput. Phys. Commun. 100 (1997) 128.

[42] S. Jadach, W. Placzek, M. Skrzypek, B. F. L. Ward, and Z. Was, Comput. Phys. Commun. 119 (1999) 272.

[43] F. A. Berends, R. Pittau and R. Kleiss, Comput. Phys. Commun. 85 (1995) 437.

[44] S. Jadach, W. Placzek, and B. F. L. Ward, Phys. Rev. D56 (1997) 6939.

[45] T. Sjöstrand, Comput. Phys. Commun. 82 (1994) 74.

[46] S. Jadach, B. F. L. Ward, and Z. Was, Phys. Lett. B449 (1999) 97.

[47] B. Andersson, G. Gustafson, T. Sjöstrand, Phys. Lett. B94 (1980) 211;
T. Sjöstrand, M. Bengtsson, Comp. Phys. Comm. 43 (1987) 367.

[48] G. Marchesini et al., Comput. Phys. Commun. 67 (1992) 465.

[49] R. Engel and J. Ranft, Phys. Rev. D54, (1996) 4244.

[50] The OPAL Collaboration, J. Allison et al., Nucl. Instr. Meth. A317 (1992) 47;
The OPAL Collaboration, J. Allison et al., Comp. Phys. Comm. 47 (1987) 55.

[51] R. Brun et al., *Simulation program for particle physics experiment, GEANT: user guide and refernce manual*, CERN DD 78-2 (1978)

[52] The OPAL Collaboration, *Study of Z Pair Production and Anomalous Couplings in* e^+e^- *Collisions at* $\sqrt{s}$ *between 190 and 209 GeV*, OPAL Physics Note PN482, July 2001.

[53] M. Verzocchi, *REW99: a library of routines for reweighting four fermion Monte Carlo samples based on the grc4f matrix elements*, OPAL Technical Note 618, August 1999.

[54] OPAL Collaboration, K. Ackerstaff et al., Eur. Phys. J. C2 (1998) 213;
S. Mihara, S. Yamashita, *MT 3.00, a new algorithm to calculate energy flow based on MT package*, OPAL Technical Note 575, November 1998;
T. Omori, S. Asai, I. Nakamura, *Attempt to Compensate Energy in OPAL Calorimeter Complex based on MT package*, OPAL Technical Note 447, December 1996;
T. Omori, S. Asai, I. Nakamura, S. Yamashita, *A Matching Algorithm: MT Package*, OPAL Technical Note 381, July 1996.

[55] Y. Dokshitzer, J. Phys. G17 (1991) 1537;
N. Brown, W. J. Stirling, Phys. Lett. B252 (1990) 657;
S. Bethke, Z. Kunszt, D. Soper, W. J. Stirling, Nucl. Phys. B370 (1992) 310;
S. Catani et al., Phys. Lett. B269 (1991) 432;
N. Brown, W. J. Stirling, Z. Phys. C53 (1992) 629.

[56] W. Bartel et al., Z. Phys. C33 (1986) 23.

[57] S. Yamashita, *Attempt to develop new jet-particle association methods for four-jet topology with OPAL detector*, OPAL Technical Note TN579, November 1998.

[58] A. G. Frodesen, O. Skjeggestad, H. Tofte *Probability and Statistics in Particle Physics*, Universitetsforlaget, Bergen-Oslo-Tromso

[59] OPAL Collaboration, G. Abbiendi et al., Eur. Phys. J. C7 (1999) 407.

[60] I. Nakamura, S Yamashita, *LB150: A new B-tagging Tool for LEP2*, OPAL Technical Note TN576, November 1998;
S. Yamashita, I. Nakamura, *LB160: Upgraded B-tagging for LEP2*, OPAL Technical Note TN578, November 1998.

[61] OPAL Collaboration, R. Akers et al., Z Phys. C63 (1994) 197;
L. del Pozo, *Jet finding with a cone algorithm*, OPAL Technical Note TN170, June 1993.

[62] O. Cooke, C. Jones, *Neural Network Electron and Photon Conversion Identification*, OPAL Technical Note TN556, July 1998.

[63] G. Parisi, Phys. Lett. B74 (1978) 65;
J. F. Donoghue, F. E. Low and S. Y. Pi, Phys. Rev. D20 (1979) 2759.

[64] OPAL Collaboration, K. Ackerstaff et al., CERN PPE/97-101, Eur. Phys. J. C2 (1998) 441-472.

[65] H. Rick, S. Rosati, *Details of the Fully Hadronic Z Pair Selection at* $\sqrt{s} = 183$ *GeV and 189 GeV*, OPAL Technical Note TN634, December 1999

[66] LEP Heavy Flavour Working Group, *Parameters for the LEP/SLD Heavy Flavour Results for Summer 1998 Conferences*, LEPHF/98-01 (1998).

[67] OPAL Collaboration, *Search for Neutral Higgs Bosons in* $\mathrm{e^+e^-}$ *collisions at* $\sqrt{s}$*=192-202 GeV*, OPAL Physics Note 426, March 2000.

[68] OPAL Collaboration, G. Abbiendi et. al., Phys. Lett. B476 (2000) 256-272

[69] M. Warsinsky, *Untersuchung des Prozesses* $\mathrm{e^+e^-} \rightarrow ZZ$ *am LEP-Speicherring mit Hilfe von optimalen Observablen*, Diplomarbeit, Bonn University, February 2001, BONN-IB-2001-05.

[70] The LEP Collaborations ALEPH, DELPHI, L3, OPAL and the LEP TGC Working Group. *A Combination of Preliminary Results on Triple Gauge Boson Couplings Measured by the LEP Experiments.*, LEPEWWG/TGC/2002-01, April 2002.

[71] W. Kilian, *WHIZARD 1.0: A generic Monte-Carlo integration and event generation package for multi-particle processes*, (see http://www-ttp.physik.uni-karlsruhe.de/Progdata/whizard/), LC-TOOL-2001-039.

[72] T. Ohl, in *Proceedings of 7th International Workshop on Advanced Computing and Analysis Techniques in Physics Research (ACAT 2000)*, [hep-ph/0011243]; in *Proceedings of 5th International Linear Collider Workshop (LCWS 2000)*, [hep-ph/0011287];
M. Moretti, T. Ohl, J. Reuter, *O'Mega: An Optimizing Matrix Element Generator*, (see http://heplix.ikp.physik.tu-darmstadt.de/ ohl/omega/), LC-TOOL-2001-040.

[73] T. Ohl, Comput. Phys. Commun., 120 (1999) 13.

[74] M. Pohl and H. Schreiber, *SIMDET-version 3, a parametric Montecarlo for a TESLA detector*, DESY 99-030, March 1999.

[75] T. Behnke, G. Blir et al. *BRAHMS: A Monte Carlo for a detector at a 500 GeV to 800 GeV Linear Collider*, LC-TOOL-2001-005, January 2001. In *2nd ECFA/DESY Study 1998-2001* 1425-1438

[76] R. Chierici, S. Rosati and M. Kobel, in *Proceedings of the V International Linear Collider Workshop*, FNAL, 24-28 October 2000. Published in *Batavia 2000, Physics and experiments with future linear e+ e- colliders* 544-549
R. Chierici, S. Rosati and M. Kobel, *Strong Electroweak Symmetry Breaking Signals in WW Scattering at TESLA*, LC-PHSM-2001-038, February 2001.

[77] R. Hawkings, *Vertex detector and flavour tagging studies for the TESLA Linear Collider*, LC-PHSM-2000-021, February 2000

A. OPAL quality criteria of tracks and energy clusters. Multi-hadronic final states.

A.1 Tracks quality criteria

Good tracks must have at least 20 hits in the Jet Chamber, and the number of hits must be at least 50% of the maximum possible number of hits according to the track polar angle. The track parameters must satisfy the following conditions: $d_0 \geq 2.5$ cm and $z_0 \geq 40.0$ cm. The transverse momentum of the track must be at least 0.12 GeV. The polar angle must be in the range $|\cos\theta| \leq 0.985$.

For the reconstruction of secondary vertices, these further requirements are applied to the tracks: $p \geq 0.5$ GeV, $d_0 \leq 0.3$ cm and $\sigma_{d_0} \leq 0.1$ cm.

A.2 Energy clusters quality criteria

Energy depositions in the electromagnetic calorimeter (ECAL-clusters) must satisfy the following criteria: (a) in the barrel $E \geq 0.1$ GeV and at least one block per cluster; (b) in the endcaps $E \geq 0.25$ GeV and at least 2 blocks per cluster.

The quality criteria for the energy depositions in the hadronic calorimeter are instead the following: in the barrel and in the endcaps $E \geq 0.6$ GeV and in the poletips $E \geq 2.0$ GeV.

The energy depositions in the detectors close to the beam axis must satisfy the following conditions: Forward Detector (FD) $E \geq 1.5$ GeV; Gamma Catcher (GC) $E \geq 5.0$ GeV, Silicon-Tungsten Calorimeter (SW) $E \geq 0.5$ GeV.

B. OPAL selection of hadronic final states

The criteria used to select hadronic events are based on energy clusters in the electromagnetic calorimeter and the charged track multiplicity, and have been developed for the selection of hadronic events at center of mass energies $\sqrt{s} > 130$ [64].

Clusters in the barrel region are required to have an energy of at least 100 MeV, and clusters in the endcap detectors are required to contain at least two adjacent lead glass blocks and to have an energy of at least 200 MeV. Tracks are required to have at least 20 measured space points. The point of closest approach to the nominal beam axis is found, and required to lie less than 2 cm in the $r - \phi$ plane and less than 40 cm along the beam axis from the nominal interaction point. Tracks are also required to have a mimimum momentum component transverse to the beam direction of 50 MeV.

The following requirements are then applied to select hadronic events:

- To reject leptonic final states, events are required to have high multiplicity: at least 7 electromagnetic clusters and at least 5 tracks.
- Background from two-photon events was reduced by requiring a total energy deposited in the electromagnetic calorimeter of at least 14% of the center of mass energy: $R_{vis} \equiv \sum E_{clus}/\sqrt{s} > 0.14$, where E_{clus} is the energy of each cluster.
- Any remaining background from beam-gas and beam-wall interactions is removed, and two-photon events further reduced, by requiring an energy balance along the beam direction which satisfies: $R_{bal} \equiv |\sum(E_{clus} \cdot \cos\theta)|/\sum E_{clus} < 0.75$, where θ is the polar angle of the cluster.

C. Likelihood method

The aim of an event selection is to classify events into two or more classes (e.g. into signal and background) by analysing a set of m observables with discriminating power. By using a *Likelihood method* it is in general possible to obtain a better performance of the selection in terms of efficiency and purity, than simply applying a set of cuts on the m observables.

In the likelihood method the discriminating variables are combined in a single variable, the so-called likelihood probability. For each of the n events classes, and for each of the m observables x_i, the normalised probability density functions $f_i^j(x_i)$ (with $i = 1, m$ and $j = 1, n$) are calculated on the basis of Monte Carlo events. The probability $p_i^j(x_i)$ that having measured the value x_i for the observable i, the event belongs to the class j, is given by:

$$p_i^j = \frac{f_i^j(x_i)}{\sum_{k=1}^{n} f_i^k(x_i)}. \tag{C.1}$$

Having measured the m variables x_1,...,x_m, the likelihood for the class j is then given by the normalised product of the probabilities for the single variables:

$$L^j = \frac{\prod_{l=1}^{m} p_l^j(x_l)}{\sum_{k=1}^{n} \prod_{l=1}^{m} p_l^k(x_l)}. \tag{C.2}$$

The likelihood can assume, by definition, values in the range between 0 and 1. If the m observables are uncorrelated, the likelihood L^j can be interpreted as the probability that the event belongs to the class j. In general, the events of the class j peak in correspondance of the value 1, while events of the other classes peak close to 0.